RADIATING INSTABLITY OF NONZONAL OCEAN CURRENTS

by

Igor V. Kamenkovich

B.Sc Moscow Institute of Physics and Technology, Moscow, Russia
(1991)

Submitted in partial fulfillment of the
requirements for the degree of

Doctor of Philosophy

at the

MASSACHUSETTS INSTITUTE OF TECHNOLOGY

and the

WOODS HOLE OCEANOGRAPHIC INSTITUTION

September 1996
[February 1997]

Signature of Author ....
Joint Program in Physical Oceanography
Massachusetts Institute of Technology
Woods Hole Oceanographic Institution
October 22, 1996

Certified by ....

Joseph Pedlosky
Senior Scientist,
Woods Hole Oceanographic Institution
Thesis Supervisor

Accepted by ....

Paola Malanotte-Rizzoli
Chairman, Joint Committee for Physical Oceanography
Massachusetts Institute of Technology
Woods Hole Oceanographic Institution

RADIATING INSTABLITY OF NONZONAL OCEAN CURRENTS.

by

Igor V. Kamenkovich

Submitted in partial fulfillment of the requirements for the degree of
Doctor of Philosophy at the Massachusetts Institute of Technology
and the Woods Hole Oceanographic Institution
October 22, 1996

Abstract

This thesis addresses the question of how a highly energetic eddy field could be generated in the interior of the ocean away from the swift boundary currents. The energy radiation due to the temporal growth of non-trapped (radiating) disturbances in such a boundary current is thought to be one of the main sources for the described variability. The problem of stability of an energetic current, such as the Gulf Stream, is formulated. The study then focuses on the ability of the current to support radiating instabilities capable of significant penetration into the far-field and their development with time.

The conventional model of the Gulf Stream as a zonal current is extended to allow the jet axis to make an angle to a latitude circle. The linear stability of such a nonzonal flow, uniform in the along-jet direction on a beta-plane, is first studied. The stability computations are performed for piece-wise constant and continuous velocity profiles. New stability properties of nonzonal jets are discussed. In particular, the destabilizing effect of the meridional tilt of the jet axis is demonstrated. The radiating properties of nonzonal currents are found to be very different from those of zonal currents. In particular, purely zonal flows do not support radiating instabilities, whereas flows with a meridional component are capable of radiating long and slowly growing waves.

The nonlinear terms are then included in the consideration and the effects of the nonlinear interactions on the radiating properties of the solution are studied in detail. For these purposes, the efficient numerical code for solving equation for the QG potential vorticity with open boundary conditions of Orlanski's type is constructed. The results show that even fast growing linear solutions, which are trapped during the linear stage of developement, can radiate energy in the nonlinear regime if the basic current is nonzonal. The radiation starts as soon as the initial fast exponential growth significantly slows. The initial trapping of those solutions is caused by their fast temporal growth. The new mechanism for radiation is related to the nonzonality of a current.

Thesis Supervisor: Joseph Pedlosky,

Title: Senior Scientist, Department of Physical Oceanography, Woods Hole Oceanographic Institution

Acknowledgements

I would like to express my gratitude to my Thesis advisor, Joseph Pedlosky for his guidance and constant encouragement in the course of this work as well as for his example of clear thinking and scientific curiosity. The discussions with the members of my Thesis Committee, Glenn Flierl and Larry Pratt, helped me a great deal in the research. I would like to especially thank Roger Samelson for the thoughtful advice and Nelson Hogg who was very helpful in providing material for Chapter 7. I would also like to acknowledge the help of the entire committee and Karl Helfrich in correcting the final version of this thesis.

I am also very grateful to the Joint Program as a whole for the opportunity to enjoy all benefits of being a student in such a wonderful program that offers excellent courses and efficient administration.

My special thanks go to my wife Larisa, my parents and my son Peter for their support and appreciation during the preparation of this thesis.

This work was supported by NSF Grant OCE 9301845.

Contents

Abstract **2**

1 Introduction **15**

1.1 Nonzonal current. 18

1.2 Overview of the thesis 20

2 Linear barotropic model **23**

2.1 Model formulation 24

2.2 New stability properties 27

2.3 Radiating modes 29

2.4 Basic state velocity profile and jump conditions. 34

2.5 Summary 36

3 Results from the barotropic problem **38**

3.1 Top-Hat Jet 39

3.2 Continuous jet 42

3.2.1 Zonal jet 43

3.2.2 Small tilt: $\alpha = 5^o$ 44

3.2.3 Large tilt: $\alpha = 30^o$ 46

3.2.4 Energy balance in LW limit 54

3.3 Summary 57

4 Linear two-layer model **60**

4.1 Formulation 61

4.2 Top-Hat Jet 64

4.3 Continuous Jet 65

4.3.1 Nonzonal jet: $\alpha = 30^o$ 67

4.3.2 Energy balance 73

4.4 Summary 76

5 Nonlinear regime. Single wave development **78**

5.1 Method of solution and analysis 80

5.1.1 Analysis of results. Fourier components. 82

5.2 Mode 1. Zonal jet. 84

5.3 Slightly nonzonal jet. 91

5.4 Mode 1. $\alpha = 30^o$ 97

5.4.1 Short wave: $k = 1$. 100

5.4.2 Long wave: $k = 0.25$. 113

5.4.3 Dependence on β. 118

5.5 Mode 2 122

5.6 Summary 127

6 Nonlinear interactions between waves **131**

6.1 Mode 1 and Mode 2 132

6.1.1 Case 1. Direct interactions. 133

6.1.2 Case 2. Indirect interactions. 139

6.2 Case 3. Mode 1. 146

6.3 Summary. 152

7 Comparison of the results with observations. **155**

7.1 Scaling of results. 157

7.2 Model-Data comparison 160

7.2.1 Kinetic energy 160
7.2.2 Reynolds stress. 168
7.2.3 Time scales. 176
7.3 Summary 181

8 Conclusions. 182

A 186

A.1 Dispersion relation for the two-layer top-hat profile 186
A.2 Continuous jet: numerical method 188
A.2.1 Barotropic problem 188
A.2.2 Two-layer problem 188
A.3 Open boundary conditions 189
A.4 Parameters used in the numerical experiments. 191

References 192

List of Figures

2.1 The barotropic model 25

2.2 Phase diagram for a Rossby wave. The non-rotated coordinate frame (marked $k - l$) and rotated frame (marked $k' - l'$) are shown in the plot. Left circle corresponds to positive ω, right circle to negative ω. See the discussion in the text. 33

3.1 Results for the Top-Hat jet for $\beta = 1.5$: (a,d,g) $\alpha = 0^o$, (b,e,h) $\alpha = 30^o$, (c,f,i) $\alpha = 45^o$. Upper panel: Real parts of the phase speed c for the two modes vs k. The maximum Rossby wave phase speed (right-hand side of Eq. 2.13) is shown by the dotted line. (d-f) Imaginary parts of c. (g-i) Ratio of the imaginary part of the y-wavenumber l to the real part $\frac{l_i}{l_r}$ vs k. The dotted line is a zero line. The curves below the zero line correspond to the region $y < -1$, above - to the region $y > 1$. Mode numbers are shown in the plot. 41

3.2 Results for the zonal continuous barotropic jet. (a) Real and imaginary parts of the phase speed c (labels are on the plot next to the corresponding curves) vs k for two modes for $\beta = 1$. Growth rates kc_i are shown in the heavy lines. (b) The same as (a) but for $\beta = 4$. (c) Stability diagram in the β-k plane. Shaded regions on the β-k plane correspond to the existence of the unstable modes. 45

3.3 Results for the tilted barotropic jet for $\alpha = 5^o$ and $\beta = 1$ (a) Real parts of the phase speed c_r vs k for two modes. Mode 1 is to the left (smaller k). (b) - imaginary parts of the phase speed c_i and growth rates (heavy lines) vs. k. (c) comparison with the zonal jet near the LWC for Mode 1. Real and imaginary parts of c are shown by the solid lines for the tilted jet and by the dashed lines for the zonal jet. The dotted line is the maximum Rossby wave speed, i.e. the right-hand side of (13). (d) the same as (c) but for Mode 2. 47

3.4 Complex y-wavenumbers l vs. k for the same parameters as in Fig.3.3. Real and imaginary parts are labeled on the plot next to the corresponding curves. l for the zonal jet is shown by the dashed line, for $\alpha = 5^o$ by the solid line. (a,c) region $y < -1$. (b,d) region $y > 1$. (a,b) Mode 1. (c,d) Mode 2. 48

3.5 Results for $\alpha = 30^o$. Complex c vs. k. Real and imaginary parts are labeled on the plot next to the corresponding curves. Growth rates are shown in the heavy lines. Dotted lines show maximum Rossby wave phase speed. Mode 1: (a) $\beta = 1$, (c) $\beta = 6$. (b) the same as for Mode 2 and $\beta = 1$. (d) Mode 2, $\beta = 4$. 50

3.6 Stability diagram for $\alpha = 30^o$. Shaded regions on the β-k plane correspond to the existence of the unstable modes. 52

3.7 Radiation of the two modes for $\alpha = 30^o$. Mode 1: a) $\beta = 1$, c) $\beta = 6$. Mode 2: b)$\beta = 1$, d)$\beta = 4$. (a-d) complex y- wavenumbers vs. k. Imaginary parts are shown by the dashed lines, real parts by the solid lines. Negative imaginary parts correspond to $y < -1$, positive correspond to $y > 1$. The appropriate regions for the real parts are labeled on the plot. (e-f) $\phi(y)$ (thick line) and $\phi_y(y)$ (thin line) as functions of y at k near the LWC: $k = .1845$ for (e) and $k = 1.0751$ for (f). 53

3.8 The balance between terms in the barotropic energy equation. $\beta = 1$, $\alpha = 30^o$. $y_b = 1.5$. $2kc_i$ is shown by the solid lines, F_{brt} and $Flux$ terms are divided by the integral of kinetic energy $\int_{-yb}^{yb} K_e dy$ and are shown by the dashed lines. (a) Mode 1; (b) Mode 2. 56

4.1 Results for the baroclinic Top-Hat jet. $\beta = 1.5$, $\alpha = 30^o$ and $F = 3$. (a) - real parts of c for all 4 modes vs. k. Dashed line shows the maximum Rossby wave phase speed. (b) - the same but for the imaginary parts of c. Wave numbers are shown on the plot next to the corresponding curves. 66

4.2 Results for the baroclinic continuous jet. $\alpha = 30^o$, $\beta = 1$. (a,b) - Real parts of c vs. k. The maximum Rossby wave phase speed is shown by the dashed line. (c,d) - Imaginary parts of c. (a,c) - $F = 3$. (b,d) - $F = 10$. Mode numbers are shown next to the corresponding dispersion curves. . . 68

4.3 Complex meridional wavenumbers l vs. k. $\beta = 1$, $\alpha = 30^o$, $F = 3$. Real parts are shown by solid lines; imaginary are shown by dashed. Numbers next to the curves indicate the type of the component: 1 - barotropic component, 2 - baroclinic component. (a,c,e) External region $y < -1$. (b,d,f) $y > 1$. (a,b) Mode 1. (c,d) Mode 2. (e,f) Mode 3. 70

4.4 Y-structure of the barotropic $\phi_{brt} = \phi_1(y) + \phi_2(y)$ (shown by the solid lines) and baroclinic $\phi_{brc} = \phi_1(y) - \phi_2(y)$ components (shown by the dashed lines). $\beta = 1$, $\alpha = 30^o$, $F = 3$. k is chosen close to the LWC: (a) Mode 1, $k = 0.155$; (b) Mode 2, $k = 1.092$; (c) Mode 3, $k = 0.165$ 72

4.5 Energetics of the problem. $\beta = 1$, $\alpha = 30^o$, $F = 3$. (a,c,e) - Integrated energy sources F_{brt} (shown by open dots), F_{brc} (shown by stars) and $Flux$ (shown by solid lines) vs. k. (b,d,f) - F_{brt} (solid line) and F_{brc} (dashed line) vs. y near the LWC. (a,b) Mode 1. (c,d) Mode 2. (e,f) Mode 3. The sum $F_{brc} + F_{brt}$ is shown by the solid line on (e). 75

5.1 The logarithm of perturbation kinetic energy for $\alpha = 0^o$, $k = 1$ and $\beta = 1$ vs. time. $log(K_e(t)/K_e(0))$ is shown by the solid line with open dots, $2kc_it$ is shown by the dashed line. 85

5.2 The streamfunction as function of y for $x = 1.4$, $\alpha = 0^o$. $k = 1$ and $\beta = 1$. The time corresponding to a snapshot is given on the top of a panel. The linear solution is shown by the dashed lines on the first three plots. . . . 86

5.3 The Fourier coefficients Φ_0 (solid lines), Φ_1 (dashed lines) and Φ_2 (dashed-dotted lines) of the streamfunction as functions of y. Corresponding times are given on the top of each panel. $\alpha = 0^o$, $k = 1$ and $\beta = 1$. 88

5.4 Kinetic energy corresponding to each Fourier component vs. time. a) K_{k_n} (energy integrated over the whole domain); b) E_{k_n} (energy integrated from $-\infty$ to -2 and from 2 to ∞) divided by the total energy K_e. Component numbers are shown on the plot. $\alpha = 0^o$, $k = 1$ and $\beta = 1$. 90

5.5 Logarithm of perturbation kinetic energy. As in Fig.5.1 but for $\alpha = 5^o$. $k = 1$ and $\beta = 1$. 91

5.6 The streamfunction as function of y. As in Fig.5.2 but for $x = 1.37$ and $\alpha = 5^o$. $k = 1$ and $\beta = 1$ 92

5.7 The Fourier coefficients Φ_0 (solid lines), Φ_1 (dashed lines) and Φ_2 (dashed-dotted lines) of the streamfunction as functions of y. $\alpha = 5^o$. $k = 1$ and $\beta = 1$. 94

5.8 External kinetic energy E_{k_n} corresponding to each Fourier component vs. time. As in the lower panel of Fig.5.4 but for $\alpha = 5^o$, $k = 1$ and $\beta = 1$. $(E_0 + E_1 + E_2)/K_e$ for the zonal jet (previous chapter) is shown by the dotted line (marked by $\alpha = 0$). 95

5.9 Growth rates as function of k for two linear modes; $\beta = 1$ and $\alpha = 30^o$. The marks on the curves show the choices of parameters for different numerical runs. 99

5.10 Logarithm of perturbation kinetic energy. As in Fig.5.1 but for $\alpha = 30^o$. $k = 1$ and $\beta = 1$. 100

5.11 Two-dimensional contour plots of the total streamfunction $\bar{\Psi}(y) + \psi(x, y)$. Corresponding times are given on the top of each plot. Heavy dashed lines are parallel to the latitude circles. Mode 1, $k = 1$, $\beta = 1$ and $\alpha = 30^o$. . 101

5.12 The streamfunction as function of y. As in Fig.5.2 but for $x = 1.37$ and $\alpha = 30^o$. $k = 1$ and $\beta = 1$ 103

5.13 The Fourier coefficients Φ_0 (solid lines), Φ_1 (dashed lines) and Φ_2 (dashed-dotted lines) of the streamfunction as functions of y. $\alpha = 30^o$. $k = 1$ and $\beta = 1$. 105

5.14 As in the Fig.5.4 but for $\alpha = 30^o$. $k = 1$ and $\beta = 1$. 106

5.15 Terms from the equation 5.8: $-\overline{\psi_{yt}}^x$ (solid lines), $\frac{\partial}{\partial y}\overline{\psi_x\psi_y}^x$ (dashed lines) and $\beta_1\overline{\psi}$ (dotted lines) as functions of y. Corresponding times are shown on the top of each plot. $k = 1$, $\beta = 1$ and $\alpha = 30^o$. 110

5.16 The function $c_1(y, t)$ defined by Eq.5.9 as a function of y for different times. The upper and lower bounds on the allowed for radiation phase speed set by the phase speed condition (2.13) is shown by the dashed lines. The jet region $[-1\ 1]$ is not shown. $k = 1$, $\beta = 1$ and $\alpha = 30^o$. 112

5.17 The Fourier coefficients Φ_0 (solid lines), $\Phi_{0.25}$ (dashed lines) and $\Phi_{0.5}$ (dashed-dotted lines) of the streamfunction as functions of y. Corresponding times are given on the top of each panel. $\alpha = 30^o$, $k = 0.25$ and $\beta = 1$. 115

5.18 E_{k_n} (external kinetic energy corresponding to each component) divided by total perturbation energy K_e. a) components "0", "0.25" and "0.5"; b) "0.75", "1" and "1.25". Component numbers are shown on the plot. $\alpha = 30^o$, $k = 0.25$ and $\beta = 1$. 116

5.19 The Fourier coefficients Φ_0 (solid lines), Φ_1 (dashed lines) and Φ_2 (dashed-dotted lines) of the streamfunction as functions of y. $\beta = 0.25$. $k = 1$, $\alpha = 30^o$. 120

5.20 As in the Fig.5.4 but for $\beta = 0.25$, $\alpha = 30^o$ and $k = 1$. 121

5.21 Logarithm of the perturbation kinetic energy. As in Fig.5.10 but for Mode 2. $k = 1.8$, $\beta = 1$ and $\alpha = 30^o$. 124

5.22 The Fourier coefficients Φ_0 (solid lines), $\Phi_{1.8}$ (dashed lines) and $\Phi_{3.6}$ (dashed-dotted lines) of the streamfunction as functions of y. Corresponding times are given on the top of each panel. Mode 2, $\alpha = 30^o$, $k = 1.8$ and $\beta = 1$ 125

5.23 As in the Fig.5.8 but for Mode 2. $\alpha = 30^o$, $k = 1.8$ and $\beta = 1$. 126

6.1 Two-dimensional contour plots of the total streamfunction $\bar{\Psi}(y) + \psi(x, y)$. As in Fig.5.11 but for Case 1: Mode 1 ($k = 1$) and Mode 2 ($k = 2$). $\alpha = 30^o$ and $\beta = 1$. 135

6.2 The Fourier coefficients Φ_0 (solid lines), Φ_1 (dashed lines) and Φ_2 (dotted lines) of the streamfunction as functions of y. Corresponding times are given on the top of each panel. Case 1: Mode 1 ($k = 1$) and Mode 2 ($k = 2$). $\alpha = 30^o$ and $\beta = 1$. 136

6.3 Kinetic energy corresponding to each Fourier component vs. time. a) K_{k_n} (energy integrated over the whole domain); b) E_{k_n} (energy integrated from $-\infty$ to -2 and from 2 to ∞) divided by the total energy K_e. Component numbers are shown in the plot. Case 1: Mode 1 ($k = 1$) and Mode 2 ($k = 2$). $\alpha = 30^o$ and $\beta = 1$. 137

6.4 Two-dimensional contour plots of the total streamfunction $\bar{\Psi}(y) + \psi(x, y)$. As in Fig.5.11 but for Case 2: Mode 1 ($k = 1$) and Mode 2 ($k = 1.5$). $\alpha = 30^o$ and $\beta = 1$. 141

6.5 The Fourier coefficients Φ_0 (solid lines), Φ_1 (dashed lines), $\Phi_{1.5}$ (dotted lines) and $\Phi_{0.5}$ (dashed-dotted lines) of the streamfunction as functions of y. Corresponding times are given on the top of each panel. Case 2: Mode 1 ($k = 1$) and Mode 2 ($k = 1.5$). $\alpha = 30^o$ and $\beta = 1$ 142

6.6 Kinetic energy corresponding to each Fourier component vs. time. As in Fig.6.3 but for Case 2: Mode 1 ($k = 1$) and Mode 2 ($k = 1.5$). Components "0", "1" and "1.5". Component numbers are shown in the plot. $\alpha = 30^o$ and $\beta = 1$. 143

6.7 As in Fig.6.3 but for components "0.5", "2" and "2.5". Case 2: Mode 1 ($k = 1$) and Mode 2 ($k = 1.5$). $\alpha = 30^o$ and $\beta = 1$. 144

6.8 Two-dimensional contour plots of the total streamfunction $\bar{\Psi}(y) + \psi(x, y)$. As in Fig.5.11 but for Case 3: Mode 1 with $k = 0.25$ and $k = 1$. 148

6.9 The Fourier coefficients Φ_0 (solid lines), $\Phi_{0.25}$ (dashed lines), Φ_1 (dashed-dotted lines) and $\Phi_{1.25}$ (dotted lines) of the streamfunction as functions of y. Corresponding times are given on the top of each panel. Case 3: Mode 1 for $k = 0.25$ and $k = 1$. $\alpha = 30^o$ and $\beta = 1$ 150

6.10 E_{k_n} (external kinetic energy corresponding to each Fourier component) divided by the total energy K_e. Case 3: Mode 1 for $k = 0.25$ and $k = 1$. $\alpha = 30^o$ and $\beta = 1$. 151

7.1 Velocity profile chosen for computations. 159

7.2 PKE for MR1. The dashed contours show low values of the energy ($< 500 cm^2/s^2$). The heavy dashed lines show latitude circles. Units are 100 cm^2/s^2 161

7.3 As in 7.2 but for MR2 162

7.4 As in 7.2 but for MR3 163

7.5 As in 7.2 but for MR4 164

7.6 Upper panel: EKE (cm^2s^{-2}) in the North Atlantic. After Richardson, (1983), Fig.10. Lower panel: EKE at 65^oW. Different curves show the effect of smoothing the data and excluding ring observations. After Richardson, (1983), Fig.13. 165

7.7 PKE averaged in the downstream direction for all four cases. Types of lines corresponding to the each of four cases are given in the plot. The negative values of y correspond to the region to the south from the jet axis. 167
7.8 uv for MR1. The solid contour lines show positive values; the dashed contour lines show negative values. The heavy dashed lines show latitude circles. Units are 100 cm^2/s^2 170
7.9 As in 7.8 but for MR2 171
7.10 As in 7.8 but for MR3 172
7.11 As in 7.8 but for MR4 173
7.12 Observed values of $\overline{uv}$ in cm^2/s^2 after Freeland *et al.*, (1975), Table 1. . . 174
7.13 Values of $\overline{u'v'}$ for Western North Atlantic (solid line, ordinate scale on left) at 55^oW at 4000 m depth. After Schmitz (1982), Figure 1. 175
7.14 Period of phase oscillations (solid lines) and e-folding time scale (dashed lines) vs. wavelengths for Mode 1 and Mode 2 of the linear problem. $\beta = 1$ and $\alpha = 30^o$. 177
7.15 Power Spectral Density computed for the time series of PKE for four cases vs. corresponding spectral periods. 179

Chapter 1

Introduction

Eddy energy increases by orders of magnitude while moving from the Eastern Atlantic and from the equator to the North-West of the North Atlantic Gyre (Wyrtki *et al.*, 1976; Richardson, 1983; Wunsch, 1983), in which region the eddy field varies in relative intensity. The ratio between eddy energy and mean energy is between 1/2 and 1 in the Gulf Stream region increasing to about 20 - 40 in the central portion of the gyre (Wyrtki *et al.*, 1976). This raises the question how such a highly energetic eddy field could be generated in the interior of the ocean away from the swift boundary currents.

The most direct mechanism of the eddy formation might be the instability of the mid-ocean. Gill et al., (1974) demonstrated that the potential energy stored in the ocean modeled by the simple two-layer model is sufficient to produce the eddy field with velocities larger than the gyre values. However, whether or not this energy can be entirely released into the eddy motions is a more complicated question. Some numerical studies of the stability of a horizontally uniform baroclinic flow suggest that the eddy energy corresponding to the scales longer than the Rossby deformation radius can exceed the background energy (Larichev and Held, 1995; Held and Larichev, 1995). In contrast, existing theoretical evidence suggests (Pedlosky, 1975) that the mean ocean velocity is a bound for the eddy velocity produced by the baroclinic instability of the oceanic interior.

One needs to examine the alternate sources of the eddy energy in the interior of the ocean gyres. Very energetic currents such as the Gulf Stream in the North Atlantic are the most likely candidates for energy sources. Some facts support this idea. As shown in Halkin and Rossby (1985) and in Rossby (1987), approximately 2/3 of the kinetic energy in the interior is attributed to the meandering Gulf Stream, leaving the rest of the variance to the mesoscale eddy field. Hogg (1994) confirms that the velocity variance is significantly (by 1/3) reduced when the process is viewed from the reference frame aligned with the Stream itself.

The above evidence leaves the Gulf Stream as the possible origin of the eddy variability in the north-western part of the Atlantic. Nevertheless, the mechanism of the eddy energy penetration into the interior of the gyre is not well understood.

Several approaches to this problem have been tried in the past. Some studies consider a boundary forced problem, in which the effect of the Gulf Stream meandering is modeled by the time-dependent boundary. This method allows us to avoid the difficulties of choosing a realistic mean velocity profile and discussing the dynamics of the stream itself and makes all results relatively simple to analyze.

A steady propagating northern boundary is considered by many authors starting from the early results by Flierl and Kamenkovich (1975) and Pedlosky (1977). The former work considers both moving zonal and western boundaries. In the latter work, the effect of the mean velocity field is also studied.

The form of the boundary is modified by Malanotte-Rizzoli et al., (1987a) to include the case of a pulsating meander that allows, more readily, radiation of energy into the interior. On the β-plane, without topography, radiation is found to be possible only if the pulsation frequency is below the critical value. Topography in the form of a simple parabolic relief does not change the process qualitatively. The problem is studied in the periodic zonal channel.

Hogg (1988) makes a statistical extension of the transient meander model, focusing on the far-field response. He found that in the case of a zonal jet, meander activity must vary in the x-direction and have growth and decay periods. If both ingredients are present, the energy is transferred from the forcing to the interior motions and the induced mean circulation in the far-field has realistic meridional distribution of eddy kinetic energy. The observed Reynolds stress maps to the north from the Gulf Stream (Bower and Hogg, 1992) show good agreement with the results of Hogg (1988).

The extension of the studies of the radiation by the pulsating meanders to the highly nonlinear regime is made by Malanotte-Rizzoli et al., (1987b). Two boundary functions are considered: a stationary pulsating meander and a slowly propagating meander. The first type of forcing can produce highly nonlinear, isolated dipoles. In the second case, the resonance mechanism in the presence of topography is effective in producing nonlinear eddies.

As it is demonstrated in Rizzoli *et al.*, (1995), the nonlinear interactions between the forced radiating wave and a free wave in the interior can produce circulation patterns that are consistent with observations. The strength of recirculation is realistic if a bowl-shaped topography is introduced. The study demonstrates the effectiveness of the energy transfer by radiating waves. The topography in the model allows coupling between meanders and topographic Rossby waves. The supporting evidence for this mechanism for radiation is presented in Pickart (1995) where the analysis of the 40-day topographic Rossby waves observed to the north from the Gulf Stream is performed.

The above cited studies provide us with an important mechanism of energy radiation from energetic ocean currents. However, the imposed boundary forced problem does not show whether the radiation is dynamically consistent with the dynamics of the stream itself. In this sense, such studies do not provide a complete dynamic picture of the process.

We consider here a different approach to understanding the structure and the origin of eddy variability and consider the unstable modes of the Gulf Stream viewed as a steady current. Talley (1983) followed this idea and focused her research on instabilities that are very weakly trapped to the current. Although, in the linear sense, these instabilities possess growth rates that are smaller than those of the strongly trapped modes, she proposed that the non-trapped solutions are dominant in the far field. Unlike the previously cited boundary-forced studies, Talley assumed that the growth of the trapped meander-type disturbances does not directly cause the radiation of energy by the non-trapped disturbances.

Talley (1983) found that zonal eastward parallel flows have difficulty radiating plane waves. Only zonal jets with some westward components (purely westward, eastward with westward undercurrent, or westward sidelobs) were found to be capable of radiating energy. The possibility of Rossby waves radiation by westward frontal jets is confirmed by some available observations. For example, the wave-like oscillations with north-west to south-east orientation found in the southeastern North Atlantic are believed to be the signature of radiating Rossby waves generated at the Cape Verde frontal Zone (Spall, 1992; Spall *et al.*, 1993).

The nonlinear evolution of radiating waves is not considered in Talley (1983).

1.1 Nonzonal current.

One of the most important decisions in the model is the form of the mean current itself. The main task is to choose the simplest possible model and yet not lose important features. In many studies, steady purely zonal flows are considered which are found non-radiating in many studies (Pedlosky, 1977; Talley, 1983). It seems important to explore other possibilities in which an ocean current can radiate. In the present study we want to consider the effect of nonzonality of the jet on the stability and radiating properties in the problem.

Some observed facts support this idea. The portion of the Gulf Stream (in Iselin's definition) between Cape Hatteras and the New England Seamounts is characterized by high values of the eddy kinetic energy (Wyrtki *et al.*, 1976; Richardson, 1983). The axis of the Gulf Stream in this region makes an angle of 30 - 40 degrees with a latitude circle.

An obvious question arises. How different is the dynamics of the zonal jet from the more general case of the flow with a meridional component? The linear stability of the mean state in the form of the purely zonal current has been investigated in detail during the last decades, for example by Pedlosky (1964). However, the results are not simple for most mean velocity profiles, and not all properties are completely understood. Why do we want to make our problem even more complicated, trying to look at a more general orientation of the mean current? We can see two main reasons.

First, we believe that the stability properties of the nonzonal jet are different from those of the purely zonal current. From the physical point of view, it is reasonable to expect that nonzonal currents are more unstable than zonal ones. In the baroclinic problem, one could refer to the fact that the direction of the maximum energy release, which is perpendicular to the jet axis is not parallel to the planetary vorticity gradient in the case of a nonzonal jet, therefore reducing the stabilizing effect of β (Pedlosky, 1987). The more unstable character of the nonzonal vertically sheared flows was reported in previous studies (Kang *et al.*, 1982; Lee and Niler, 1987). The horizontal tilt may excite new unstable modes, or destabilize stable modes (if there are any). These possibilities will be demonstrated in the following sections.

Second, in our analysis, we want to focus on the solutions that can penetrate significantly far into the mid-ocean, in other words, radiating solutions. The ability of a zonal flow to support these solutions is, however, limited. The dominant disturbances in the Gulf Stream are eastward-propagating (Hogg, 1988). These disturbances are also favored by the semi-circle theorem for the zonal jets on the β-plane derived by Pedlosky (1964). In contrast, in the simple barotropic model without topography, only upstream traveling solutions can be of radiative character (Flierl and Kamenkovich, 1975; Pedlosky, 1977; Talley, 1983; Malanotte-Rizzoli *et al.*, 1987a), which limits the radiating ability of the zonal jets.

At the same time, there are reasons to expect that nonzonal jets more easily support radiating solutions. Downstream propagating motions are now not necessarily strongly trapped to the northward boundary current (Flierl and Kamenkovich, 1975; Ierly and

Young, 1991). The latter study is concerned with the stability of a parallel western boundary flow described by the Orr-Sommerfeld equation with the β-term. The viscous instabilities supported by the flow can have long oscillatory tails if a basic flow is highly inertial. Nevertheless, these modes are classified as non-radiating because they cannot be coupled with free basin modes; see section 2.3 for the description of the phase speed condition.

In the study by Rizzoli *et al.*, (1995), it is demonstrated that when the topography makes the effective planetary vorticity gradient non-meridional and, therefore, not perpendicular to the jet axis, the very energetic radiation of Rossby waves is possible. The change in the jet orientation relative to the mean potential vorticity gradient can lead to significant changes in the radiating properties.

1.2 Overview of the thesis

We consider the problem first in a simple linear barotropic model. The model is described in Chapter 2. In the chapter, we use the relative simplicity of the model to derive some useful analytical results. In particular, the sufficient condition for stability of a barotropic zonal current is re-derived for a nonzonal current to become a sufficient condition for the absence of a neutral mode. On a simple example, we also demonstrate the destabilizing role of the horizontal tilt of the jet axis with respect to the latitude circles. We then formulate the criteria for determining whether a linear solution is radiating. The task is generally not trivial, because of the fast exponential growth of the solution.

We report the results of the barotropic problem in Chapter 3. We consider two mean velocity profiles: top-hat broken line profile and a continuous jet. In both the cases, we compare the results for the nonzonal jet with those for the purely zonal current. We report the qualitative change in the radiating properties related to the changed orientation of the currents. In particular, we find strong radiation by the waves that are long in the along-jet direction. The radiation is observed even if the horizontal tilt of the jet axis is very small.

The second moving layer is added to the model in Chapter 4. We focus on the effects of such a simplified baroclinic structure on the radiating properties. We observe the appearance of an additional baroclinic mode and changes in the dispersion curves. However, the changes in the radiating properties are not significant. The radiating response remains basically barotropic in structure.

The nonlinear development of the linear solutions is studied in detail in Chapter 5. We develop an efficient numerical method for solving the nonlinear equation for potential vorticity with the open boundary conditions in the cross-jet direction. The modified Orlanski numerical open boundary conditions are employed for this purpose. For the analysis of results, we decompose the streamfunction into Fourier modes, which provides the detailed information about the structure of the solution. The decomposition also simplifies the analysis of the energetics in the problem.

We start with the analysis of the nonlinear development of a single linear mode that is put as an initial condition. As in the linear problem, we first consider the dynamical properties of the solution for a zonal current. Then we make the jet nonzonal and compare the results with the previous case. The main finding is that short linear waves that grow rapidly initially, start to radiate when their growth substantially slows. The radiation typically begins in the form of an x-independent component. The physical mechanism for that is illustrated on a simple example. We also check if the radiation is consistent with the criteria of the linear theory.

An attempt to understand the effects of interactions between different waves is made in Chapter 6. For simplicity, we study the mutual development of a pair of linear waves. We consider three types of interactions that are expected in the development of a set of linear solutions. First is the case in which a strongly radiating wave and a weakly radiating wave half as long strongly influence each other. In the second case, the direct influence is not possible because of the relation between corresponding wavenumbers. Both waves are long and strongly radiating in the third case.

The relevance of the results to observations is discussed in Chapter 7. We compare results of four different numerical experiments with the observations in the Western North Atlantic. For the comparison, we analyze eddy kinetic energy, Reynolds stress and characteristic time scales.

Chapter 2

Linear barotropic model

We begin here the study of radiating properties of nonzonal ocean currents. The overall idea is to analyze the effect of nonzonality of a current on stability and radiating properties. The approach taken is to simplify the analysis by considering the simplest possible model, but yet not to loose the main dynamical features. In particular, we want to single out the effects of the jet crossing the latitude circles.

We start from formulating such a simplified model for the vertically homogeneous ocean in section 2.1. We take a steady nonzonal current as a basic state to which perturbations of small amplitudes are added. The development of these perturbations in time is a focus of our research. Nonlinear terms are neglected everywhere in chapters 2 and 3. All results are expected to be valid only during the initial stage of development, while the magnitudes of perturbations remain small enough to make nonlinear terms negligible. The extension of the model to nonlinear regime is made in Chapters 5 and 6.

In our model, we balance the nonzonal current by a vorticity source. We believe that the dynamical role of this source is limited to supporting the parallel nonzonal flow. The new radiating properties of nonzonal currents, reported in the following chapters, therefore, are not the direct consequence of the non-conservation of potential vorticity in the model. We base this claim mainly on the results of section 5.4 below, which demonstrate that the magnitude of forcing does not control the strength of radiation.

One can anticipate a more unstable nature of a nonzonal current beforehand, based on a physical argument valid in the baroclinic model (Pedlosky, 1987) and results from the previous studies; see section 1.2 for details. The simplicity of the formulated linear problem allows us to demonstrate the qualitatively different stability properties of a nonzonal current compared to a zonal flow in section 2.2. We will derive the stability theorem for the simple nonzonal flow considered.

To proceed with the analysis, we need to define what we mean by a radiating mode in our linear problem. In section 2.3, we both reformulate some existing and derive new analytical criteria for an unstable mode to be of radiating character for our problem. Under the limitations of the linear theory, we can only try to determine if a solution has a radiating form during the initial stage of development while its amplitude remains small. However, the ideas involved in derivation of some of the criteria are useful for nonlinear consideration and will be additionally discussed in Chapter5.

Section 2.4 describes the general form of the mean velocity profile used for calculations which is specified in the three intervals in y. We then derive the matching conditions that are used to connect a solution obtained in each of the intervals and to obtain a dispersion relation. One of the resulting conditions takes the form which is different from that in the problem with a zonal flow. We present a detailed derivation to ensure the clarity of the technique.

2.1 Model formulation

We assume that the motions are quasi-geostrophic, and we neglect friction and bottom topography although the effect of a constant bottom slope can be included in the β-term. We make a further assumption that the along-jet spatial variation scale is much longer than the cross-jet spatial variation scale, so our jet is essentially uniform in the along-jet direction.

Then we orient the x-axis of our coordinate frame along the jet and y-axis perpendic-

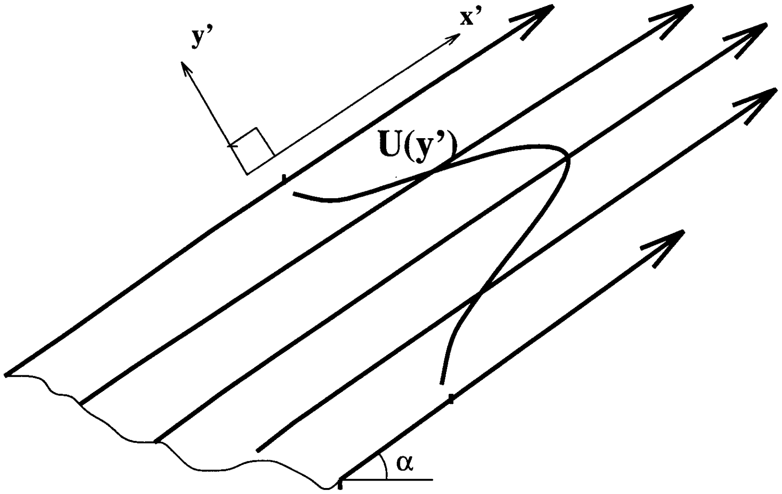

Figure 2.1: The barotropic model

ular to the jet axis (see Fig.2.1). The advantage of such a rotated coordinate is a clear distinction between along-jet and cross-jet directions, which is convenient for our studies of the energy radiation away from the jet. The barotropic potential vorticity equation (Pedlosky, 1987) in the new coordinate frame takes the form:

$$\frac{\partial}{\partial t}\nabla^2\psi + J(\psi + \bar{\Psi}(y), \nabla^2\psi + \bar{Q}) = \mathcal{F}, \tag{2.1}$$

where unperturbed state is given by

$$\bar{Q} = \beta_1 x + \beta_2 y - \bar{u}_y; \quad \bar{\Psi} = -\int \bar{u}(y)dy, \tag{2.2}$$

with $\beta_2 = \beta cos\alpha, \beta_1 = \beta sin\alpha$ with α being the angle between our x-axis and a latitude circle and β is the planetary vorticity gradient. We assume that Eq.2.1 holds for $\psi = 0$ with unchanged forcing term $\mathcal{F}$ (Pedlosky, 1987). The potential vorticity is not conserved in the model. Rather, we introduce a vorticity source, which could be associated, for example, with the wind forcing and resulting Ekman pumping at the surface:

$$\mathcal{F} = -\beta_1\bar{\Psi}_y. \tag{2.3}$$

The introduced forcing depends on the *mean flow only* and is different in nature from the viscosity that supports a western boundary layer in, for example, Ierley and Young, (1991). The viscous term depends on the basic flow *and* perturbations in the latter case.

Before we proceed any further, one property of the equation 2.1 should be mentioned. If the angle of the horizontal tilt of the jet axis α is changed to $-\alpha$, the equation stays the same if y is changed to $-y$ and ψ to $-\psi$. Therefore, the solution for a south-eastward flowing current can be easily gotten from the solution for a north-eastward flowing current by the above described transformation.

For small perturbations, we can linearize Eq. 2.1 and rewrite it in the following form:

$$\left(\frac{\partial}{\partial t} + \bar{u}(y)\frac{\partial}{\partial x}\right) \nabla^2\psi + J(\psi, \bar{Q}) = 0. \tag{2.4}$$

This is the equation that we solve for particular choices of the mean velocity profile $\bar{u}(y)$ in chapters 2 and 3. The solution of our problem can be found in the form:

$$\psi = \phi(y)e^{ik(x-ct)}, \tag{2.5}$$

where phase speed c is allowed to be complex $(c = c_r + ic_i)$ and x-wavenumber k is real. The solution is, therefore, a Fourier mode in x which both oscillate in time and has an amplitude growing in time exponentially. $\phi(y)$ satisfies the following ODE:

$$\phi_{yy} + \left(\frac{\beta_2 - \bar{u}_{yy}}{\bar{u} - c} - k^2\right)\phi + \frac{i\beta_1}{k(\bar{u} - c)}\phi_y = 0. \tag{2.6}$$

The last term on the left-hand side of Eq.2.6 is related to the nonzonal orientation of the jet axis in our model. The term is proportional to the downstream component of the planetary vorticity gradient β_1 and is zero for a zonal current.

Boundary conditions in y-direction are

$$\phi(\pm L) = 0, \tag{2.7}$$

where L is allowed to be infinite. We study the problem on the infinite β-plane, but the results of the following section 2.2 are also valid for finite L (the problem in a channel).

This gives us the eigenvalue problem for c for a given value of k, resulting in the function $c = c(k)$ for chosen values of β_0 and α. The function defines a dispersion curve for a given set of parameters.

2.2 New stability properties

Let us multiply (2.6) by $\phi*$, integrate in y over the domain and take the imaginary part of the result. We get ($c = c_r + ic_i$):

$$kc_i \int_{-L}^{L} \frac{|\phi|^2}{|\bar{u}-c|^2}(\beta_2 - \bar{u}_{yy})dy + \beta_1 Re \int_{-L}^{L} \frac{\phi^* \phi_y}{(\bar{u}-c)} dy = 0. \tag{2.8}$$

The second term on the left-hand side can be modified:

$$Re \int_{-L}^{L} \frac{\phi^* \phi_y}{(\bar{u}-c)} dy = \int_{-L}^{L} Re(\phi^* \phi_y) Re \frac{dy}{(\bar{u}-c)} - \int_{-L}^{L} Im(\phi^* \phi_y) Im \frac{dy}{(\bar{u}-c)} =$$

$$= \int_{-L}^{L} \frac{1}{2}(|\phi|^2)_y Re \frac{dy}{(\bar{u}-c)} - c_i \int_{-L}^{L} \frac{Im(\phi^* \phi_y)}{|\bar{u}-c|^2} dy =$$

$$= \frac{1}{2} Re \int_{-L}^{L} \frac{(|\phi|^2)_y}{(\bar{u}-c)} dy - c_i \int_{-L}^{L} \frac{Im(\phi^* \phi_y)}{|\bar{u}-c|^2} dy =$$

$$= \frac{1}{2} Re \int_{-L}^{L} \frac{|\phi|^2 \bar{u}_y}{(\bar{u}-c)^2} dy - c_i \int_{-L}^{L} \frac{Im(\phi^* \phi_y)}{|\bar{u}-c|^2} dy. \tag{2.9}$$

The integration by parts on the last step involves the assumption that the solution vanishes at the boundaries $y = \pm L$. On the infinite plane, that implies the decay at infinity.

Finally, we get

$$kc_i \int_{-L}^{L} \left(\frac{|\phi|^2}{|\bar{u}-c|^2}(\beta_2 - \bar{u}_{yy}) - \beta_1 \frac{Im\phi^* \phi_y}{k|\bar{u}-c|^2} \right) dy + \frac{\beta_1}{2} Re \int_{-L}^{L} \frac{|\phi|^2 \bar{u}_y}{(\bar{u}-c)^2} dy = 0. \tag{2.10}$$

Now one can see that if the last term is non-zero, $kc_i \neq 0$. In other words, we have a sufficient condition for a mode being not neutral. Note now that the existence of a decaying solution means the existence of a growing one and vice versa; in other words there is always a growing mode as long as $kc_i \neq 0$. To demonstrate that, we change k to $-k$ in the Eq. 2.6 which changes the sign of the growth rate kc_i. The solution is then $\psi(-y)$ where ψ is the solution of the original problem and c is the same.

Suppose now, that the first term in the brackets is of the same sign everywhere in the domain, but that $\bar{u}_y$ is single-signed, and $\beta_1 \neq 0$. Then if a solution exists, it is growing in time, despite the fact that the y-derivative of the mean vorticity field $\beta_2 - \bar{u}_{yy}$ is single-signed, which is the sufficient condition for stability in the case of a zonal current.

We should keep in mind that the derived criterion cannot guarantee the existence of the unstable modes. We can only say that if, for example, $\bar{u}_y$ is single-signed, there cannot be any neutral modes in the problem. The last statement is true because for a purely real c, $(\bar{u} - c)^2$ is always positive and the last term on the left-hand side is non-zero.

Based on the above properties, one can expect to find nonzonal jets to be more unstable. The same form of the cross-stream velocity profile $\bar{u}$ can correspond to a larger number of unstable modes in the case of the jet oriented nonzonally compared to the zonal orientation. In particular, one can anticipate the existence of the neutral modes of the zonal jet destabilized by the change in the mean flow orientation or the appearance of the completely new unstable solutions. We can illustrate the possibility of the destabilization effect by a particular example.

Consider a neutral solution for the zonal jet. The example can be taken from Drazin *et al.,* (1982) problem in a channel $|y| \leq 1$:

$$\bar{u} = -\frac{\beta}{2\pi^2} sin \pi y,$$

$$\phi = cos \frac{\pi y}{2},$$

$$k^2 = \frac{3\pi^2}{4}, c = -\frac{\beta}{\pi^2},$$

The mean flow is chosen to satisfy the sufficient condition for stability, so $(\beta - \bar{u}_{yy})$ is positive everywhere in the domain.

We now introduce an infinitesimal horizontal tilt of the jet ($\alpha << 1$), expand phase speed in a power series in α and collect leading order terms. In this case, with $c_i = O(\beta_1)$ the second term in the brackets on the left-hand side of (2.10) is negligible. Thus, we can calculate the imaginary part of the frequency kc:

$$kc_i = -\frac{\alpha\beta}{2}\left[\int_{-L}^{L}\frac{|\phi|^2\bar{u}_y}{(\bar{u}-c)^2}dy\right]\left[\int_{-L}^{L}\frac{|\phi|^2}{|\bar{u}-c|^2}(\beta_2-\bar{u}_{yy})\right]^{-1}$$

$$= \frac{\alpha\beta}{4\pi}\left[\int_{-1}^{1}\frac{cos\pi y cos^2\frac{\pi y}{2}}{(1-\frac{1}{2}sin\pi y)^2}dy\right]\left[\int_{-1}^{1}\frac{cos^2\frac{\pi y}{2}dy}{(1-\frac{1}{2}sin\pi y)}\right]^{-1} =$$

$$= \frac{\alpha\beta}{4\pi}\left[\int_{-1}^{1}\frac{cos^2\pi y}{(1-\frac{1}{2}sin\pi y)^2}dy\right]\left[\int_{-1}^{1}\frac{dy}{(1-\frac{1}{2}sin\pi y)}\right]^{-1} = \frac{\alpha\beta}{\pi}(1-\frac{\sqrt{3}}{2}) > 0. \qquad (2.11)$$

The obtained growth rate is proportional to the value of the tilt angle.

We observe how a neutral mode becomes unstable when the zonal jet becomes non-zonal, while the mean potential vorticity gradient remains single-signed. In other words, the horizontal tilt plays the role of a destabilizing factor in the problem. This simple example demonstrates the fundamental destabilizing character of the tilt of the basic current.

We return now to the original domain and in what follows will consider the problem on the infinite horizontal plane.

2.3 Radiating modes

The concept of radiation can be easily applied to the purely neutral modes of the problem. If a mode has the form of a plane wave in the region with no mean flow, it is a radiating one. In contrast, if it decays in space away from the jet, it is trapped. But neutral modes are unable to extract energy from the mean flow. Hence, we have to consider unstable modes growing in time if we want to look at the process of the energy conversion from the mean current into the far-field motions. However, the distinction between trapped and radiating for the growing modes is less obvious, since the complex phase speed always corresponds to the complex y-wavenumber and, consequently, to the spatial decay in y.

However, some quantitative means of determining if a solution is radiating are available.

In the far-field ($\bar{u} = 0$), the Eq. (2.6) becomes an ODE with constant coefficients, and our solution there reduces to a plane wave:

$$\psi(x, y, t) = Ae^{kc_i t - l_i y} e^{ik(x - c_r t) + il_r y}.$$

One can call radiating those modes which "look" wavy in y (Talley, 1983). Thus, we could require that for any c_i the decay scale $1/l_i$ is longer than the oscillation scale $1/l_r$:

$$\frac{l_i}{l_r} < 1. \tag{2.12}$$

This criterion, however, is not sufficient for our purposes. Strong spatial trapping of a solution does not necessarily rule out the possibility of radiation. Spatial decay can be present, as Talley (1983) states, because it takes a finite time for the packets of disturbance to reach a point far from the jet while the disturbance itself is growing. From the kinematic point of view, we can imagine that packets smaller in amplitude are radiated earlier and, therefore, are farther from the source in space; the decaying structure in space is, therefore, formed from the sequence of ever larger disturbances produced at the source. If the spatial trapping in the problem is due *only* to the unstable growth, then the trapping should disappear when the growth disappears. There are two possibilities for making the growth rate small.

Following Talley (1983), we can consider the limit $c_i \to 0$ on the dispersion curve $c = c(k)$. If, in this limit, both $l_i \to 0$ and $l_i/l_r \to 0$, we can claim that the spatial decay of the solution is due only to the nonzero values of growth rate kc_i, and the solution is not trapped. However, this valuable criterion often has difficulties characterizing the nature of a solution that is not close to the limit of small c_i in parameter space. There is no guarantee that a solution does not change its character along a dispersion curve.

Another way to "make" the growth rate small is to follow the nonlinear equilibration during which the initial fast exponential growth slows down significantly. As it will be shown in chapters 5 and 6, in many cases the radiation often starts when fast exponential growth of the trapped linear solution is halted by the nonlinear effects. The strong spatial trapping is, therefore, as temporary as the validity of the linear theory itself in those cases and solution is of the truly radiating nature. We should note now the importance of nonlinear considerations for the analysis of the radiating properties in the problem especially for the solution that does not correspond to the point close to the cut-off of the dispersion curve.

Keeping that in mind, we however choose to stay within the limits of the linear theory in this preliminary study. For the consistency we can ask if the solution can simultaneously reach the far field while not being increased significantly by the exponential growth in time and, henceforth, satisfying the assumptions of linearity. The wave packet propagates with the speed kc_i/l_i (Talley, 1983). Then, in order for the wave to move over a distance much greater than the scale of the jet during the e-folding time $1/kc_i$, we need

$$\frac{kc_i}{l_i}\frac{1}{kc_i} = \frac{1}{l_i} >> L_{jet},$$

or $l_i << 1/L_{jet}$, where L_{jet} is the jet scale. It is interesting, that the above argument does not involve the oscillation scale $1/l_r$.

Another physically meaningful condition for radiation is that the frequency and wave number of the solution of our linear problem match those of the Rossby wave in the far-field (Pedlosky, 1977; McIntyre and Wessman, 1978; Talley, 1983; Malanotte-Rizzoli *et al.*, 1987a; Ierly and Young, 1991). It is usually called the phase speed condition. We know that the Rossby wave always has a westward propagating phase. For this reason, it is difficult to satisfy the phase speed condition for the mostly eastward traveling unstable disturbances (Flierl and Kamenkovich, 1975; Pedlosky, 1977; Talley, 1983; Malanotte-Rizzoli *et al.*, 1987a). For the tilted jet, the change in geometry leads to the change in the limits on the phase speed in the new x-direction required by the criterion.

We can find the minimum and maximum values that the Rossby wave phase speed in the x-direction of the tilted frame can take for a fixed k. The phase speed of the freely propagating Rossby wave in the far-field ($\bar{u} = 0$) lies, therefore, between these values:

$$-\beta\frac{(1+cos\alpha)}{2k^2} < c < \beta\frac{(1-cos\alpha)}{2k^2}. \tag{2.13}$$

One can see from (2.13), that the tilt of the jet ($\alpha \neq 0$) allows downstream propagating modes ($c > 0$) to satisfy the phase speed condition. To futher clarify the difference in the direction of phase propagation between zonal and nonzonal cases, we present here the phase diagram for a free Rossby wave in the far-field (Fig.2.2).

Both non-rotated and rotated coordinate frames on the wavenumber plane are presented in the plot; the wavenumbers in the rotated frame are defined by k' and l'. The radius of each circle equals $\beta/2\omega$. The reader is referred to Pedlosky (1987), p.123 for the derivation of the form of the diagram. We now consider a positive x'-wavenumber k'. There are two waves with different values of a y'-wavenumber l' with equal positive ω and k'. The wave-vectors of both waves are shown by vectors $\vec{OA}$ and $\vec{OB}$ in the plot.

First, we notice that both waves have their phase propagating *downstream*, since $\omega/k' > 0$ for them. Their phase still propagates *westward* ($\omega/k < 0$) in the agreement with the general property of the Rossby waves. The example illustrates the differences in the direction of the phase propagation between problems with $\alpha = 0$ and $\alpha = 30^o$, also expressed in terms of the condition (2.13).

We also consider the group velocity vectors, $\vec{AC}$ and $\vec{BC}$ (Pedlosky, 1987). The group velocity of the wave that is longer in the y'-direction (vector $\vec{BC}$) has a positive component in the cross-stream direction and therefore corresponds to the solution for positive y', since the energy must propagate away from the jet axis. Analogously, the wave that is shorter in y' and has a group velocity $\vec{AC}$ corresponds to the region of negative y'. It is also interesting to note that the group velocities of both waves are directed *upstream* of the basic current.

We expect that eastward zonal jets that are not radiating can become capable of

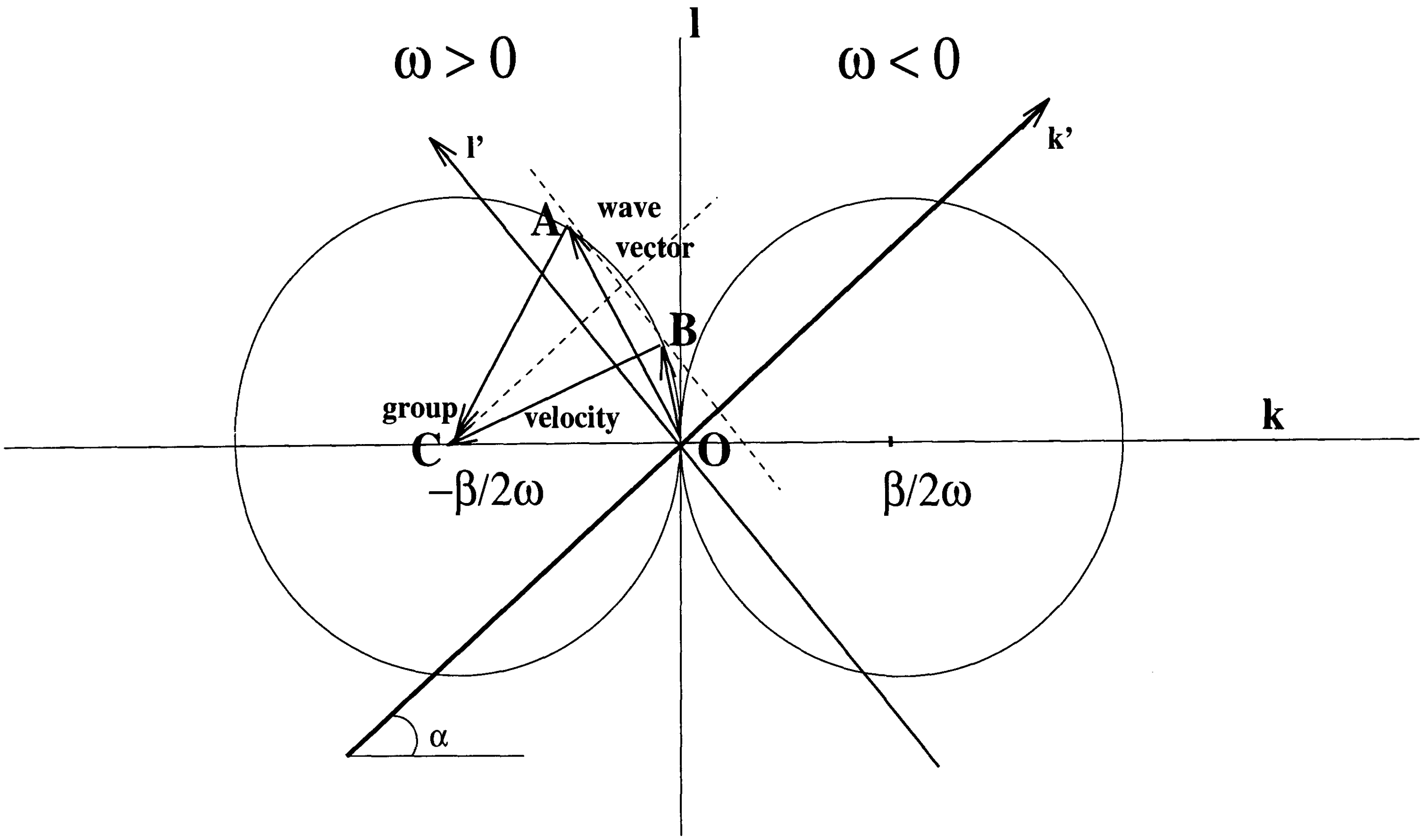

Figure 2.2: Phase diagram for a Rossby wave. The non-rotated coordinate frame (marked $k - l$) and rotated frame (marked $k' - l'$) are shown in the plot. Left circle corresponds to positive ω, right circle to negative ω. See the discussion in the text.

radiation if made nonzonal. For example, Ierley and Young (1991), in their studies of the stability of the western boundary layer, find modes with the extended oscillatory tail for small downstream wave numbers. In a study of the dynamic properties of nonzonal jets, Jae Yul-Yun (1986) reports the existence of the radiating solutions in the boundary forced problem with a disturbance traveling along a nonzonal current.

We will use the phase speed condition (2.13) as the necessary condition for radiation and then check the smallness of l_i/l_r and look at the limit of $c_i \to 0$. This does not guarantee that the radiation from the mean current will be energetically significant. Even if the trapping is very weak, the amplitude of the exterior motions can be negligible compared to that in the jet region. We also need to examine the spatial structure of the calculated modes to convince ourselves in the existence of the radiation of energy.

2.4 Basic state velocity profile and jump conditions.

One way of representing a mean state, which is convenient for the analysis of the stability problem, is to divide our domain into intervals in y with different forms of $\bar{u}(y)$ in each of them. For example, we can study the problem on the two external semi-infinite regions with zero mean velocity and one internal finite interval with nonzero value of $\bar{u}(y)$:

$$\bar{u} = \begin{cases} U(y) & \text{if } |y| < 1 \\ 0 & \text{if } |y| > 1. \end{cases} \tag{2.14}$$

We non-dimensionalized our problem by using the half-width of the jet L_{jet} and its ratio to the dimensional maximum jet velocity L_{jet}/U_* as characteristic space and time scale correspondingly.

Note now, that the problem with the nonzonal jet is no longer symmetric in y. In the case of zero tilt ($\alpha = 0$), we find modes symmetric in the y structure of the eigenmode (sinuous mode) and modes with an antisymmetric structure of the eigenmode (varicose mode). When the tilt is nonzero, neither a purely symmetric nor antisymmetric eigenmode structure is possible. It is easy to see by changing y to $-y$ in (2.6), the equation then changes to its complex conjugate (note also that c changes to its complex conjugate as well). Henceforth, $\phi(-y) = \pm\phi(y)^*$ and not $\pm\phi(y)$ as in the case of $\alpha = 0^o$. Therefore, we have to consider the solution for negative and positive y separately.

We first solve the equation 2.6 in each of the three regions and then use matching or jump conditions to connect the solution. Jump conditions are obtained by integration of (2.6) for $\bar{u}(y)$ continuous, but rapidly varying across each interface from $y = \pm 1 - \epsilon$ to $y = \pm 1 + \epsilon$:

$$\int \frac{d}{dy}\left(\phi_y(\bar{u} - c) - \phi\bar{u}_y + \frac{i\beta_1}{k}\phi\right) dy = -\int \left[(\beta_2 - k^2(\bar{u} - c))\phi\right] dy \qquad (2.15)$$

Now we let the interval of integration, in which the jump in the basic flow structure occurs, go to zero: $\epsilon \longrightarrow 0$. The right-hand side of the above equation does not contain y-derivatives and, therefore, goes to zero in the limit. We get:

$$\Delta(\phi_y(\bar{u} - c) - \phi\bar{u}_y + \frac{i\beta_1}{k}\phi) = 0, \qquad (2.16)$$

where Δ stands for the "jump" across the point and is zero if a function is continuous. The condition is essentially the requirement of the continuity of pressure accross a material interface.

One should note the presence of the term $i\phi\beta_1/k$ in the equation (2.16). The term is zero only for a zonal jet; it is very important for a problem with a nonzonal current, especially for those solutions that are long in x (small k). In the following sections, we will observe that there are the long waves that are of radiating character in the problem.

For the derivation of the second jump condition, we rewrite (2.16) in the form:

$$(\bar{u} - c)^2 \frac{d}{dy}\left(\frac{\phi}{\bar{u} - c}\right) = G(y) - \frac{i\beta_1}{k}\phi,$$

where $G(y)$ is a continuous function. Then by dividing by $(\bar{u} - c)^2$ and following the same procedure as outlined above, we obtain:

$$\Delta\left(\frac{\phi}{\bar{u}-c}\right)=0 \tag{2.17}$$

The condition is the requirements of the continuity of streamline slope. Indeed, consider streamline displacement defined by $\eta = N(y)e^{ik(x-ct)}$. Then, the continuity of the slope η_x requires the continuity of $ikN(y)$, where $N(y) = \phi(y)/(\bar{u}-c)$ from the equation $(\frac{\partial}{\partial t}+\bar{u}\frac{\partial}{\partial x})\eta = v$.

The jump conditions (2.16, 2.17) together with the boundary conditions (2.7) allow us to solve the eigenvalue problem and obtain the dispersion relation

$$c = c(k;\beta_1,\beta_2).$$

2.5 Summary

We have formulated the stability problem for a barotropic model with a basic state in the form of a nonzonal current. The dynamical properties in the model are different from those in a conventional model with a zonal flow.

The difference in the basic stability properties can be seen in the example of the stability theorem which is an analog of the sufficient condition for stability of a zonal current. The conventional sufficient condition for stability of a zonal current is modified in the case of a nonzonal flow to become a sufficient condition for the absense of stable normal modes. We have also demonstrated the destabilizing effect of the horizontal tilt on a simple analytical example. The more unstable character of a nonzonal current can also be seen in the following chapter that describes the results of computations.

Among several criteria derived above for radiation of a linear solution, two are especially important. First uses the idea that spatial trapping of the solution can be caused by the initially fast exponential growth alone. If this is the case, the radiating nature of the solution should become transparent when the growth slows down. Within the linear theory, the latter can be achieved by changing parameters so one approaches the cut-off of a dispersion curve. The idea of observing changes in solution caused by the decreasing growth rate also becomes very useful in a nonlinear problem during the stage of nonlinear equilibration. The new form of another useful conditions for radiation, namely the phase speed condition, demonstrates the more radiating character of nonzonal currents compared to zonal flows. The more radiating character is supported by the results of the following chapters.

Chapter 3

Results from the barotropic problem

We have formulated the problem and defined what we understand by radiation in the linear theory, therefore, we are ready to proceed with the solution. The eigenvalue problem formulated in section 2.1 is solved numerically by using MATLAB. We report the results of computations in this chapter for two different forms of the mean velocity profile. We start from the simplest example of the broken-line top-hat jet in the section 3.1 and then consider the problem with a continuous profile of the basic velocity in section 3.2. For a better demonstration of the effects of a horizontal tilt, we first consider a zonal flow (section 3.2.1), and then start to increase the value of the tilt (sections 3.2.2, 3.2.3). The main finding is that even a very small value of the tilt causes non-radiating zonal flow to radiate waves that are long in the along-jet direction. To confirm the radiation, we look at both dispersion curves and spatial structure of the solutions. In addition, we report the more unstable character of a nonzonal current as compared to the zonal flow as suggested in section 2.2.

In section 3.2.4, we also consider the balance between terms in the energy equation. The balance is interesting for the solutions that are close to the cut-offs of the dispersion curves, in other words for modes with very small growth rates. The terms in the energy equation in this limit either go to zero or, instead, remain finite and balance each other.

3.1 Top-Hat Jet

The simplest possible example of a mean profile for the problem formulated in the previous section is the top-hat jet, for which the velocity in the internal region is constant: $U(y) = U$ in (2.14). The instability found in this problem is most likely related to the discontinuity in the velocity field at $y = \pm 1$ and the artificial delta-function in the potential vorticity (Kelvin-Helmholtz type of instability). We consider this example because we want to compare our results with the case of zonal top-hat jet studied by Talley (1983). Some interesting changes in the radiating properties will be demonstrated.

The $U(y)$ is piece-wise constant: It is 1 for $-1 < y < 1$ and zero for $y < -1$ and $y > 1$. The solution $\phi(y)$, therefore, is a sum of two waves with complex y-wavenumbers in each of the three regions:

$$Ae^{il_{1,2}y} + Be^{il_{4,3}y}$$

where indexes $(1, 4)$ correspond to the regions $|y| > 1$ where $U(y) = 0$:

$$l_{1,4} = \frac{1}{2c}\left(\frac{\beta_1}{k} \pm \sqrt{\left(\frac{\beta_1}{k}\right)^2 - 4c(ck^2 + \beta_2)}\right) \tag{3.1}$$

We denote the wavenumber with a negative imaginary part as l_1, so $Ae^{il_{1,2}y}$ decays at $y = -\infty$. The imaginary part of l_4 is positive, so $Be^{il_{4,3}y}$ decays at $y = +\infty$. Note the different form of the y-wavenumber in each of the external regions as a result of the above mentioned non-symmetry in y. Boundary conditions (2.7) require the amplitude of the wave that increases away from the jet to be set to zero. Therefore, $B = 0$ for $y < -1$ and $A = 0$ for $y > 1$.

Indices $(2, 3)$ correspond to the region $|y| < 1$ where $U(y) = U$:

$$l_{2,3} = \frac{1}{2(c-U)}\left(\frac{\beta_1}{k} \pm \sqrt{\left(\frac{\beta_1}{k}\right)^2 - 4(c-U)(k^2(c-U)+\beta_2)}\right). \qquad (3.2)$$

We now write two jump conditions (2.16, 2.17) and get the dispersion relation of the problem:

$$(l_2(U-c)^2 + U\beta_1/k - l_1c^2)(l_3(U-c)^2 + U\beta_1/k - l_4c^2)e^{2i(l_3-l_2)} =$$

$$(l_3(U-c)^2 + U\beta_1/k - l_1c^2)(l_2(U-c)^2 + U\beta_1/k - l_4c^2), \qquad (3.3)$$

For the top-hat jet, we fix the planetary vorticity gradient β and "rotate" the jet changing tilt angle α from zero looking at the effects of the tilt. Then, we can compare our results with those from the studies of the zonal top-hat jets (Talley, 1983) and look at the changes in the radiating properties of the solution caused by the changed jet orientation. We present our results in Fig. 3.1 in the form of the dispersion curves that are solutions of the dispersion relation 3.3 for complex c as a function of x-wavenumber k; and where we recall that the x-axis is tilted with the jet axis. Three values of the tilt angle are chosen for comparison: $\alpha = 0^o$, 30^o and 45^o.

The first fact that comes to our attention is the change in the shape of the curves. There is a long-wave cut-off (LWC) for Mode 1 when $\alpha \neq 0$, which is a varicose mode of the zonal top-hat jet modified by the nonzero value of the tilt angle α. The real part of the phase speed of Mode 1 is larger than the maximum value of the mean flow speed for small k. The phase of the wave travels faster than the flow itself in the downstream direction.

The long-wave (LW) limit of Mode 1 is also a radiating limit, which supports our expectation to have more radiating solution when $\alpha \neq 0$. One can check the conditions for radiation formulated in section 2.3. The real part of the phase speed c_r is in the range for the Rossby wave phase speed (2.13); henceforth the phase speed condition is satisfied. To demonstrate that, we present the right-hand side of (2.13) by the dotted line in Fig. 3.1b,c; the curve $c_r(k)$ goes beneath the dotted line in the figure.

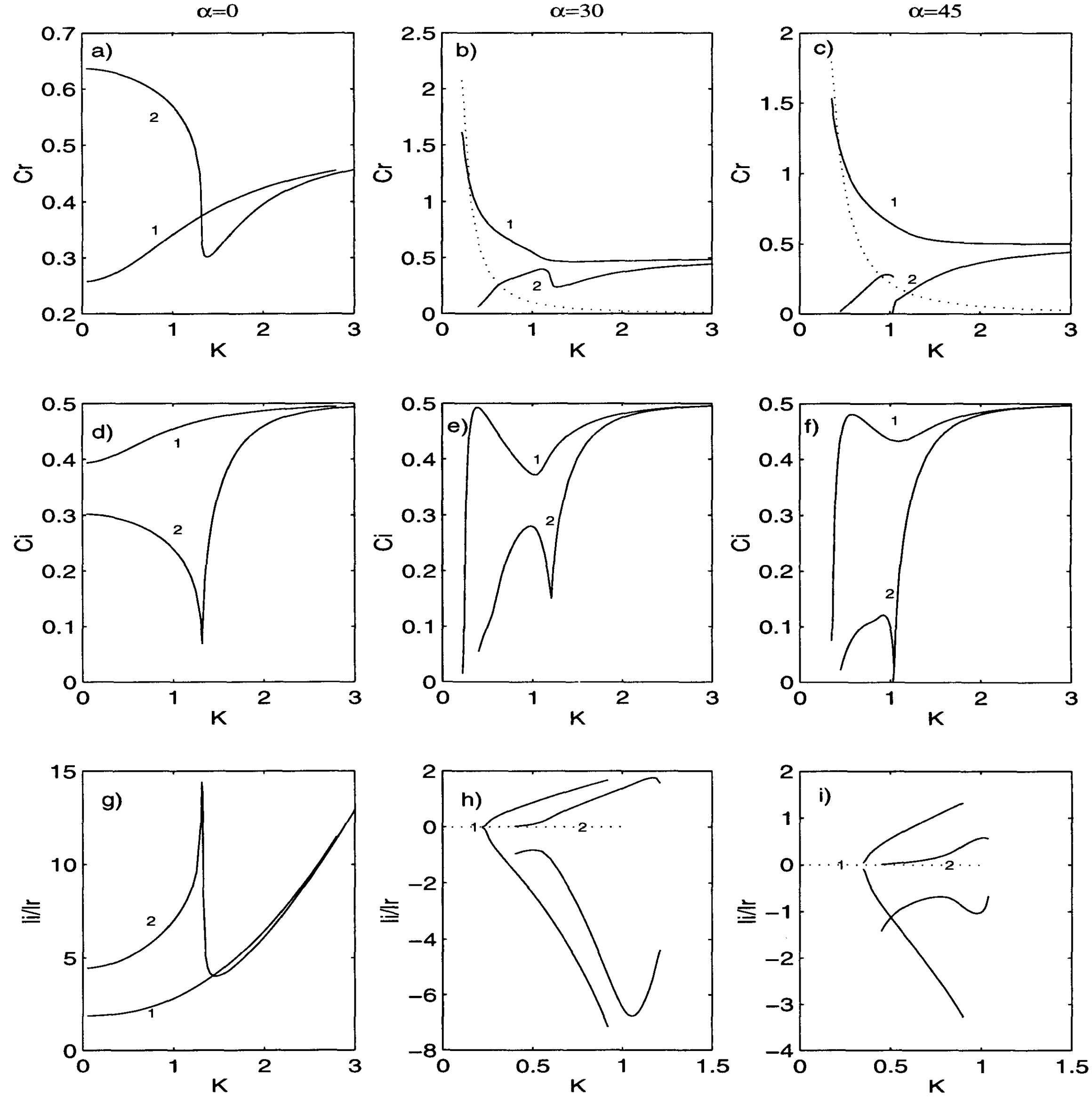

Figure 3.1: Results for the Top-Hat jet for $\beta = 1.5$: (a,d,g) $\alpha = 0^o$, (b,e,h) $\alpha = 30^o$, (c,f,i) $\alpha = 45^o$. Upper panel: Real parts of the phase speed c for the two modes vs k. The maximum Rossby wave phase speed (right-hand side of Eq. 2.13) is shown by the dotted line. (d-f) Imaginary parts of c. (g-i) Ratio of the imaginary part of the y-wavenumber l to the real part $\frac{l_i}{l_r}$ vs k. The dotted line is a zero line. The curves below the zero line correspond to the region $y < -1$, above - to the region $y > 1$. Mode numbers are shown in the plot.

The y-structure confirms the radiating properties of the solution in LW limit. The spatial decay scale is much longer than the oscillation scale; therefore, the solution is "wavy" in the exterior. Moreover, the ratio between two scales l_i/l_r goes to zero as c_i approaches zero (Fig.3.1e,f). From all of the above we can conclude that Mode 1 is radiating in the LW limit.

The situation for Mode 2, which is a modified sinuous mode of the zonal top-hat jet, is less clear. The solution seems to be radiating only for $y > 1$, because the ratio l_i/l_r gets small only for the positive y. This example demonstrates us that the phase speed condition is only a *necessary* condition for radiation and does not guarantee us the radiation. In addition, the very existence of Mode 2 seems to be closely connected with the discontinuity of the velocity profile. Mode 2 does not have an analog in the problem with more realistic continuous profile of the mean velocity discussed in the next section.

We also note the absence of a short-wave cut-off (SWC) in the problem as another very special feature of the piece-wise constant velocity profiles. We do not expect the waves arbitrarily short in x to be unstable in the inviscid problem with continuous mean velocity profile.

We want to be confident that the changes in radiating properties we have found are not only consequences of the unrealistic choice of the broken-line mean velocity profile. For this purpose, we proceed now with a study of a continuous velocity profile.

3.2 Continuous jet

In order to keep the mean potential vorticity gradient finite, we require $U, \frac{d}{dy}U$ in (2.14) to be continuous across $y = \pm 1$. For all our computations we use the following form:

$$U(y) = (1 - y^2)^3.$$

As one can check, for this choice $U(\pm 1) = 0$ and $U_y(\pm 1) = 0$. We also make the vorticity gradient continuous by choosing $U_{yy}(\pm 1) = 0$. The method of solution and main results do not depend on the particular choice of $U(y)$ as long as the velocity itself and its two first derivatives are continuous. In calculations not presented in the following subsection, we considered three different velocity profiles: non-symmetric profile $U(y) = exp[2(y - \sqrt{2} + 1)](1 - y^2)^2[4(3 - 2\sqrt{2})]^{-1}$ and a less "sharp" symmetric one $U(y) = \frac{1}{2}(1 + cos\pi y)$. All results agree qualitatively with those reported below.

The solution of this eigenvalue boundary problem is obtained by a shooting technique involving an iterative improvement of the initial guess in phase speed c. The method is described in the Appendix.

To concentrate on the effects of the nonzonality on the radiating properties, we start from the zonal jet case (in other words, from $\alpha = 0$).

3.2.1 Zonal jet

We find two unstable modes: the varicose mode (Mode 1) and the sinuous mode (Mode 2). The typical form of the dispersion curves is presented in Fig.3.2(a,b) for the two values of the planetary vorticity gradient: $\beta = 1$ and $\beta = 4$. The corresponding growth rates kc_i are shown in the heavy lines providing the information about the relative linear stability of both the modes.

The range of the unstable x-wavenumbers is wider for $\beta = 1$. Mode 1 is unstable for arbitrary long waves: LWC is absent. We observe a short-wave cut-off (SWC) for Mode 1 and two cut-offs for Mode 2. Mode 2 is the most unstable mode in the problem for both values of β chosen. Both the range of the unstable x-wavenumbers and the growth rate kc_i decrease with larger β ($\beta = 4$) as a consequence of the stabilizing effect of the planetary vorticity gradient.

The real part of the phase speed c_r of both modes is positive and less than the maximum value of the mean flow speed; the latter is in agreement with the semi-circle theorem valid for the zonal current (Pedlosky, 1964).

Since c_r is always within the range for the mean flow speed, the presence of critical layers, at which $\bar{u} = c$, for all cut-off values of k should be anticipated.

We present the general stability properties of the problem by showing the stability diagram in the $k - \beta$ parameter plane (Fig.3.2c). We construct this diagram using the following method. At a regular critical layer ($y = y_c$) we have $\bar{u}(y_c) - c = 0$ and $\beta - \bar{u}_{yy}(y_c) = 0$. From the latter condition, we can find $y_c(\beta)$, then find phase speed c_c from the condition $c_c = \bar{u}(y_c)$ and get the corresponding value of the critical x-wavenumber k_c treating k as an eigenvalue in the original problem. The curves $k_{LWC}(\beta)$ and $k_{SWC}(\beta)$ give us information about the regions of instability on the parameter plane. Shaded regions correspond to the existence of the unstable mode. The problem is stabilized for the large values of the planetary vorticity gradient; for $\beta > max(U_{yy}) = 4.8$, the solution is stable satisfying the sufficient condition for stability of a zonal current.

The solution is always trapped in agreement with the results of several previous investigations (Flierl and Kamenkovich, 1975; Pedlosky, 1977; Malanotte-Rizzoli *et al.*, 1987a; Talley, 1983). The phase speed condition cannot be satisfied as $c_i \rightarrow 0$, since all cut-offs correspond to the critical layers for which $c_c = \bar{u}(y_c) > 0$; whereas, free Rossby waves always travel westward.

3.2.2 Small tilt: $\alpha = 5^o$

We now look at the changes caused by the nonzonality of the jet. In this section we demonstrate that even a very small change in the flow orientation modifies the radiating properties of the problem significantly. We rotate the jet by 5^o from the east-west position and compare the results with those for the purely zonal jet that are shown by the dashed line in Fig.3.3.

First we notice that the shape of the dispersion curves changes significantly in the LW limit of both modes. Longer waves in x are more likely to "feel" the presence of the downstream component of the planetary vorticity gradient according to Eq. 2.6. That is why the changes for the longer waves appear to be the largest, which is in a general agreement with the results for the top-hat profile. The results for the shorter waves are

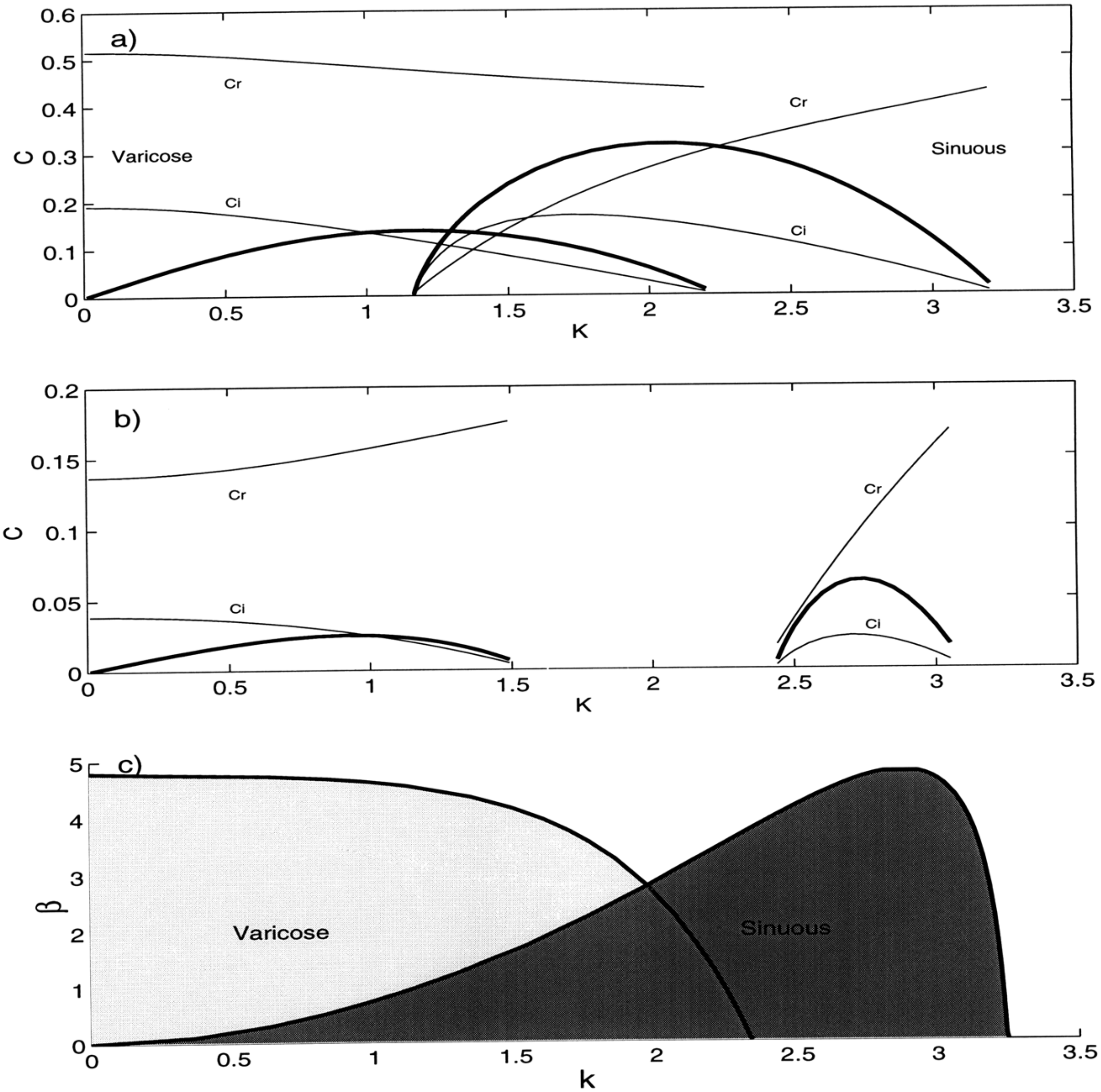

Figure 3.2: Results for the zonal continuous barotropic jet. (a) Real and imaginary parts of the phase speed c (labels are on the plot next to the corresponding curves) vs k for two modes for $\beta = 1$. Growth rates kc_i are shown in the heavy lines. (b) The same as (a) but for $\beta = 4$. (c) Stability diagram in the β-k plane. Shaded regions on the β-k plane correspond to the existence of the unstable modes.

practically indistinguishable for $\alpha = 0^o$ and for $\alpha = 5^o$.

In the LW limit of Mode 1, in a way similar to the top-hat jet results, the phase always travels faster than the mean flow ($c_r > U(y)$) eliminating the possibility of a critical layer. The wave vector becomes nearly normal to the jet axis at the LWC ($k = k_{LWC}$), resulting in the fast phase propagation in the along-jet direction. The real part of the phase speed is also inside the interval for the Rossby wave phase speed (Eq.2.13). The upper bound on c in the phase speed condition, that is the right-hand side of (2.13), is shown by the dotted line in the figure.

Changes in properties taking place with the change in the orientation of the flow are also observed for Mode 2. At the LWC c_r is negative (Fig.3.3d) for this mode, leading to the two important consequences. First, as in the case of Mode 1, no critical y_c exists in the problem such that $c = \bar{u}(y_c)$. Second, the phase speed condition is satisfied, hinting at the possibility of radiation; the left-hand side of (2.13) is much smaller than the c_r and is not shown on the plot.

The most interesting thing to observe is that both modes, strongly trapped in the case of the zonal jet, change their radiating properties when the jet is slightly rotated as it can be seen from looking at the y-structure (see Fig.3.4). Both the ratio between imaginary and real part of the y-wavenumber l_i/l_r and l_i itself go to zero as the x-wavenumber k approaches k_{LWC}. This fact, together with the phase speed condition, allows us to conclude that both modes are radiating in the LW limit. The radiation is clearly made possible due to the small but non-zero value of the horizontal tilt.

Near the SWC on the dispersion curve, both modes remain trapped, because the phase speed condition is not satisfied. The radiation remains the feature of only the long waves of each mode.

3.2.3 Large tilt: $\alpha = 30^o$

To emphasize the effects of the nonzonality on the radiating properties, we now proceed with the analysis of the strongly tilted nonzonal jet. In this section, the jet makes

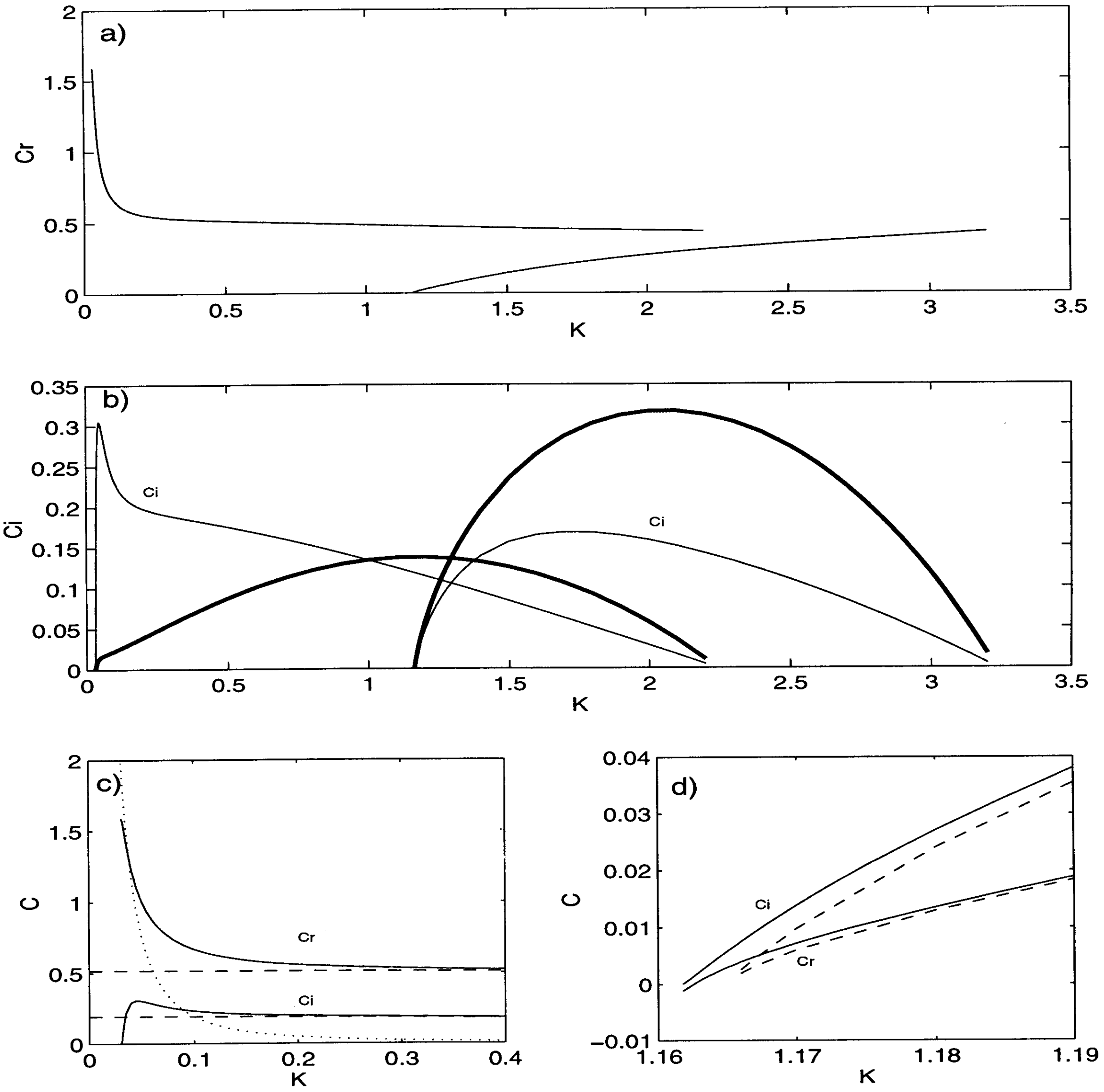

Figure 3.3: Results for the tilted barotropic jet for $\alpha = 5^o$ and $\beta = 1$ (a) Real parts of the phase speed c_r vs k for two modes. Mode 1 is to the left (smaller k). (b) - imaginary parts of the phase speed c_i and growth rates (heavy lines) vs. k. (c) comparison with the zonal jet near the LWC for Mode 1. Real and imaginary parts of c are shown by the solid lines for the tilted jet and by the dashed lines for the zonal jet. The dotted line is the maximum Rossby wave speed, i.e. the right-hand side of (13). (d) the same as (c) but for Mode 2.

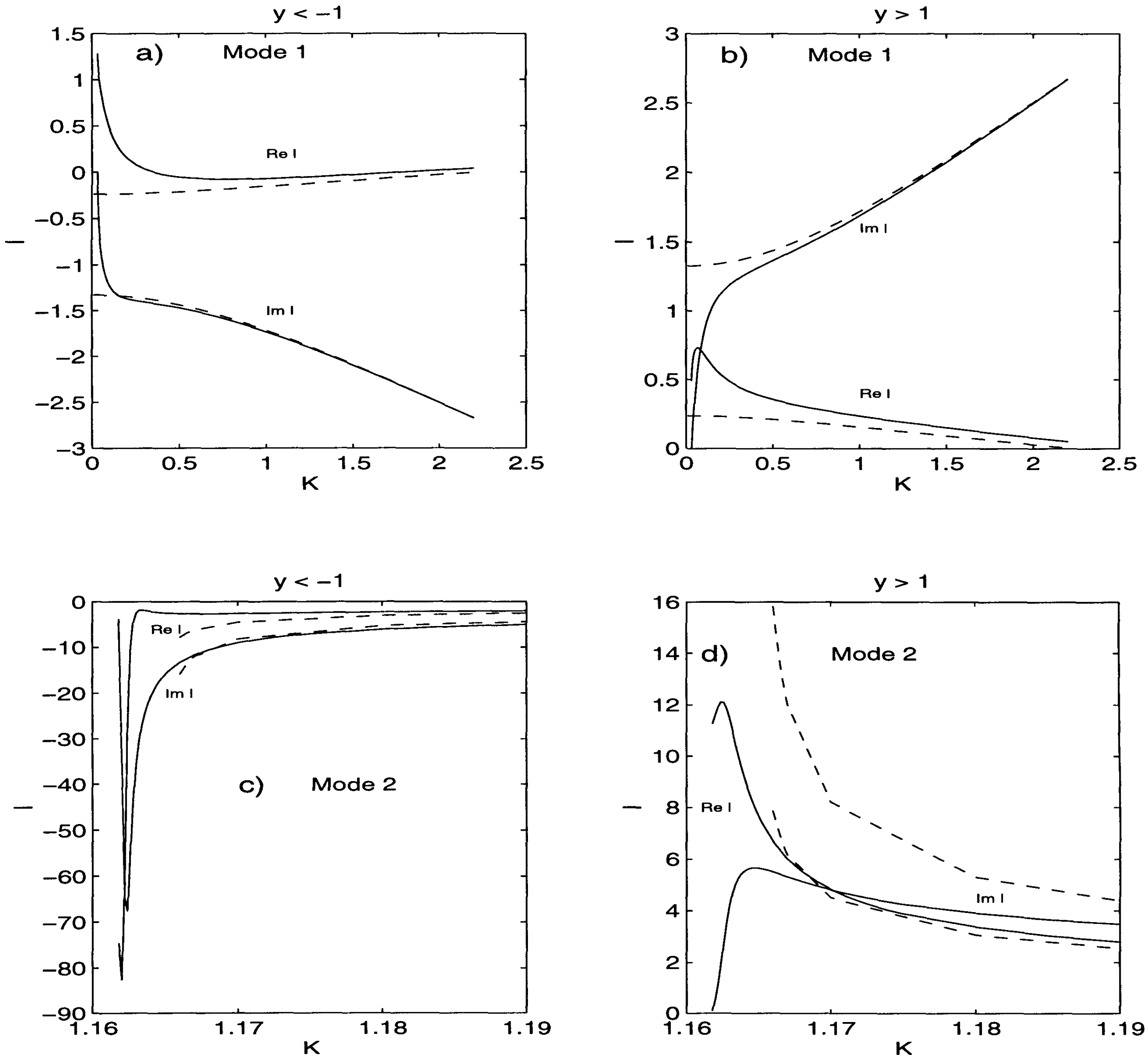

Figure 3.4: Complex y-wavenumbers l vs. k for the same parameters as in Fig.3.3. Real and imaginary parts are labeled on the plot next to the corresponding curves. l for the zonal jet is shown by the dashed line, for $\alpha = 5^o$ by the solid line. (a,c) region $y < -1$. (b,d) region $y > 1$. (a,b) Mode 1. (c,d) Mode 2.

an angle of 30^o with a latitude circle. We observe the evolution of the two unstable modes found earlier with a now larger value of the tilt. Both modes are shown in Fig.3.5(a,b) for $\beta = 1, 4$ and 6. Note, that some interesting properties of the dispersion curves found in the case of $\alpha = 5^o$ are enhanced by the larger horizontal tilt.

The behavior in the LW limit for $\alpha = 5^o$ does not change qualitatively with a larger angle. The real part of the phase speed c_r tends to be larger than the maximum value of $\bar{u}(y)$ for Mode 1 and smaller than the minimum value of $\bar{u}(y)$ for Mode 2. Critical layers are, therefore, absent in this limit.

It is also interesting to note that we find no solution for k larger than k_{LWC}. In other words, no neutral modes longer than the cut-off wave-length exist. The fact is a consequence of the infiniteness of the interval in y. In the experiment not described here, the neutral mode for $k > k_{LWC}$ exists if reflecting walls are put at some distance from the jet axis; the basic radiating properties remain qualitatively unchanged.

The phase speed condition is satisfied in the LW limit, since c_r is within the range (2.13). In fact, for Mode 1, c_r is slightly smaller than the upper bound on c in (2.13). Mode 2 has negative c_r, which is significantly larger than the lower bound on c in the phase speed condition, that is, the left-hand side of (2.13). As a result, radiation is possible, according to the phase speed condition. The range of k for which c_r satisfies (2.13) increases with larger β for Mode 2, which indicates the enhancement of the radiating properties by the planetary vorticity gradient.

The shape of the dispersion curves for the long waves of Mode 1 can also be compared with the Mode 1 in the problem with the top-hat jet. The interesting fact is that despite the primitive character of the discontinuous velocity profile, the behavior of Mode 1 in the LW limit is represented quite well in the top-hat problem.

The SWC is present for both modes. The temporal growth of arbitrarily short waves in the case of the top-hat profile is clearly the consequence of the infinitely narrow shear zone in its mean velocity profile. The phase speed at SWC ($k = k_{SWC}$) is within the range of the mean velocity (at least for not very large values of β). The presence of critical

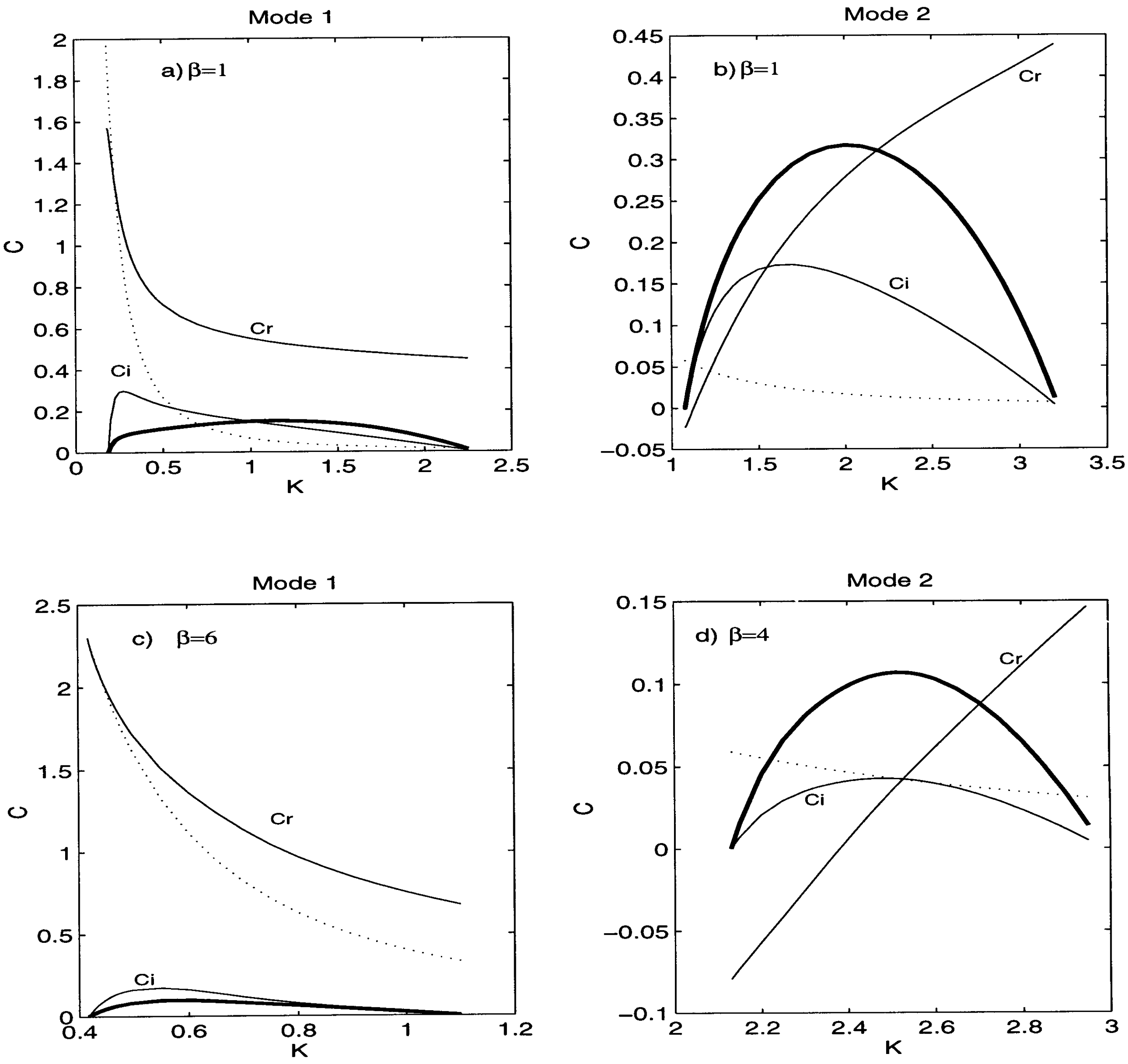

Figure 3.5: Results for $\alpha = 30^o$. Complex c vs. k. Real and imaginary parts are labeled on the plot next to the corresponding curves. Growth rates are shown in the heavy lines. Dotted lines show maximum Rossby wave phase speed. Mode 1: (a) $\beta = 1$, (c) $\beta = 6$. (b) the same as for Mode 2 and $\beta = 1$. (d) Mode 2, $\beta = 4$.

layers should be anticipated although their structure is less clear than in the zonal jet case because of the presence of the x-component of the planetary vorticity gradient β_1. The phase speed condition is not satisfied, therefore, the solution is trapped.

The stability diagram is shown on Fig.3.6. The first thing to notice is that the tilted jet is unstable for very large values of β, even for those for which the y-component of the mean potential vorticity gradient $\beta_2 - \bar{u}_{yy}$ is single-signed: $\beta > 5.54$ since $Max(\bar{u}_{yy}) = 4.8$. Unstable Mode 1 exists for $\beta < 16$, while the zonal jet is stable for $\beta > 4.8$. Mode 2 is stabilized for smaller β ($\beta = 7$), but is still unstable for $\beta > 4.8$. Our expectations for a nonzonal flow to be more unstable than a zonal current (see Chapter 1 and section 2.2) are supported by the results. However, the stabilizing effect of the planetary vorticity gradient is still present: with larger β growth rate kc_i becomes smaller (fig. 3.5), and the interval in the x-wavenumber $k_{LWC} < k < k_{SWC}$ corresponding to instability shrinks (fig. 3.6).

The ability of radiation is not lost with a larger tilt of the jet, as we can see from Fig.3.7(a-d). We have already observed that the phase speed condition is satisfied. Let us check the other conditions for radiation. The imaginary parts of the y-wavenumbers are small for the long waves of both the modes. This means, as we have remarked in section 2.3, that modes are weakly trapped in the LW limit and wave packets can propagate far from the jet, while their amplitude is not significantly increased through the unstable temporal growth. The ratio $l_i/l_r \to 0$ as $k \to k_{LWC}$ for both modes. The spatial trapping disappears when the mode becomes neutral, that is as $c_i \to 0$, which hints to the radiating nature of the solution. For Mode 2, l_i is typically smaller for $y > 1$. It is interesting to note that, although for Mode 2 the ratio l_i/l_r is small, l_i itself for the negative y is not, and only gets to zero for k close to k_{LWC}. In contrast, the decay scales in both directions are similar for Mode 1.

The y-structure of the eigenmode is shown in Fig.3.7(e,f) for k chosen close to k_{LWC}. For Mode 1 the amplitude of the wave-like response of the exterior is large, compared to the interior motions, and is larger for $y < -1$ than in the rest of the region. For the

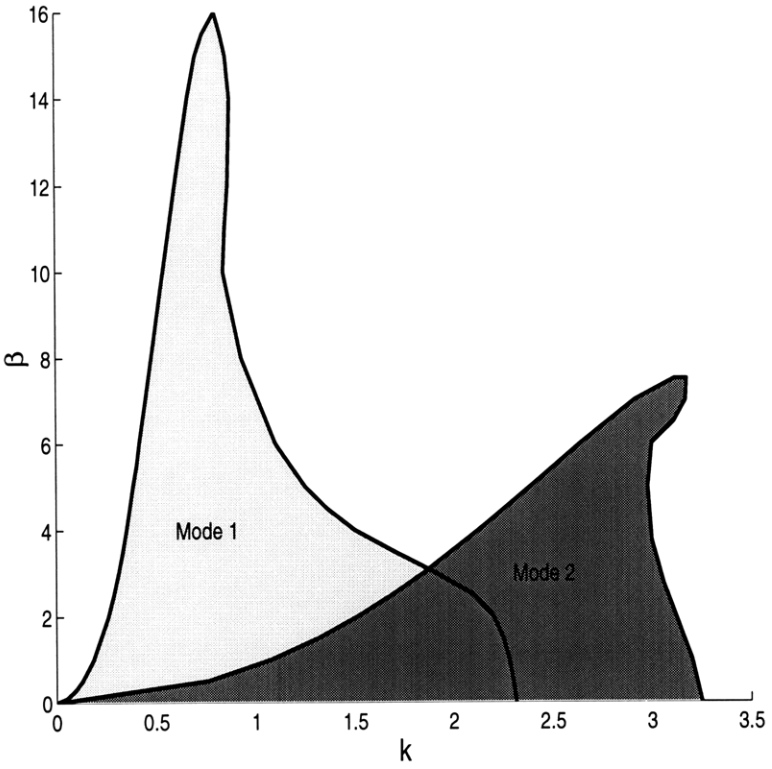

Figure 3.6: Stability diagram for $\alpha = 30^o$. Shaded regions on the β-k plane correspond to the existence of the unstable modes.

north-eastward oriented flow, the above fact means a significant radiation of energy to the South-East from the current. We also observe that the radiating response for the negative y is represented by the wave that is shorter than the wave that radiates for positive y. See the discussion of the energy propagation diagram in section 2.3. for the explanation of this fact.

The streamfunction of Mode 2 is very small in amplitude in both external regions. However, since the solution for $y < -1$ takes the form of a very short wave, $-\phi_y$ (the zonal velocity) is rather large but still smaller than the amplitude in the interior region. It is more difficult to say that Mode 2 corresponds to energetic radiation. In fact, it is only at the very LWC at which the exterior motions are identifiable. For shorter waves in x the perturbation streamfunction either rapidly decays in space or is extremely small in amplitude in the region. Mode 1 obviously corresponds to a more significant radiation

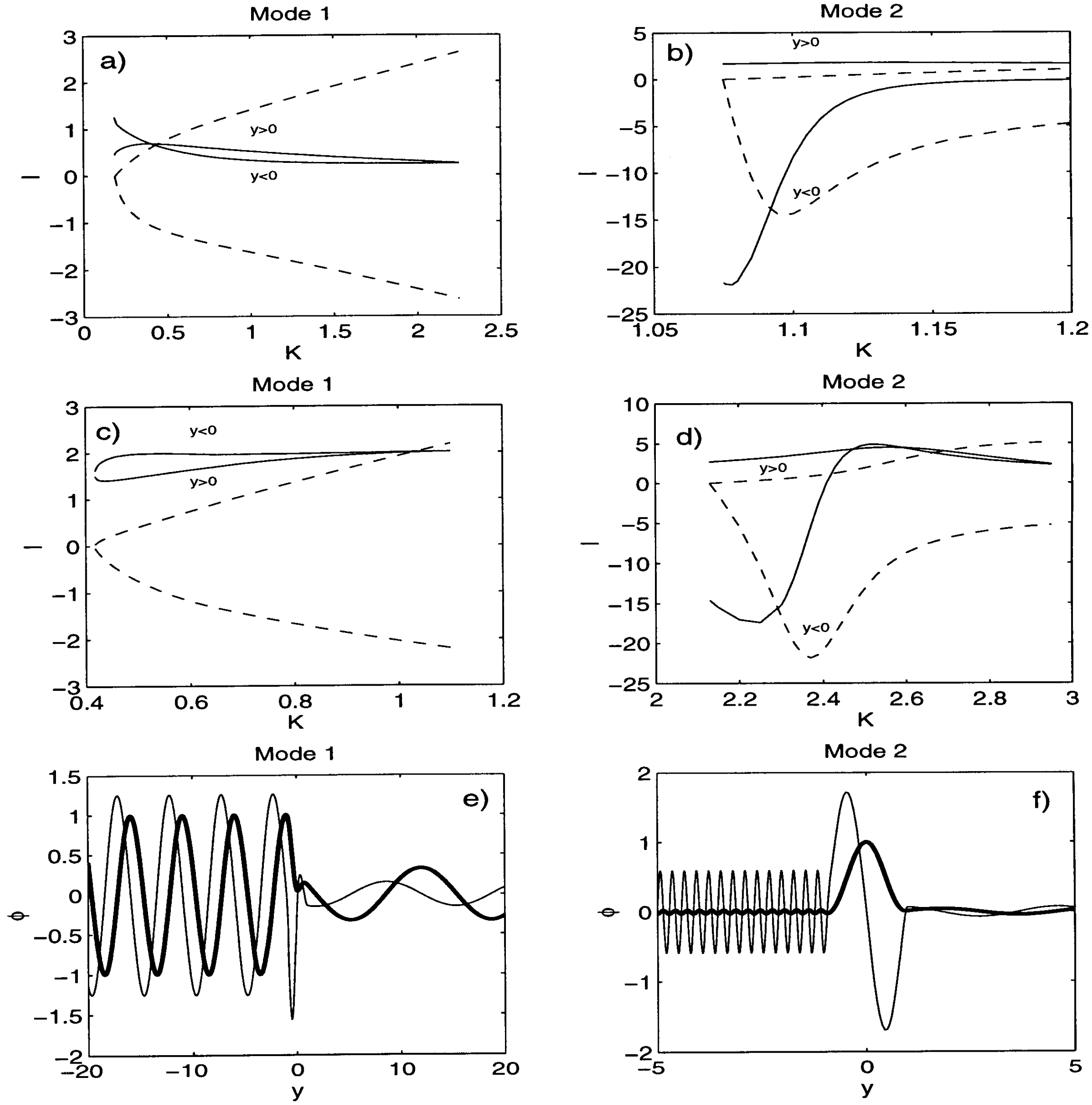

Figure 3.7: Radiation of the two modes for $\alpha = 30^o$. Mode 1: a) $\beta = 1$, c) $\beta = 6$. Mode 2: b)$\beta = 1$, d)$\beta = 4$. (a-d) complex y- wavenumbers vs. k. Imaginary parts are shown by the dashed lines, real parts by the solid lines. Negative imaginary parts correspond to $y < -1$, positive correspond to $y > 1$. The appropriate regions for the real parts are labeled on the plot. (e-f) $\phi(y)$ (thick line) and $\phi_y(y)$ (thin line) as functions of y at k near the LWC: $k = .1845$ for (e) and $k = 1.0751$ for (f).

of energy; however, this is not clear from looking only at the values of l_i. We therefore underline the importance of the analysis of the y-structure for the consideration of the radiating properties of a mode.

3.2.4 Energy balance in LW limit

We now want to study the balance between different terms in the energy equation in the radiating limit discovered above. First, we derive the equation itself. We multiply Eq. 2.4 which is the linearized equation for the streamfunction by the streamfunction ψ and integrate it in x from 0 to L, and in y from $-y_b$ to y_b. We assume that a solution is periodic in x with a period L, i.e. $\psi(0,y,t) = \psi(L,y,t)$. After integration by parts, we obtain:

$$\frac{\partial}{\partial t}K_e = \overset{F_{brt}}{\int_{-y_b}^{y_b} \bar{u}_y \overline{\psi_x \psi_y}^x dy} + \overset{Flux}{\left[-\bar{u}\overline{\psi_x \psi_y}^x + \overline{\psi \psi_{yt}}^x - \frac{1}{2}\beta_1 \overline{\psi^2}^x \right]_{-y_b}^{y^b}} \tag{3.4}$$

where a horizontal bar represents averaging in x:

$$\overline{G}^x = \frac{1}{L}\int_0^L G dx,$$

and

$$K_e = \int_{-y_b}^{y_b} \frac{1}{2}\overline{(\psi_x^2 + \psi_y^2)}^x dy.$$

is the averaged in x and integrated in y perturbation kinetic energy. There are two terms on the right-hand side that are responsible for the temporal change in the perturbation kinetic energy. First (F_{brt}) is the energy conversion term, which represents the conversion of energy from the mean current to the perturbations. Second ($Flux$) is the group of flux terms that show how much energy is being fluxed into the region $[-y_b \; y_b]$. Note, that the flux terms are zero if the whole domain is considered ($y_b = \infty$). The terms represent the rate of working by the ageostrophic pressure force on a unit volume of fluid.

As we can see, there is no energy source directly associated with the introduced forcing in the equation for potential vorticity (2.1), which depends on α. The tilt of the jet which is capable of destabilizing the current (section 2.2) explicitly enters the equation only in the *Flux* terms, which do not change the total perturbation kinetic energy.

We now can calculate all terms for solutions found in the previous section. We will focus on the balance between terms in the radiating limit of k approaching the LWC. In the limit of vanishing growth rate $kc_i \rightarrow 0$, the time derivative of the perturbation kinetic energy on the left-hand side of Eq. 3.4 vanishes. Do both terms on the right-hand side go to zero as well?

The results are presented in Fig.3.8 for $y_b = 1.5$. All terms in the energy equation are weighted by the kinetic energy integrated from $-y_b$ to y_b; the left-hand side of the equation 3.4 then becomes $2kc_i$ (is shown by the solid lines in the plots). We should remind the reader that the jet itself occupies the region $[-1\ 1]$. For Mode 1, one can see that terms F_{brt} and *Flux* do not vanish. Instead, they balance each other with *Flux* terms being negative. That means that the energy that is extracted from the kinetic energy of the mean flow through the energy conversion term is then being fluxed *away* from the jet region into the external domain. The kinetic energy in the internal ($[-y_b\ y_b]$) region does not grow, no energy is "spent" on the temporal growth of perturbations. The described dynamical process characterizes the radiation.

In the described above limit, the growth rate is zero and the linear solution cannot grow to finite amplitudes; the fluxed kinetic energy remains small. A solution that is not on the cut-off of the dispersion curve and, therefore, possesses nonzero growth rates is more interesting dynamically. However, the balance in the equation for shorter waves is dominated by terms $\frac{\partial}{\partial t}K_e$ and F_{brt}, while *Flux* terms remain small (Fig.3.8). When we characterize the Mode 1 as radiating, we claim that if the growth rate of such a mode *were set to zero* the mode would become purely radiating and the balance between energy conversion term and the energy that is fluxed away from the jet would be established. The only way to achieve that within linear theory is to look at the dynamics of a solution at the cut-off itself.

The energy balance for Mode 2 near the LWC is different. As one can see on Fig.3.8,

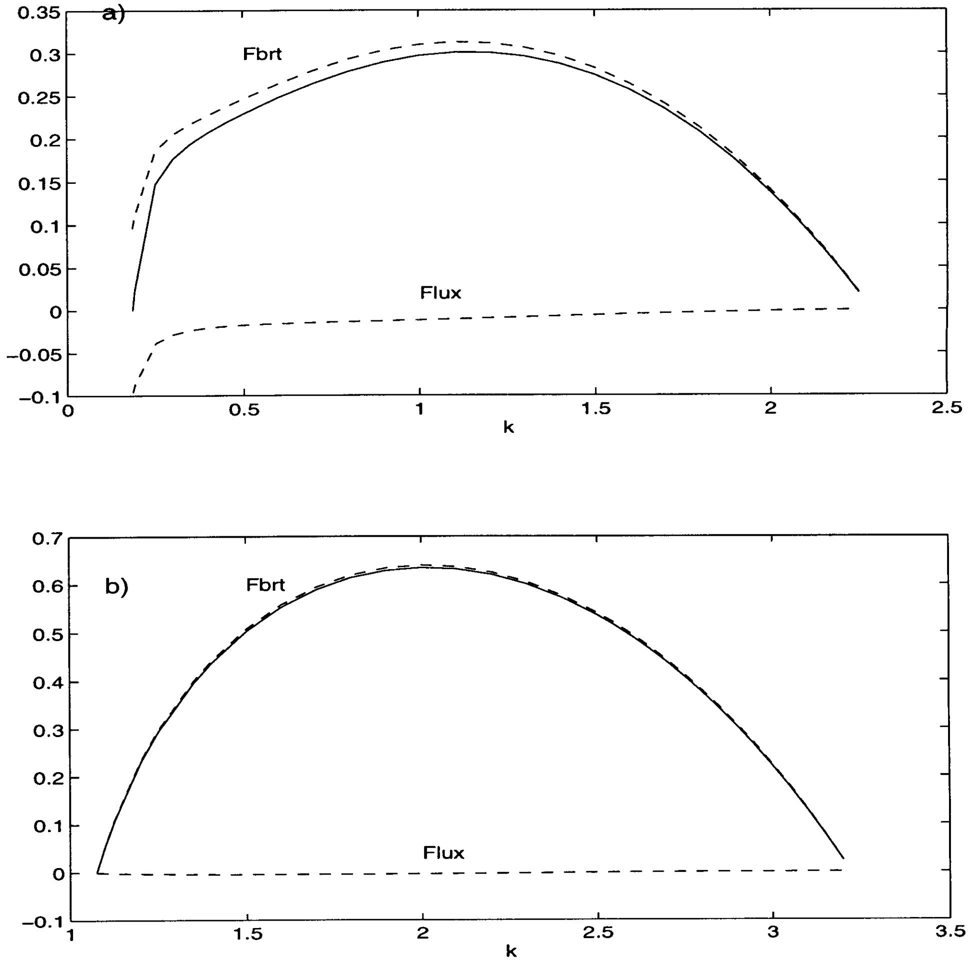

Figure 3.8: The balance between terms in the barotropic energy equation. $\beta = 1$, $\alpha = 30^o$. $y_b = 1.5$. $2kc_i$ is shown by the solid lines, F_{brt} and $Flux$ terms are divided by the integral of kinetic energy $\int_{-yb}^{yb} K_e dy$ and are shown by the dashed lines. (a) Mode 1; (b) Mode 2.

in the LW limit *all* terms in the energy equation go to zero. The extraction of energy from the mean current disappears together with the growth of the perturbation energy in the jet region. Once again, we face the less clear situation for Mode 2. As we recall from the previous section, in the LW limit spatial trapping of Mode 2 disappears, however the amplitude of motions is relatively small. In addition, now we see that the energy balance also suggests that the energy is not fluxed from the region in the LW limit. Based on the above facts, we can say that according to the linear theory, Mode 2 corresponds to insignificant radiation in the LW limit.

3.3 Summary

We have discussed the results of the stability analysis of several simple examples of nonzonal currents. In the analysis, we focused on the radiating properties of a solution as well as on some new stability properties.

Two velocity profiles were considered. First is the simplest top-hat broken-line profile with piece-wise constant velocity. The main mechanism for instability of this profile is the Kelvin-Helmholtz type of instability related to the infinitely narrow shear zone. The second is the more realistic continuous profile which is strongly barotropically unstable. Despite the difference in two choices, some results appear to be very similar in both cases. We now summarize the common properties of the solutions of two problems.

In section 2.3, we formulated what we mean by the radiation in the linear theory. The real difficulty with determining whether a linear solution is of radiating character is due to the fact that fast exponential growth can lead to the strong spatial trapping. The question then is whether the trapping disappears if the growth is stopped. The only way to "stop" the growth in the linear problem is to consider the solution near the cut-off of a dispersion curve. Is a solution wave-like in the exterior in this limit? The other criterion is the phase-speed condition that is also formulated in section 2.3.

In the case of a zonal jet, all solutions are trapped according to all criteria. Since spatial trapping does not disappear when growth rate is made small, we predict that all solutions will remain trapped in the nonlinear regime as well. This prediction will be confirmed in Chapter 5.

When the horizontal tilt is increased slightly from zero to 5^o for the continuous jet, the dynamical picture changes. The changes are the biggest for long waves of each mode found. The phase travels faster than the mean flow itself, therefore critical layers cannot be found at the LWC. The solution in the LW limit is radiating, which is confirmed by both phase speed condition and by the y-structure. We conclude that even a very small horizontal tilt of the jet axis changes trapped solutions to radiating in the LW limit.

The radiating properties are well-pronounced for the larger value of the tilt, $\alpha = 30^o$. For both the velocity profiles, phase speed condition is satisfied by long waves. The solution has a wave-like radiating form in the limit of $c_i \rightarrow 0$ at the LWC. However, the radiation is very energetic for Mode 1 only. The amplitude of the radiating response by Mode 2 of the continuous jet is rather small and the phase speed condition is satisfied for very narrow range of parameters.

The stability properties change for a nonzero horizontal tilt as well. In an agreement with the results from section 2.2, a continuous nonzonal current is more unstable. The unstable solutions are found for very large values of the planetary vorticity gradient, unlike in the case of a zonal jet.

The energy balance in the radiating limit for a nonzonal continuous jet reveals more information about the dynamics of radiation. In this limit for the Mode 1, the balance is established between the energy conversion term and the flux terms, which represent a flux of energy from the region of the jet. The growth rate and the time derivative of the perturbation kinetic energy both go to zero in the limit, since we approach a cut-off. The situation for Mode 2 is less clear. All terms in the energy equation vanish in the limit, which leaves open the question whether the energy is really being radiated into the exterior.

To summarize the results of this section, we should note that barotropic nonzonal currents are capable of radiating long slowly growing waves. Fast growing waves remain trapped, but it is very likely that their spatial trapping is only due to their fast growth. Consideration of nonlinear development is needed for the complete understanding of the process.

Chapter 4

Linear two-layer model

We have observed the effects of nonzonality on simple barotropic currents. Our next objective is to look at the linear stability and radiating properties of the flows with some vertical structure. What overall effect does the baroclinicity have on radiating properties of nonzonal flows? Several changes could be anticipated.

Generally, we expect an increase in the number of unstable modes in the baroclinic model. The radiating properties of the new baroclinic modes will be interesting to investigate. The structure of solution should also change. A solution in the baroclinic problem has a depth-averaged barotropic component and vertically sheared baroclinic one. We will investigate whether both the components are radiating, or, rather, radiating response is dominated by the barotropic component only.

In the baroclinic model, instability is due to both barotropic and baroclinic effects. The growth of the perturbation energy is due to the barotropic and baroclinic energy conversion terms in corresponding energy equation. We will look at both the terms and determine whether they are equally important for radiating solutions. In section 3.2.4, we observed for Mode 1 that in a radiating limit there is a balance between the barotropic energy conversion term and the flux of energy into the exterior region. This type of balance is characteristic for radiation and is very likely to be found in the baroclinic problem. However, whether both the energy conversion terms will play an important role in the balance is an intriguing question.

We can try to answer the posed questions by considering the simplest baroclinic model: the two-layer model with no mean velocity in the lower layer. We formulate the problem and re-derive a sufficient condition for instability and criteria for radiation from the Chapter 2 in the section 4.1. As in Chapter 3, we will consider two velocity profiles: top-hat jet (section 4.2) and continuous jet (section 4.3).

4.1 Formulation

In the quasigeostrophic approximation the potential vorticity equation is written in the following form (Pedlosky, 1987):

$$\frac{\partial}{\partial t}\nabla^2\psi_n + J(\psi_n + \bar{\Psi}_n(y), \nabla^2\psi_n + (-1)^n F(\psi_1 - \psi_2) + \bar{Q}_n) = \mathcal{F}_n, \tag{4.1}$$

with $n = 1, 2$. We follow the usual notation and use F for the squared ratio of the horizontal jet scale to the Rossby deformation radius $(L_* f)^2/g'H$. We take the layer thickness H to be the same for both layers for simplicity.

The unperturbed state is given by

$$\bar{Q}_1 = \beta_1 x + \beta_2 y - \bar{u}_y - F\bar{\Psi}_1; \qquad \bar{Q}_2 = \beta_1 x + \beta_2 y + F\bar{\Psi}_1$$

$$\bar{\Psi}_1 = -\int \bar{u}(y)dy; \qquad \bar{\Psi}_2 = 0. \tag{4.2}$$

As in the barotropic problem, we introduced the forcing $\mathcal{F}_n$ in the equation (note that only $\mathcal{F}_1 \neq 0$). After linearization it follows that a solution in each layer is given by

$$\psi_n(x, y, t) = \phi_n(y)e^{ik(x-ct)}$$

and satisfies the following system of equations:

$$\begin{cases} \phi_{1yy} + (\frac{\beta_2 - \bar{u}_{yy} + F\bar{u}}{\bar{u}-c} - (k^2+F))\phi_1 + \frac{i\beta_1}{k(\bar{u}-c)}\phi_{1y} + F\phi_2 = 0 \\ \\ \phi_{2yy} + (\frac{\beta_2 - F\bar{u}}{-c} - (k^2+F))\phi_2 + \frac{i\beta_1}{k(-c)}\phi_{2y} + F\phi_1 = 0. \end{cases} \tag{4.3}$$

We pick the velocity profile in the upper layer in the same form as in the barotropic problem (2.14). To satisfy the boundary conditions at the infinity we require each wave with nonzero amplitude to decay at $y = \pm\infty$. Thus, the statement of the eigenvalue problem is completed. As before, we search for the complex values of the phase speed corresponding to the unstable eigenmodes.

Some results of the Chapter 2 can be re-derived for the two-layer problem. In particular, the sufficient condition for instability of the section 2.2 can be generalized to include the second moving layer. Multiply the first equation in the system 4.3 by ϕ_1^*, second by ϕ_2^* (asterix stands for a complex conjugate) integrate form $-\infty$ to ∞, take the imaginary part and add the results together. We get:

$$kc_i \int_{-L}^{L} \left[\frac{|\phi_1|^2}{|\bar{u}-c|^2}(\beta_2 - \bar{u}_{yy} + F\bar{u}) + \frac{|\phi_2|^2}{|c|^2}(\beta_2 - F\bar{u}) \right] dy +$$

$$\beta_1 Re \int_{-L}^{L} \left[\frac{\phi_1^*\phi_{1y}}{(\bar{u}-c)} + \frac{\phi_2^*\phi_{2y}}{(-c)} \right] dy = 0. \tag{4.4}$$

We modify the second pair of terms in the way identical to that in the section 2.2. We now note that

$$Re \int_{-L}^{L} \frac{\phi_2^*\phi_{2y}}{(-c)} dy = -\int_{-L}^{L} \left[\frac{1}{2}\frac{\phi_2^*\phi_{2y}c_r}{|c|^2} - Im(\phi_2^*\phi_{2y})\frac{c_i}{|c|^2} \right] dy$$

and the first term on the right-hand side of the above equation is zero. We finally get:

$$kc_i \int_{-L}^{L} \left[\frac{|\phi_1|^2}{|\bar{u}-c|^2}(\beta_2 - \bar{u}_{yy} + F\bar{u}) + \frac{|\phi_2|^2}{|c|^2}(\beta_2 - F\bar{u}) - \beta_1 \left(\frac{Im\phi_1^*\phi_{1y}}{k|\bar{u}-c|^2} + \frac{Im\phi_2^*\phi_{2y}}{k|c|^2} \right) \right] dy +$$

$$+ \frac{\beta_1}{2} Re \int_{-L}^{L} \frac{|\phi|^2\bar{u}_y}{(\bar{u}-c)^2} dy = 0. \tag{4.5}$$

One can see that the condition 2.10 of section 2.2 does not change in the two-layer model with zero mean flow in the lower layer: If the last term is not zero and $\beta_1 \neq 0$, the solution is unstable. The former is true if, for example, $\bar{u}_y$ is of the same sign everywhere in the domain. As in the section 2.2, we can conclude that nonzonal baroclinic currents tend to be more unstable than zonal flows.

We now reformulate the conditions for radiation analogous to those of section 2.3. We first note that our solution now consists of the sum of two Rossby waves in each of the external regions where $\bar{u}(y) = 0$. Both waves have equal frequencies and x-wavenumbers and different y-wavenumbers. One wave is the non-divergent barotropic Rossby wave with the dispersion relation

$$kc = \frac{-\beta_2 k + \beta_1 l}{(k^2 + l^2)}.$$

The other is the baroclinic Rossby wave:

$$kc = \frac{-\beta_2 k + \beta_1 l}{(k^2 + l^2 + 2F)}.$$

Since the non-divergent wave is faster in terms of the phase propagation, the necessary condition for radiation becomes the ability of the real part of the phase speed to match the phase speed of the free barotropic Rossby wave. That is, it is the barotropic mode that allows a broader range of phase speeds to excite radiation and its phase speed should be used in the necessary condition for radiation. In other words, the phase speed condition stands the same as in the barotropic problem (Eq. 2.13). Since the range of phase speeds for radiation to exist is more narrow for the baroclinic component, it is very likely that the latter will be trapped and the radiating response in the far-field will be essentially depth-independent. We will see in the following sections that it is true in many cases.

All other conditions remain the same, since they do not depend on the particular structure of the solution: One should also consider the limit $c_i \rightarrow 0$ and pay close attention to the y-structure of an eigenmode.

The last group of conditions that need to be re-derived for the two-layer model is the set of jump conditions analogous to (2.16),(2.17). The conditions are necessary for joining the solution across $y = \pm 1$ and for obtaining the dispersion relation.

We follow the same procedure as outlined in detail in the section 2.4. In the upper layer we obtain the conditions identical to (2.16), (2.17):

$$\Delta(\frac{\phi_1}{\bar{u}-c}) = 0; \quad \Delta(\phi_{1y}(\bar{u}-c) - \phi_1\bar{u}_y + \frac{i\beta_1}{k}\phi) = 0 \tag{4.6}$$

In the lower layer where $\bar{u} = 0$ the conditions are the requirements of the continuity of the velocity field:

$$\Delta(\phi_2, \quad \phi_{2y}) = 0 \tag{4.7}$$

Having reformulated the conditions for radiation and jump conditions, we now proceed with the analysis of solutions.

4.2 Top-Hat Jet

As in the barotropic problem, we start from the simplest choice: the top-hat jet with piece-wise constant velocity profile. The resulting dispersion relation takes a complicated form and is presented in the Appendix A.1.

A similar problem was first formulated in Yun *et al.*,(1995). The authors used jump conditions different from the (4.6); that is, the second condition in 4.6 in their formulation does not have the term $\frac{i\beta_1}{k}\phi_1$. That error in the formulation of the problem resulted in a disagreement of the results in Yun *et al.*,(1995) with the results presented below; see Kamenkovich and Pedlosky (1996).

We observe some changes imposed by the addition of the second layer to the problem. The number of unstable modes increases: two more modes are found in addition to the modified barotropic modes 1 and 2. We will call these new modes baroclinic modes 3 and 4 since their existence is clearly connected to the presence of the lower layer.

Let us look at fig.4.1. The results for the 4 most unstable modes are presented in the usual form of the dispersion curves $c = c(k)$ for the jet tilted by 30°. First, we see that Modes 1 and 2 are modified by the presence of the second layer although the general shape looks very familiar. The behavior of the Mode 1 in the LW limit holds qualitatively the same: c_r gets larger than the maximum flow speed for Mode 1. As in the barotropic problem, SWC is absent for both modes due to the discontinuity of the mean velocity profile.

Two additional baroclinic modes have somewhat different shapes: each of them has both long wave and short wave cut-offs. Mode 4, that corresponds to a shorter scale in x, has negative phase speed in the LW limit. Long waves of Mode 3 travel very fast reminding us of the similar behavior of the Mode 1; they are, however, always slower than the maximum mean current speed.

We see that in the LW limit the real parts of the phase speeds of all modes are within the range of the barotropic Rossby wave phase speed (2.13). The phase speed condition is satisfied making the radiation possible. In the short-wave portion of the dispersion curves of all modes, the solutions are trapped.

Keeping in mind the very special character of the discontinuous velocity profile and, at the same time, its ability to represent some general properties, we now move on to the more general form of the $\bar{u}(y)$.

4.3 Continuous Jet

In this section we are going to study the stability of the same continuous velocity profile for the upper layer as in the section 3.2, while the mean flow in the lower layer is zero. We will concentrate on the effects of the added second layer on the stability and radiating properties of the problem.

We use the Shooting technique for the numerical solution of the formulated eigenvalue problem. Details are presented in the Appendix A.2. As a result, we obtain the complex phase speed c as a function of the parameters of the problem: k, β_1, β_2 and F.

The addition of the lower active layer changes the dynamics of the problem significantly. To observe these changes, one can vary the parameter F which is the square of

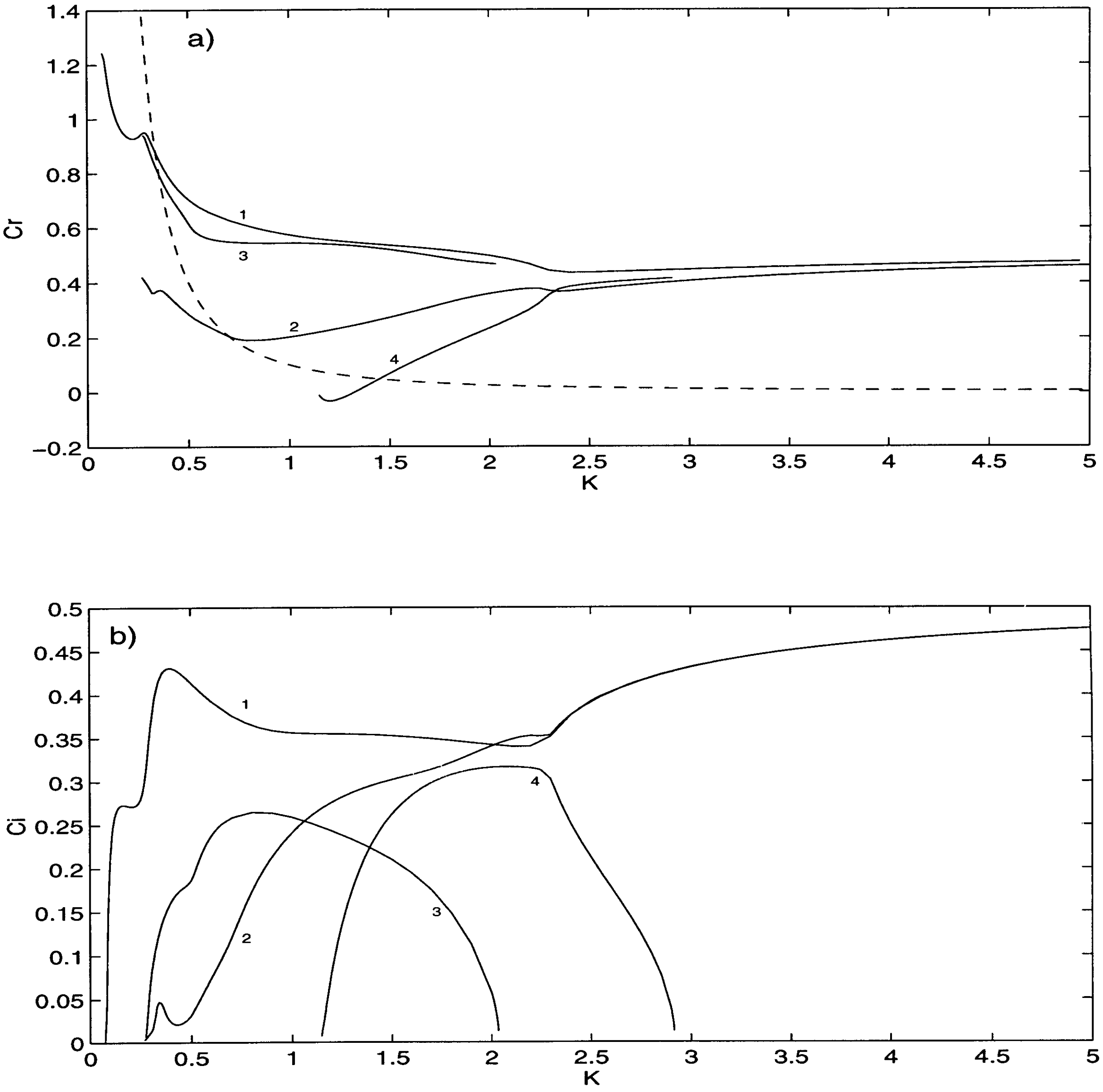

Figure 4.1: Results for the baroclinic Top-Hat jet. $\beta = 1.5$, $\alpha = 30^o$ and $F = 3$. (a) - real parts of c for all 4 modes vs. k. Dashed line shows the maximum Rossby wave phase speed. (b) - the same but for the imaginary parts of c. Wave numbers are shown on the plot next to the corresponding curves.

the ratio between the horizontal spatial scale and the internal Rossby deformation radius. The parameter plays a role of the measure of baroclinicity in the problem: The larger it is, the stronger is the coupling between two layers. For example, in the calculations for $F = 0.1$, not presented here, Modes 1 and 2 are practically indistinguishable from those in the barotropic model (see section 3.2.1) and no additional strongly unstable modes are found.

4.3.1 Nonzonal jet: $\alpha = 30^o$

In addition to barotropic Mode 1 and Mode 2 now modified by the presence of the second layer, we now find an additional Mode 3. The existence of Mode 3 is clearly tied to the baroclinic effects of the coupling between layers. The mode does not exist for very small and zero F. For the results presented here (Fig.4.2) we choose our parameter F such that it allows a significant coupling between two layers; i.e. $F = 3$ and $F = 10$.

Mode 1 and Mode 2 are familiar barotropic modes of section 3.2.3 modified by the presence of the lower layer. Some changes are, however, observable. For example, both real and imaginary parts of the phase speed are smaller than those in the barotropic problem. Nevertheless, the general properties of these two modes stay the same. We observe the familiar behavior in the LW limits of the each mode; at LWC phase always travels faster than the mean flow speed for the Mode 1 and slower than the mean flow for the Mode 2. A critical layer, therefore, is not present at LWC. At the SWC, on the contrary, it is present as a result of c lying inside the interval for the mean velocity: $[0, 1]$.

Mode 3 is absent for very small values of F for $\alpha = 30^o$ and $\beta = 1$, because it is the baroclinic effect that allows its existence. However, the mode can be found for F as small as 1. The fact illustrates the more unstable nature of the baroclinic nonzonal currents: if $F = 3$, for example, two unstable modes if $\alpha = 0^o$ are found; but there are three unstable modes for $\alpha = 30^o$. Mode 3 has growth rate, kc_i, which is smaller than the growth rates of Mode 1 and 2 for $F = 3$. Larger F enhances the baroclinic mechanism for instability. Both the growth rate and interval in k corresponding to the baroclinic Mode

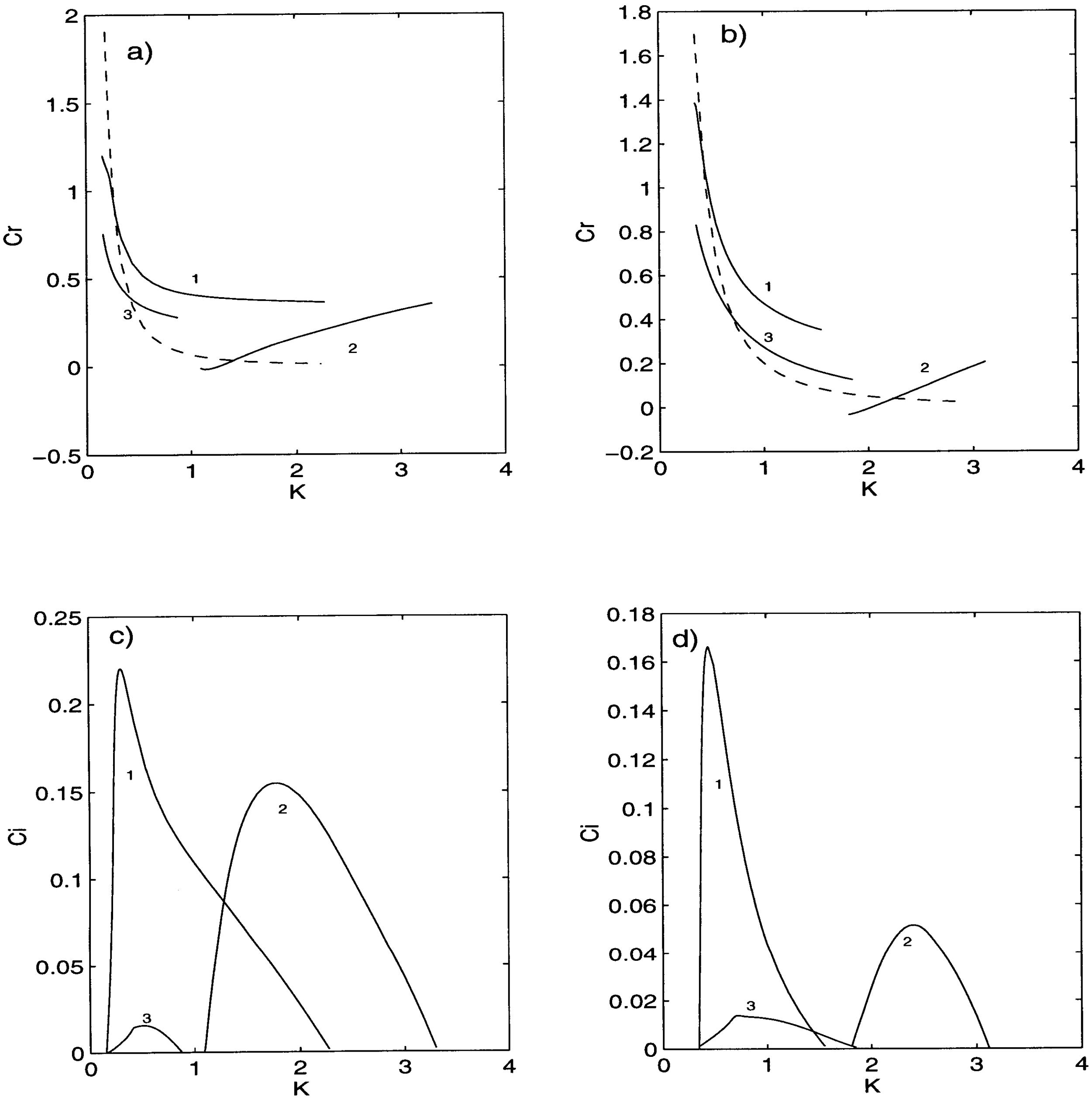

Figure 4.2: Results for the baroclinic continuous jet. $\alpha = 30^o$, $\beta = 1$. (a,b) - Real parts of c vs. k. The maximum Rossby wave phase speed is shown by the dashed line. (c,d) - Imaginary parts of c. (a,c) - $F = 3$. (b,d) - $F = 10$. Mode numbers are shown next to the corresponding dispersion curves.

3 increase with larger F for all modes. The typical shape of the dependence of c_r on k for Mode 3 is somewhat similar to that of Mode 1. Longer waves travel faster, although c_r is never larger than the maximum $\bar{u}(y)$ resulting in the possibility of the critical layer at the LWC.

We now notice that the dispersion curve of Mode 3 of the continuous jet is similar to that of Mode 3 of the Top-Hat jet especially in the LWC. Once again (see sections 3.1 and 3.2.3, we point out the ability of the simple problem with broken-line profile to reproduce some of the results for the more realistic continuous current. The difference between two cases is nevertheless substantial. In particular, no analog for the baroclinic Mode 4 of the Top-Hat jet is found in the case of the continuous current. The mode is believed to be an artifact of the top-hat profile.

The phase speed condition is satisfied for all three modes in the LW limit, making the radiation possible. The interval in k in which c_r is within the range (2.13) is relatively wide for the Mode 3.

The analysis of the complex meridional wavenumbers in each of the external regions confirms the radiation of the long waves by each mode; see fig.4.3. We remember, that we need to check the largeness of the spatial decay scale and the smallness of l_i/l_r in the limit of $c_i \to 0$ to conclude that solution radiates. In contrast, short waves of all three modes are trapped. One also should keep in mind that the solution is the sum of two waves with different wavenumbers; see section 4.1. From the fig.4.3 we can see that, for example, for Mode 2 both y-wavenumbers become real at LWC in both the external regions. For Modes 1 and 3, in contrast, only the non-divergent barotropic component of the solution in the external regions is radiating. Imaginary parts of l of the baroclinic component in the external region are still large for these modes.

We could better illustrate this fact from fig.4.4 which shows barotropic ($\phi_{br} = \phi_1 + \phi_2$) and baroclinic ($\phi_{bc} = \phi_1 - \phi_2$) streamfunctions as functions of y for values of k chosen at the LWC. For Mode 1 the magnitude of barotropic wave-like response is very large in the negative y-direction (fig.4.4a). The barotropic component ϕ_{br} is significant at the

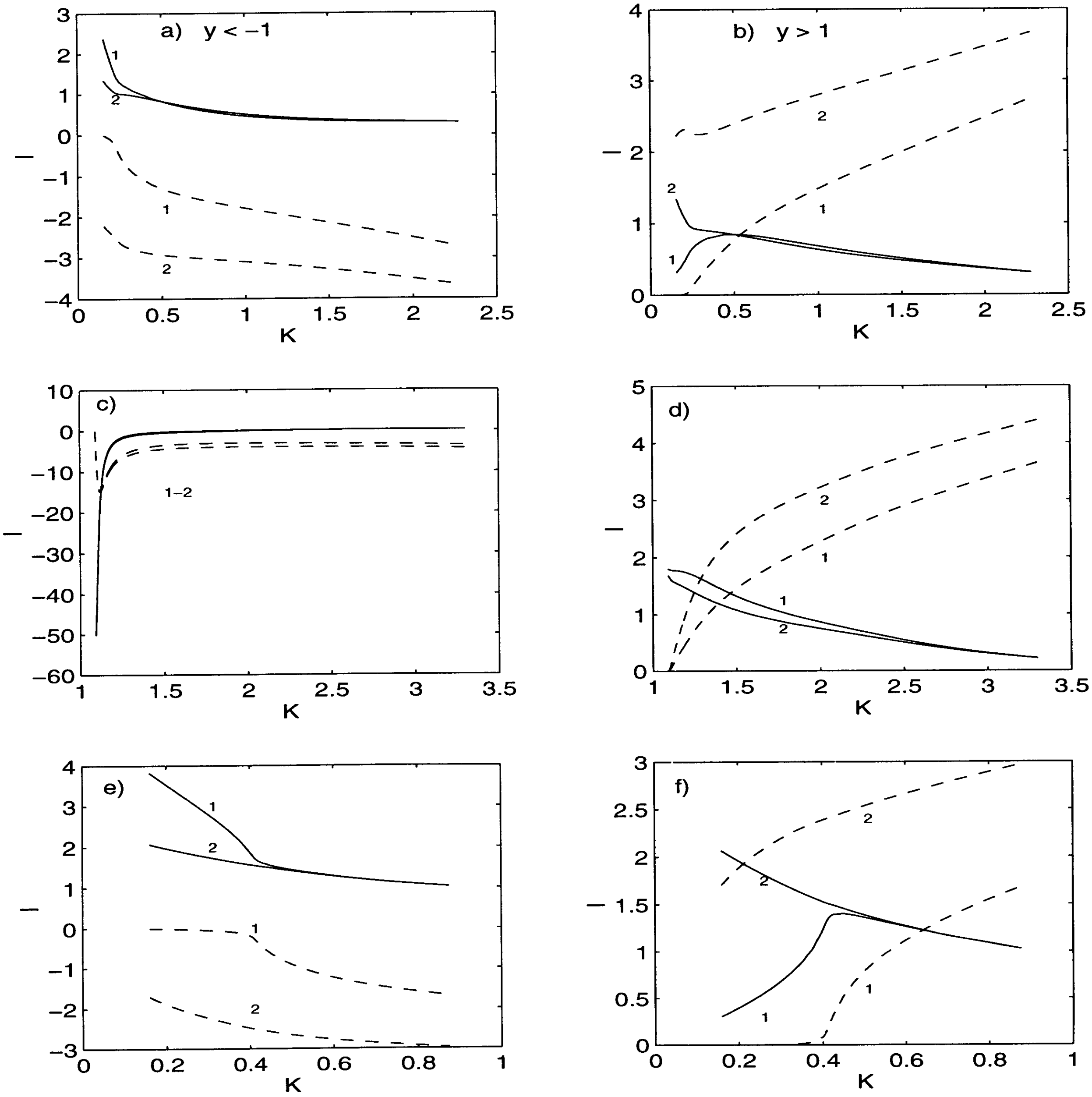

Figure 4.3: Complex meridional wavenumbers l vs. k. $\beta = 1$, $\alpha = 30^o$, $F = 3$. Real parts are shown by solid lines; imaginary are shown by dashed. Numbers next to the curves indicate the type of the component: 1 - barotropic component, 2 - baroclinic component. (a,c,e) External region $y < -1$. (b,d,f) $y > 1$. (a,b) Mode 1. (c,d) Mode 2. (e,f) Mode 3.

southern jet edge $y = -1$, so we can conclude that it is the barotropic instability mode that projects on the radiating response in the exterior. At the other jet edge $y = 1$, the ϕ_{bc} dominates, although the ϕ_{br} is prevailing in the region $y > 1$ as a result of the strong trapping of the baroclinic component.

Mode 3 corresponds to the large amplitude of the streamfunction inside the jet region with the baroclinic component being the largest in amplitude (fig.4.4c). We should also keep in mind, that the very existence of the Mode 3 is connected with the presence of the second layer in the problem; it is, therefore, reasonable to expect that baroclinic effects are important role in the energy conversion process. The instability mode at both the jet edges is a mixture of ϕ_{br} and ϕ_{bc}, although ϕ_{bc} is larger in amplitude. The barotropic response in the exterior is smaller in amplitude than in the interior region, but is still clearly dominant over the trapped baroclinic component. It looks as though the mixed barotropic-baroclinic instability mode in the interior projects on the radiating barotropic response in the exterior.

In contrast, both barotropic and baroclinic components of Mode 2 are not trapped in the external regions. However, the wave-like response in the exterior is very small in amplitude compared to that in the interior region. As in the barotropic case, the y-derivatives are rather large for $y < -1$ because of the short-wave structure of the solution in the region. The perturbations are surface intensified for $y < 1$; we can see it from the fact that ϕ_{brt} and ϕ_{brc} are very close to each other. ϕ_2 is, therefore, small in amplitude compared to ϕ_1.

In the LW limit of all modes a radiating component is typically presented by the long wave for $y > 1$. For $y < -1$ the solution is a much shorter wave in y.

To better understand how the process of the energy conversion from the mean current to the far-field motions takes place one need to closely consider the energy balance in the equation.

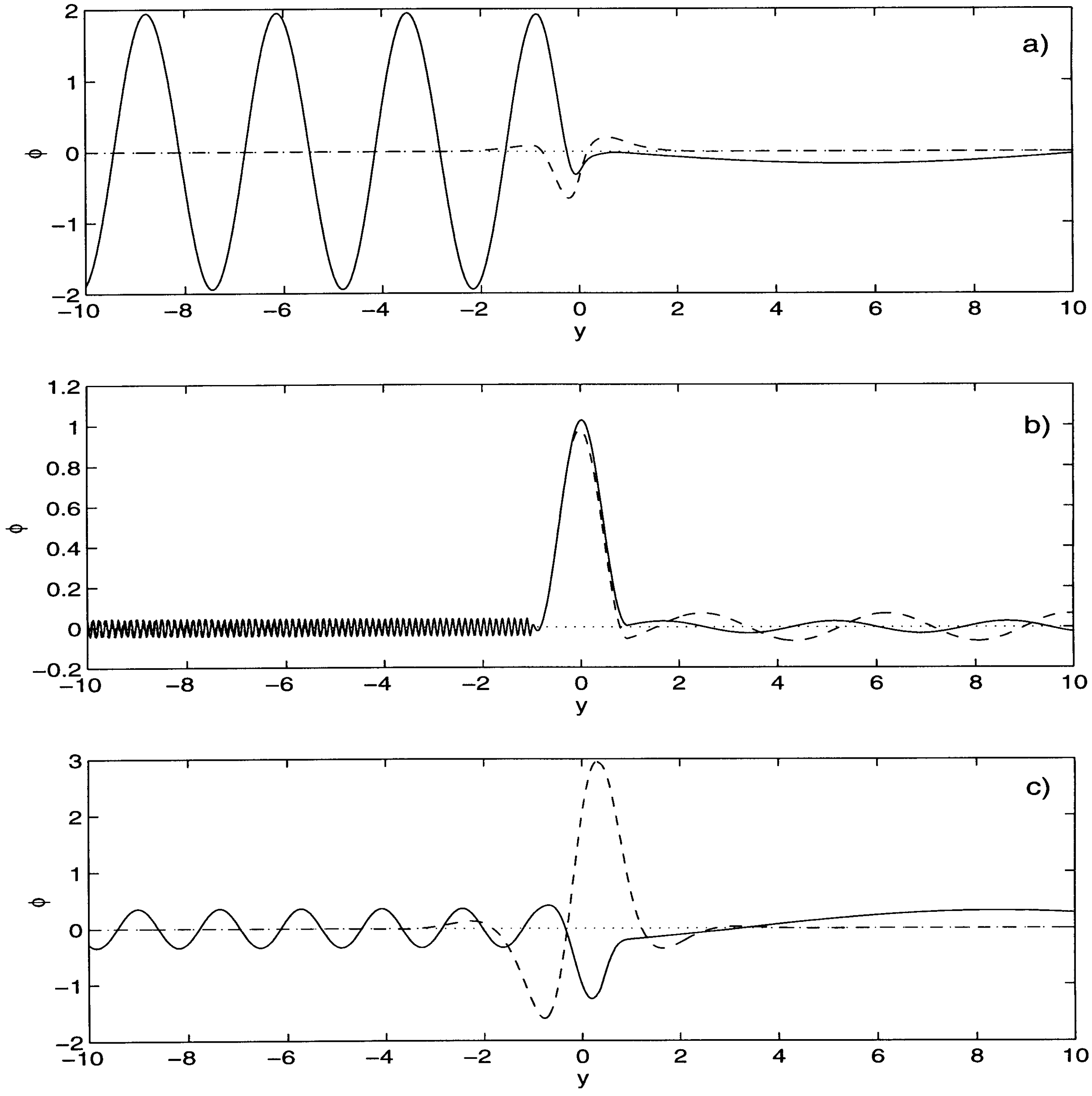

Figure 4.4: Y-structure of the barotropic $\phi_{brt} = \phi_1(y) + \phi_2(y)$ (shown by the solid lines) and baroclinic $\phi_{brc} = \phi_1(y) - \phi_2(y)$ components (shown by the dashed lines). $\beta = 1$, $\alpha = 30^o$, $F = 3$. k is chosen close to the LWC: (a) Mode 1, $k = 0.155$; (b) Mode 2, $k = 1.092$; (c) Mode 3, $k = 0.165$

4.3.2 Energy balance

We multiply the linearized equation (4.1) by $\psi_n(x, y, t)$ and integrate in x over the period and in y from $-y_b$ to y_b repeating the procedure employed in section 3.2.4. We end up with the energy equation; the horizontal overbar represents the averaging in x defined in section 3.2.4:

$$\frac{\partial}{\partial t}E = \overset{F_{brt}}{\int_{-y_b}^{y_b} \bar{u}_y(y)\overline{\psi_{1x}\psi_{1y}}^x dy} + F \overset{F_{brc}}{\int_{-y_b}^{y_b} \bar{u}(y)\overline{\psi_1\psi_{2x}}^x dy} +$$

$$+ \overset{Flux}{\left[-\bar{u}\overline{\psi_{1x}\psi_{1y}}^x + \sum_{n=1}^{2} \left(\overline{\psi_n\psi_{nyt}}^x - \frac{1}{2}\beta_1\overline{\psi_n^2}^x \right) \right]_{-y_b}^{y^b}} \tag{4.8}$$

where E is a perturbation energy (a sum of kinetic and potential energy)

$$E = \int_{-y_b}^{y_b} \frac{1}{2}\sum_{n=1}^{2} \overline{(\psi_{nx}^2 + \psi_{ny}^2)}^x + \frac{F}{2}\overline{(\psi_1 - \psi_2)^2}^x dy$$

We can traditionally distinguish two sources of the perturbation energy: 1)barotropic energy conversion term F_{brt}, related to the horizontal shear in the mean current and 2)baroclinic term F_{brc}, related to the vertical shear. The flux terms familiar from section 3.2.4 now represent the flux of energy in both layers.

Now we can compare relative sizes of the terms in the energy equation in an attempt to understand what mechanism draws energy from the mean current to the growing in time perturbations. Let us take a look at fig.4.5(a,c,e) where all three terms F_{brt}, F_{brc} and $Flux$ terms, normalized by the perturbation energy E, are shown as the functions of the x-wavenumber.

For Mode 1, F_{brt} is typically larger than F_{brc} (fig.4.5a). The energy embedded in the horizontal shear of the mean current is the main source for the growing perturbation energy. The radiating LW limit of $kc_i \to 0$ is interesting. In this limit, in a way similar to that for the barotropic problem (see section 3.2.4), the balance between F_{brt} and $Flux$ terms is established. The baroclinic source for perturbation energy vanishes if the exponential growth of the energy disappears. The energy is being obtained through the barotropic term and is being fluxed away from the region in this limit. The process of radiation is therefore barotropic in nature for Mode 1.

The integrands in both the energy sources F_{brt} and F_{brc} are shown as functions of y for the k close to the LWC value on fig.4.5(b,d,f). For Mode 1 we also see that the integrand in F_{brt} reaches its maximum near the southern edge of the jet at $y = -1$ (fig4.5b). It is not surprising, therefore, that the radiating response to the south from the jet (negative y in our formulation) is so energetic.

The long waves of Mode 2 grow due to the mixed barotropic-baroclinic mechanism for energy conversion, with F_{brt} being the largest in magnitude. Short waves are amplified mainly by the process of barotropic instability. The $Flux$ terms remain negligible for all values of k and all terms in the equation vanish in the LW limit. As in the barotropic model, it is hard to identify long waves of Mode 2 as radiating despite the fact that they are weakly trapped in the limit (see figs.4.3,4.4). The y-structure of the integrand in F_{brt} (fig.4.5d) indicates that energy is taken from the perturbations to the mean flow for negative y and from the mean field to the perturbations for positive y.

Situation for Mode 3 is more complicated. In fact, for the long waves of this mode the energy is being drawn *from* the perturbations *to* the mean current by the barotropic mechanism: $F_{brt} < 0$. The baroclinic source overcomes the stabilization effect of the F_{brt} and provides the perturbations with enough energy to grow and to flux energy away from the region considered. $Flux$ terms become very small but do not vanish completely in the LW limit. It is interesting that despite the fact that the energy for growing perturbations is provided by the baroclinic mechanism, the radiating response is basically depth-independent in this limit (see fig.4.4). For short waves the situation is the opposite, with F_{brt} being the positive and F_{brc} playing the stabilization role. The sum of this two sources always stays positive. The presence of the critical layer at LWC is well-pronounced in the y-structure of the integrand in the barotropic energy source (fig.4.5f).

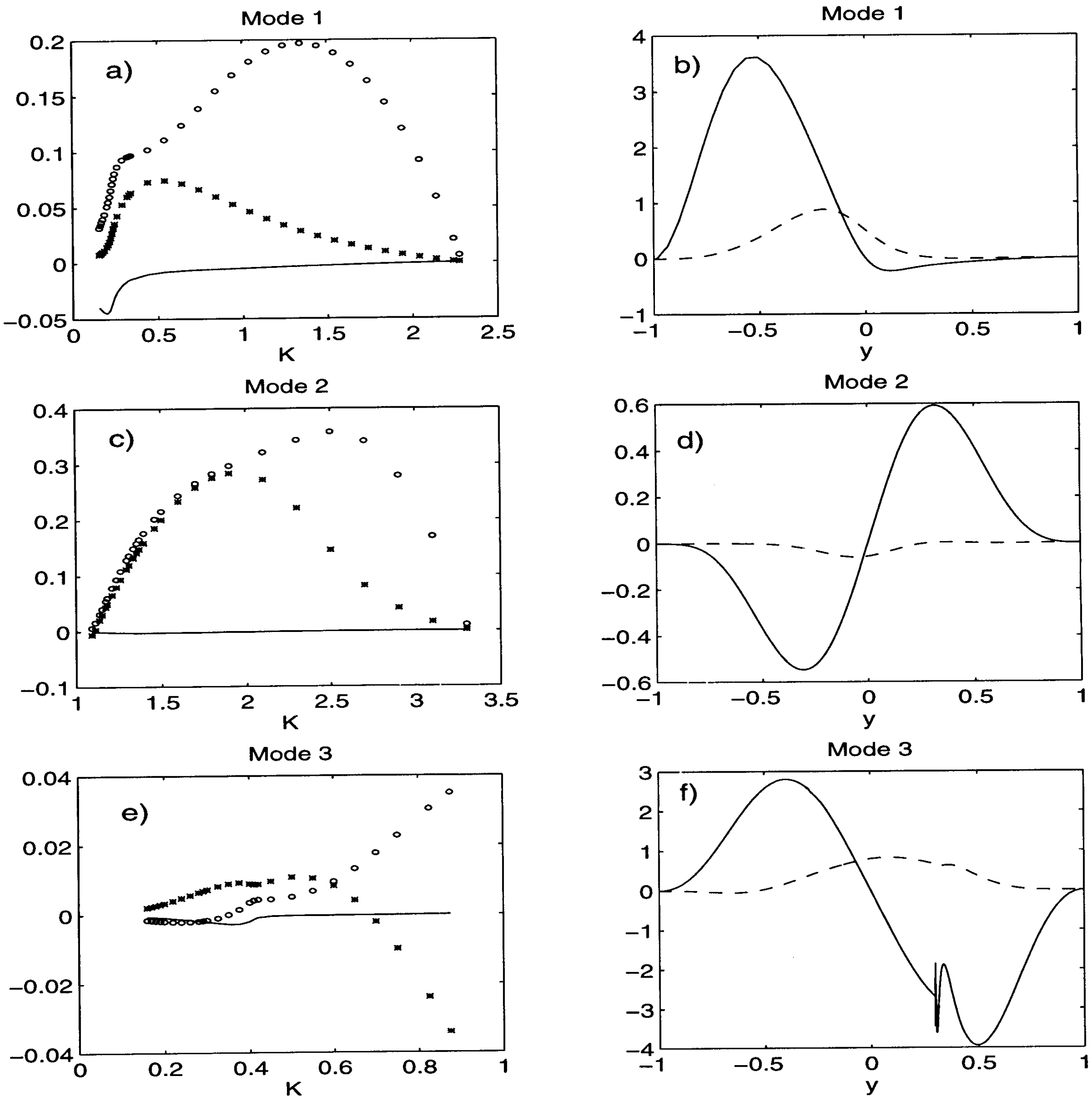

Figure 4.5: Energetics of the problem. $\beta = 1$, $\alpha = 30^o$, $F = 3$. (a,c,e) - Integrated energy sources F_{brt} (shown by open dots), F_{brc} (shown by stars) and $Flux$ (shown by solid lines) vs. k. (b,d,f) - F_{brt} (solid line) and F_{brc} (dashed line) vs. y near the LWC. (a,b) Mode 1. (c,d) Mode 2. (e,f) Mode 3. The sum $F_{brc} + F_{brt}$ is shown by the solid line on (e).

4.4 Summary

We have considered the model with a simple example of a baroclinic flow. The second moving layer with zero mean current is added to the barotropic model studied in chapters 2 and 3. The resulting baroclinicity has several effects on the properties of solutions. We considered two forms of mean velocity profile, a piece-wise constant broken-line profile and a continuous jet.

The number of unstable modes increases. In addition to the modes 1 and 2 of the barotropic problem, we have found two baroclinic modes in the case of a top-hat jet and one mode in the case of a continuous current. The existence of these additional modes is clearly tied to the baroclinic effects. We find these modes only if the nondimensional parameter F measuring the strength of the dynamical coupling between two layers F is large enough.

The very existence of slowly growing radiating solutions in the LW part of each dispersion curve is not affected by the baroclinicity. All criteria for radiation formulated in section 2.3 are satisfied in the LW limit for each mode. In particular, the spatial trapping disappears in this limit if the growth rate vanishes. The additional baroclinic modes share this property with previously found modes of the barotropic problem. We will now briefly summarize the results of the analysis of the spatial structure of the solutions for the problem with a continuous mean velocity profile in the upper layer.

For the analysis, we split the streamfunction in the external regions into depth-independent component and a baroclinic addition to it. The structure of these components appears to be very different. The amplitude of the barotropic wave-like response is large especially for negative y for Mode 1. The baroclinic component is trapped. Moreover, the barotropic energy source in the described LW limit balances the flux terms, while both baroclinic energy conversion term and the growth rate vanish. The radiation is, therefore, dominated by the barotropic mechanism for Mode 1.

Long waves of Mode 2 exist due to the mixed barotropic-baroclinic mechanism. Both barotropic and baroclinic components are not trapped in the LW limit. Their amplitudes, however are very small. All energy terms vanish in the LW limit. As in the barotropic problem (see section 3.2), it is difficult to confirm significant energy radiation for Mode 2.

Similar to the Mode 1, wave-like response associated with Mode 3 is barotropic in structure. However, the baroclinic energy conversion term is the only source for radiating energy. The barotropic term is a *sink* of perturbation energy for the long waves of the mode. The balance is reversed for short waves.

The problem reveals new aspects in the dynamics of radiation. The radiating response has barotropic structure for modes 1 and 3 no matter whether the main energy source is barotropic as for Mode 1 or baroclinic as for Mode 3. Given the more narrow range for the phase speed allowed by the phase speed condition for the baroclinic Rossby waves, it is not surprising to find that they are usually evanescent in structure. We can anticipate now that in a linear continuously stratified model with infinite number of Rossby modes, the radiating response is still going to be mainly barotropic in most cases.

Chapter 5

Nonlinear regime. Single wave development

In chapters 2, 3 and 4 we have studied the radiation of energy by nonzonal currents in linear models. As we noted, the task of verifying the radiating nature of the solution is difficult in the linear theory. The fast exponential growth of a linear solution can lead to the spatial trapping. The radiating nature of the solution is then disguised by the effects of the fast growth. We observed for those cases that when we choose the parameters that make the growth rate small, the radiating nature becomes transparent for the waves long in x. However, the dynamical development during the initial linear stage is dominated by faster growing and therefore trapped modes. Their growth cannot last forever, the nonlinear effects should halt it at some point in time. Will the solution start to radiate then or the radiation remain the feature of the long slowly growing linear waves? In the latter case, the radiation would be energetically insignificant. In the former, not only can we claim that radiation is energetic, but also that it can happen in the form of shorter waves that have more realistic length scale on the order of the jet half-width (if $k \sim 1$).

That is why it is crucial for the present study to analyze the nonlinear development of the linear solutions found in the previous chapters. We want to keep our results simple yet not lose the important aspects of the dynamical picture. For this purpose, we will consider the nonlinear development in a barotropic model. As was demonstrated in Chapter 4, the incorporation of baroclinicity does not qualitatively change the radiating properties of the problem: The radiating response has essentially depth-independent structure. Therefore, we choose to consider the nonlinear development of barotropic linear solutions only. We believe, that it is sufficient for drawing general conclusions about the radiation in a nonlinear model.

For solving our nonlinear problem, we need an efficient numerical method. The biggest challenge in developing such a method is formulating numerical boundary conditions. In the present study, we use a routine that assumes periodicity in x and open boundary conditions in y. The numerical formulation of the latter conditions is not generally an easy task. To further complicate the matter, the numerical solution appears to be very sensitive to the open boundary conditions because the radiating solutions are of finite amplitude far from the jet region. We employ modified Orlanski boundary conditions and they work well for most cases. The whole method is described in detail in section 5.1 and in the Appendix.

The results of nonlinear computations are generally difficult to analyze. A spectrum of modes is always excited by the nonlinear interactions. In section 5.1, we propose to decompose the solution in Fourier modes in x; which is possible to do because the solution is periodic in x. The analysis of the temporal evolution of each component helps us to understand the complicated process of the nonlinear evolution.

We start with the analysis of the nonlinear development of a single mode. The linear solution is used as initial condition and is given small amplitude to ensure its validity during the initial stage of development. Mode 1 from the linear barotropic problem is first considered. As in Chapter 3, we first analyze the process in the model with a zonal current. We then increase the value of the tilt and concentrate on changes caused by the changed orientation of the mean current in section 5.2. The case of a strong tilt ($\alpha = 30^o$) is studied in detail in section 5.3. The dependence of the results on the value of the planetary vorticity gradient is analyzed in section 5.2.3. The nonlinear development of Mode 2 is studied in section 5.4.

5.1 Method of solution and analysis

The nonlinear terms were ignored in the previous chapters due to their smallness during the initial stage of development. We now include the nonlinear terms into consideration. The equation 2.4 changes accordingly:

$$\left(\frac{\partial}{\partial t} + \bar{u}(y)\frac{\partial}{\partial x}\right)\nabla^2\psi + (\beta_2 - \bar{u}_{yy})\psi_x - \beta_1\psi_y + J(\psi, \nabla^2\psi) = 0. \tag{5.1}$$

We now need to discuss the form of initial and boundary conditions. Together they are the decisive factors in choosing the appropriate numerical method of solving 5.1. The problem is first formulated on the infinite β-plane in Chapter 2. A single Fourier mode in x is then considered as a general solution. Due to the linearity, the separate consideration of each mode is sufficient for the accurate solution.

Unlike the linear solution, the results of nonlinear computations strongly depend on initial conditions. For the representation of arbitrary initial conditions, the continuous spectrum of linear Fourier modes is needed and boundary conditions in x become very difficult to formulate. To keep all results simple, we choose to initialize a problem with either a single mode or a sum of two modes. Although it is hard to claim that a complete dynamical picture can be obtained by doing that, we hope to mimic the important properties of nonlinear interactions and the effects they have on the radiating properties in the problem.

In this chapter, we study the nonlinear development of a single wave with a wavenumber k. In the course of nonlinear self-interactions, a set of secondary modes that are shorter in x is created in addition: $2k$, $3k$, etc. together with the x-independent component. Because of this special structure of the solution, we can assume periodicity in x with a period equal to the longest period in the set: $2\pi/k$. The extension to the case with the sum of two waves as initial condition is straightforward and is done in Chapter

6.

The boundary conditions in y are more difficult to formulate. The conditions need to remain the same as in the linear problem and be the requirements of the boundness at $\pm\infty$. It is not however easy to implement such conditions numerically. Ideally, one should require that any disturbance that approaches the numerical boundary in y should be able to leave the domain without even partial reflection. Essentially, one tries "to do nothing" at the boundary, as if the boundary did not exist at all.

One way to allow free transmission of a wave through the boundary is to use Orlanski' boundary conditions (Orlanski, 1976). In one-dimensional problem, one can write the following relation:

$$\frac{\partial}{\partial t}\psi + c(y,t)\frac{\partial}{\partial y}\psi = 0 \tag{5.2}$$

The speed c, with which a disturbance propagates can be calculated numerically and is used to determine ψ at the boundary. In the one-dimensional case it is possible to demonstrate (Orlanski, 1976) that the reflection is totally absent.

The situation in our problem, however, is more complicated. First, the problem is two-dimensional. As outlined in Durran *et al.*, (1993), the additional dimension may require a more elaborate formulation. The second important problem is numerical stability. Even in a one-dimensional problem, the conditions in the form formulated above quickly lead to the numerical instability at the boundary (Blumberg and Kantha, 1985). To overcome this difficulty, it is proposed in Blumberg and Kantha (1985) to put a "damping" term on the right-hand side of the last equation:

$$\frac{\partial}{\partial t}\psi + c(y,t)\frac{\partial}{\partial y}\psi = -\psi\frac{1}{T_f} \tag{5.3}$$

where T_f controls the strength of damping. A large value of T_f returns us to the original formulation with the zero right-hand side, whereas infinitely small values of the parameter are equivalent to putting a rigid wall at the boundary. For all our computations we choose $T_f = 1$ which is sufficient for the above condition to work in our case. The finite-difference form of the conditions are given in the Appendix.

The next important task is to convince ourselves that the conditions actually work. We check that by first changing the size of our numerical domain. If the results do not change, we are convinced that the boundary effects, such as a reflection or the amplification of the boundary trapped numerical modes, are minimal. Otherwise the solution would depend on the size of the numerical domain. We normally stop the integration at the point when we suspect growing boundary effects.

We then choose the numerical method for the solution that is the most efficient given the boundary conditions just formulated. We use a rectangular basin with N_x points in x and N_y points in y, where N_y is typically larger than N_x, the grid spacing are Δx and Δy correspondently. The equation 5.1 for the vorticity $\zeta = \nabla^2\psi$ is time stepped forward using the leap-frog scheme. The resulting ζ is then inverted to obtain streamfunction ψ; in other words we have to to solve the Poisson equation:

$$\zeta = \nabla^2\psi \tag{5.4}$$

where ζ is known.

The designed inverter is spectral in x and finite-difference in y. The numerical Fast Fourier Transform, or FFT, (Press *et al.*, 1992) is first performed making use of the periodicity of the solution. It results in the set of N_x finite-difference ODEs in y. The equations have simple structure and are easy to solve numerically using the open boundary conditions 5.3. The inverse FFT is used to finally obtain ψ for the next time-step. The code is efficient and is easily made stable numerically by decreasing the time step Δt. The parameters used for various numerical experiments are given in the Appendix.

5.1.1 Analysis of results. Fourier components.

The solution obtained by the method outlined above has complicated structure. As was noted in the previous section, several Fourier components in x are created in the course of nonlinear development. Because the solution is periodic in x, it is possible to perform the decomposition into Fourier series:

$$\psi(x,y,t) = Re\sum_{n=0}^{\infty} \Phi_{k_n}(y,t)e^{ik_nx} \tag{5.5}$$

where

$$\Phi_{k_n}(y,t) = \frac{1}{L_x}\int_0^{L_x} \psi(x,y,t)e^{-ik_nx}dx$$

are the Fourier coefficients and $k_n = 2\pi n/L_x$.

When we use the term, for example, "component "0.25"" it will mean the Fourier component with $k_n = 0.25$ and corresponding coefficient $\Phi_{0.25}$.

It is obvious that at the very beginning of the development, when only a single linear wave is present, we have

$$\Phi_k(y,t) = \phi(y)e^{-ikct}$$

Other coefficients grow with time due to the nonlinear interactions that produce new components. We observe the temporal evolution of those components which helps us to understand how the structure of the solution changes with time. As we noted in the previous section, only a few of them are significant. Components "0", "$2k_n$" are created by the self-interactions of the initial wave with $k = k_n$. Components "$3k_n$", "$4k_n$" etc., emerge later as a result of secondary interactions.

The Fourier representation of solution (5.5) possesses another convenient property. If we compute the x-averaged kinetic energy using the Eq. 5.5. We find:

$$K_e = \sum_{n=0}^{\infty} K_{k_n} = \int_{-\infty}^{\infty} \frac{1}{2}\Phi_{0y}^2 dy + \sum_{n=0}^{\infty} \frac{1}{4}\int_{-\infty}^{\infty} \left(\Phi_{k_ny}^2 + k_n^2\Phi_{k_n}\right) dy \tag{5.6}$$

All terms that are x-dependent disappear because of the x-averaging over the interval $[0\ L_x]$. We see that the contributions of each component to the total perturbation kinetic energy are additive. The property is convenient for analyzing the energetics in the problem. By analyzing the values of K_{k_n}, we will be able to see which components contribute the most to the total value of K_e.

In the analysis of the energetics in the problem we will use another quantity which is the kinetic energy of each component $\frac{1}{4}\left(\Phi_{k_n y}^2 + k_n^2\Phi_{k_n}\right)$ integrated from $-\infty$ to -2 and from 2 to $+\infty$. We therefore, exclude the region that contains the jet ($\bar{u} \neq 0$ for y in the $[-1\ 1]$) and consider only the external part of energy. We will denote this value by E_{k_n} and will consider its ratio to the total perturbation energy K_e. The ratio serves as the measure of the effectiveness of radiation by each component. It is a more meaningful quantity than the absolute value of E_{k_n} since the latter strongly depends on initial conditions and would be hard to use in the comparison between different cases.

For evaluation of the integral over the infinite interval in y, we will use the integration over the numerical interval. The latter is typically 15 or 20 times wider than the jet itself (see Appendix A.4); the numerical integration is usually stopped when the solution reaches finite amplitudes at the numerical open boundaries. Therefore, it makes sense to base the discussion of the value of the integral over an infinite domain on the analysis of the numerical integral.

5.2 Mode 1. Zonal jet.

We start our analysis with the study of the nonlinear development of a single mode the case of a zonal current, $\alpha = 0^o$. The linear theory predicts the strong spatial trapping of all solutions for all wavelengths. Does the solution remain trapped during the nonlinear development as well?

We initialize the problem with a linear varicose mode for $k = 1$ and $\beta = 1$. We now proceed with the analysis of the numerical results.

We first plot the perturbation kinetic energy as a function of time. The logarithm of $K_e(t)/K_e(0)$ is shown in Fig.5.1. One can see that at $t = 16$ the curve starts to deviate from the straight line that shows the linear growth $2kc_it$. After that, the fast exponential growth of the energy slows significantly and remains small until $t = 68$. Then the solution starts to grow and later the growth slows once again. One can suspect

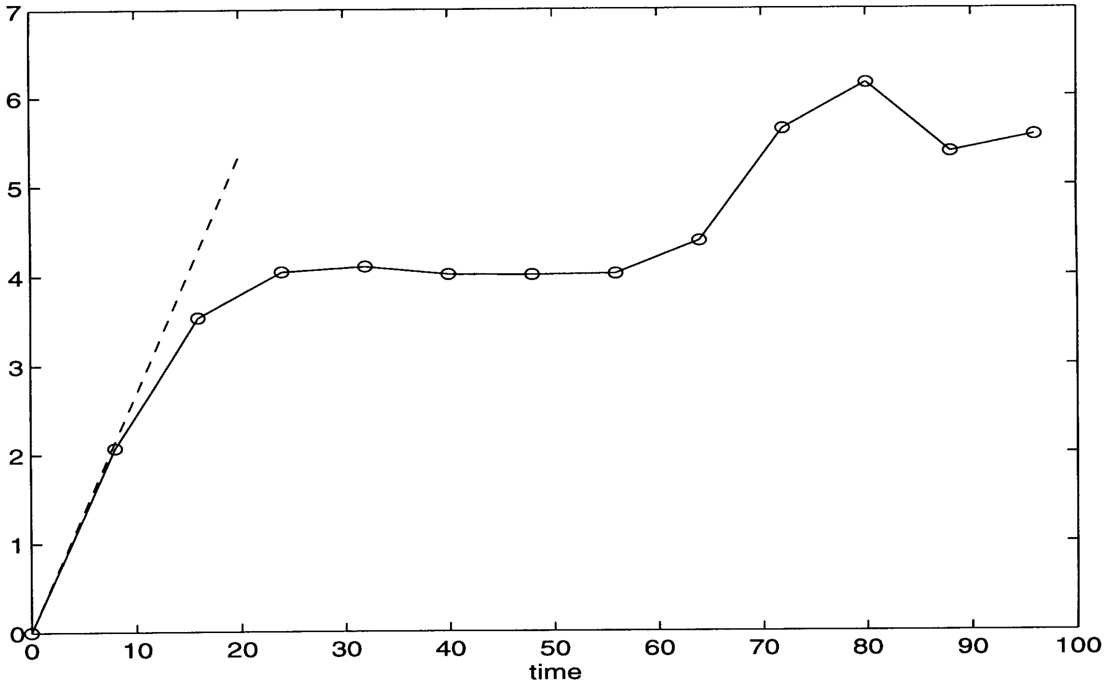

Figure 5.1: The logarithm of perturbation kinetic energy for $\alpha = 0^o$, $k = 1$ and $\beta = 1$ vs. time. $log(K_e(t)/K_e(0))$ is shown by the solid line with open dots, $2kc_it$ is shown by the dashed line.

that the second phase of the fast growth is most likely related to the appearance of the additional strongly unstable mode. In order to check our guess and fully understand the dynamics and radiating properties, we now turn to the analysis of the spatial structure.

The 1D plots of the perturbation streamfunction vs. y for a fixed value of x are shown in fig.5.2. The solution is trapped initially in the agreement with the linear theory and is antisymmetric in y, since we consider a varicose mode. We now remark that the nonlinear interactions cannot change the antisymmetry of the solution, because nonlinear terms in the equation $J(\psi, \nabla^2\psi)$ are antisymmetric if ψ is antisymmetric itself. In other words, the solution should remain antisymmetric for all times.

Nevertheless, we observe the change in the structure of the solution for $t > 64$. The strong symmetric component of the solution is present, and it amplifies even further for later times. In addition, we observe wave-like response in the exterior region that reaches

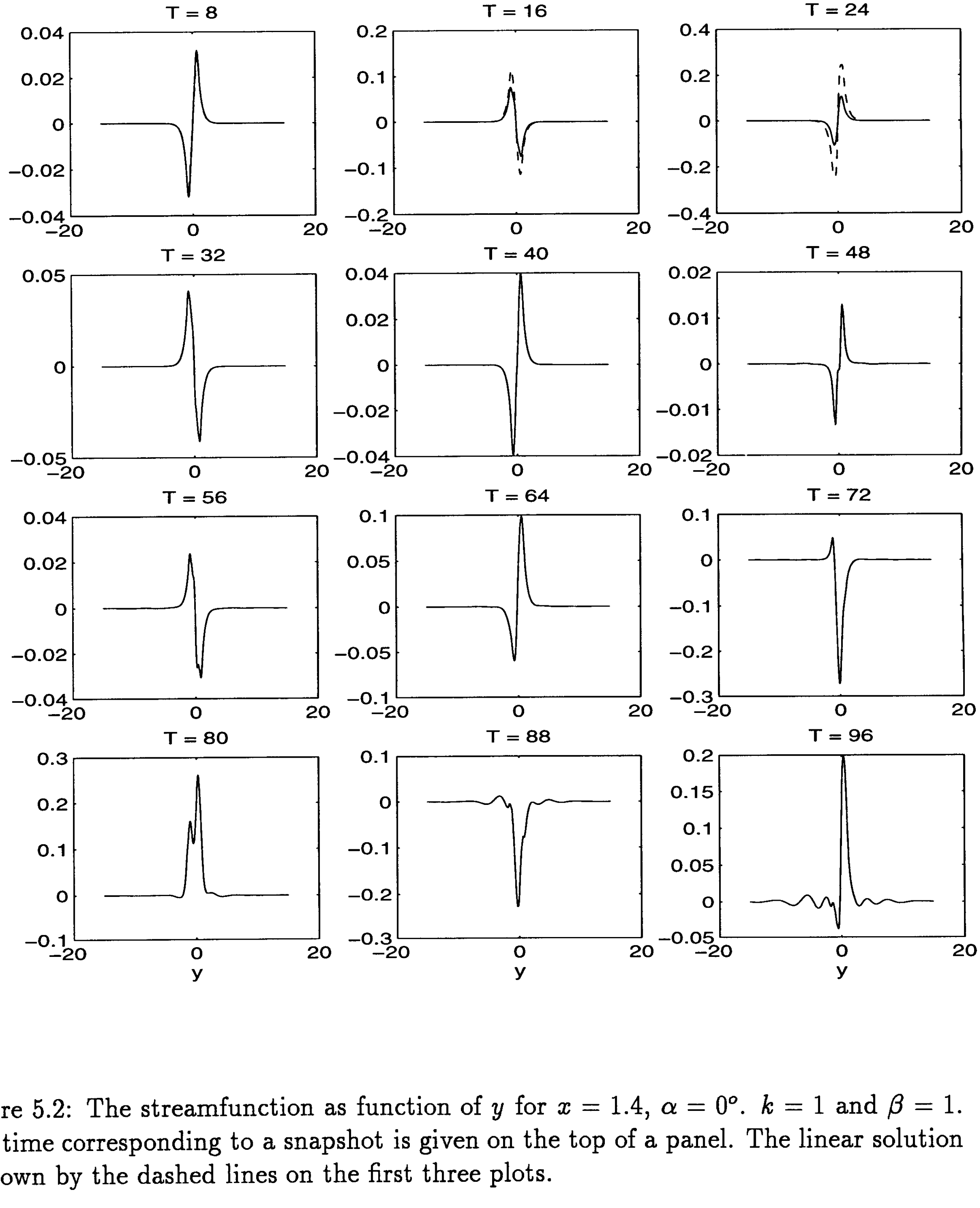

Figure 5.2: The streamfunction as function of y for $x = 1.4$, $\alpha = 0^{o}$. $k = 1$ and $\beta = 1$. The time corresponding to a snapshot is given on the top of a panel. The linear solution is shown by the dashed lines on the first three plots.

far from the jet at $t > 96$. Do we indeed observe the influence of an additional strongly unstable symmetric mode as we guessed before?

The analysis of the Fourier components of the streamfunction helps to clarify the picture. Components "0", "1" and "2" are shown in Fig.5.3. The problem is initialized at $k = 1$; the component "1" is much larger in amplitude than component "2" for $t \leq 48$. The latter is antisymmetric in y and, therefore, remains to be mainly produced by the nonlinear self-interactions of component "1".

The situation changes at later times. At $t = 64$, the component "2" is practically symmetric and is almost the same amplitude as component "1"; it further amplifies with time. This moment in time also corresponds to the second stage of the rapid growth in the perturbation kinetic energy seen in Fig.5.1. We can conclude that starting from $t = 64$, the sinuous mode with $k = 2$ dominates the development ($t = 80$). The sinuous mode at $k = 2$ is the most unstable wave in the problem; in particular, it has a growth rate that is twice as big as that of a varicose mode for $k = 1$ (see Fig.3.2a). The wave is most likely initialized by the presence of round-off numerical error in the numerical method during the development of the component "2" created by the self-interactions of Mode 1.

In a numerical experiment not presented here, we put the sinuous mode with $k = 2$ in addition to the varicose mode as an initial condition. The sinuous mode initially has much smaller amplitude (by the factor of 350). The nonlinear development is very similar to that observed in the numerical run with a single varicose mode alone. Thus, this mimics the production of the sinuous mode in the previous experiment. Here it shows up earlier as if in a more advanced stage of nonlinear development.

What is also interesting to see is that the component "1" with which the model is initialized starts to decrease in amplitude after $t = 64$. The amplitude of component "1" reduces by the factor of 10 from $t = 64$ to $t = 96$. Simultaneously it radiates away waves from the jet region to which it is initially trapped. The whole process looks as a transition from the development of the single varicose mode "1" to the development

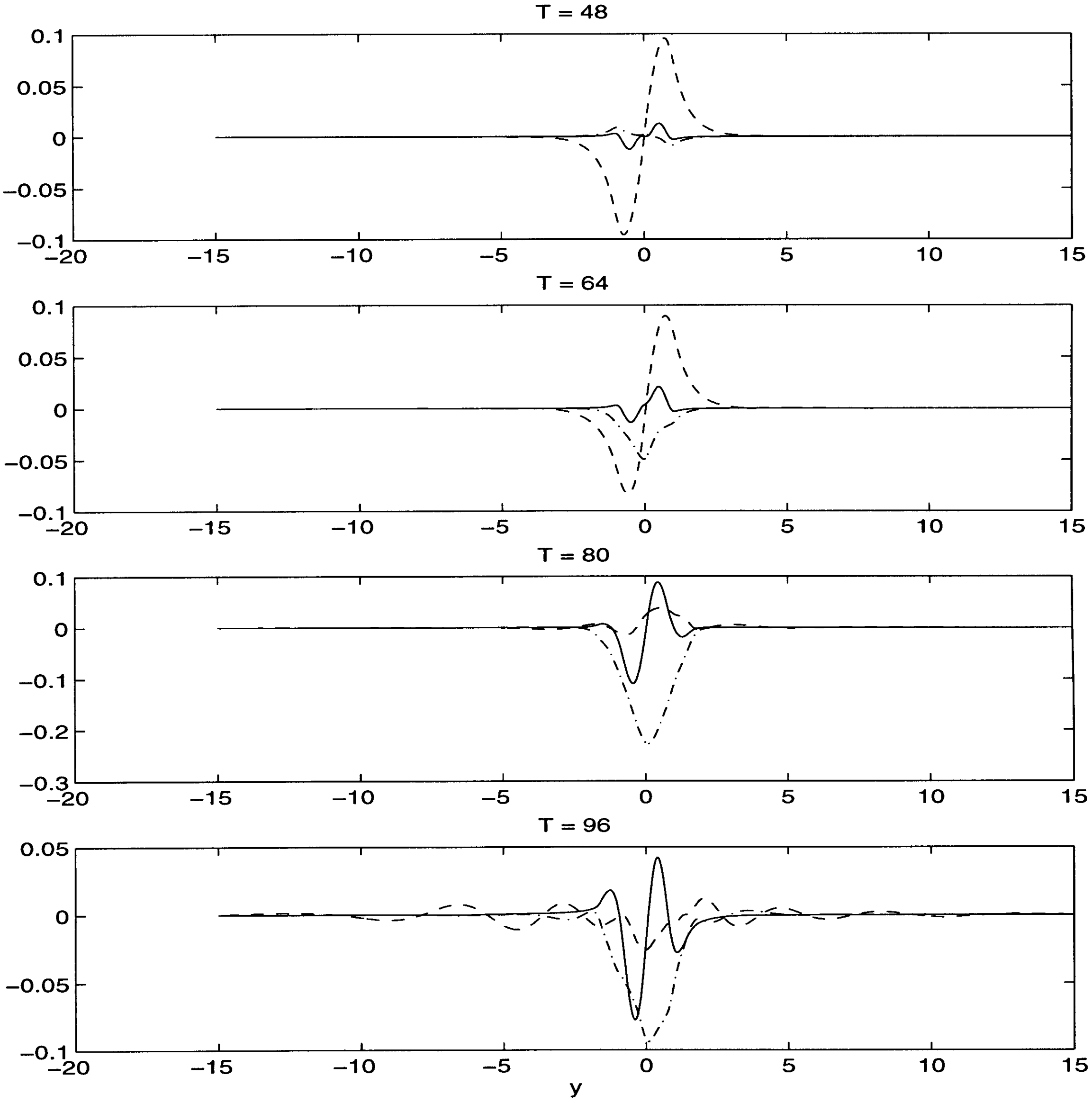

Figure 5.3: The Fourier coefficients Φ_0 (solid lines), Φ_1 (dashed lines) and Φ_2 (dashed-dotted lines) of the streamfunction as functions of y. Corresponding times are given on the top of each panel. $\alpha = 0^o$, $k = 1$ and $\beta = 1$.

of the single sinuous mode "2". During the transition, the component "1" gives way to the component "2" and radiates away the energy that it previously gained during the initial unstable growth. The radiating response is of transient nature and has very small amplitudes.

One should also note the presence of the component "0"; its significance will be discussed in detail in the following sections. The x-independent component remains trapped throughout the whole process of nonlinear development.

The next plot, Fig.5.4, showing the energy corresponding to each Fourier component (see section 5.1.2) helps to further clarify the dynamical picture. We see that component "2" starts to dominate the process after $t = 64$; the integrated over the whole domain energy corresponding to this mode K_2 is the largest after that time (Fig.5.4a).

The balance is very different if the energy for each component is integrated everywhere except the region $[-2\ 2]$ which contains the jet itself. The component "1" is clearly dominant in the external region defined above; see the lower panel of Fig.5.4. The ratio E_1/K_e further increases after the beginning of the radiation by this component. However, the radiation is not energetic; E_1 is about one percent of the total kinetic energy K_e. The contribution of the other components to the external kinetic energy is much smaller.

We conclude that the above described transient radiation is not efficient in our model. The radiation starts on the late stage of the development and the radiating response in the exterior is weak. The more effective mechanism for radiation related to the nonzonality of the mean current will be discussed in detail in the following sections. However, we should anticipate the emergence of a short, more linearly unstable wave in the course of the nonlinear development of a long wave. The process can have a significant effect on the dynamics of the problem.

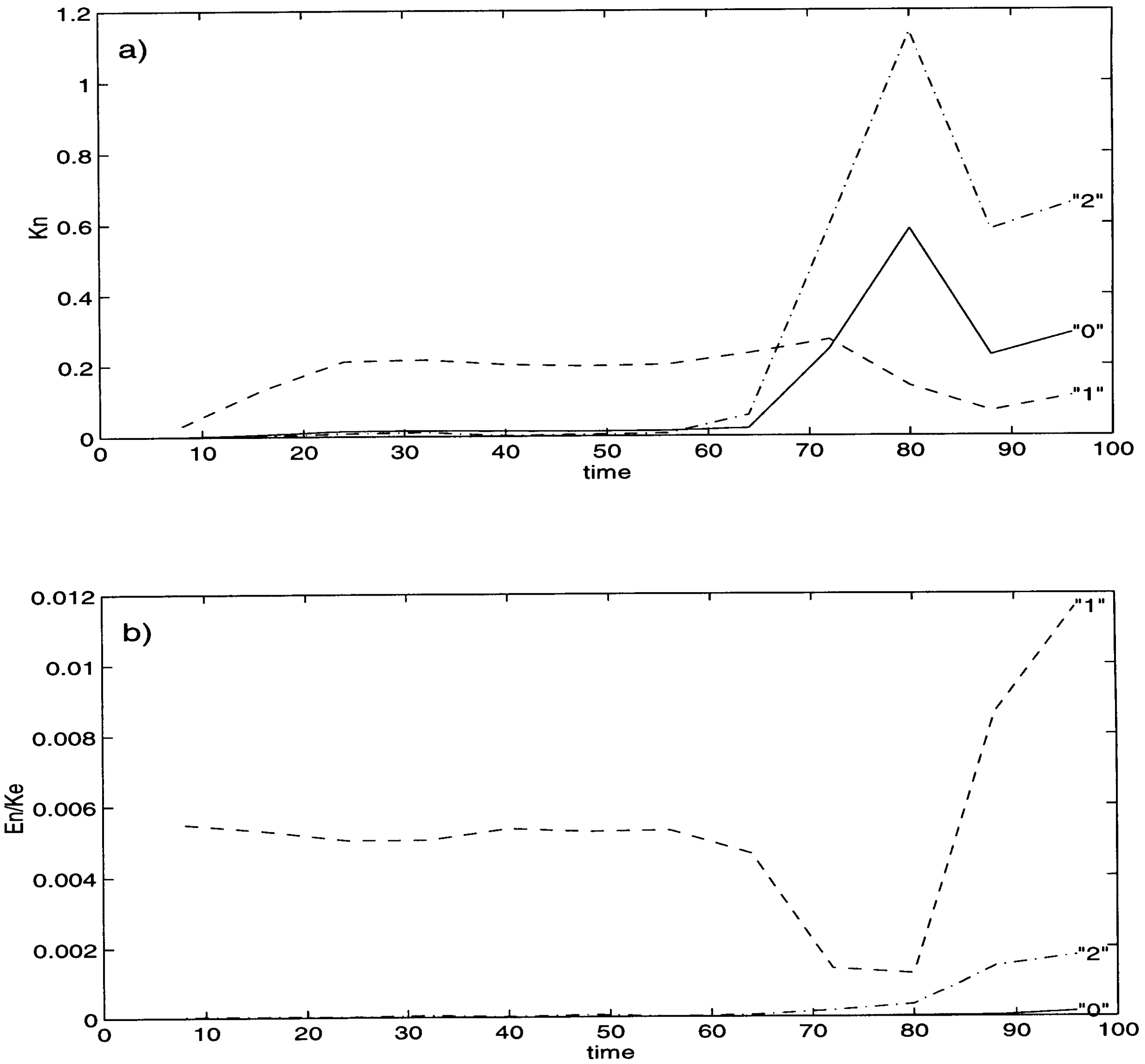

Figure 5.4: Kinetic energy corresponding to each Fourier component vs. time. a) K_{k_n} (energy integrated over the whole domain); b) E_{k_n} (energy integrated from $-\infty$ to -2 and from 2 to ∞) divided by the total energy K_e. Component numbers are shown on the plot. $\alpha = 0^o$, $k = 1$ and $\beta = 1$.

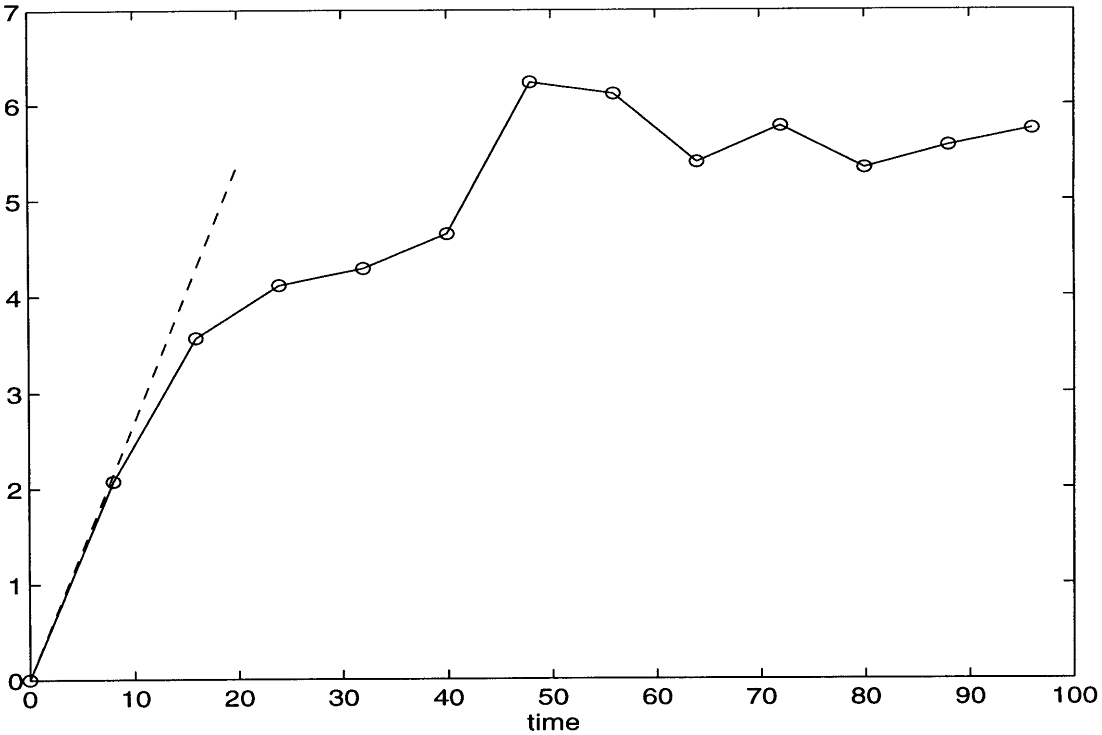

Figure 5.5: Logarithm of perturbation kinetic energy. As in Fig.5.1 but for $\alpha = 5^o$. $k = 1$ and $\beta = 1$.

5.3 Slightly nonzonal jet.

We now increase the value of the horizontal tilt from zero to the small value of 5^o as we did for the linear problem in section 3.2.2. We recall from that section that the solution changes its radiating properties qualitatively. The slowly growing long waves in the model become radiating, whereas the shorter linear waves remain trapped during the linear stage of development. Do the radiating properties of short waves change in the course of nonlinear development?

To answer this question, we initialize the problem with Mode 1 which is the modified varicose mode of the zonal jet for $k = 1$, $\beta = 1$. According to the linear theory (see section 3.2.2), the solution for this choice of k is strongly trapped.

We start by analyzing the dependence of kinetic energy on time. As for the zonal jet, the logarithm of perturbation kinetic energy is presented in Fig.5.5. The shape of the

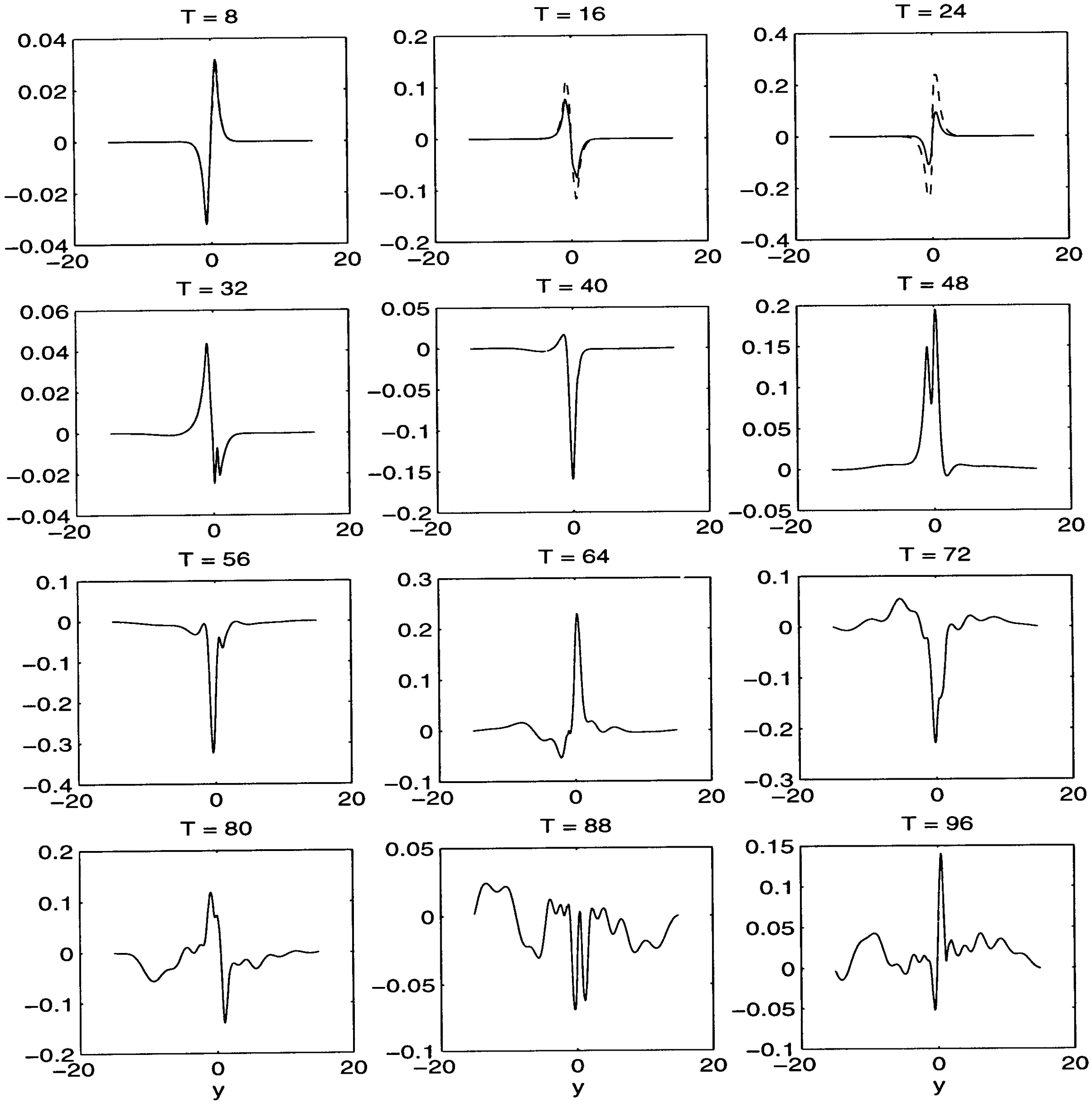

Figure 5.6: The streamfunction as function of y. As in Fig.5.2 but for $x = 1.37$ and $\alpha = 5^o$. $k = 1$ and $\beta = 1$

curve is similar to that in Fig.5.1. The solution is very different from the linear one for $t > 16$. The curve shows the period of secondary growth from $t = 32$ to $t = 42$ and then tends to vacillate around a mean value. The integration for a longer time interval may be needed for the detailed dynamical picture. However the investigation of the development on very long time intervals is beyond the scope of the present research and is difficult because of the growing boundary effects (see section 5.1). Instead, we are interested in the existence of radiation on the relatively early ($t < 100$) stage of nonlinear development of the initially strongly trapped solution. We might expect equilibration to occur at later time in the sense of reaching a saturation amplitude. Only, it might not equilibrate to a steady solution but rather a vacillating one in the absence of dissipation.

We now turn our attention to the 1D plots of the streamfunction which are presented in Fig.5.6. The observed dynamical picture is similar to that in the case of $\alpha = 0$. The strong symmetric component is clearly seen in the structure of the solution at $t > 48$ and the radiation starts after that. These facts suggest the presence of the dynamical process described in the preceding section in which the interactions between initially posed varicose mode and the excited later highly unstable sinuous mode (Fig.3.4b) cause the former to radiate. As we recall from section 3.2.2, for the tilt as small as 5^o the results are almost the same as for the zonal jet unless a wave is very long in x. It is not therefore surprising to find the nonlinear behavior in both cases similar as well.

However, some differences with the case $\alpha = 0$ are obvious. First of all, the radiation starts earlier, at $t > 40$. The amplitude of the radiating response is larger than that in the case $\alpha = 0^o$ and has more complicated structure. Do we observe the new mechanism for radiation of short waves related to the nonzonality of the current at work here?

We now consider the Fourier coefficients Φ_{k_n} in Fig.5.7. The comparison of this plot with Fig.5.3 reveals a significant difference in the dynamical development. The radiation in the exterior region now starts as early as $t = 40$ and is in the form of x-independent component "0" (Φ_0). Component "1" (Φ_1) radiates for $t > 64$ and remains at least as large as Φ_2. Its amplitude does not decrease with time as it does for $\alpha = 0^o$. The

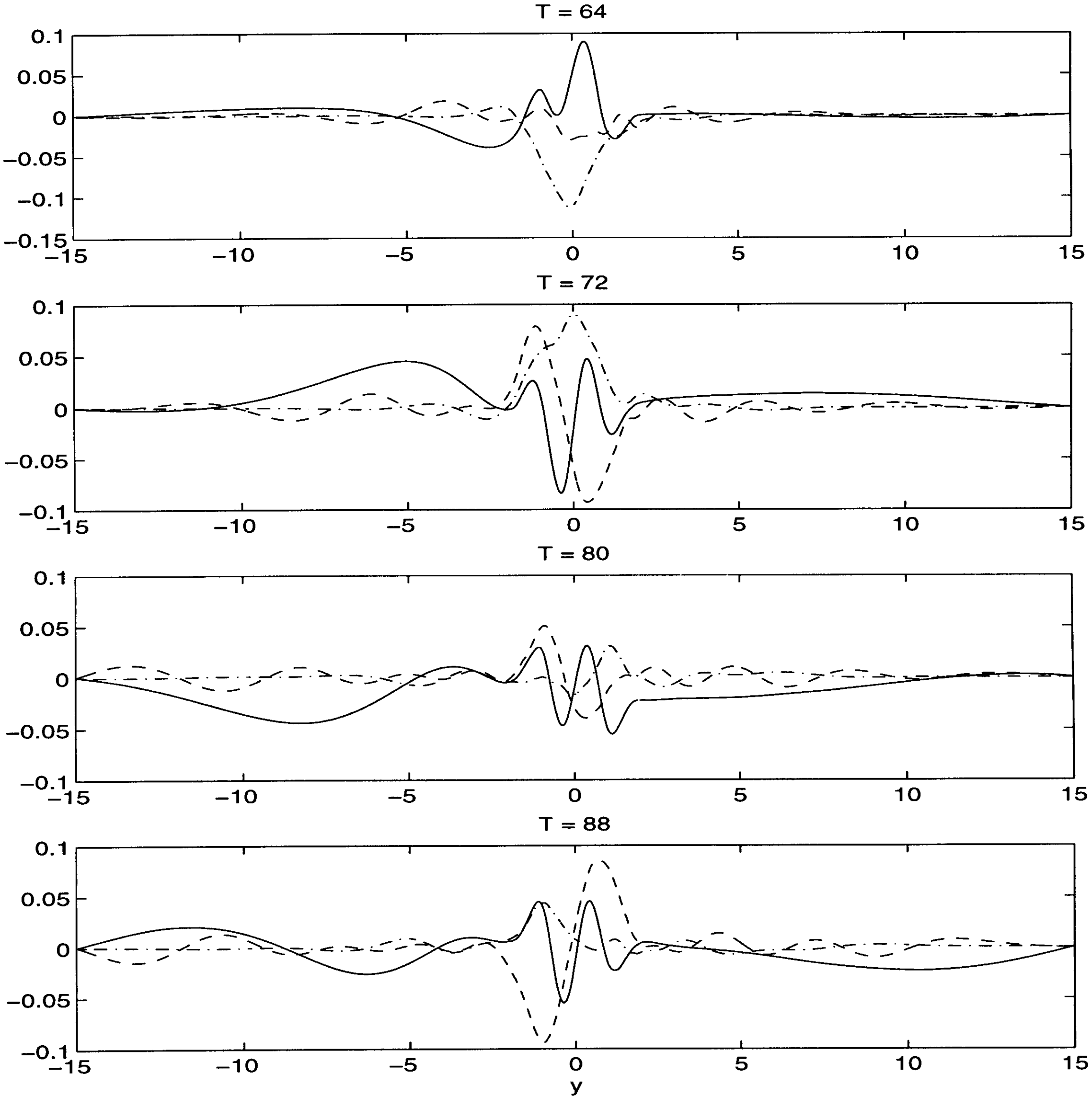

Figure 5.7: The Fourier coefficients Φ_0 (solid lines), Φ_1 (dashed lines) and Φ_2 (dashed-dotted lines) of the streamfunction as functions of y. $\alpha = 5^o$. $k = 1$ and $\beta = 1$.

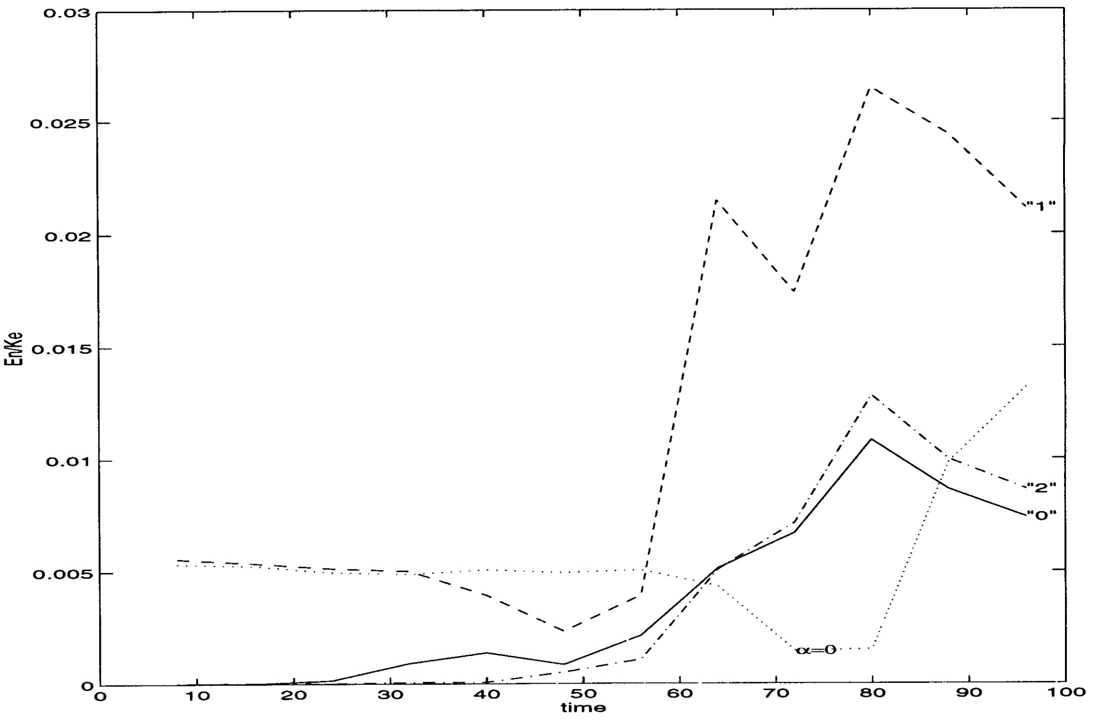

Figure 5.8: External kinetic energy E_{k_n} corresponding to each Fourier component vs. time. As in the lower panel of Fig.5.4 but for $\alpha = 5^o$, $k = 1$ and $\beta = 1$. $(E_0+E_1+E_2)/K_e$ for the zonal jet (previous chapter) is shown by the dotted line (marked by $\alpha = 0$).

radiation therefore does not simply accompany the transition from the Mode 1 to Mode 2, but rather is a robust feature of the late stage of the development of component "1".

The radiation is also more energetic now, as we can see in Fig.5.8. The external part of the energy corresponding to the component "1" is now approximately 2.5 percent of the total perturbation energy. One percent of the total energy is radiated into the exterior by each of the components "0" and "2". The sum of these numbers, $(E_0 + E_1 + E_2)/K_e$, is 4.5 percent which is much bigger than the same quantity for $\alpha = 0^o$ (dotted line in Fig.5.8). The more energetic radiation in the case of the slightly nonzonal current is apparent.

The described radiation for $\alpha \neq 0$ is different from the weak transient radiation in the case of the zonal jet. The radiation is more energetic and occurs much earlier in the case of a nonzonal jet. The radiating response has complex structure and does not weaken with time. The discovered new mechanism for nonlinear radiation will be observed in many cases and studied in detail in the following sections.

The role of component "0".

Another very interesting feature of the nonlinear development for $\alpha \neq 0$ is the strong x-independent component of the radiating exterior response (component "0"). The component represents the change in the x-averaged momentum, the influence that the growing perturbations have on the mean current. The component is strongly trapped for the zonal jet. In contrast, Φ_0 has a large amplitude in the exterior for the nonzonal current. However, this component of the streamfunction corresponds to zero v-velocity and that results in the kinetic energy of component "0" (K_0) being almost twice smaller than the kinetic energy of component "1".

Well-pronounced radiating properties of the component "0" will be observed for all numerical experiments as long as the tilt is nonzero. In all those cases, component "0" starts to radiate first. Why is it that the x-independent component radiates more easily than others?

Imagine the forced-boundary problem in which the boundary is x-independent and oscillates with a given frequency ω. No linear solution is possible if the boundary is oriented zonally. The x-independent forced streamfunction corresponds to zero v-velocity and the oscillating response in the form of a Rossby wave is not possible.

However, Rossby waves can exist if the boundary is tilted. The dispersion relation for the response in the rotated coordinate frame is

$$\omega = \frac{\beta_1}{l}.$$

If the frequency of the boundary oscillations ω is complex (the magnitude of oscillations is growing in time), the l is complex as well and solution decays away from the boundary. As long as ω is purely real, the response is a plane wave *regardless* of the value of the frequency. In other words, the only reason for the spatial trapping of the solution is its exponential growth in time. No additional constrains on the value of the frequency analogous to the phase speed condition exist. The added physical effects, such as the free surface, can restore some constraints on the frequency.

This simple example explains why component "0" can radiate so easily if $\alpha \neq 0$. As soon as the growth of the solution significantly slows due to the nonlinear effects, the spatial trapping of component "0" disappears. The frequency of the component does not have to satisfy any criterion in order for solution to radiate. The radiation in the form of x-independent component is then followed by the radiation of components "1" and "2". Their fast phase propagation in the x-direction has to slow before the beginning of radiation; see section 5.4.1 for details.

The other property of this simple example that illustrates the properties of component "0" is the fact that the group velocity in y-direction is single-signed:

$$c_{gy} = -\frac{\beta_1}{l^2}.$$

Since the c_{gy} is always negative, the linear radiation from the boundary can only exist for negative y. One can see that this holds true in our case for $\alpha = 5^o$. In Fig.5.7 we observe that component "0" initially radiates only to the left from the jet region. The radiation to the right starts later most likely as a local result of nonlinear interactions in the exterior and is not directly forced by the jet edge.

5.4 Mode 1. $\alpha = 30^o$

We now proceed with the analysis of the nonlinear development in the case of the large horizontal tilt. As usual, we are going to focus on the change in the radiating properties caused by the strongly nonzonal orientation of the current. As we have observed in the previous section, the nonzonality of the current allows the new mechanism for radiation to exist. The large tilt should enhance this mechanism and allow us to fully understand it.

The assumption that we made in the linear problem is that radiating nature of the solution can be disguised by the spatial trapping caused by the fast exponential growth (section 2.3). In an attempt to determine the radiating properties of a solution, one can only consider the structure of the solution for the small growth rates and speculate about the radiating properties of faster growing solutions. As we have seen in the previous section, the decrease in the growth due to the nonlinear effects is an important factor that leads to radiation in the model. That makes a connection to the aforementioned hypothesis of the linear theory and makes the idea very useful for the nonlinear analysis of radiating properties.

As we recall from the section 3.2.3, the radiating properties are different at two cut-offs of both modes 1 and 2. At the long-wave cut-off the solution is radiating, whereas at the short-wave cut-off it is trapped. Are the radiating properties different between long and short waves in the nonlinear problem? To answer that question, we consider here the development of both short ($k = 1$) and long ($k = 0.25$) waves.

However, in comparing the results one should keep in mind that the more realistic spatial scales in the problem are associated with shorter waves. For example, $k = .25$ corresponds to the dimensional wavelength of $8\pi L_{jet}$ which is too long for being realistic in the ocean; $k = 1$ gives $2\pi L_{jet}$. The more complete discussion of the relevance of the results to the available observations are presented in Chapter 7.

One of the most important parameters in the problem is the growth rate, that sets the time scale for the exponential growth of the linear solution. Therefore, it is helpful to present growth rates for $\beta = 1$ and $\alpha = 30^o$ before we start. The growth rates for two linear modes are shown in Fig.5.9 as functions of the x-wavenumber k. The Mode 2 is the most unstable mode in the problem with the maximum growth rate almost twice larger than the maximum growth rate for Mode 1.

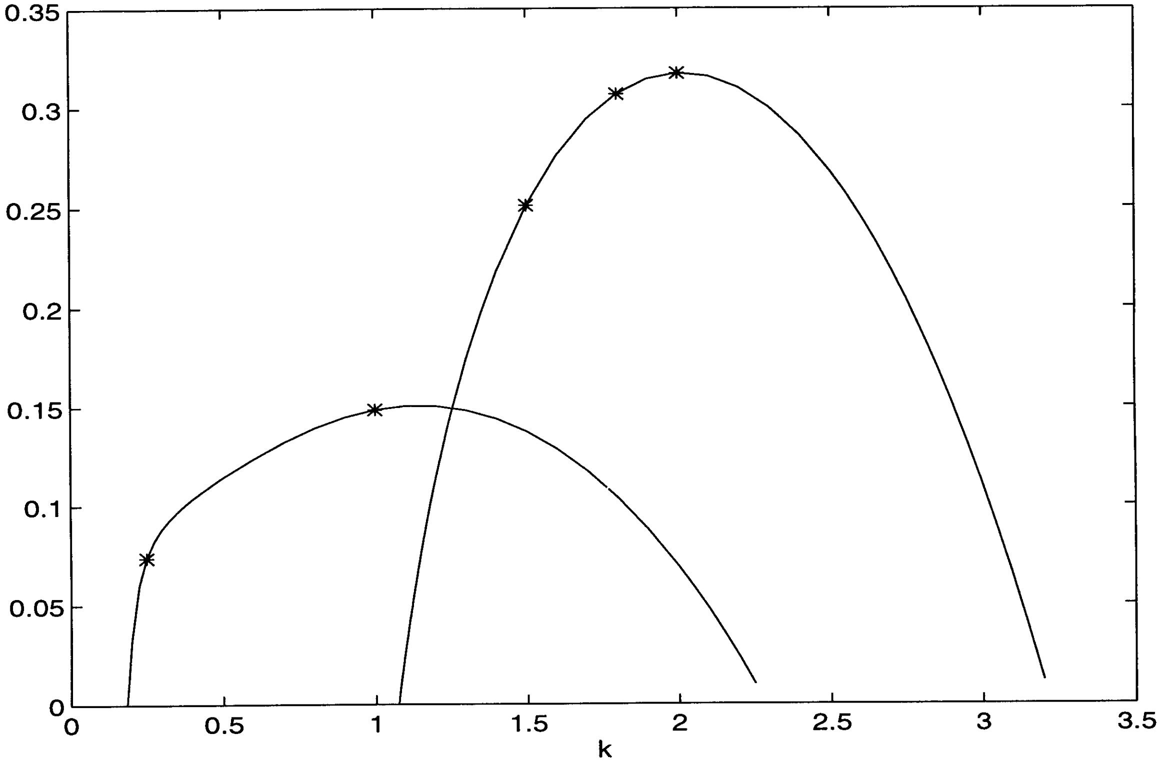

Figure 5.9: Growth rates as function of k for two linear modes; $\beta = 1$ and $\alpha = 30^o$. The marks on the curves show the choices of parameters for different numerical runs.

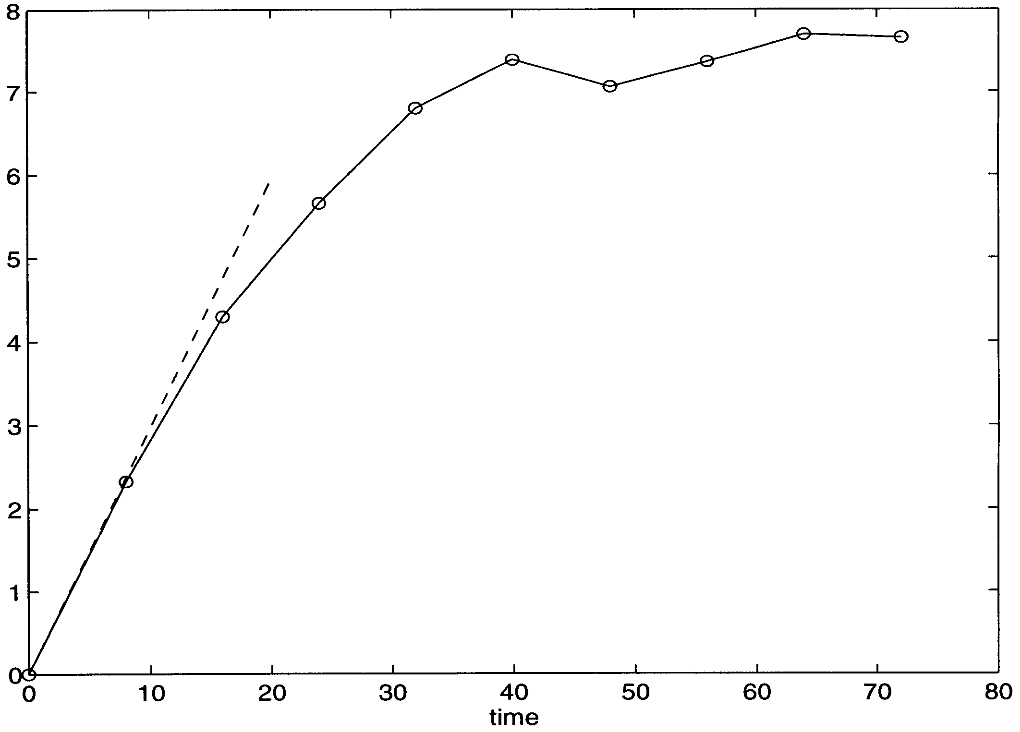

Figure 5.10: Logarithm of perturbation kinetic energy. As in Fig.5.1 but for $\alpha = 30^o$. $k = 1$ and $\beta = 1$.

5.4.1 Short wave: $k = 1$.

We start with the analysis of the development of a short wave, $k = 1$. The comparison of the following results with the results from the previous sections 5.2 ($\alpha = 0^o$) and 5.3 ($\alpha = 5^o$) for the same k will help us to understand the dynamical effects of the nonzonality.

The logarithm of kinetic energy is shown in Fig.5.10. We observe the familiar picture: The solution starts to grow in the agreement with the linear theory, then the growth slows at $t = 40$, and the curve starts to oscillate reaching the period of relatively slow growth.

We observe the evolution of the structure of the solution in the 2D contour plots of the total streamfunction $\bar{\Psi}(y) + \psi(x,y)$ (Fig.5.11). The full flow field is noticeably different from the basic state starting at $t = 16$. The initially parallel basic flow is strongly modified by the presence of meanders that are trapped to the jet region. The

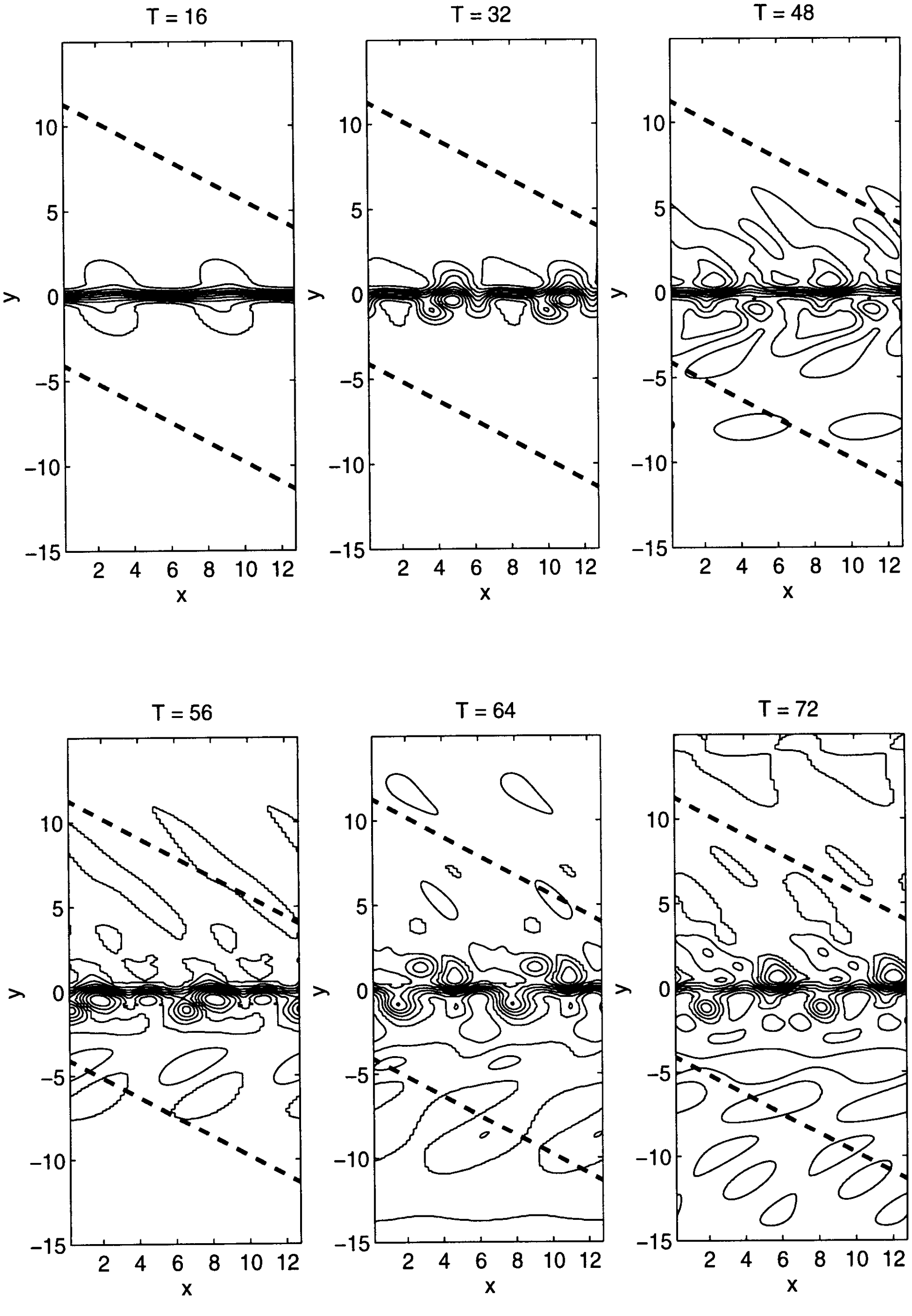

Figure 5.11: Two-dimensional contour plots of the total streamfunction $\bar{\Psi}(y) + \psi(x, y)$. Corresponding times are given on the top of each plot. Heavy dashed lines are parallel to the latitude circles. Mode 1, $k = 1$, $\beta = 1$ and $\alpha = 30^o$.

dominant wavenumber of those meanders is $k = 1$, since we observe that two wavelengths are fitted in the x-direction and $2 \times 2\pi/L_x = 1$.

The solution remains trapped during the initial phase of development for $t < 32$. The perturbation field extends in the cross-jet direction for later times: $t > 40$. We remember that this time corresponds to the transition from the fast exponential growth to the phase of the very slow rate of increase in the kinetic energy. Therefore, that is at the moment at which the fast growth significantly slows when we observe the beginning of radiation.

For negative y, eddies, that are elongated in the x-direction, are formed in the far-field by the end of the numerical experiment ($t = 72$). For positive y, the eddies are elongated in the direction that makes an angle to the jet axis, that, in turn, is tilted itself. The heavy dashed lines in the figure that are parallel to the latitude circles give us an idea about the orientation of these eddies in the conventional, non-rotated coordinate frame. As we can see from the figure at $t = 72$, the eddies for positive y are oriented nearly east-west once again demonstrating the asymmetry of the dynamical field in the cross-jet direction.

We now analyze the 1D plots of the streamfunction in Fig.5.12 which provide us with additional information about the structure and the amplitudes of perturbation motions. The amplitude of the wave-like radiating response in the exterior grows in time after the start of radiation at $t = 40$. We can see that by $t = 56$ the perturbations with large amplitudes have filled the entire numerical domain, which is 15 times wider that the jet itself. What we observe is the process that effectively transfers energy from the energetic unstable current to the remote exterior regions. The importance of this process requires a detailed study.

Before we proceed any further, we should notice one important feature. Compare the structure of the solutions inside the jet region ($-1 < y < 1$), where the most of the energy transformation occurs, between the discussed radiating case and non-radiating case with a zonal flow (section 5.2, Fig.5.2). The comparison reveals very little difference between both cases; the similarity in the structure points to the similar energy conversion

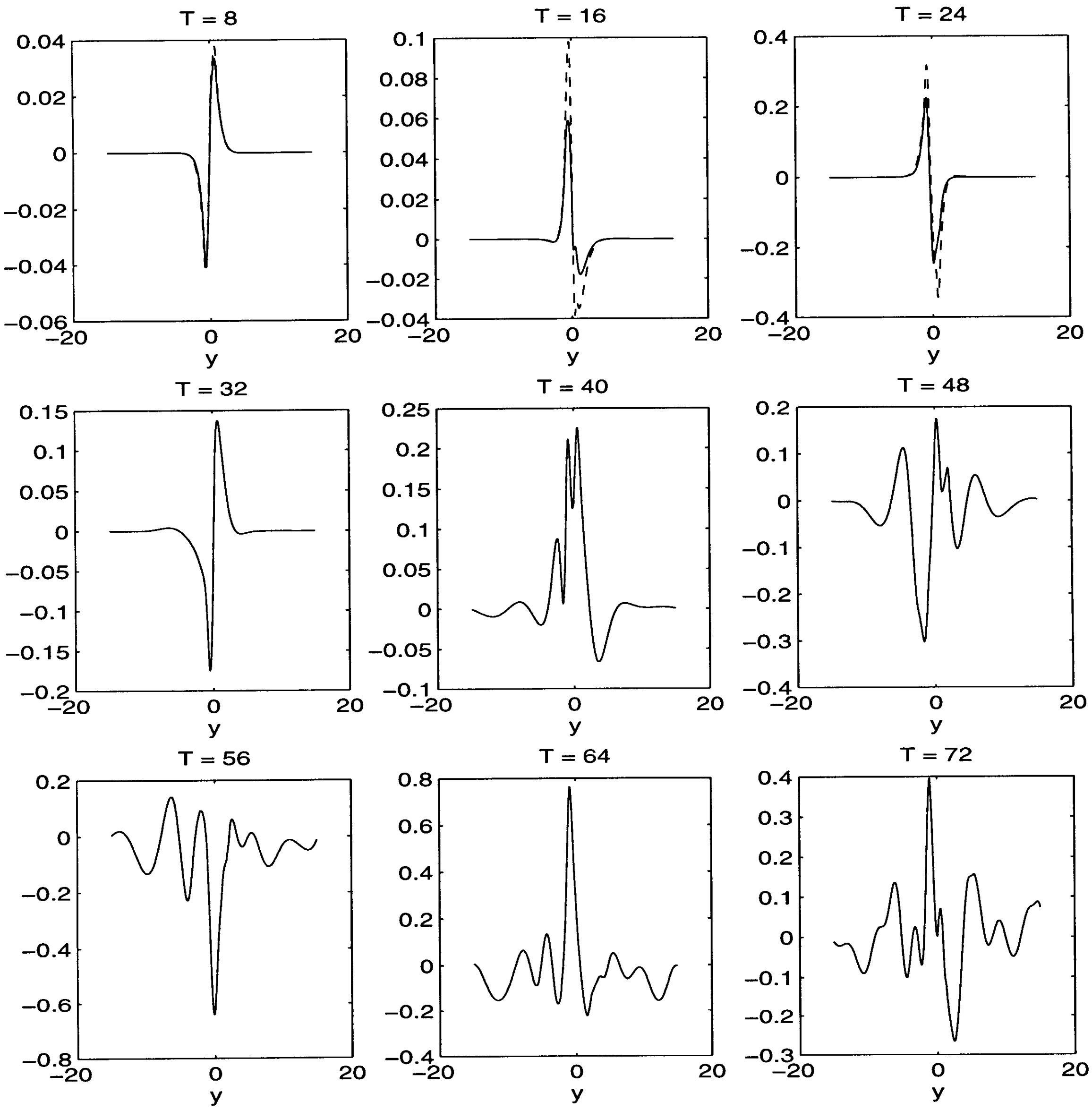

Figure 5.12: The streamfunction as function of y. As in Fig.5.2 but for $x = 1.37$ and $\alpha = 30^o$. $k = 1$ and $\beta = 1$

mechanisms in both cases. The main effect of the nonzonal orientation of the current axis is therefore in producing the energetic radiation and not in changing the general features of the dynamical processes inside the jet region, which are responsible for the energy transformation.

At first glance, the structure of the radiating response appears rather complex. As in the case of a slightly nonzonal current, several waves have radiating form in the exterior. What is the detailed structure of the obtained solution? Is Mode 2 excited the way it is in the previous numerical experiments for $\alpha = 0^o$ and $\alpha = 5^o$, and if so what is its role now? We note, that even if $\alpha = 30^o$ short linear waves in the problem are still easy to identify as modified symmetric (Mode 2) and antisymmetric (Mode 1) modes of a zonal jet, which simplifies the answer to the last question.

We present the Fourier coefficients as functions of y in Fig.5.13 for chosen times. The overall dynamical picture is similar to that for the case with $\alpha = 5^o$. The radiation starts in the form of x-independent component Φ_0 after $t = 40$ and the radiation occurs mainly in the half-plane where y is negative. The component represents the change in the x-averaged velocity field; it reaches large amplitudes for $y > 0$ at later times.

The component "1" starts to radiate immediately following component "0". The amplitude of the radiating response in both the exterior regions is almost as large as that inside the jet region $[-1\ 1]$. In contrast, component "2" mainly radiates for positive y.

As in previous cases, we also find nearly symmetric $\Phi_2(y)$ at $t = 40$. It is the sum of the very unstable nearly symmetric Mode 2 that is generated due to the presence of the numerical noise in the problem and the secondary component produced by self-interactions of component "1" which is antisymmetric. The symmetric structure in the interior points to the dominance of Mode 2 in component "2" in the region. However, despite the large growth rate (see Fig.5.9) of Mode 2 for $k = 2$, component "2" is never larger than the component "1" and does not dominate the development. The amplitude of component "1" remains the largest.

We now consider the plots of the kinetic energy calculated for each component

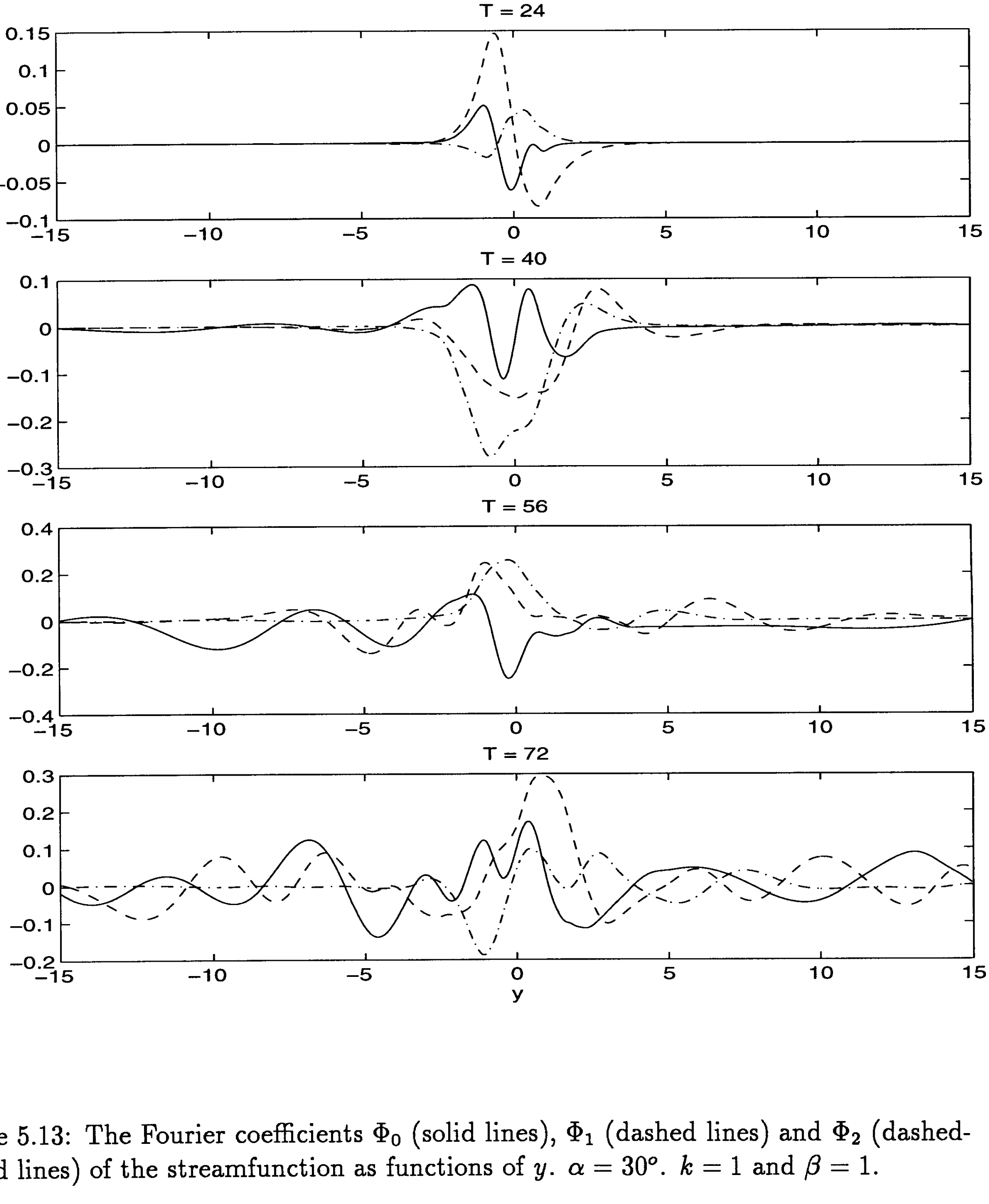

Figure 5.13: The Fourier coefficients Φ_0 (solid lines), Φ_1 (dashed lines) and Φ_2 (dashed-dotted lines) of the streamfunction as functions of y. $\alpha = 30^o$. $k = 1$ and $\beta = 1$.

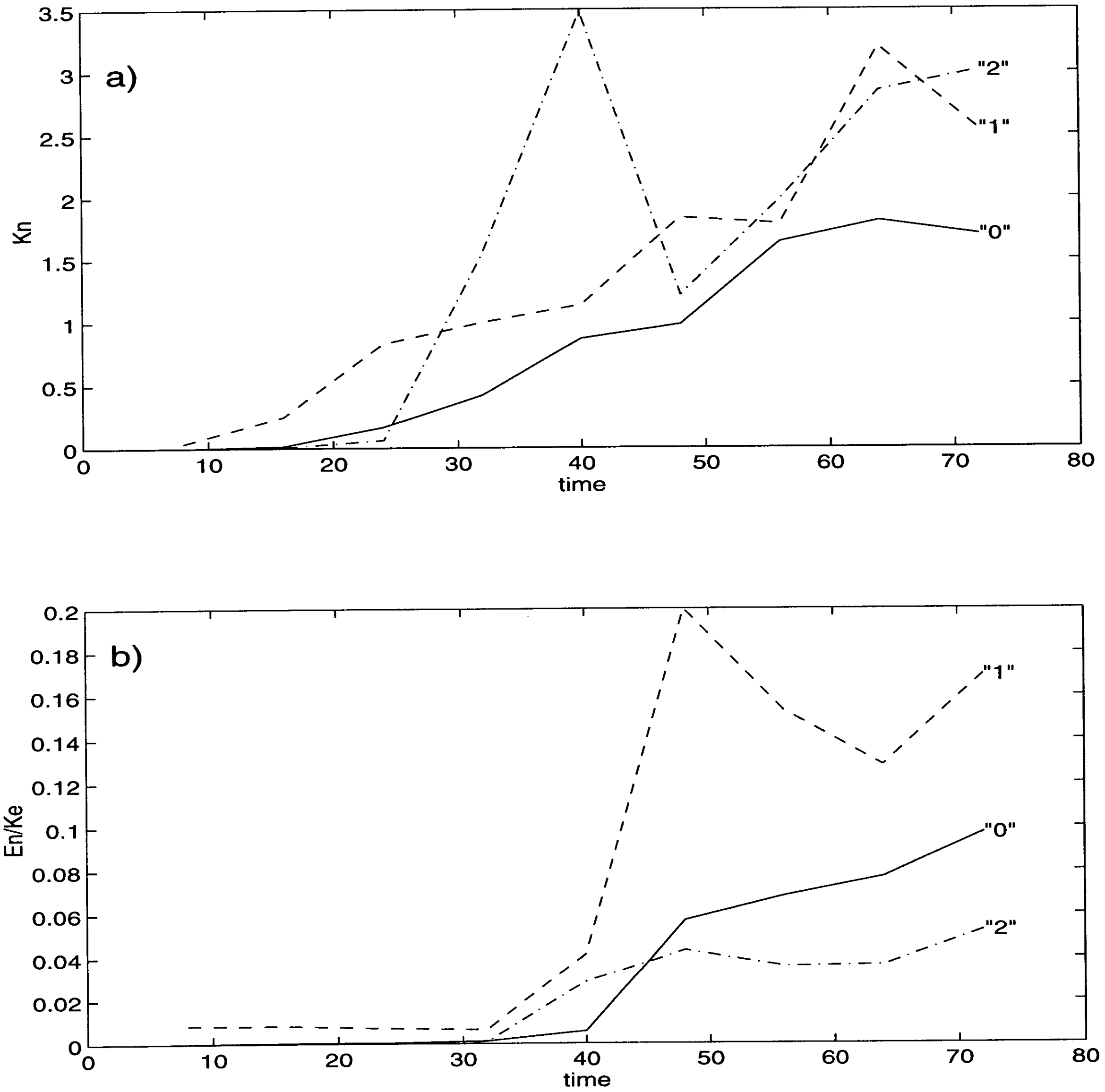

Figure 5.14: As in the Fig.5.4 but for $\alpha = 30^o$. $k = 1$ and $\beta = 1$.

(Fig.5.14). The integrated over the whole domain values of K_{k_n} are shown in the upper panel. Component "1" is very important energetically. Component "2" does not dominate the late stage of the development unlike the case with $\alpha = 0$, despite the presence of Mode 2 for $k = 2$ that definitely adds to the value of K_2.

In the lower panel, the external kinetic energy E_{k_n} is divided by K_e to give the portion of the total energy that is contained in both the regions $[-\infty\ -2]$ and $[2\ \infty]$. The picture further emphasizes the efficiency of the mechanism for radiation in the case of nonzonal current. The plotted values are very small before the beginning of the radiation, which is approximately at $t = 40$. After this time, we observe the increase in the radiated energy associated mainly with the component "1". More than 17 percent of K_e is radiated by this component by the time $t = 72$.

The components "0" and "2" contribute approximately 10 and 6 percent of K_e to the total value of the external energy. The x-independent component of the solution has large amplitudes; its contribution to the kinetic energy is however smaller mainly because of the zero v-velocity associated with it.

As we have already remarked in section 5.2, the modified sinuous Mode 2 excited in the course of nonlinear development can play an important role in the process. As will be demonstrated below (section 5.5), the radiation in the case with a single Mode 2 is weak but its ratio of the external energy to K_e is close to that by component "2" reported in the current section. Therefore, the radiation by component "2" is a result of both self-interactions of component "1" and the development of Mode 2.

We can conclude that the mechanism which causes the solution to radiate as soon as its growth becomes very slow is much more effective compared to the relatively weak transient process of radiation that is found in the case of $\alpha = 0$. More than 30 percent of K_e is eventually transferred into the external regions at $\alpha = 30^o$. The ability of short waves to radiate is related to the change in their dynamical nature related to the nonzonal orientation of the current. The change is the strongest for slowly growing solutions; in the linear problem, it can only be observed for long waves in the linear problem. Nonlinear effects, that slow the growth, enable short waves to radiate.

Evolution of the mean flow.

As we have remarked in the discussion of the role of component "0" (section 5.3), the component represents the change in the x-averaged momentum in the system. We now want to derive the equation for the rate of change of the x-averaged velocity and discuss the role of different terms responsible for that change.

We first write the momentum equation in the x-direction in terms of the perturbation streamfunction:

$$-\psi_{yt} + (\bar{u} - \psi_y)(-\psi_{yx}) + \psi_x(-\psi_{yy}) - (\beta_2 y + \beta_1 x)\psi_x = -\frac{1}{\rho}p'_x \tag{5.7}$$

where $p'(x, y, t)$ is the ageostrophic pressure.

We now x-average equation 5.7 and, after integration by parts, obtain:

$$-\overline{\psi_{yt}}^x = \frac{\partial}{\partial y}\overline{\psi_x\psi_y}^x + \beta_1\overline{\psi} + G(y, t) \tag{5.8}$$

where

$$G(y, t) = \beta_1 L_x \psi(0, y, t) - \frac{1}{\rho}\left[p'(L_x, y, t) - p'(0, y, t)\right]$$

We now can prove that the terms $G(y, t)$ are zero. Take the y-derivative of the equation 5.8; we get

$$-\overline{\psi_{yyt}}^x - \frac{\partial}{\partial y}\overline{\psi_x\psi_{yy}}^x - \beta_1\overline{\psi_y} = G_y(y, t),$$

since $\frac{\partial}{\partial y}\overline{\psi_{xy}\psi_y}^x = 0$. Now we x-average the potential vorticity equation 5.1; the result is identical to the above equation with a zero right-hand side. Therefore, $G_y = 0$, and $G(y, t)$ is a function of t only. We then recall that $\psi \to 0$ as $y \to \pm\infty$, therefore $G(y, t) = 0$.

The derived equation 5.8 has clear physical interpretation. The left-hand side represents the change in the x-averaged momentum and is therefore expressed in terms of the component "0", since $\overline{\psi(x, y, t)}^x = \Phi_0(y, t)$.

The first term on the right-hand side of (5.8) is the x-averaged divergence of the off-diagonal component uv of the Reynolds stress tensor with a minus sign. The term equals the x-average of the y-component of the perturbation potential vorticity flux in the system (see Pedlosky, 1987, p.398). We will use the term "PV flux" for brevity in the rest of this section. The second term is the product of the perturbation streamfunction and the downstream component of the planetary vorticity gradient β_1; the term is nonzero only for a nonzonal jet.

We now illustrate the role of both terms on the right-hand side of equation 5.8 in a particular example. All three terms in Eq. 5.8 calculated for the numerical experiment described in the current section are presented in Fig.5.15.

The rate of change in the x-averaged velocity is similar in general structure to the component "0" itself (see Φ_0 in Fig.5.13 shown by the solid lines). $-\Phi_{0yt}$ grows fast until $t \sim 32$. The radiation starts at later times first for negative y, then in the rest of the region.

The second term plotted, namely the PV flux in the y-direction, is localized in space throughout the entire numerical experiment. The term plays an important role in the energy transfer to the perturbation field. Indeed, multiplied by the mean velocity, it can be modified to yield

$$\bar{u}\frac{\partial}{\partial y}\overline{\psi_x\psi_y}^x = -\bar{u}_y\overline{\psi_x\psi_y}^x + \frac{\partial}{\partial y}\left(\bar{u}\overline{\psi_x\psi_y}^x\right)$$

The right-hand side, if integrated in y, can be easily identified with the first and second terms on the right-hand side of the barotropic energy equation 3.4 taken with a minus sign. Since $\bar{u}$ is positive, the sign in the PV flux determines if the phase shift between two velocity components acts to transfer the energy *to* perturbations if the PV flux is *negative*, or *from* perturbations if the term is *positive*. The analysis makes sense only in the jet region, where $\bar{u} \neq 0$. We now note, that the PV flux tends to be negative for negative y therefore acting to increase the perturbation kinetic energy and positive for positive y acting to decrease the energy. The u and v velocities are nearly in phase in the far-field, resulting in zero values of PV flux.

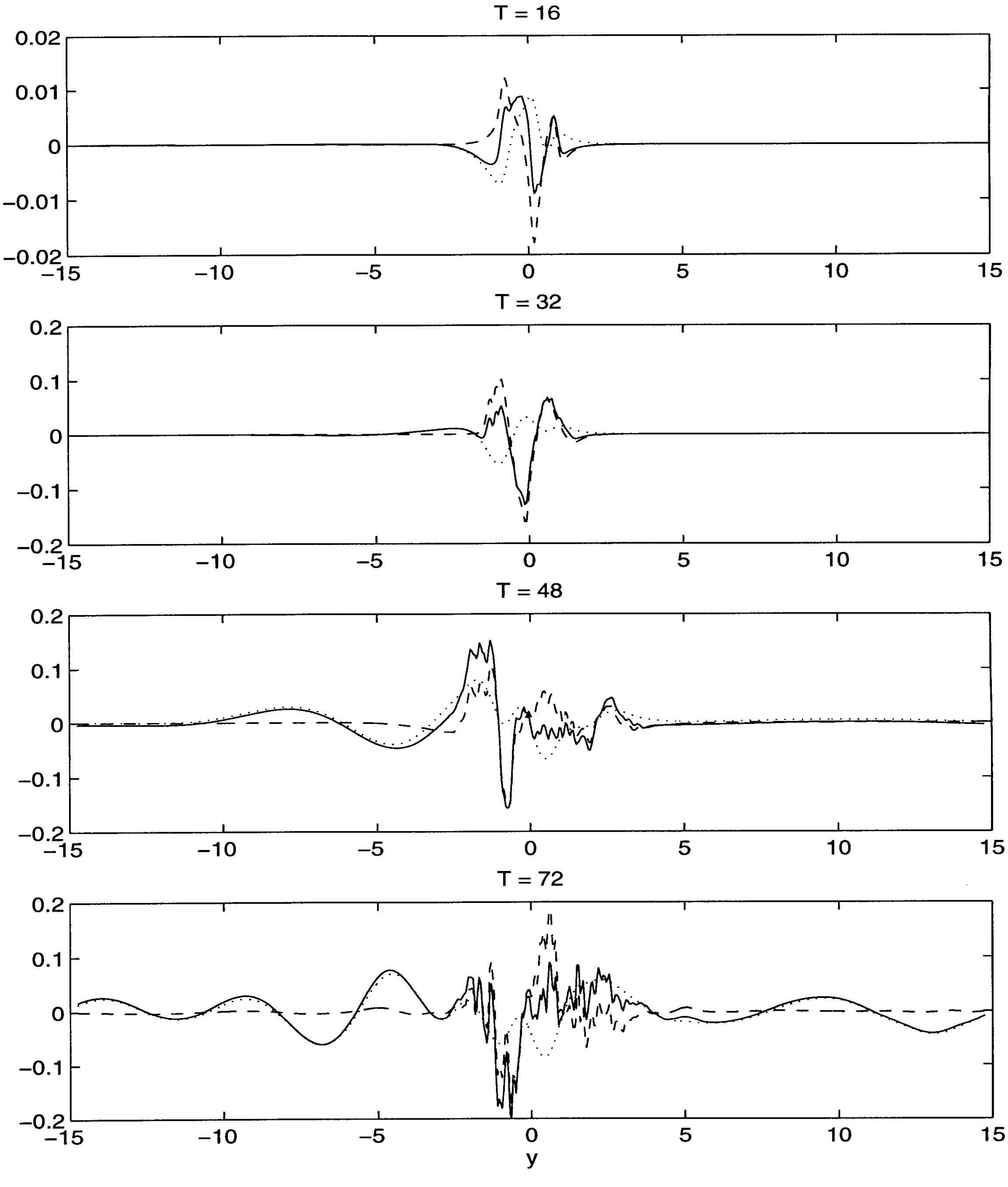

Figure 5.15: Terms from the equation 5.8: $-\overline{\psi_{yt}}^{x}$ (solid lines), $\frac{\partial}{\partial y}\overline{\psi_x\psi_y}^{x}$ (dashed lines) and $\beta_1\overline{\psi}$ (dotted lines) as functions of y. Corresponding times are shown on the top of each plot. $k = 1$, $\beta = 1$ and $\alpha = 30^o$.

The last term plotted, $\beta_1\overline{\psi}$, is not localized in space during the radiative phase of the development. Instead, the term balances the change in the x-averaged momentum which is radiated to the far-field. This fact emphasizes the importance of the downstream component of the planetary vorticity gradient for the radiation in the model.

Component phase speed.

One of the most important criteria for radiation that we used in the linear problem was the phase speed condition that sets the limits on the phase speeds of a radiating wave (section 2.3). It is hard to apply the same condition to the finite amplitude solution because solution is no longer a wave with well-defined phase speed. However, it may be relevant to the radiating response in the exterior. The motions there have small amplitudes, at least during the beginning phase of radiation, and should be in a linear balance locally. Is the radiating response, which is a composition of several Fourier components, in the agreement with the phase speed condition?

To answer this question, one needs to consider each component separately since bounds on the phase speed are determined by the x-wavenumber k. Our solution is not purely linear and is not in the form of the plane wave for which the frequency ω and the corresponding phase speed $c = \omega/k$ are easy to determine. However, as long as the amplitude of the Fourier coefficient is small, we can define the phase speed through the time-derivative of the complex phase:

$$c_{k_n}(y,t) = -\frac{1}{k_n}\frac{\partial}{\partial t} atan \left(\frac{Re\Phi_{k_n}(y,t)}{Im\Phi_{k_n}(y,t)}\right) \tag{5.9}$$

It is easy to check that in the case of a plane wave, the above relation gives the correct constant phase speed. In our nonlinear problem, the phase speed defined by (5.9) is generally a function of time and y, but should be close to the constant value if Φ_{k_n} is nearly in the linear balance. The values c_1 computed for the component "1" are presented in Fig.5.16.

At $t = 16$ the solution is still practically linear and the phase speed is very close

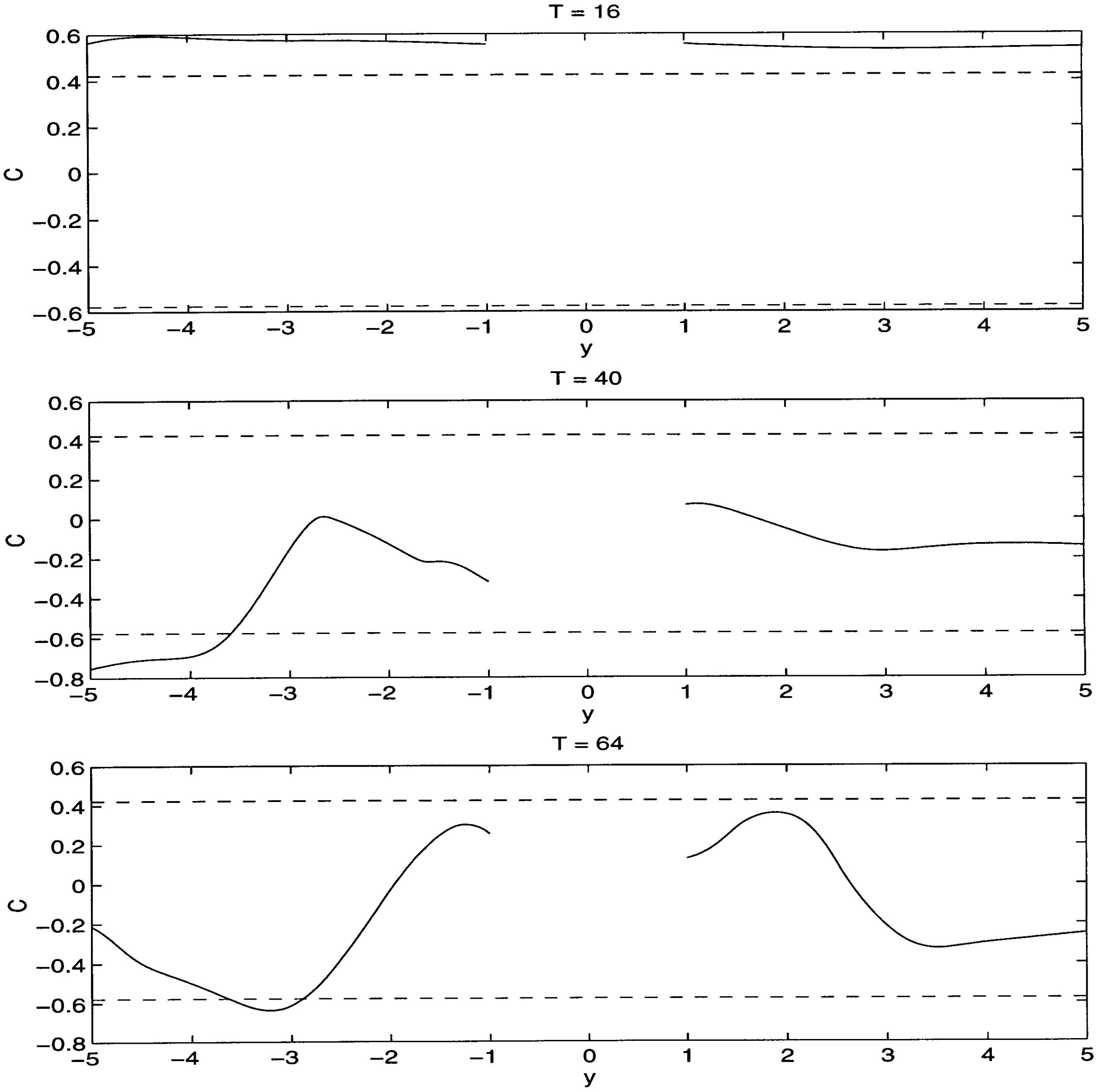

Figure 5.16: The function $c_1(y, t)$ defined by Eq.5.9 as a function of y for different times. The upper and lower bounds on the allowed for radiation phase speed set by the phase speed condition (2.13) is shown by the dashed lines. The jet region [−1 1] is not shown. $k = 1$, $\beta = 1$ and $\alpha = 30^o$.

to constant. Its value lies outside the interval set by the phase speed condition (2.13), which implies spatial trapping according to the linear theory. The propagation of the phase slows at later times; in fact c_1 at $t = 8$ is already smaller than that for the linear solution. At $t = 40$ which is the beginning of the strong radiation in the model, c_1 satisfies the phase speed condition (2.13) which is the necessary condition for radiation in the linear problem. The phase speed is mostly negative and small in absolute value.

The solution in the exterior at $t = 40$ is still nearly linear because of its small amplitude. As a result, the phase speed calculated using Eq.5.9 is reasonably close to the constant in the region $-3 < y < -1$ and for positive y. Therefore, the beginning of radiation is dynamically consistent with the linear theory. The phase speed c of the initially trapped solution decreases due to the nonlinear effects and the radiating response starts to develop as soon as c becomes small enough to satisfy the phase speed condition.

The situation changes for later times: c strongly depends on y at $t = 64$ which can be explained by the nonlinear nature of the radiating response. The phase speed still satisfies the phase speed condition, however, the analogy with the linear boundary forced problem is difficult to draw in this case.

5.4.2 Long wave: $k = 0.25$.

In the linear problem, the influence of the x-component of the planetary vorticity gradient $\beta_1 = \beta sin\alpha$ is the strongest for waves long in x making them radiating in the linear problem. In the nonlinear development of a long wave considered in this section, we also expect the nonzonal orientation of the current to further strengthen the nonlinear radiation found in the preceding sections. In addition, the excitation of the more unstable linear Mode 2 is unlikely in this case at least during sufficiently long period of time, since Mode 2 is stable for long waves ($k < 1.1$; see Fig.5.9). The process is more characteristic for the development of shorter waves (see preceding sections 5.2, 5.3 and 5.4.1).

The results for a long wave presented below should therefore emphasize the effectiveness of the mechanism for radiation related to nonzonality (as it is described in sections

5.3 and 5.4.1).

We choose our initial conditions in the form of a single linear wave for $k = 0.25$, $\beta = 1$ and $\alpha = 30°$. Despite the fact that its growth rate is almost half as that of the wave with $k = 1$, the wave still grows fast (see Fig.5.9). As a result, the solution is initially weakly trapped (section 3.2.3). We make the initial amplitude five times bigger than before to simplify the comparison to the previous cases in which $k = 1$. The wave with $k = 0.25$ then reaches the finite amplitudes at roughly the same times as in those cases. What are the dynamical characteristics of the radiation? What are the differences with the development of a shorter wave with $k = 1$?

The Fourier coefficients are presented in Fig.5.17. We observe that $\Phi_{0.25}$ is weakly trapped starting from the very early stage of development. The spatial decay scale is longer than for a wave with $k = 1$; the difference is explained by smaller growth rate for $k = 0.25$. The radiation further develops at later times when nonlinear effects cause other components of the solution to emerge.

Component "0" reaches finite amplitudes at $t = 40$ and the radiation starts quickly after that and occurs initially to the left from the jet region only ($t = 64$). Component "0.5" produces radiation as vigorous as that produced by the component "0.25" ($t = 64$).

The radiation is very dramatic at later times; see Fig.5.17 for $t = 88$. All three components correspond to the very energetic radiation in the exterior region. The process of the transfer of energy from the jet to the remote in the cross-jet direction regions is very effective in the discussed case.

The effectiveness of the above mentioned transfer of energy is further outlined by the values of the ratio of the external part of energy E_{k_n} to the total perturbation energy K_e (see Fig.5.18).

The component "0.25" dominates the radiating response initially since the linear wave used as initial condition is weakly trapped. The corresponding energy in the external regions increases in absolute value together with the kinetic energy integrated over the whole domain. As a result, the ratio between two values increases only slightly from

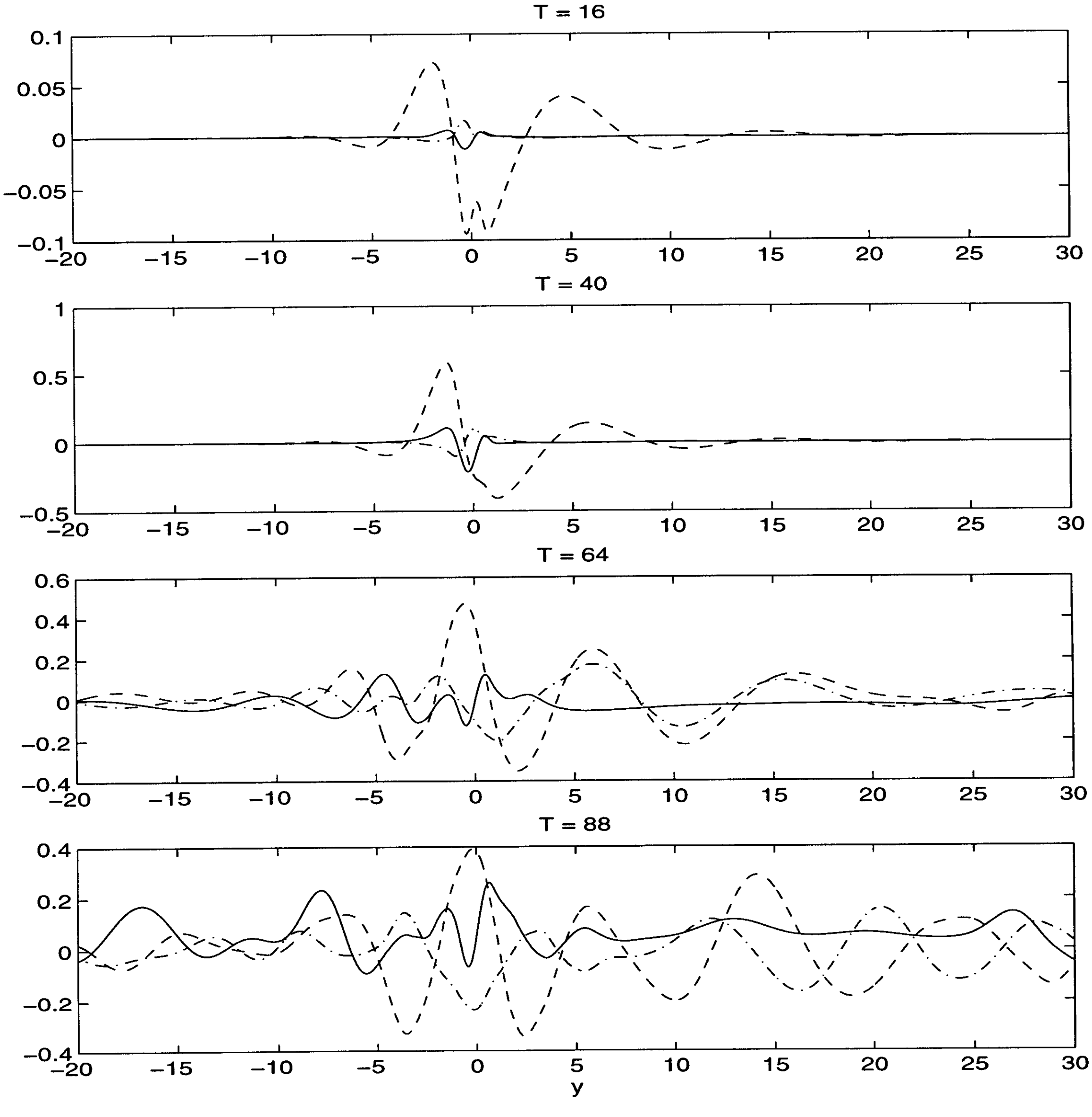

Figure 5.17: The Fourier coefficients Φ_0 (solid lines), $\Phi_{0.25}$ (dashed lines) and $\Phi_{0.5}$ (dashed-dotted lines) of the streamfunction as functions of y. Corresponding times are given on the top of each panel. $\alpha = 30^o$, $k = 0.25$ and $\beta = 1$.

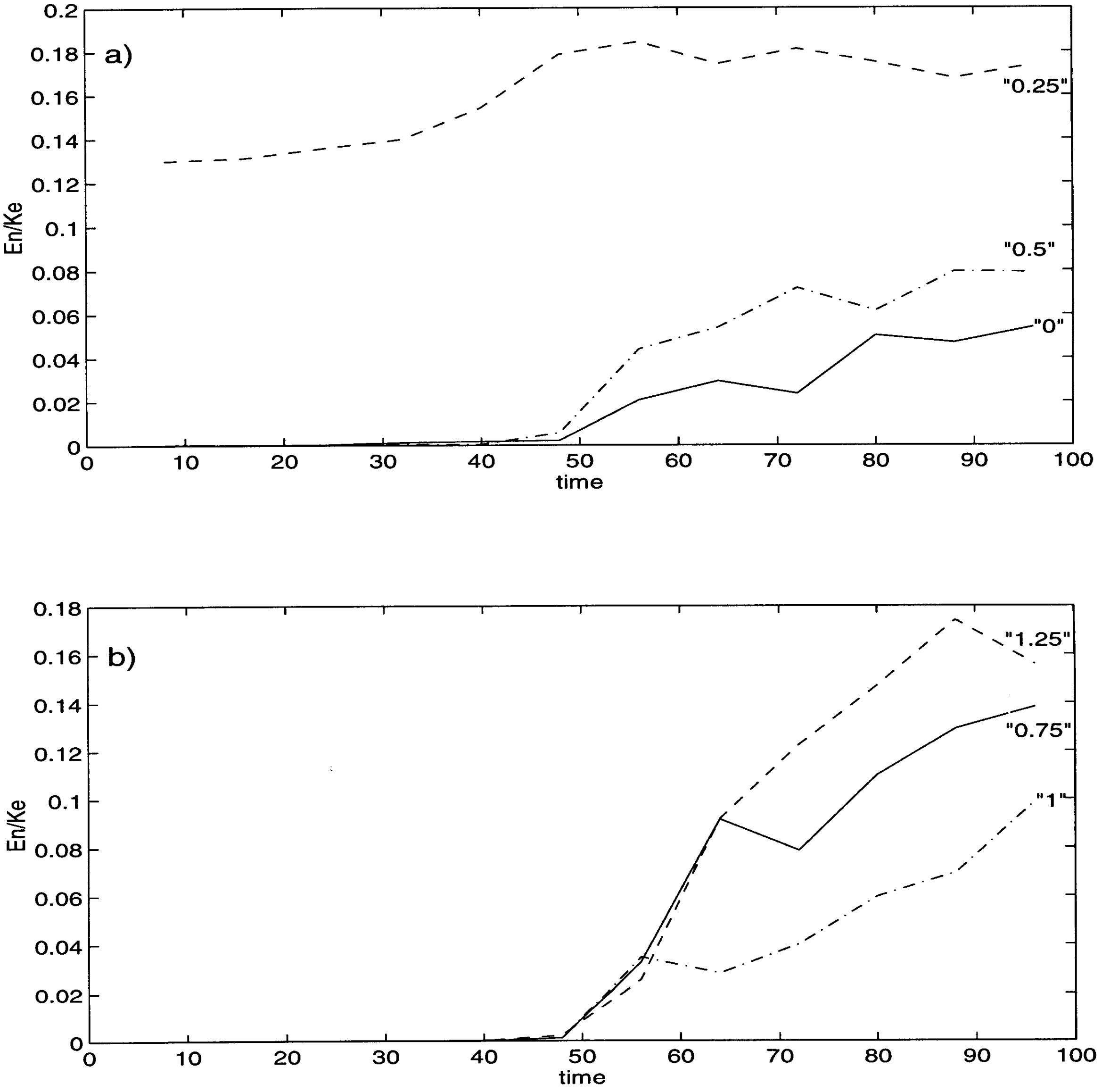

Figure 5.18: E_{k_n} (external kinetic energy corresponding to each component) divided by total perturbation energy K_e. a) components "0", "0.25" and "0.5"; b) "0.75", "1" and "1.25". Component numbers are shown on the plot. $\alpha = 30^o$, $k = 0.25$ and $\beta = 1$.

about 13 to 17.5 percent in the course of nonlinear development.

In contrast, the relative importance of other components rapidly increases with time. All of them are negligible initially, but start to play an important role in the radiation at later times, after $t = 56$ (fig.5.18). As a result, the energetically significant part of spectrum is broad in the described numerical experiment. By the time $t = 96$, component "0" gives 5 percent and component "0.5" gives 8 percent.

Short waves are very significant energetically (see section 5.1.1). Their wavenumbers correspond to large growth rates in the linear problem (see Fig.5.9). The secondary harmonics that are created by the nonlinear interactions can in turn cause the growth of unstable linear modes for the same wavenumbers because of the round-off error in the numerical method. The anticipated process is similar to the excitation of Mode 2 in the preceding section and can explain the widening of the spectrum in the case being described.

The secondary harmonic "1.25" contributes almost as much as the primary component "0.25" to the value of the external energy. Component "0.75" which is excited by the secondary interactions between components "0.25" and "0.5" quickly overcome the latter in terms of corresponding energy in the external region. Its external portion of energy is almost 14 percent of the K_e by the end of the numerical experiment. As we have discussed before in section 5.3, these short waves correspond to more realistic spatial scales. It is therefore especially important that they also possess large amounts of energy.

One should expect the structure of the radiating response to become more complex in the course of development with larger number of short waves forming. One fact that will hold true is the remarkably energetic radiation. If we add individual contributions of each the component presented in the plot together we get almost 70 percent by $t = 96$! (compare to less than 40 percent for $k = 1$).

The vigorous radiation observed in the numerical experiment initialized by the long wave is clearly a result of the change in the dynamical nature of the solution caused by the nonzonality of the mean current. In general, the long part of the spectrum is favored by the radiation of nonzonal currents although energetic shorter and radiating waves also develop in the course of nonlinear interactions.

5.4.3 Dependence on β.

We have observed that the nonzonality of the mean current and the resulting presence of the downstream component β_1 of the planetary vorticity gradient have a large effect on the radiating properties in the problem. Large β_1 (see sections 5.4.1-5.4.2) results in the energetic radiation even for initially trapped short waves of Mode 1 ($k = 1$, for example). The ability to radiate energy to the regions remote from the jet itself is further enhanced if long waves are considered ($k = .25$). We recall from section 3.1, that the x-component of the planetary vorticity gradient has especially large influence on long waves.

The value of $\beta_1 = \beta sin\alpha$ in our model is controlled by both the nondimensional planetary vorticity gradient $\beta = L_{jet}^2/U$ and the horizontal tilt α. We need to consider the influence of each of the parameters individually on the radiating properties in the model.

We have already studied the case in which β is relatively large, but the tilt is small: $\alpha = 5^o, \beta = 1$ in section 5.3. A slightly nonzonal, strong and narrow jet was therefore considered in the experiment and planetary vorticity gradient had small downstream component: $\beta_1 = 0.087$. The comparison with the experiment for $\alpha = 30^o$ and the same β (section 5.4.1) reveals the enforcing effect that larger tilt has on the radiation. But does the tilt by itself or, rather the related increase in β_1 enhance the radiation in the latter case? The question is especially important because the magnitude of forcing needed for balancing the basic flow $\beta_1\bar{u}$ is directly proportional to the value of β_1.

In addition, the task of determining the oceanographically realistic value of the nondimensional planetary vorticity gradient $\beta L_{jet}^2/U$ in our simplified model is not trivial. One reason is that it is not easy to derive the realistic value for the spatial scale L_{jet} from the observations of Gulf Stream. Reader is referred to Chapter 7 for a complete discussion. At this point, we can mention that it is important to study the range of the values of β.

How sensitive are the radiating properties to the value of β?

It is possible to try to answer these questions by doing the numerical experiment with smaller β. We are going to keep β_1 as small as in the case $\beta = 1$, $\alpha = 5^o$, but make α as large as in the case $\alpha = 30^o$, $\beta = 1$. For the next numerical experiment we consider smaller value of the planetary vorticity gradient, $\beta = 0.25$ for $k = 1$, $\alpha = 30^o$. The corresponding growth rate of the linear solution is .146 which is roughly equal to that for $\beta = 1$. The downstream component β_1 is small and equals 0.125 making the comparison with the case $\beta = 1, \alpha = 5^o$ meaningful. If β_1 governs the process of radiation, the two cases will be very similar in radiating properties.

The Fourier coefficients Φ_0, Φ_1 and Φ_2 are presented in Fig.5.19. The difference with the results for larger β (see Fig.5.13) is apparent.

The x-independent component of the solution reaches finite amplitudes by $t = 48$ and start to radiate very long waves to the left from the current. By the end of the numerical experiment, the component reaches very large amplitudes. In fact, the component is much larger in amplitude than others. The change in the downstream-averaged field is much larger than in the case of larger β. The planetary vorticity gradient acts as a restoring force for Rossby wave oscillations, therefore a smaller beta destabilizes the jet even further leading to the large changes in the x-averaged momentum over the whole domain.

Despite the absence of the corresponding v-velocity, the kinetic energy of component "0" at $t = 96$ is larger than of component "1" (Fig.5.20a). Unlike all cases considered before (see in particular Fig.5.14b and Fig.5.8), the radiating response is dominated energetically by the x-independent component of the solution. Nearly 40 percent of the total perturbation energy is radiated by this component; one can compare this number to 10 percent for $\beta = 1$ (Fig.5.14b) in which case the radiation is also very strong.

Component "1" is mainly confined to the region from -2 to 2 until $t = 56$ which can be seen in both Fig.5.19 and Fig.5.20. After that, the component slowly extends in the y-direction especially to the right from the jet (Fig.5.19). However, even at $t = 104$ signif-

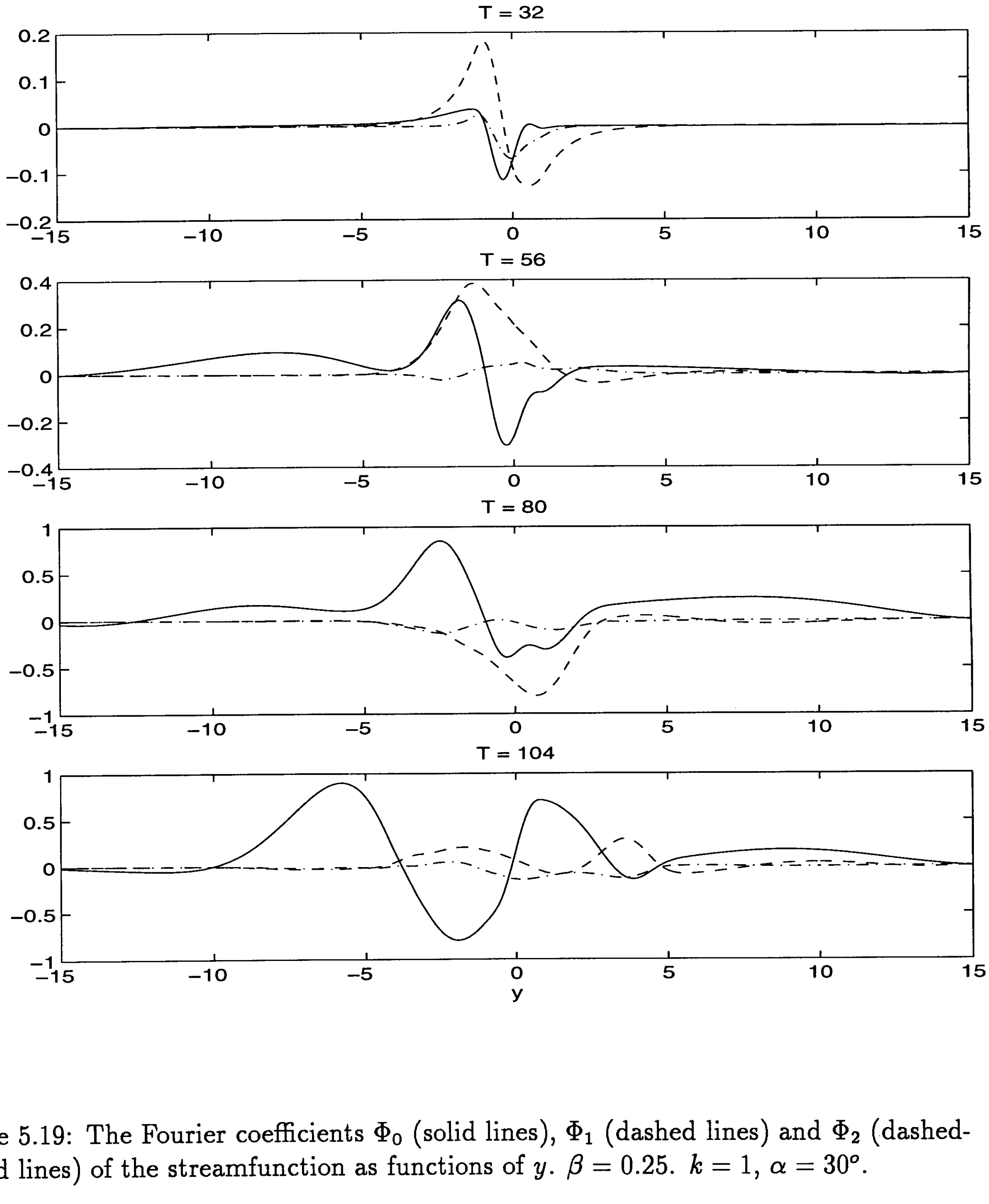

Figure 5.19: The Fourier coefficients Φ_0 (solid lines), Φ_1 (dashed lines) and Φ_2 (dashed-dotted lines) of the streamfunction as functions of y. $\beta = 0.25$. $k = 1$, $\alpha = 30^\circ$.

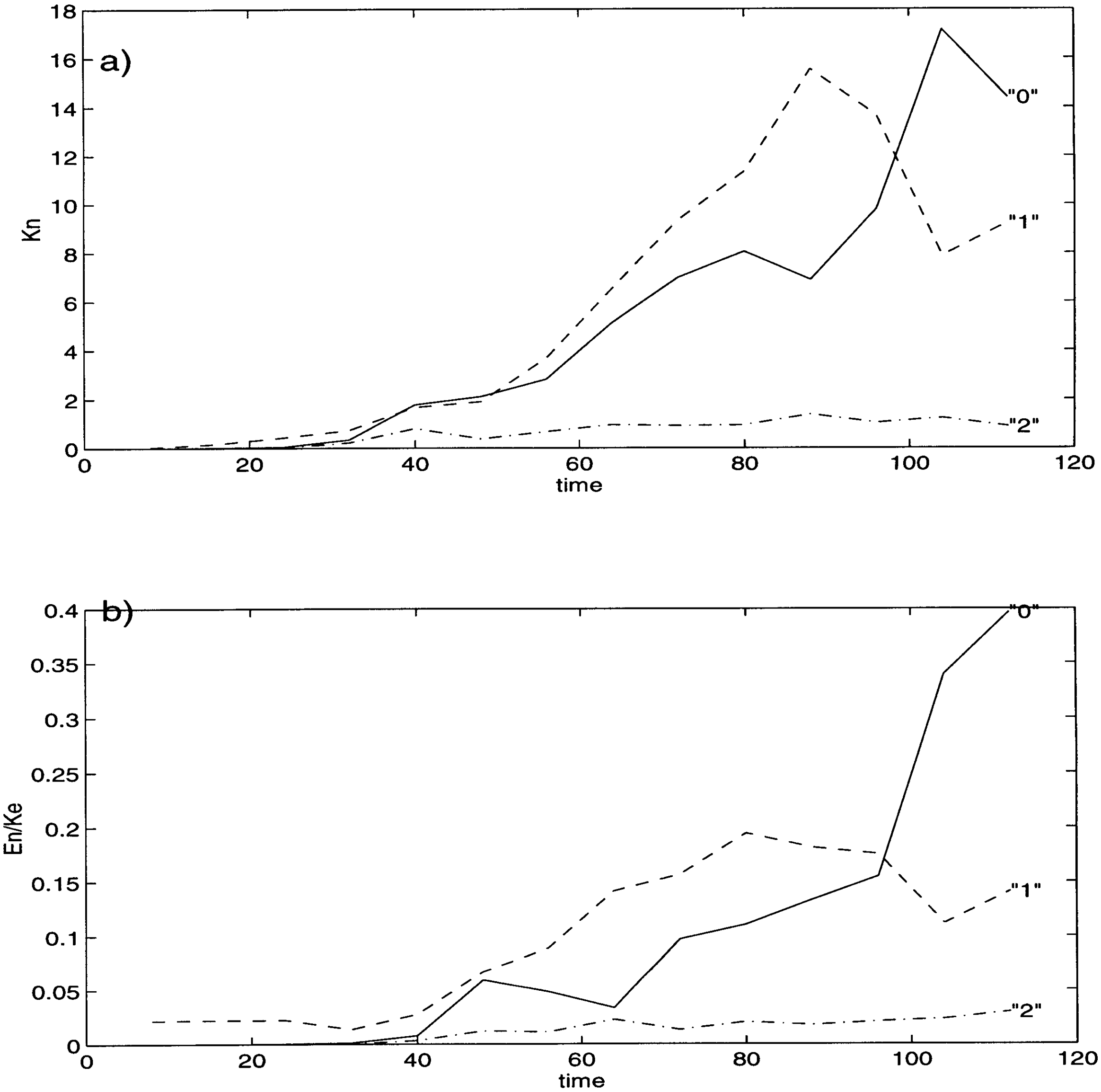

Figure 5.20: As in the Fig.5.4 but for $\beta = 0.25$, $\alpha = 30^o$ and $k = 1$.

icant amplitudes of the streamfunction are only observed in the interval $[-5\ 5]$ (Fig.5.19). The amplitudes are still smaller than those of component "0" of the streamfunction.

This slow spreading of the component is different from the vigorous radiation of waves observed, for example, in section 5.4.2. The rate of spreading is in fact on the order of magnitude of the group velocity of the linear solution, which is about .12 in both directions.

Nevertheless, we observe the transfer of energy from the jet to the regions that are five times further from the jet axis than the edge of the jet. The kinetic energy of component "1" is largely due to the big gradients of the streamfunction and larger resulting velocities. Although by the end of the numerical experiment the radiation by component "1" is less energetic than the radiation by component "0", the corresponding external energy E_1 is still approximately 15 percent of K_e. The number is only slightly smaller than that for the case $\beta = 1$, $\alpha = 30^o$ and is significantly larger than in the case of $\alpha = 5^o$ (less than 2.5 percent; see Fig.5.8).

The remarkable growth in the external part of the kinetic energy in the described case leads us to the conclusion that the main factor in setting the radiation is the nonzonal orientation of the mean current, not the downstream component of the planetary vorticity gradient β_1 and the related magnitude of the potential vorticity source in the model $\beta_1 \bar{u}$, which are both small. Small β leads to the very energetic development of x-averaged component, but slows the radiation of the component "1".

5.5 Mode 2

We have already observed in section 5.2 that the emergence of the very unstable Mode 2 in the course of nonlinear development of Mode 1 leads to the weak radiation by the latter. What are the radiating properties of Mode 2 alone?

The mode is strongly trapped in the linear problem if the jet is zonal. The radiating properties in the problem change significantly if the horizontal tilt of the jet is made nonzero. As we have observed in sections 3.2.2 and 3.2.3, the phase speed of long waves of Mode 2 satisfies the phase speed condition and the solution is non-trapped. However, the amplitude of the wave-like response of this mode in the exterior is small compared to the amplitude in the interior and the radiation is not very energetic. What happens in the nonlinear regime?

In the numerical experiment not presented here, no radiation is found in the case of a zonal jet for $k = 2$. The solution remains trapped to the jet throughout the whole nonlinear development (the problem is integrated until $t = 96$). It is, therefore, the interaction with shorter wave of Mode 1 that produced weak radiation in the section 5.2.

The next step is to make the mean current nonzonal and observe changes in the radiating properties of the solution. For this purpose, we initialize the model with Mode 2 for $k = 1.8$, $\beta = 1$, $\alpha = 30$. The wave evolves very rapidly because of the very fast initial growth; the growth rate is more than twice as large as that of Mode 1 for $k = 1$ (see Fig.5.9). As one can see from the plot of kinetic energy in the Fig.5.21, the nonlinear effects are important as early as at $t = 8$. The equilibration begins at $t = 12$ and the growth slows significantly at later times. The problem is integrated until $t = 52$.

We now turn our attention to the Fourier coefficients of the solution (see Fig.5.22). In the way typical of the nonlinear development of in our model, the radiation starts in the form of the x-independent component of the solution at $t = 24$ and occurs for negative y. We note, that the beginning of the radiation is earlier than for the Mode 1, because of the faster development of the linear solution. The beginning of the nonlinear equilibration is once again the beginning of the radiative phase in the development.

Component "1.8" dominates the development (Fig.5.23a). Unlike Mode 1, the nonlinear development of Mode 2 does not result in the excitation of the shorter, very unstable linear waves; the linear problem is stable for k larger than 3.2 (Fig.5.9).

The x-dependence of the radiating response develops for $t > 36$, when components "1.8" and "3.6" start to radiate. However, the radiating response formed by component "1.8" decays in space away from the jet region. The radiation still reaches as far as

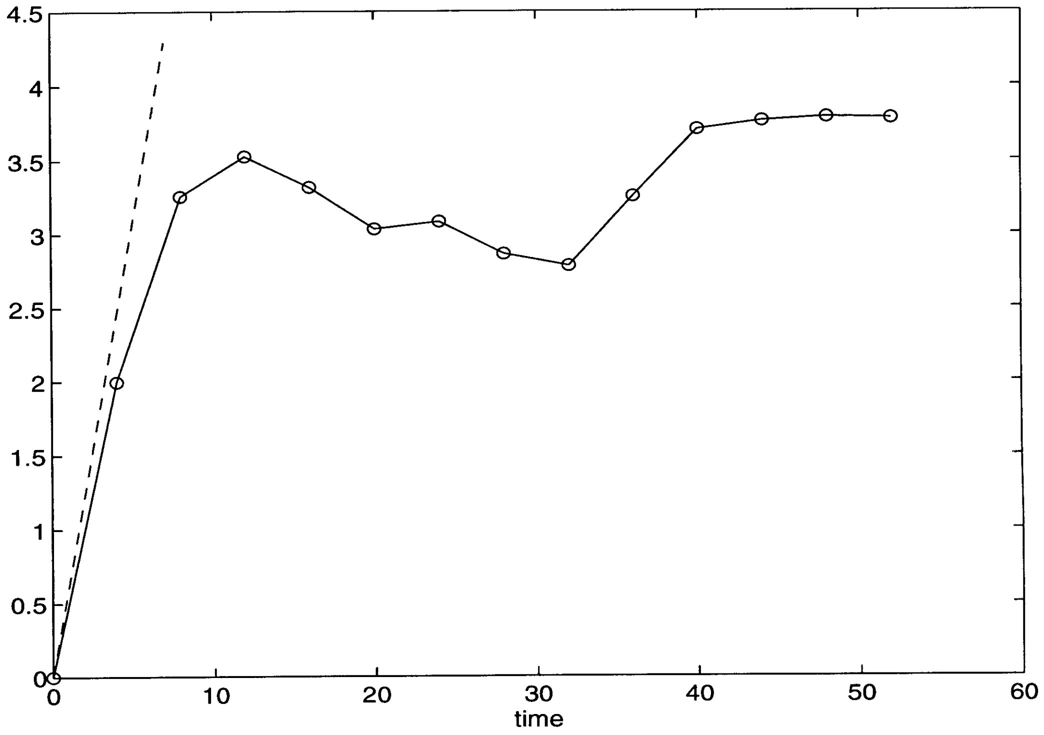

Figure 5.21: Logarithm of the perturbation kinetic energy. As in Fig.5.10 but for Mode 2. $k = 1.8$, $\beta = 1$ and $\alpha = 30^o$.

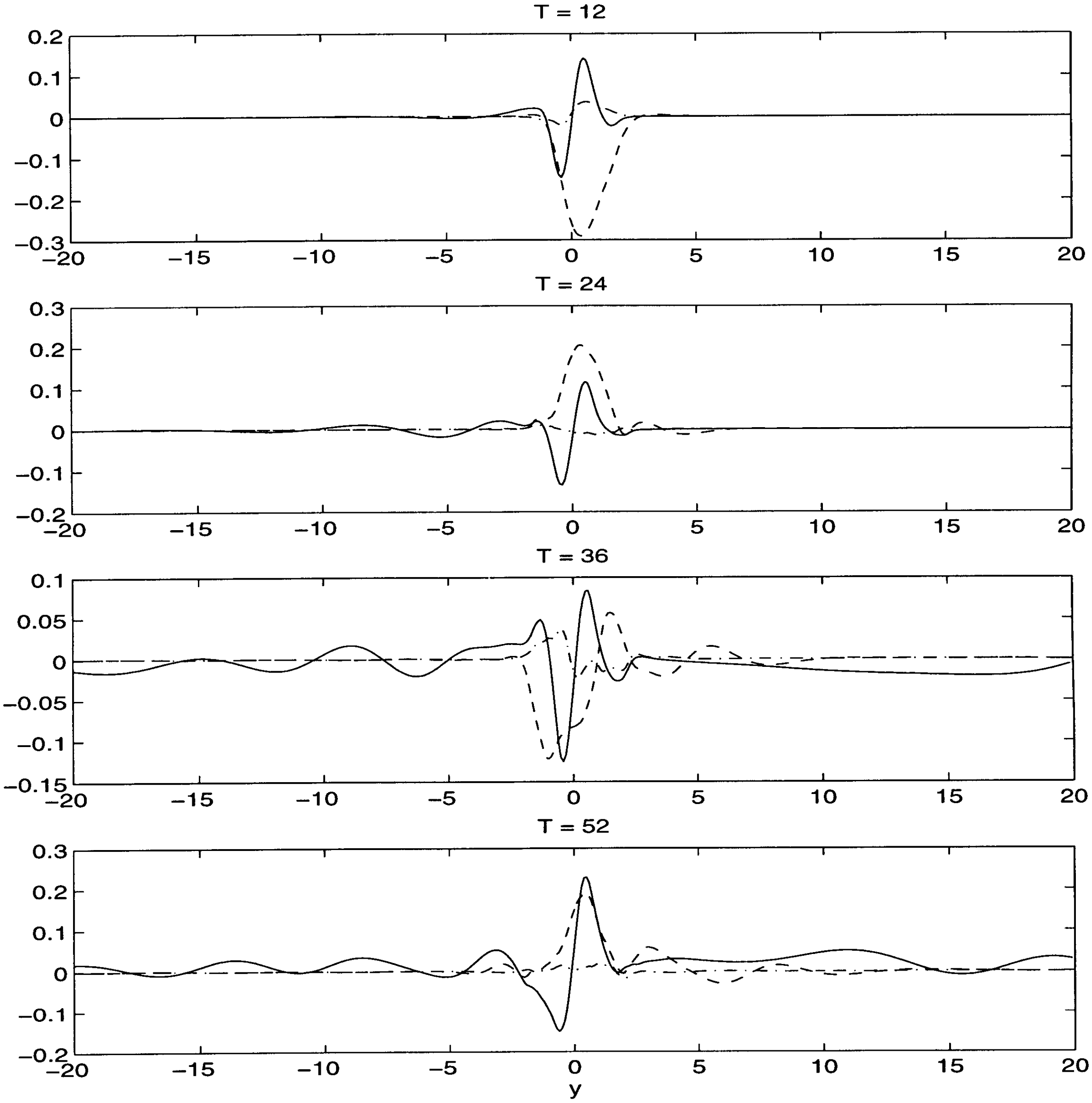

Figure 5.22: The Fourier coefficients Φ_0 (solid lines), $\Phi_{1.8}$ (dashed lines) and $\Phi_{3.6}$ (dashed-dotted lines) of the streamfunction as functions of y. Corresponding times are given on the top of each panel. Mode 2, $\alpha = 30^o$, $k = 1.8$ and $\beta = 1$

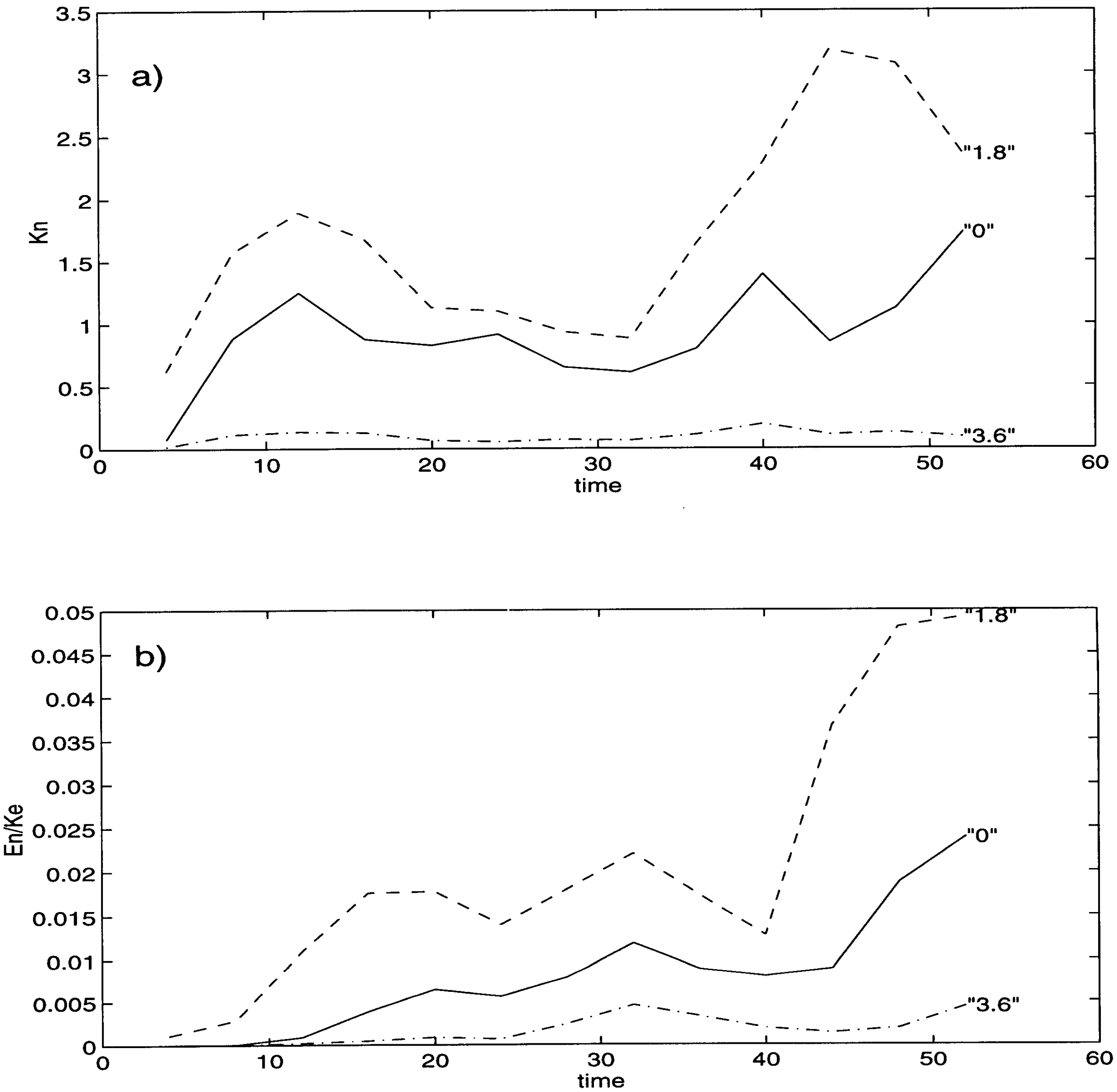

Figure 5.23: As in the Fig.5.8 but for Mode 2. $\alpha = 30^o$, $k = 1.8$ and $\beta = 1$.

$y = -5$ and $y = 10$ for negative and positive y correspondently by $t = 52$, but the amplitudes are much smaller than those for Mode 1.

The energy $K_{1.8}$ of component "1.8" that is contained in both the external regions is about 5 percent of the perturbation kinetic energy K_e. Large gradients of the streamfunction compensate the smallness of its amplitude in the value of corresponding energy. We have observed the similar situation in the linear problem as well (see the discussion of the y-structure of the eigenfunctions in section 3.2.3). Component "3.6" contributes very little (less than 0.5 percent).

One can recall from the linear problem, that even long waves of Mode 2 are weakly radiating. Despite the absence of spatial trapping of the solution at the LWC, the process of radiation is significantly less energetic than that for the long waves of Mode 1. As we have just observed, nonlinear effects do not significantly change the radiating properties of Mode 2; radiation is weak. The difference with the longer nonlinear waves of Mode 1, which radiate a significant portion of kinetic energy into the external regions, is apparent.

5.6 Summary

We have discussed a series of numerical experiments in which the nonlinear development of a single wave was considered. In the course of the nonlinear development, a number of additional modes are excited and the structure of the solution becomes more complex.

The excitation of the very unstable Mode 2 in the course of nonlinear development of Mode 1 causes weak radiation by the latter in the case of a zonal jet. The transient radiation reported in this case is very closely related to the radiation by pulsating meanders discovered in a series of zonal boundary forced models (Malanotte-Rizzoli *et al.*, 1987a; Hogg, 1988; Malanotte-Rizzoli *et al.*, 1995). In these studies, it is demonstrated that the growth and decay periods in the life-cycle of meanders are essential for the mechanism discovered. In our case, the radiation in the form of component "1" starts at an advanced stage of nonlinear development, when component "1" starts to decay in amplitude. The decay follows the period during which the component remains trapped to the jet region and has a large amplitude, therefore representing meanders of the jet with nondimensional wavelength 2π. Thus, the slow decay of these meanders can produce radiation in according with the mechanism described in (Malanotte-Rizzoli *et al.*, 1987a; Hogg, 1988; Malanotte-Rizzoli *et al.*, 1995). The mechanism, however, is not very effective in our case. The radiation is very weak in part as a result of the smallness of component "1" in the jet region.

The situation changes if the mean current is nonzonal. We mostly consider waves that are rather short in x ($k = 1$); they grow fast and are strongly trapped according to the linear theory. However, the solution becomes radiating during the nonlinear development even if the tilt is very small. For $\alpha = 5^o$, the radiation starts when initially fast exponential growth significantly slows. The corresponding radiating response is much more energetic than that in the case of the zonal current. The trapping of a linear solution is most likely caused by the fast initial growth as discussed in section 2.3.

The observed radiation by a nonzonal current is caused by the reduction in the disturbance growth, which happens during the equilibration of solutions. On the other hand, the radiation does not seem to cause the equilibration in the model, since the latter also occurs in the case of a zonal current, in which case no energetically significant radiation is found.

The radiating properties are further enhanced by the larger horizontal tilt. For $\alpha = 30^o$, the radiation is very energetic for $k = 1$. The process starts with the radiation of x-independent component of the solution and is then immediately followed by the x-dependent harmonics. The latter usually correspond to the large values of the kinetic energy that is being transferred from the mean current into the far-field. The radiating response in the exterior is initially in agreement with the phase speed condition of the linear theory while the amplitudes are still small.

The radiation is especially remarkable when longer waves are considered. For $k = 0.25$, the broad spectrum of vigorously radiating waves is excited, eventually transporting more than 70 percent of the total perturbation energy into the far-field. The radiation starts very quickly largely because of the small initial growth rate and resulting weak trapping of the linear solution.

The most unstable mode in the problem is Mode 2 that is characterized by smaller x-wavenumbers. The long linear waves of this mode are weakly radiating and the nonlinear effects do not significantly change the radiating properties of the entire mode. For $k = 1.8$, the radiation is weaker than in the case with Mode 1 for $k = 1$.

For fixed both the orientation and strength of the current (expressed in terms of α and β), the radiative properties are mainly controlled by the relative importance of the downstream component of the planetary vorticity gradient, $\beta_1 = \beta sin\alpha$. The effects of the term are the largest for longer waves, therefore it is not surprising that short waves are usually less radiating; compare cases $k = 1$ and $k = 0.25$ for Mode 1 and Mode 1 for $k = 1$ and Mode 2 for $k = 1.8$.

However, it is not always accurate to call short waves weakly radiating since they are usually more energetic than longer waves. The corresponding pressure field is typically smaller in amplitude than that for longer waves but has larger gradients. That results in large geostrophic velocities and often makes the radiation more energetically significant.

The effects of smaller β are also studied in detail. For $\beta = 0.25$, the downstream component of planetary vorticity gradient β_1 is as small as in the case of larger β but smaller tilt ($\beta = 1$ and $\alpha = 5^o$). The radiation, however, is significantly stronger. We can conclude that the nonzonal orientation of the current is the main factor controlling the effectiveness of the mechanism for radiation.

We recall that the forcing, that acts as a vorticity source necessary to balance the mean field, is proportional to β_1 (section 2.1). The fact that radiation is strong despite the smallness of β_1 demonstrates that the radiation is not directly related to the forcing itself, but is rather caused by the nonzonal orientation of the mean current. The role of forcing is limited to sustaining the nonzonal current.

It is also interesting that the external part of perturbation energy for $\beta = 0.25$ is even larger than in the case of $\beta = 1$ and $\alpha = 30^o$; the component "0" reaches especially large amplitudes. The planetary vorticity gradient normally acts as the restoring force stabilizing the Rossby waves. Smaller values of β therefore further destabilize the problem which results in the large amplitudes of unstable solutions.

We have considered only the nonlinear development in the problem initialized with a single Fourier mode. In the more general case in which initial conditions consist of a set of linear waves, the short waves that typically grow faster initially can eventually dominate the development in the region of the jet. The longer nonlinear waves that are more radiating can be either suppressed by those trapped short waves and not produce radiation or they can continue radiation dominating the far-field. In any case, the dynamical properties of both types of modes should change. These changes will be studied in the following chapter.

Chapter 6

Nonlinear interactions between waves

In the preceding chapter, we have considered the nonlinear development of a single linear wave. Although that study provides us with important information about the nonlinear evolution in the model, the single wave development cannot completely describe the dynamics in the model. Realistic initial conditions generally contain the whole spectrum of Fourier modes and the nonlinear results strongly depend on its particular form.

It is impossible to consider all possible combinations of linear solutions, but we can greatly simplify the task and study the effects that two initially excited modes have on each other. The interactions between those waves will alter the dynamical properties of each of them. Considering those changes, we can deduce important information about the effects of nonlinear interactions between waves in an arbitrary set of linear modes.

We are mainly interested in the radiating properties in the problem and we have observed that those properties differ between waves that are long in x and waves that are short in x. Shorter waves are generally less radiative than long ones largely because long waves are more influenced by the downstream component of the planetary vorticity gradient. As we recall, the component is a key factor in the mechanism for nonlinear radiation discovered in the preceding chapter. However short, strongly trapped linear waves have larger growth rates and have a potential to eventually dominate the dynamical picture. Nevertheless, their properties will be affected by the development of of longer more radiating waves. It is therefore especially interesting to consider nonlinear interactions between a long and a short wave and study the changes in the resulting radiation.

In this chapter, we initialize the problem with a sum of two primary waves with x-wavenumbers k_1 and k_2. As in the case of single wave, a set of secondary harmonics is generated: components "0", "$k_1 + k_2$", "$k_2 - k_1$", "$2k_1$", "$2k_2$" and so forth. Both primary modes can directly influence each other through these harmonics if $2k_1 = k_2$, in which case the interactions are the strongest. Two waves can also interact indirectly if $2k_1 \neq k_2$ and neither of secondary harmonics can directly affect both primary modes.

We will study three types of interactions that occur in the development of a set of primary modes. By doing that, we do not pretend to obtain the complete dynamical picture. Rather, we hope to illustrate on these simple examples the processes going on in the nonlinear development of more complicated initial conditions.

Both direct and indirect interactions will be modeled on the example of the evolution of strongly radiating Mode 1 and weakly radiating Mode 2 in section 6.1. The interactions between a long wave and a short wave of Mode 1, that both are strongly radiating will be analyzed in section 6.2.

The individual evolutions of all waves which interactions are considered in the numerical experiments in this chapter were studied in the preceding Chapter 5. The comparison of the results between two chapters should help to understand the effects of the joint evolution of linear waves on their individual radiating properties.

6.1 Mode 1 and Mode 2

As we observed in Chapter 5, the nonlinear evolution of Mode 1 leads to the excitation of the more unstable Mode 2. The latter is generated because of the presence of the round-off error in the numerical method and it usually emerges at a late stage of the development. Its role varies from dominant in the cases with $\alpha = 0$ and $\alpha = 5^o$, to secondary in the case of $\alpha = 30^o$. Very energetic radiation was reported in the case of a large horizontal tilt in the mean current ($\alpha = 30^o$). In that case, Mode 1 prevails during the nonlinear development and radiating properties in such cases are studied in detail (section 5.4.1).

In contrast, the evolution of the single Mode 2 results in the radiation which is much weaker than in the numerical experiment with a single Mode 1 (chapter 5.5). However, as we recall from the linear problem, Mode 2 is generally more unstable than Mode 1 (Fig.5.9). Mode 2 is, therefore, likely to eventually prevail, if a pair of waves corresponding to both Mode 1 and Mode 2 with initially similar amplitudes is considered. It is therefore interesting to study such a case in which, unlike the case with a single Mode 1, both modes are equally important from the start. Both the waves are going to evolve differently than if they developed separately. What are the changes in their radiating properties that can be attributed to the interactions between them?

Our task in this section is to consider the mutual development of Mode 1 and Mode 2. We choose their initial amplitudes in such a way to make both waves similar in size during the course of nonlinear development. We consider two cases: Case 1 in which we take Mode 1 with $k = 1$ and Mode 2 with $k = 2$, and Case 2 with Mode 1 with $k = 1$ and Mode 2 with $k = 1.5$. The interactions between waves are the strongest in Case 1, where the waves interact directly. In all cases $\alpha = 30^o$ and $\beta = 1$.

6.1.1 Case 1. Direct interactions.

In this numerical experiment we put the sum of Mode 1 with $k = 1$ and Mode 2 with $k = 2$ as initial conditions. We make the initial amplitude of a latter wave 2.4 smaller than that of Mode 1. If both waves were growing exactly proportionally to e^{kc_it}, Mode 2 would be 3 times as large as Mode 1 by the time $t = 12$. The nonlinear effects, however, slow the growth of both modes and make them similar in size during the whole development.

Both modes are going to strongly feel the presence of each other. Indeed, the secondary harmonic produced by self-interactions of Mode 1 has the wavenumber that equals 2; at the same time Mode 1 interacts with Mode 2 and creates a harmonic with $k = 1$. Both the harmonics add to the primary modes and can significantly change the energy partition between different wavelengths.

As we recall from section 5.2, the secondary harmonic of nearly antisymmetric Mode 1 is antisymmetric as well. In contrast, Mode 2 with $k = 2$ is almost symmetric and this difference in structure makes it possible to determine how strongly Mode 2 is modified by the secondary harmonic of Mode 1.

We first present the 2D contour plots of the total streamfunction $\bar{\Psi}(y) + \psi(x, y)$ (Fig.6.1). The solution remains trapped until $t = 24$ when radiation in the x-independent form starts for negative y. Individual eddies are formed later in both the external regions. The dominant x-wavenumber of these eddies is $k = 1$, since two identical eddies are observed in the x-direction ($2 \times 2\pi/12.57 = 1$). The eddies are elongated in the east-west direction to the north of the jet axis and are nearly parallel to the jet axis to the south from the jet similar to the case with a single Mode 1 (section 5.4.1, Fig.5.11).

In contrast, the meanders, that are trapped to the basic flow axis have a different structure than in the case with a single Mode 1. In particular, the meanders with the wavenumber $k = 2$ are clearly very important (see Fig.6.1 at $t = 40$).

To study the structure of the solution in greater detail, we now consider the plots of Fourier coefficients Φ_0, Φ_1 and Φ_2 shown in Fig.6.2. Component "0" follows a familiar path of development and radiates first for negative y and then for the other half-plane. The amplitudes of the radiating part are larger than in the case with a single Mode 2 (Fig.5.22), because the self-interactions of a primary component "1" produce a significant portion of the x-independent component of the streamfunction.

The evolution of x-dependent components "1" and "2" deserves further attention. Initially, components "1" and "2" are easily recognized as almost antisymmetric Mode 1 and symmetric Mode 2. Both the components are significantly modified later by nonlinear

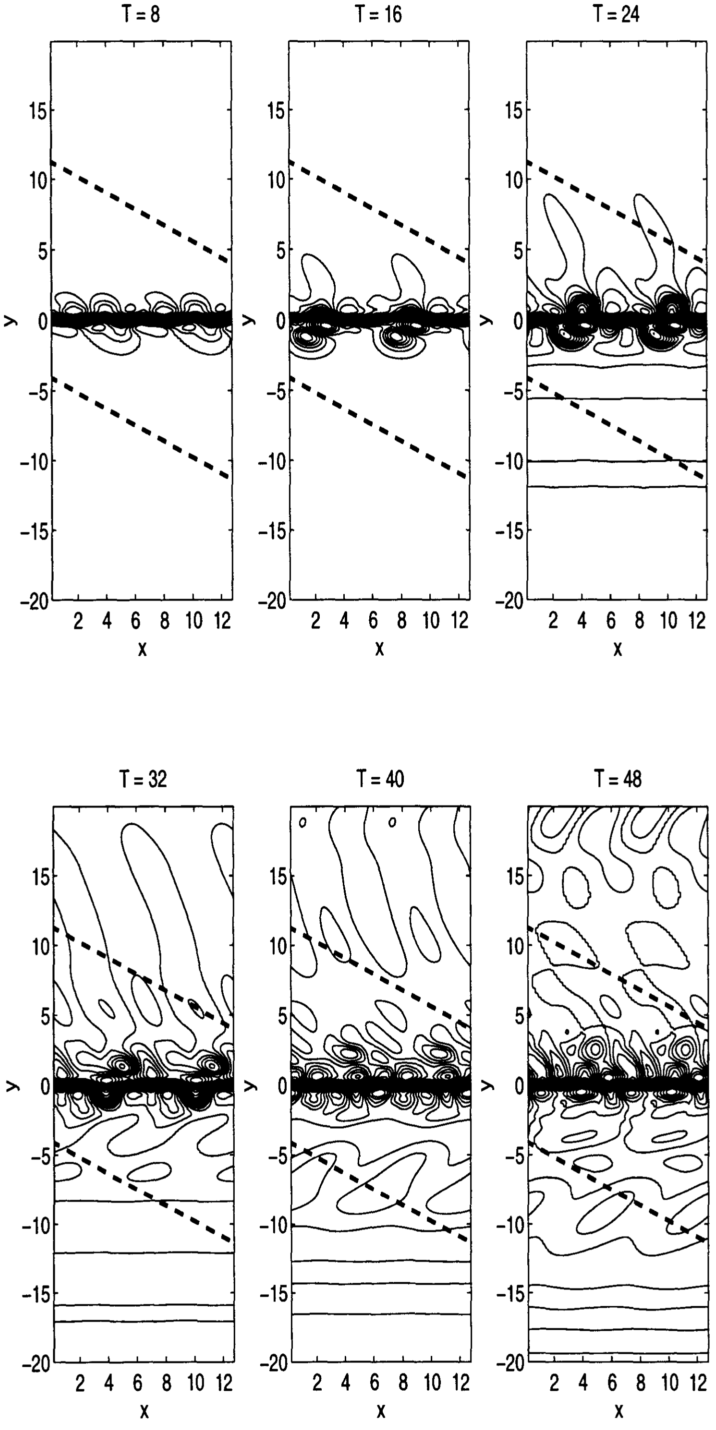

Figure 6.1: Two-dimensional contour plots of the total streamfunction $\bar{\Psi}(y) + \psi(x,y)$. As in Fig.5.11 but for Case 1: Mode 1 ($k = 1$) and Mode 2 ($k = 2$). $\alpha = 30^o$ and $\beta = 1$.

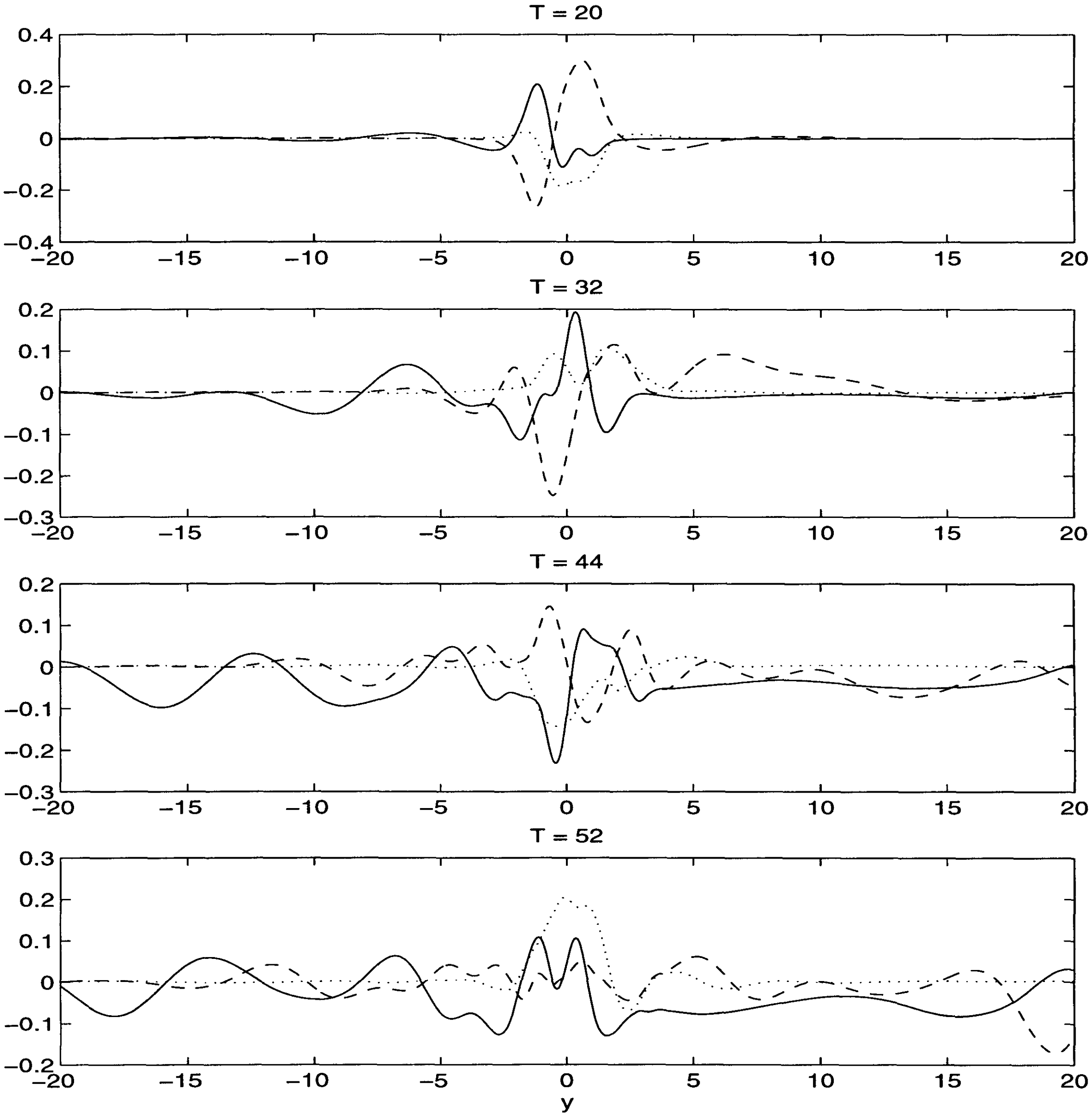

Figure 6.2: The Fourier coefficients Φ_0 (solid lines), Φ_1 (dashed lines) and Φ_2 (dotted lines) of the streamfunction as functions of y. Corresponding times are given on the top of each panel. Case 1: Mode 1 ($k = 1$) and Mode 2 ($k = 2$). $\alpha = 30^o$ and $\beta = 1$.

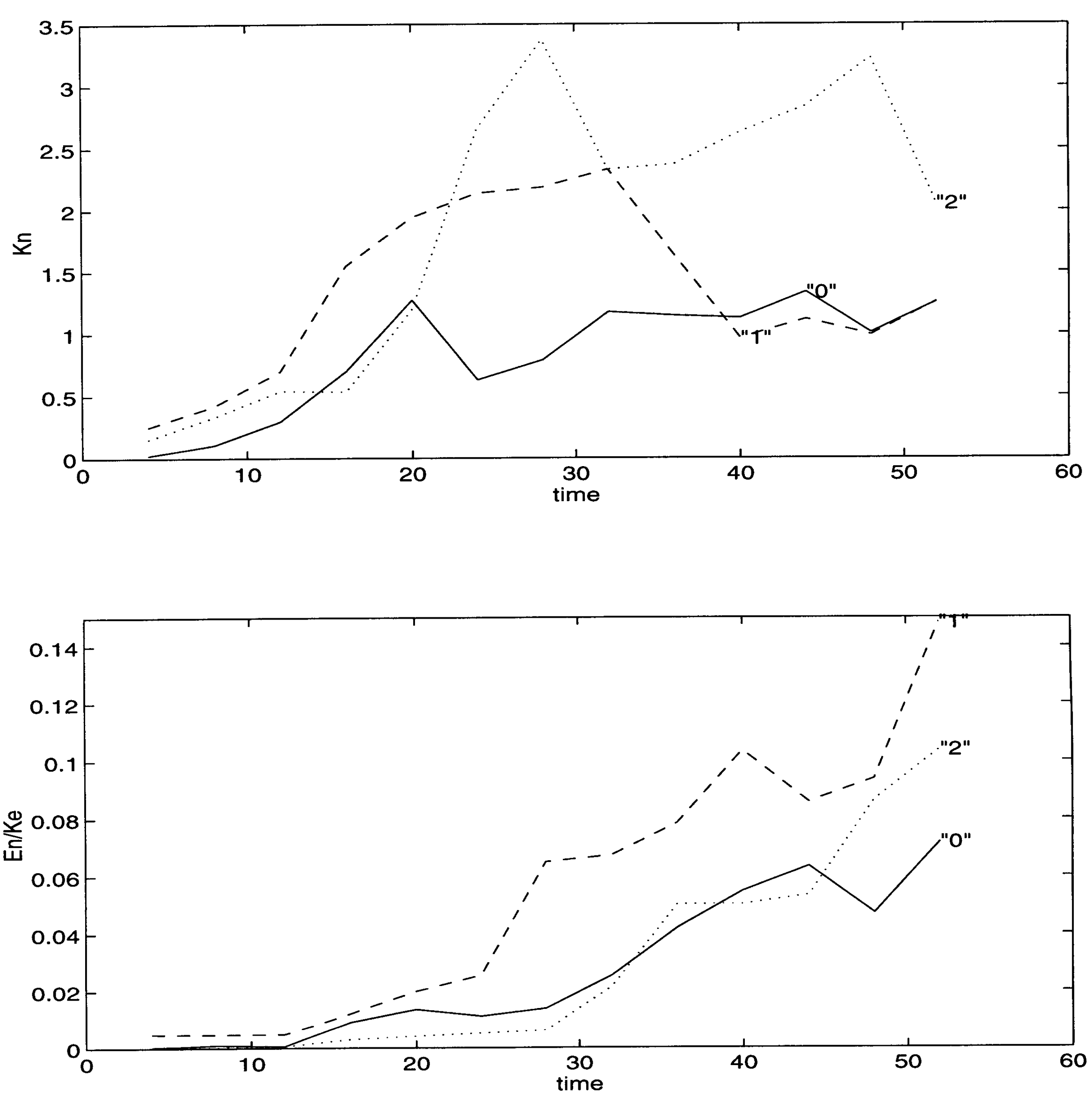

Figure 6.3: Kinetic energy corresponding to each Fourier component vs. time. a) K_{k_n} (energy integrated over the whole domain); b) E_{k_n} (energy integrated from $-\infty$ to -2 and from 2 to ∞) divided by the total energy K_e. Component numbers are shown in the plot. Case 1: Mode 1 ($k = 1$) and Mode 2 ($k = 2$). $\alpha = 30^o$ and $\beta = 1$.

interactions with each other (see for example $t = 44$).

As we remarked before, it is useful to compare the results of this section with the individual evolution of either of modes. We begin with component "1" and see that the radiation now starts much earlier than in the case with single Mode 1 ($t = 48$ in section 5.4.1). That is attributed to the fact that now Mode 1 is given 5 times larger initial amplitude. The radiation in the model typically starts at the beginning of nonlinear equilibration following the stage of the rapid exponential growth; the equilibration begins earlier if initial amplitude is larger.

During the late stage of development, the amplitude of component "1" is small compare to that in the case with a single Mode 1 ($t > 44$ in Fig.6.2 and Fig.5.13). In addition, in the energy plots (Fig.6.3a), we see that K_2 becomes larger than K_1 after $t = 32$ and K_1 further decreases after that. It is also interesting to note, that component "2" remains nearly symmetric in the immediate vicinity of the jet which points to the weak contribution of nearly antisymmetric secondary harmonic of Mode 1. We can conclude that the jet region is dominated by Mode 2 during the advanced stage of nonlinear development; see also the discussion of the 2D field (Fig.6.1) above.

In contrast, component "1" clearly dominates over component "2" in the exterior starting from $t = 32$ (see also Fig.6.1). The radiation of component "1" is very similar to that by a single Mode 1 (section 5.4.1). The amplitudes are large in both cases and the spatial scales are similar. As a result, component "1" radiates as much as almost 15 percent of K_e by the end of the described numerical experiment. The value of E_1/K_e is therefore very close to that for the case with a single Mode 1; see Fig.6.3.

The radiation by component "2" starts much later than in the case with a single Mode 2 with $k = 1.8$ ($t = 52$ compared to $t = 24$ in section 5.5). The start of radiation is delayed by development of the radiating response by component "1". The radiation is also weaker than that by component "1". Component "2" slowly extends into both the external regions, which are dominated by the longer and more radiating component "1".

Nevertheless, as much as 11 percent of K_e is transferred by component "2" into the external regions (Fig.6.3b). The number is twice as large as $E_{1.8}/K_e$ reported in section 5.5. The difference can be explained by the contribution of the secondary harmonic "2" produced by self-interactions of the radiating component "1" in Case 1. The value of E_2/K_e is also twice as big as the same quantity in the case with a single Mode 1, in which Mode 2 with $k = 2$ is excited only on the late stage of development.

The joint radiation by all components is very effective: $(E_0 + E_1 + E_2)/K_e$ is more than 35 percent. The value of the ratio is close to the same quantity in the case of a single Mode 1 (section 5.4.1).

6.1.2 Case 2. Indirect interactions.

We have observed in the previous section, that the weakly radiating Mode 2 eventually dominates the nonlinear development in the jet region, but does not prevent Mode 1 from radiation. Rather, component "1" prevails in the exterior regions; it produces a second harmonic with $k = 2$ that increases the radiation by component "2". What changes if direct mutual feedback between two primary modes are not possible?

To answer this question, we carry out a numerical experiment in which we initialize the model with Mode 1 with $k = 1$ and Mode 2 with $k = 1.5$. The self-interactions of Mode 1 produce component "2" as before but now it does not affect Mode 2. The nonlinear interactions produce secondary harmonics "0.5", "2", "2.5" and "3"; neither of them can influence component "1" directly. It is therefore interesting to compare the results in Case 2 with the results in Case 1. That will help us to understand the role of interactions between modes in the dynamics of the problem.

As in Case 1, Mode 1 is given larger initial amplitude than Mode 2. If both waves were growing exactly proportionally to e^{kc_it}, Mode 2 would be larger than Mode 1 by 3 times by the time $t = 14$.

2D contour plots of the total streamfunction $\bar{\Psi}(y) + \psi(x, y)$ (Fig.6.4) provide us with general information about the structure of the solution. As in Case 1 (Fig.6.1), the solution is asymmetric in the y-direction. Eddies to the north from the jet are oriented east-west, whereas eddies to the south ($y < 0$) are elongated in the direction of the jet axis. The differences between Case 1 and Case 2 are also obvious to a viewer. The dominant scale in the x-direction is now twice as large as in Case 1, which indicates the dominance of the component with $k = 0.5$ wavenumber (since $2\pi/12.57 = 0.5$). The trapped meanders seem to be a mixture of two components with wavenumbers $k = 1$ and $k = 0.5$.

The Fourier coefficients are shown in Fig.6.5. As in Case 1, component "0" starts its radiation for negative y after $t = 20$. The amplitude of its radiating part reaches large amplitudes at later times. We now focus on the differences in the development between components "1" and "1.5" and components "1" and "2" in Case 1.

Component "1" in Case 2 has larger amplitudes than in Case 1 especially during the late stage of development ($t > 32$), as can be seen in Fig.6.5. The difference is striking at $t = 52$. In contrast, component "1.5" remains small until $t = 36$. As in Case 1, it then slowly overcomes component "1" in terms of the amplitude in the jet region ($t = 36$). Component "1.5" then start to slowly expand into both the external regions. The switch in the relative importance between two components is clearly seen in Fig.6.6a where the corresponding kinetic energies are presented. Shortly after $t = 40$, $K_{1.5}$ becomes larger than K_1.

It is also interesting to observe the rapid growth of component "0.5" (Fig.6.5 and Fig.6.7a; see also the discussion of Fig.6.4 above). The component is produced by the interactions between two primary components "1" and "1.5". Its energy $K_{0.5}$ becomes larger than the energies of other secondary components in the plot at the same time as component "1.5" begins to dominate in the development ($t > 40$; Figs. 6.6a and 6.7a). Simultaneously, the energy of component "2" which is the result of self-interactions of component "1" decreases together with K_1 (Fig.6.6a). $K_{0.5}$ is by an order of magnitude larger than $K_{2.5}$ which is another secondary harmonic produced by the interactions between two primary modes. The longest of two secondary harmonics is clearly more energetic.

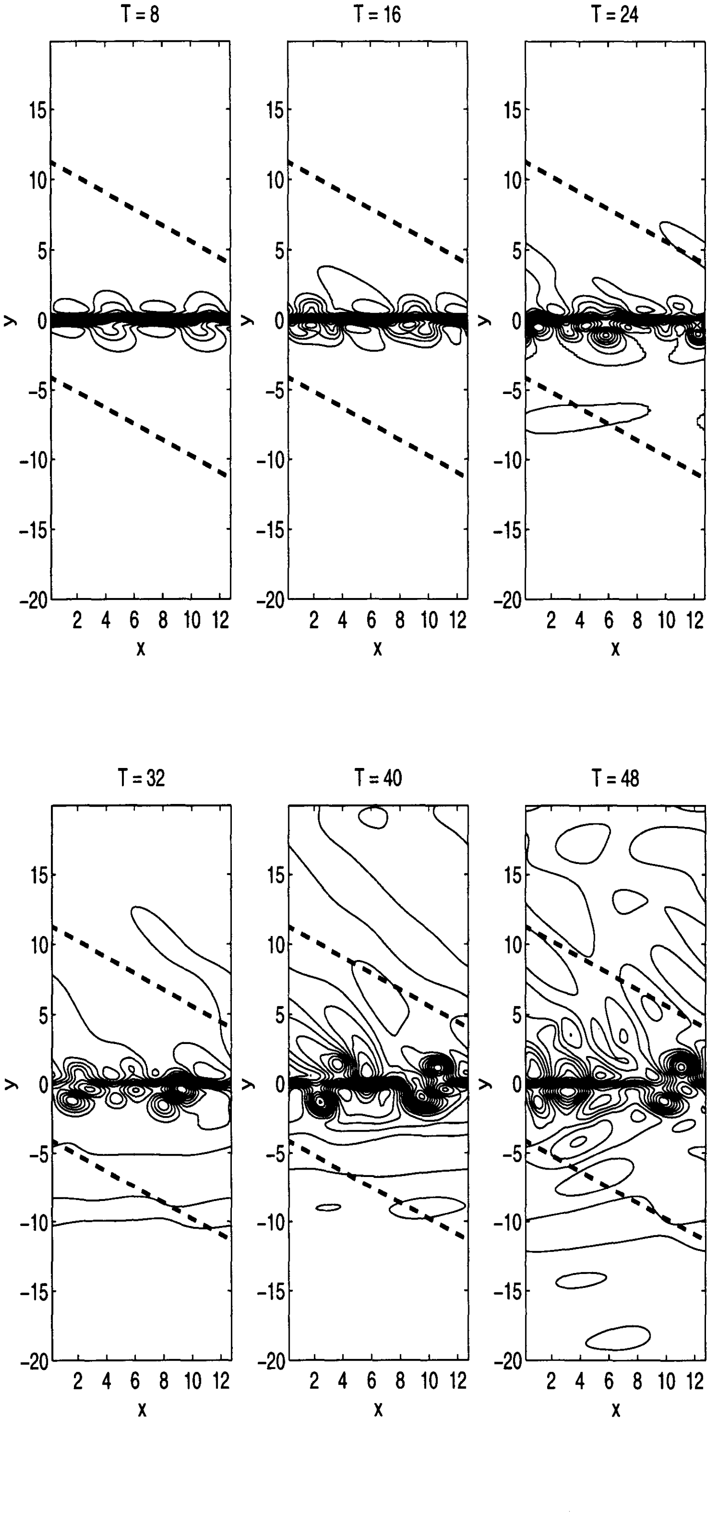

Figure 6.4: Two-dimensional contour plots of the total streamfunction $\bar{\Psi}(y) + \psi(x, y)$. As in Fig.5.11 but for Case 2: Mode 1 ($k = 1$) and Mode 2 ($k = 1.5$). $\alpha = 30^o$ and $\beta = 1$.

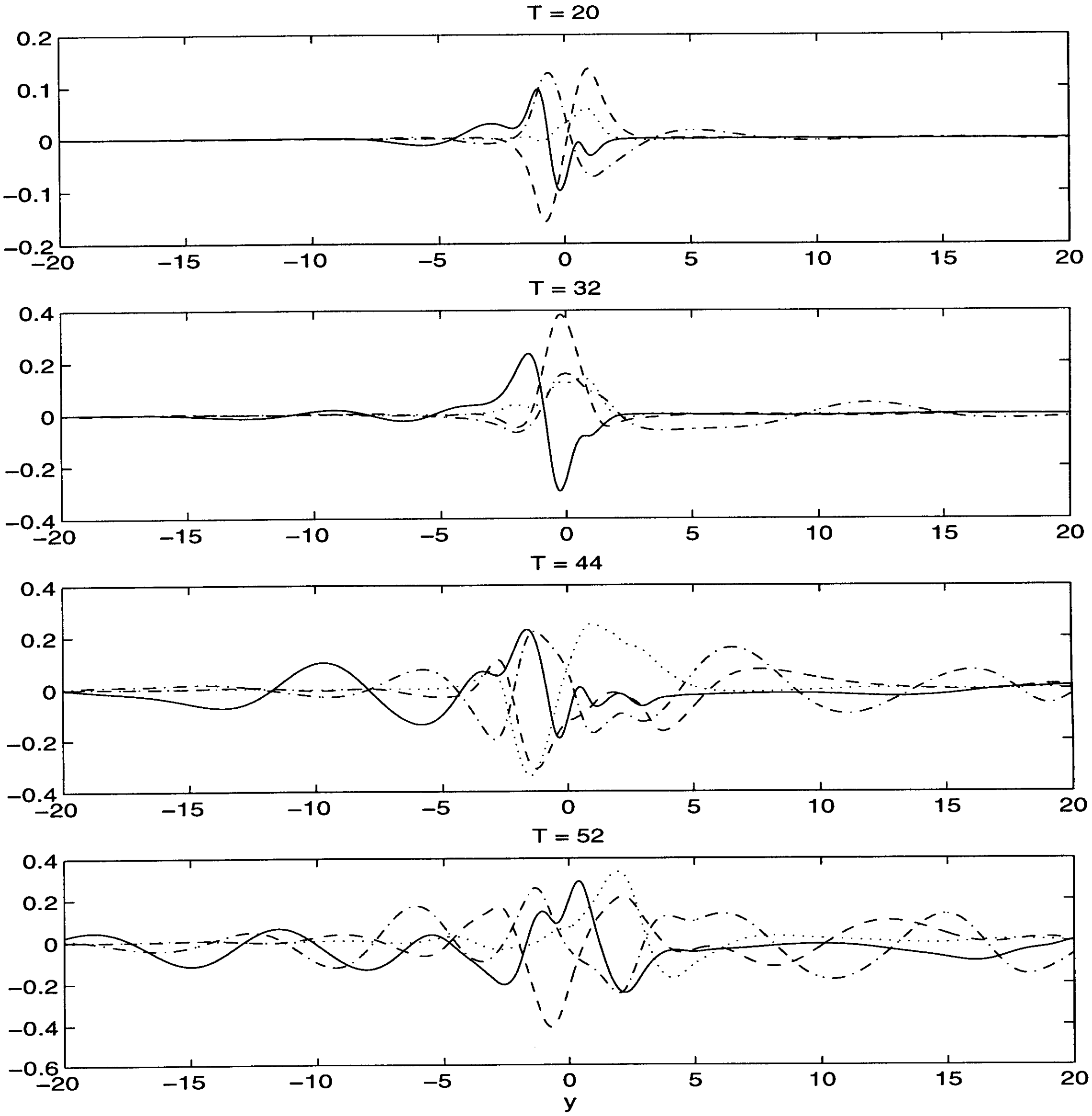

Figure 6.5: The Fourier coefficients Φ_0 (solid lines), Φ_1 (dashed lines), $\Phi_{1.5}$ (dotted lines) and $\Phi_{0.5}$ (dashed-dotted lines) of the streamfunction as functions of y. Corresponding times are given on the top of each panel. Case 2: Mode 1 ($k = 1$) and Mode 2 ($k = 1.5$). $\alpha = 30^o$ and $\beta = 1$

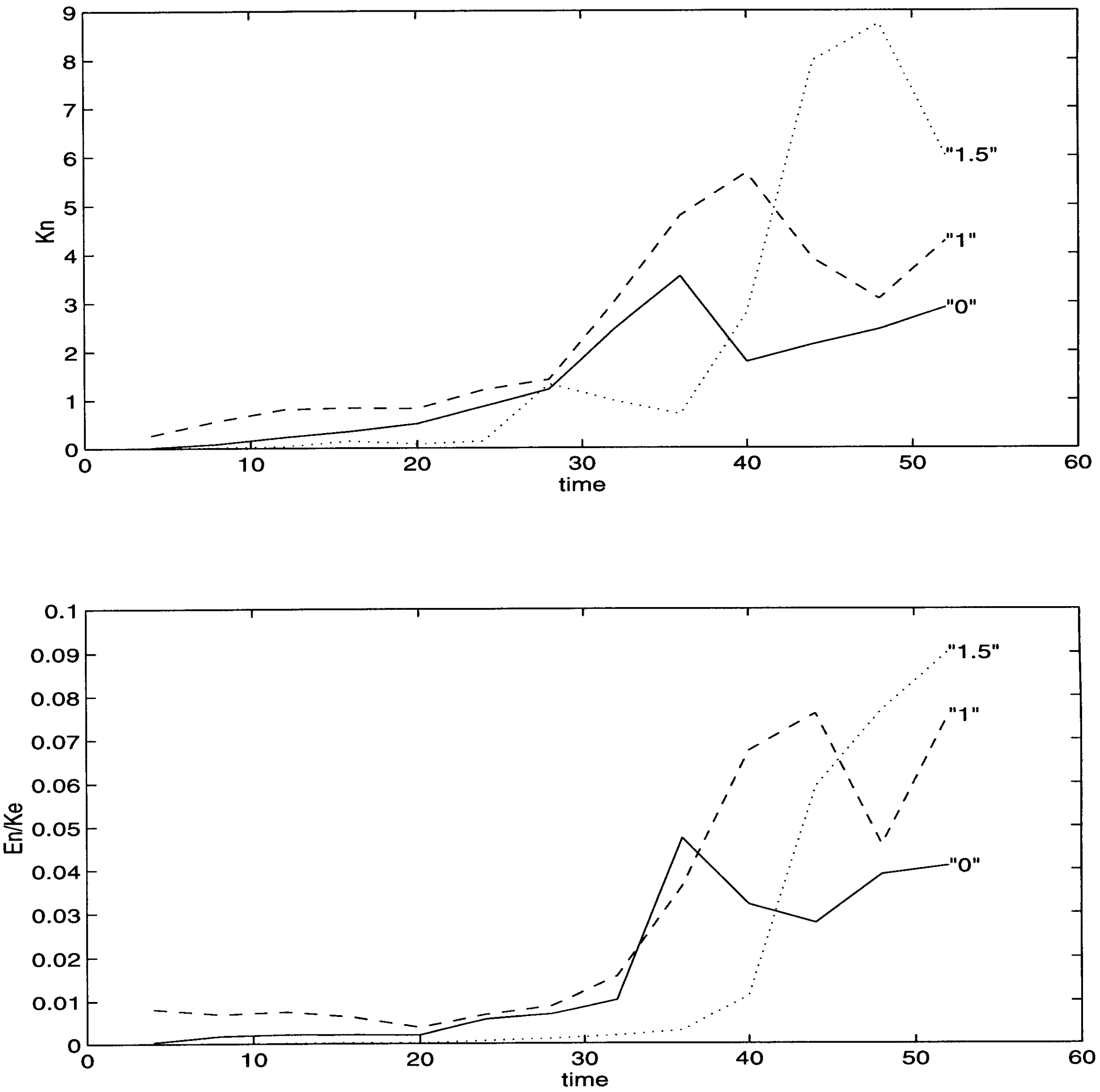

Figure 6.6: Kinetic energy corresponding to each Fourier component vs. time. As in Fig.6.3 but for Case 2: Mode 1 ($k = 1$) and Mode 2 ($k = 1.5$). Components "0", "1" and "1.5". Component numbers are shown in the plot. $\alpha = 30^o$ and $\beta = 1$.

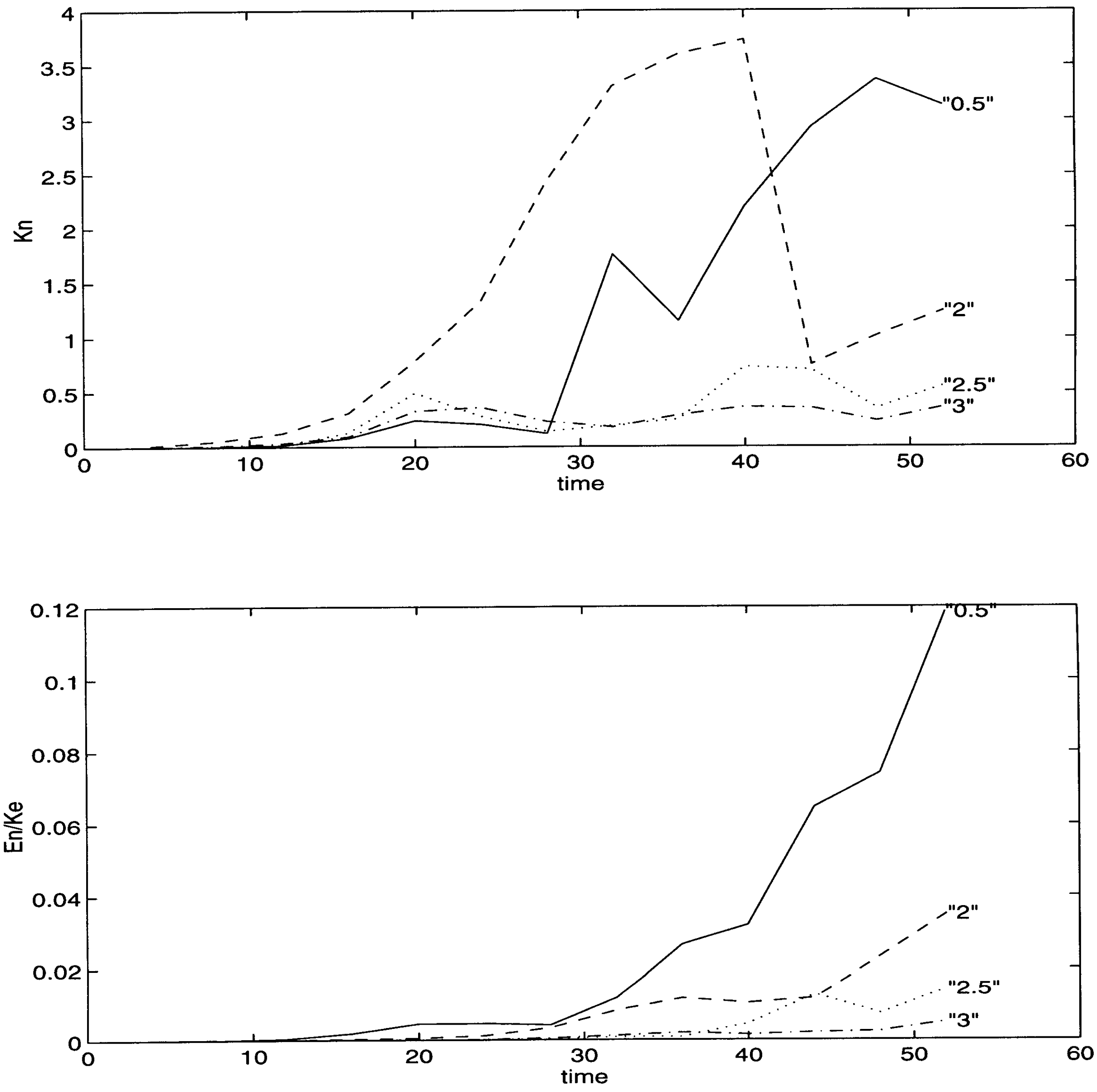

Figure 6.7: As in Fig.6.3 but for components "0.5", "2" and "2.5". Case 2: Mode 1 ($k = 1$) and Mode 2 ($k = 1.5$). $\alpha = 30^o$ and $\beta = 1$.

One interesting and somewhat puzzling fact is the high values of a perturbation energy corresponding to each of the components. Both K_1 and $K_{1.5}$ are much larger than K_1 and K_2 in Case 1. In an experiment not presented here, the problem was initialized with a single Mode 1 with the same amplitude as in Case 1 and Case 2. The resulting K_1 was as large as in the Case 2; small K_1 in Case 1 can be explained by the direct suppression by the Mode 2.

$K_{1.5}$ is also significantly larger than $K_{1.8}$ in the case with a single Mode 2 (see section 5.5). Secondary components further contribute to the total value of the perturbation kinetic energy; see Fig.6.7a. As a result, the value of K_e is much larger than in Case 1.

The absence of direct interactions with component "1" has a dual effect on the radiating properties of component "1.5". The latter is no longer directly suppressed by the vigorously radiating component "1" in the external regions. In fact, $E_{1.5}$ becomes larger than E_1 at the same time as the total energy of this component $K_{1.5}$ becomes the largest as well (Fig.6.6b). On the other hand, secondary harmonic of component "1" cannot put the external energy into component "1.5" as in Case 1.

As a result, $E_{1.5}/K_e$ is almost the same as E_2/K_e in Case 1 by the end of development. Presumably, the absence of both the suppression and the feedback by the component "1" compensate each other and result in little overall effect on the effectiveness of radiation by component "1.5".

In contrast, the radiating ability of component "1" is weaker in Case 2 than in Case 1; compare 8 percent in Fig.6.6b to almost 16 percent in Fig.6.3b. In Case 1, the presence of direct mutual feedback between two primary modes enables long and more radiating component "1" to account for the major part of the radiated energy.

In Case 2, the energy instead escapes into radiating secondary harmonics that do not project back onto any of primary modes. In particular, self-interactions of component "1" produce component "2" that develops on its own. One can see in Fig.6.7b component "2" is associated with E_2 that is almost 4 percent of K_e.

As was noted above, the interactions between two primary components "1" and

"1.5" produce another very energetic harmonic, component "0.5". The component is also strongly radiating: $E_{0.5}/K_e$ is almost 12 percent, which is even bigger than E_1/K_e (Fig.6.7b). Its large amplitudes in both the external regions are evident in Fig.6.5 and in Fig.6.4. Once again we observe that waves that are longer in x are more radiating; in our case even a secondary component "0.5" can dominate the radiating response in the exterior.

The radiation in Case 1 with no direct mutual feedback between two primary components is more energetic than in Case 1 with direct interactions. The ratio of the sum of all external energies to the total energy $(E_0 + ... + E_3)/K_e$ is more than 39 percent by $t = 52$ which is slightly bigger than 35 percent in Case 1. We now recall that the value K_e is much larger in Case 2.

We can conclude that the absence of direct mutual feedback between a strongly radiating wave of Mode 1 and a weakly radiating wave of Mode 2 allows the development of strongly radiating secondary harmonics. The radiating properties of Mode 2 appear to be almost not affected.

6.2 Case 3. Mode 1.

The study of interactions between different types of linear solutions would be incomplete without the experiment in which the development of a long and a short wave of Mode 1 is considered. For the experiment we choose $k = 0.25$ and $k = 1$ as corresponding wavenumbers. The amplitude of the longest wave of a pair is 4 times larger than the amplitude of the wave with $k = 1$.

As we recall from chapter 5 (sections 5.3.1 and 5.3.2), both waves are strongly radiating in the nonlinear regime. The wave with $k = 1$ has the growth rate which is almost twice as large as that of a wave with $k = 0.25$ (Fig.5.9). Therefore, the former has a tendency to dominate in the development. On the other side, a wave with $k = 0.25$ is more radiating (section 5.3.2). Which of the two waves will dominate the development in the exterior regions?

The direct mutual feedback between two waves is not possible for our choice of parameters. The situation is similar to Case 2 described above, in which neither of secondary harmonics created in the course of nonlinear development can directly affect primary modes. However, some differences should be anticipated. First, the shortest primary wave with $k = 1$ is capable of significant radiation, unlike Mode 2 for $k = 1.5$ in Case 2. Second, both secondary harmonics "0.75" and "1.25" produced by the interactions between primary modes are shorter than the longest primary wave with $k = 0.25$. In contrast, one of the secondary harmonics in Case 2, namely component "0.5", is the longest in a set and dominates the radiative response in the far-field. Which component is the most energetically significant in the far-field in Case 3?

To answer these questions, we first present the 2D contour plots of the total streamfunction $\bar{\Psi}(y) + \psi(x, y)$ in Fig.6.8. The evolution of the structure of the solution is very different from Case 1 and Case 2 (Fig.6.1 and Fig.6.4). The radiation starts as early as $t = 32$ and is in the form of isolated eddies of various forms, unlike either of Case 1 or Case 2 in which the radiating response is x-independent initially.

By the end of numerical experiment at $t = 64$, the radiated eddies fill the entire numerical domain which is 50 times as large as the width of the jet itself. The orientation of these eddies is different from that in either of previous cases described in this chapter. In fact, eddies are elongated in the direction nearly perpendicular to the jet axis for $y > 0$. The eddy axes to the south from the jet are tilted relative to both the jet axis and the latitude circles. The complicated structure of the solution indicates the importance of several x-wavenumbers.

We now proceed with the detailed analysis of the structure of the solution and show the Fourier coefficients in Fig.6.9. The evolution of component "1" is very similar to that in the case with a single Mode 1 (Fig.5.13). The radiation of this component starts at the same time ($t = 40$) immediately following the radiation by component "0". The exterior part of component "1" later reaches amplitudes that are as large as in the case with a

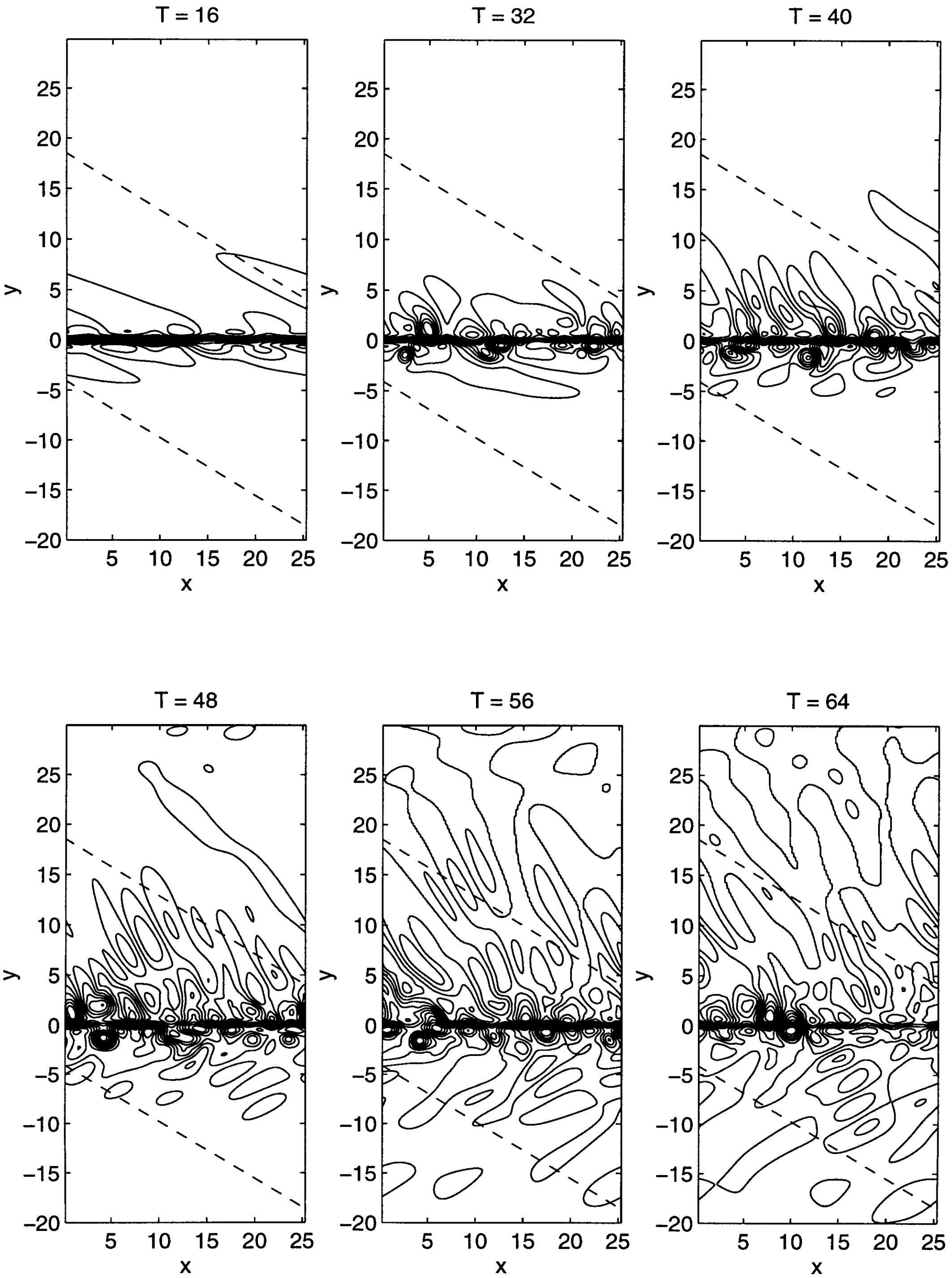

Figure 6.8: Two-dimensional contour plots of the total streamfunction $\bar{\Psi}(y) + \psi(x, y)$. As in Fig.5.11 but for Case 3: Mode 1 with $k = 0.25$ and $k = 1$.

single Mode 1 (section 5.4.1). The development of component "1" seems to be very little affected by the presence of the long component "0.25", which does not directly influence the former.

In contrast, component "0.25" develops differently in Case 3 compared to the case with a single Mode 1 for $k = 0.25$ (section 5.4.2, Fig.5.17). The structure of component "0.25" is identical in both cases until $t = 16$. Although, component "1" does not directly influence component "0.25", a smaller portion of the total energy is available for the development of the latter because of the rapid growth of component "1". As a result, the amplitude of the component becomes smaller in Case 3 than in the case with a single mode for $t > 40$.

Another very interesting property of the development in Case 3, is the very energetic component "1.25" that is a harmonic created by the nonlinear interactions between two primary modes. The amplitude of this component becomes larger than the amplitudes of both the primary modes by $t = 64$ in the jet region. The harmonic also has a well-pronounced symmetric component there, which suggests at the possible excitation of Mode 2 with $k = 1.25$. As we recall from chapter 5, the nonlinear interactions of nearly antisymmetric Mode 1 create harmonics that are almost antisymmetric as well.

We now consider the values of E_{k_n}/K_e plotted in Fig.6.10. Component "0.25" is weakly trapped initially which is reflected in the high values of $E_{0.25}/K_e$ at the beginning of the numerical experiment: 11 percent at $t = 8$. The number then starts to decrease indicating rapidly growing importance of other components in the external regions. The decrease is especially sharp after $t = 24$; $E_{0.25}/K_e$ is only 3 percent during the second half of the experiment. The contribution of component "0.25" to the energy in the exterior regions is surprisingly small in comparison to 18 percent in section 5.4.2, Fig.5.18.

Simultaneously with the decline of the importance of component "0.25" in the external regions, E_1/K_e rapidly increases. The ratio reaches 11 percent by $t = 64$. As we observed in Fig.6.9, the second primary component "1" is of approximately the same amplitude as component "0.25". The latter is not suppressed by component "1". However, since

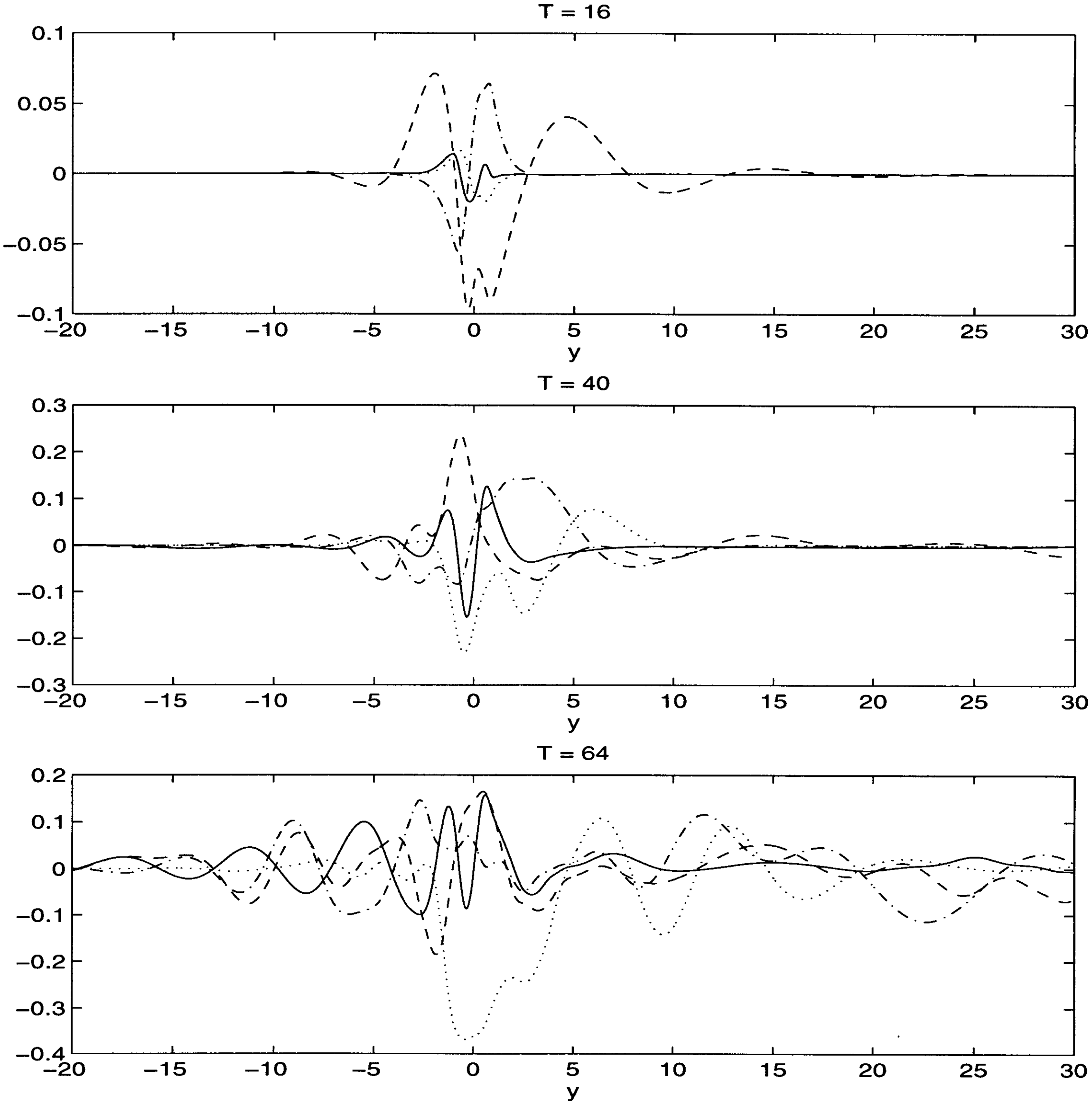

Figure 6.9: The Fourier coefficients Φ_0 (solid lines), $\Phi_{0.25}$ (dashed lines), Φ_1 (dashed-dotted lines) and $\Phi_{1.25}$ (dotted lines) of the streamfunction as functions of y. Corresponding times are given on the top of each panel. Case 3: Mode 1 for $k = 0.25$ and $k = 1$. $\alpha = 30^o$ and $\beta = 1$

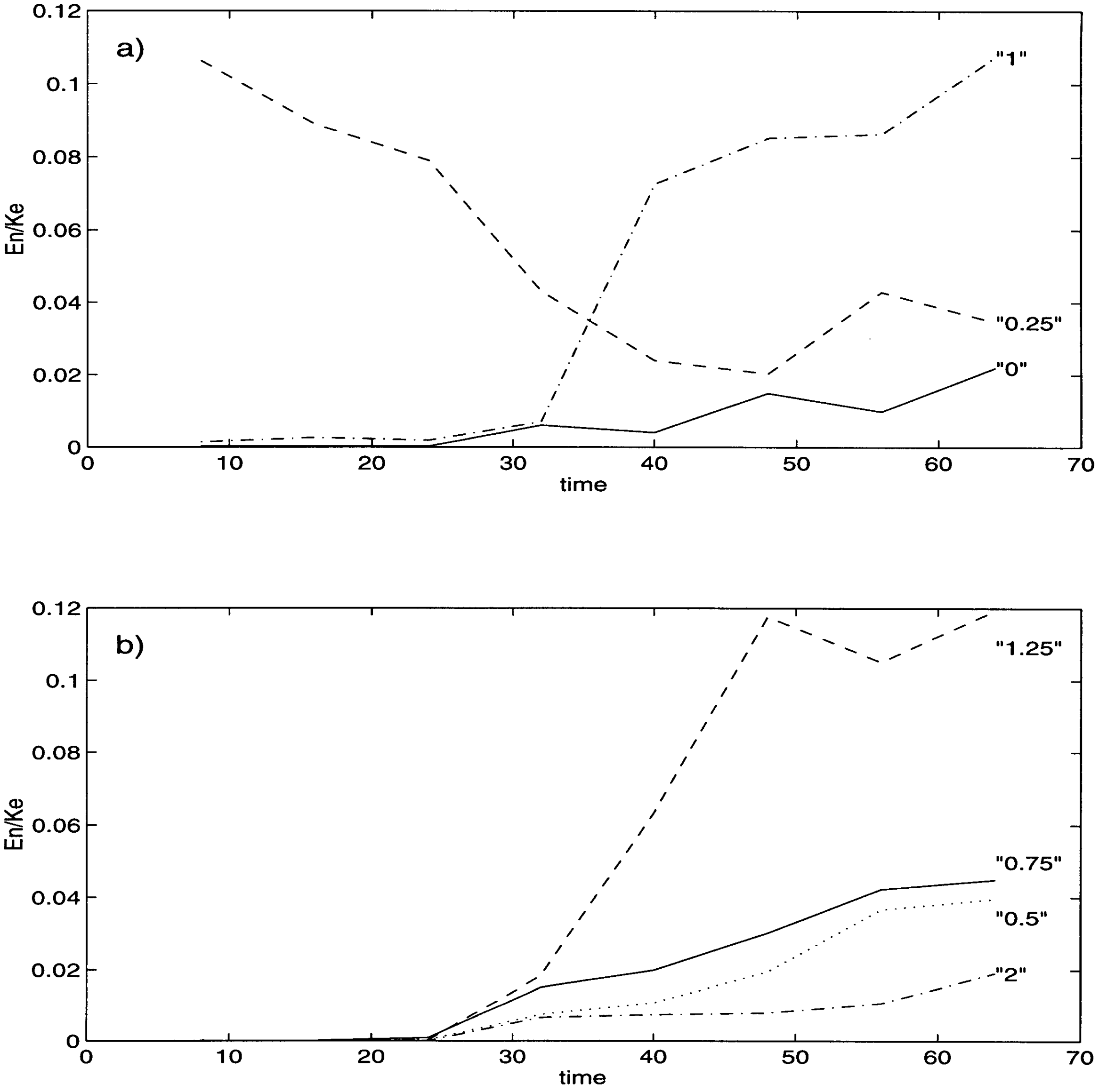

Figure 6.10: E_{k_n} (external kinetic energy corresponding to each Fourier component) divided by the total energy K_e. Case 3: Mode 1 for $k = 0.25$ and $k = 1$. $\alpha = 30^o$ and $\beta = 1$.

component "1" is shorter in x, it corresponds to larger kinetic energy than a longer primary component "0.25".

The values of E_{k_n}/K_e for secondary harmonics plotted in Fig.6.10b are very interesting. In particular, component "1.25", which is created by the interactions between two primary components "0.25" and "1", corresponds to the value of the external kinetic energy that is as large as $E_{0.25}$. $E_{1.25}$ is more than 11 percent of K_e. The same component is also very energetic in the case with a single component "0.25" (see section 5.4.2).

Other secondary harmonics radiate less than 4 percent of the total energy K_e each. However, the radiation in Case 3 is very efficient. Altogether, all components radiate almost 45 percent of the total kinetic energy into both the external regions. This number is higher than the same quantity in the case with a single wave for $k = 1$ but lower than in the case with a wave for $k = 0.25$ (see sections 5.4.1 and 5.4.2).

We can conclude that although component "0.25" radiates very efficiently when the problem is initialized with a single wavenumber $k = 0.25$ (section 5.4.2), it does not dominate the radiating response in Case 3. Shorter waves, that correspond to more realistic spatial scales, have amplitudes that are at least as large as those of component "0.25". Moreover, the major part of radiated energy corresponds to those shorter scales in Case 3.

6.3 Summary.

We have considered three types of interactions between different waves that take place in the nonlinear development of a set of initially linear waves. All types are modeled by the numerical experiments in which the evolution of a pair of linear waves is studied.

As Case 1 shows, the direct mutual feedback between a radiating wave of Mode 1 and a twice as short weakly radiating wave of Mode 2 does not affect the strong radiating ability of the former. Mode 1 still dominates the radiating motions in the far-field and the radiation is very effective. However, Mode 1 is suppressed by Mode 2 in the jet region and its amplitude becomes smaller than in the case with a single Mode 1. The case models the "direct" interactions between those waves which wavenumbers are such to allow secondary harmonics to immediately add to the primary waves.

In Case 2, direct mutual feedback between two primary waves is not possible because of the values of their wavenumbers. Instead, very energetic secondary harmonics develop. One of those harmonics is the longest wave in the created set; it is also the most radiating component in the experiment. The total perturbation energy is much larger than in Case 1.

Unlike the Case 1, Case 2 models the "indirect" interactions between a strongly radiating wave of Mode 1 and a weakly radiating short wave of Mode 2. Such interactions produce secondary harmonics that do not immediately add to any of primary harmonics. The spectrum broadens as a result. Those harmonics that are long in x are capable of radiation which is more energetic than the radiation by a primary wave alone. The latter fact illustrates the possibility of a cascade of radiating energy into the longer x-wavelengths.

In both Case 1 and Case 2, the radiating field is asymmetric in the cross-jet direction. In the northern half-plane, the eddies are elongated in the east-west direction, whereas the eddies are parallel to the jet axis to the south from the jet.

The mutual development of two strongly radiating waves of Mode 1 is considered in Case 3. One of the waves is four times longer than the other and radiates more energetically if considered alone. However, in Case 3 both short and long waves have similar amplitudes in the exterior regions. Short wave together with its secondary harmonics are associated with the major part of radiated energy. Case 3 models the indirect interactions between strongly radiating waves in a set.

The general dynamical picture of a development of an initially white spectrum of linear modes is complex. However, we have observed the general tendency of a spectrum of kinetic energy in the far-field to develop a maximum at $k \sim 1$. In other words, one should expect the short waves with x-wavenumber $k \sim 1$ to be energetically important in the nonlinear development of any broad spectrum of initial conditions.

Chapter 7

Comparison of the results with observations.

In the preceding chapters, we have formulated and solved the problem of stability of a nonzonal ocean current. The focus of the research was on the ability of unstable perturbations to effectively transfer energy from an energetic mean current into far-field. By doing that, we attempted to model the Gulf Stream as an energy source for the eddy field in the interior of the North Atlantic Gyre. How relevant are our results to the real phenomena observed in the region?

To answer this question, we need to compare the model predictions of such physical values as eddy kinetic energy, Reynolds stresses and etc., to the observed values in the region in the North Atlantic. In doing the comparison, we hope to understand to what degree the complicated dynamical process of the generation of highly energetic eddy fields can be explained by the radiation of energy from the Gulf Stream described by our model.

We cannot claim that our simple model is an accurate representation of the Gulf Stream system and instead we are more interested in its ability to capture general dynamic properties in the region. For this purpose, we need to understand what consequences certain assumptions made in the model have on the results. Below we list those simplifications; one should realize that the main purpose of making them was to make the dynamics in the model easier to understand.

Our nonlinear model is barotropic, therefore we neglect the effects of stratification and the movement of the free surface. As was demonstrated in Chapter 4, the addition of the second moving layer in the linear problem does not change depth-independent structure of the radiating response. Nevertheless, the real Gulf Stream is strongly vertically sheared (Halkin and Rossby, 1985; Hall and Bryden, 1985; Johns *et al.*, 1995, etc.) and it is therefore still hard to claim that a barotropic model can fully describe the process of energy radiation.

In addition to the unrealistic vertical structure, the horizontal structure of the Gulf Stream does not closely match the mean velocity profile chosen for the stability analysis. The jet is assumed to be uniform in the along-jet direction which is not the case for the Gulf Stream whose transport increases in the downstream direction (Johns *et al.*, 1995; Hogg, 1992, etc.) and whose path is not a straight line. As a result of the assumption, the vorticity source is required in order to maintain our nonzonal jet within the constraints of the QG dynamics. The effects of the downstream dependence of the mean velocity on the radiating properties deserve a separate study and it is hard to comment on them at this point.

The cross-jet structure is modeled by a symmetric profile, whereas the Gulf Stream is asymmetric in the cross-stream direction. Although the linear results do not qualitatively depend on the particular choice of the mean velocity profile (Chapter 3), the quantitative dependence of the results on the shear in the mean velocity should be expected. The recirculation zones in the basic state are also absent in the model that can affect the radiating properties in the problem (Talley, 1983) and further complicate the comparison with observations.

The simplified representation of both the vertical and horizontal structure of the Gulf Stream also makes the choice of the appropriate scaling difficult as will be discussed in section 7.1.

The effects of topography are neglected in the model. The model attempts to represent the portion of the Gulf Stream after it leaves the Cape Hatteras and before its path becomes very complicated due to the strong meandering. The region is characterized by the presence of the continental slope that can have a large effect on the results of the barotropic model especially to the north from the Gulf Stream, changing the vector of planetary vorticity gradient (Hogg, 1988).

For the comparison with observations, we will analyze the results of chapters 5 and 6, in which the nonlinear development of either a single wave or a pair of waves is considered. The results of all nonlinear computations depend on the initial conditions used in any particular numerical experiment. Since the realistic initial conditions are difficult to define, we do the comparison for four cases with different initial conditions and look at the common dynamical features of corresponding solutions.

Despite the model simplicity, our hope is that it captures the main features of the eddy field, which as we assume is mainly produced by the process of energy radiation. In this chapter we look for the supporting evidences of such an assumption. The choice of oceanographically consistent with observations scales is discussed in section 7.1. The comparison of observed physical fields to those produced by the model is presented in section 7.2.

7.1 Scaling of results.

As is remarked in the introduction to this chapter, the comparison of our simple barotropic model to the real Gulf Stream is not easy because of the simplified vertical and horizontal structure of the mean current in the model. We base our scaling on keeping such physical quantities as the total transport, the width and maximum velocity of the current as close as possible to being realistic.

For our barotropic model, we need two dimensional numbers: the half-width of the jet L_{jet}, which is defined as a distance from the point of maximum velocity to the point of zero velocity, and the maximum jet velocity U. Those two parameters define the spatial scale and scale for velocity correspondently. They also set the advection time-scale $T = L_{jet}/U$ used in the model and non-dimensional planetary vorticity gradient $\beta_* L_{jet}/U$.

The data for the Gulf Stream are taken from the article by Johns *et al.*, 1995, in which the authors report the structure and transport of the current near $68^o W$ using SYNOP current meter observations. Velocities are considered in the rotated, downstream coordinate frame.

Based on the cross section of the stream-averaged velocity structure (Figure 9 in the article), we can estimate the distance between the point of maximum velocity and the southern zero contour to be more than 125 km. We choose L_{jet} equal to this distance although the observed profile is asymmetric and the part of the jet to the north from the axis is more narrow than the southern counterpart. We also observe that the assumption that the width of the current is depth-independent is rather realistic.

The next parameter to be estimated from observations is the maximum velocity of the barotropic jet in the model. The difficulty is that the Gulf Stream velocity changes in the vertical and its maximum value at each depth varies from almost 2 m/s at 50 m depth to 0.12 m/s at the depth of 2 kilometers. For the value of U, we choose to average these peak values over the depth of 2 km which gives us approximately $U = 0.5 m/s$.

Before we proceed any further, we need to check if the volume transport in the model is reasonably close to the observed value. We point out that our choice of L_{jet} and U does not necessarily result in the realistic value for the transport in the model, because the profile chosen for the stability analysis does not closely match the observed one (see Fig.7.1).

The dimensional transport per unit depth can be easily computed in the model to yield:

$$U L_{jet} \int_{-1}^{1} (1 - y^2)^3 dy = .9 U L_{jet}$$

Substituting the obtained above values for U and L_{jet}, we get approximately 56

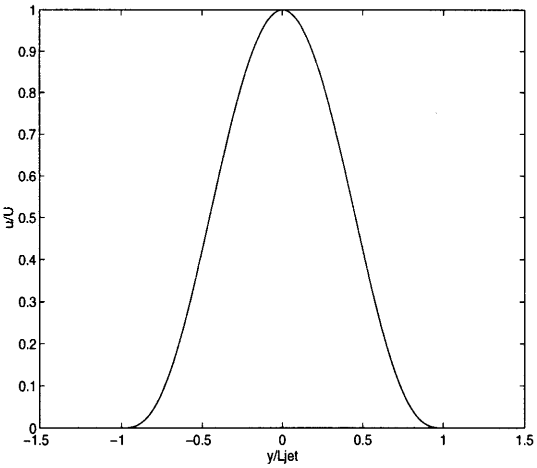

Figure 7.1: Velocity profile chosen for computations.

Sv/km. We now take the number for the total transport at 68^oW from the surface to 2 km from Table 1 in Johns *et al.*, (1995), and divide the obtained 99 Sv by the water column depth. We get 50 Sv/km which is very close to the corresponding value in the model. Our choice of dimensional parameters is consistent with the observed value of the volume transport.

We now estimate other parameters used in the model. All values are listed below:

$$L_{jet} = 125km$$

$$U = 0.5m/s \quad or \quad 43.2km/day$$

$$T = L_{jet}/U = 2.9days$$

$$\beta = \beta_* L_{jet}^2/U = .65$$

In the numerical experiments analyzed in the following chapter we use non-dimensional planetary vorticity gradient equal to either 0.25 or 1. As one can see, $\beta = .65$ falls between those values.

We also keep in mind that the topography in the region can increase the value of effective β; in fact the value is nearly doubled to the north from the Gulf Stream axis (Hogg, 1988).

7.2 Model-Data comparison

We are now ready to proceed with the comparison of the model results with the observations. The following physical fields are chosen for the comparison: eddy kinetic energy, Reynolds stress and the characteristic time scales. We will analyze the model results for four cases with different initial conditions and values of β: 1) Mode 1, $\beta = 1$, $k = 1$ (MR1) with initial amplitude 5 times larger than for the case described in section 5.4.1; 2) Mode 1, $\beta = 0.25$, $k = 1$ (MR2), section 5.4.3; 3) Case 2 of Chapter 6 (MR3); 4) Case 3 of Chapter 6 (MR4). $\alpha = 30^o$ for all cases. The analysis is performed on the advanced stage of nonlinear development during the nonlinear equilibration in the model. We will use the notations in brackets for brevity.

7.2.1 Kinetic energy

We start with the analysis of the perturbation kinetic energy (PKE) fields. In the next four contour plots (Fig. 7.2-7.5), we present the results from our model for all four cases (MR1 - MR4). First thing to notice in all four plots is the high values of PKE centered in the jet region. The band of high energy (values exceeding 500 cm^2/s^2) stretched for more than 500 km in the cross-stream direction for MR2 and MR3. The high-energy band is narrower for MR1 and MR4. The maximum values of PKE reach 1500 cm^2/s^2 in the model for MR1, MR2 and MR3. Only in MR4 are the areas found in which PKE reaches 3000 cm^2/s^2.

The values of PKE decrease away from the jet region. The values of 200 cm^2/s^2 are produced by the model at the distances of approximately 500 km both to the north and to the south from the stream axis in all four cases analyzed. The PKE penetration scale is slightly longer to the south for MR2.

Here, we use the article by Richardson, (1983) as a source for data for the comparison. In the article, the author used the velocities of the near surface currents in the North Atlantic measured by the satellite-tracked drifting buoys to construct kinetic energy

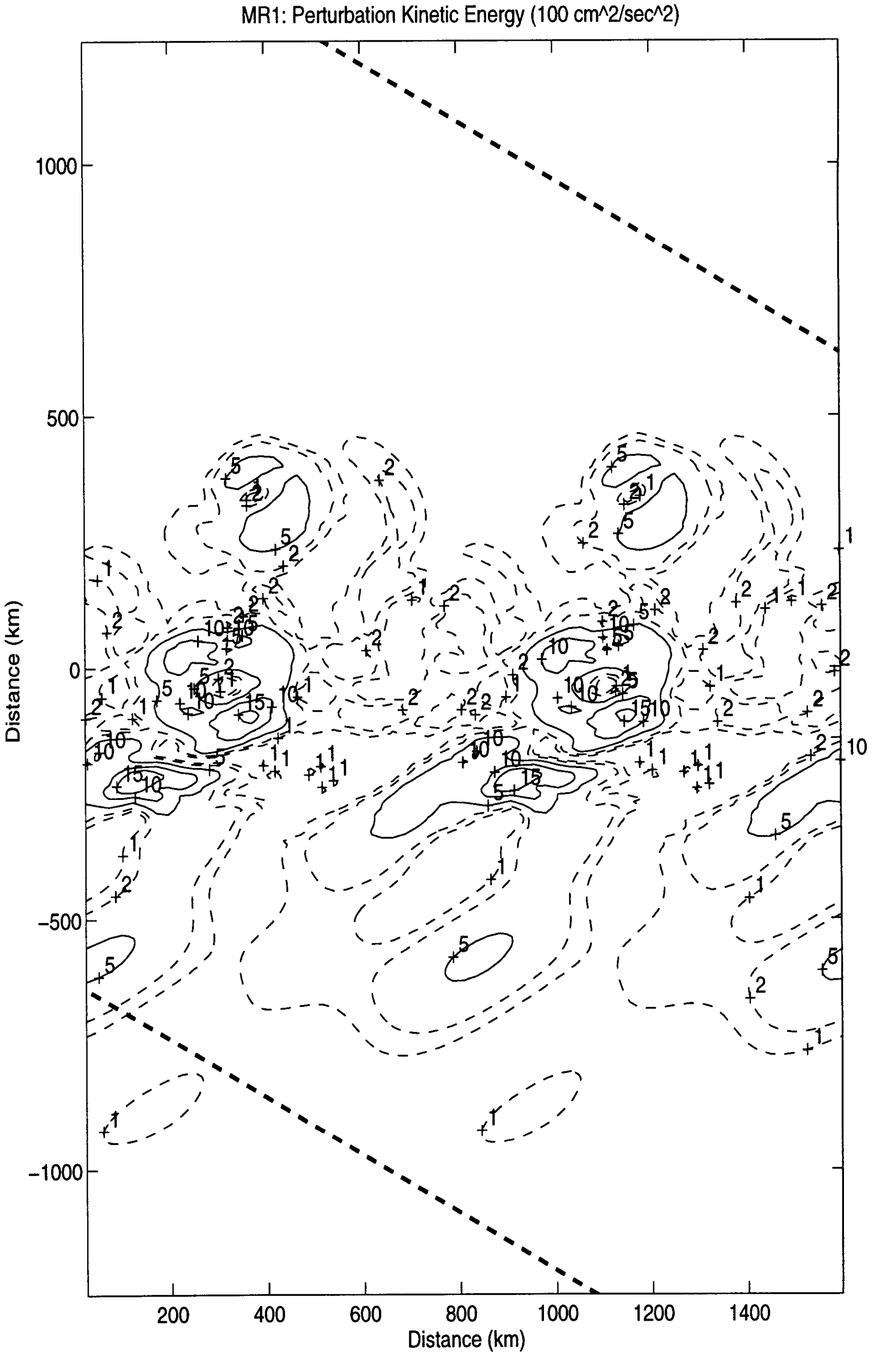

Figure 7.2: PKE for MR1. The dashed contours show low values of the energy ($< 500 cm^2/s^2$). The heavy dashed lines show latitude circles. Units are 100 cm^2/s^2

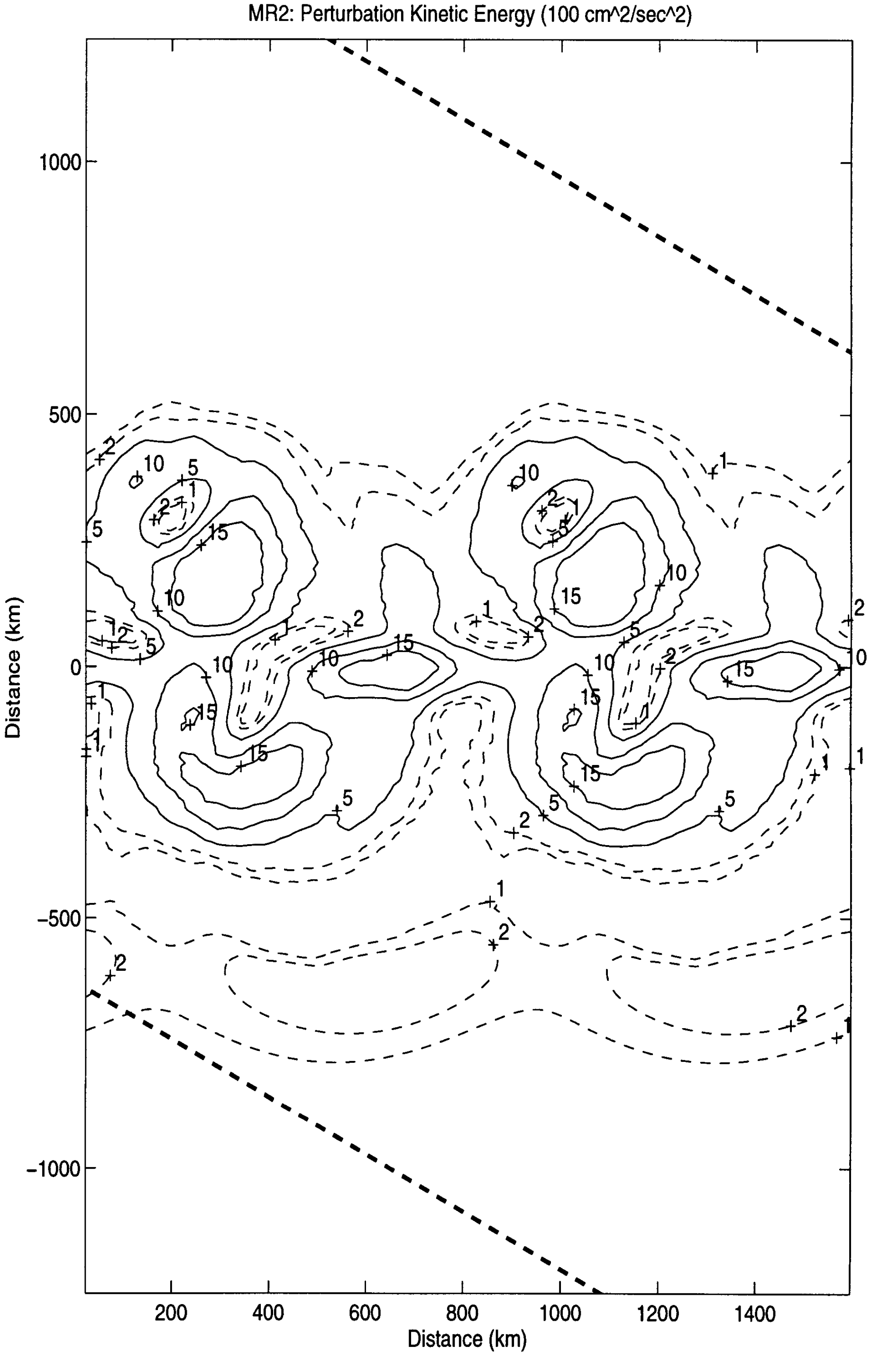

Figure 7.3: As in 7.2 but for MR2

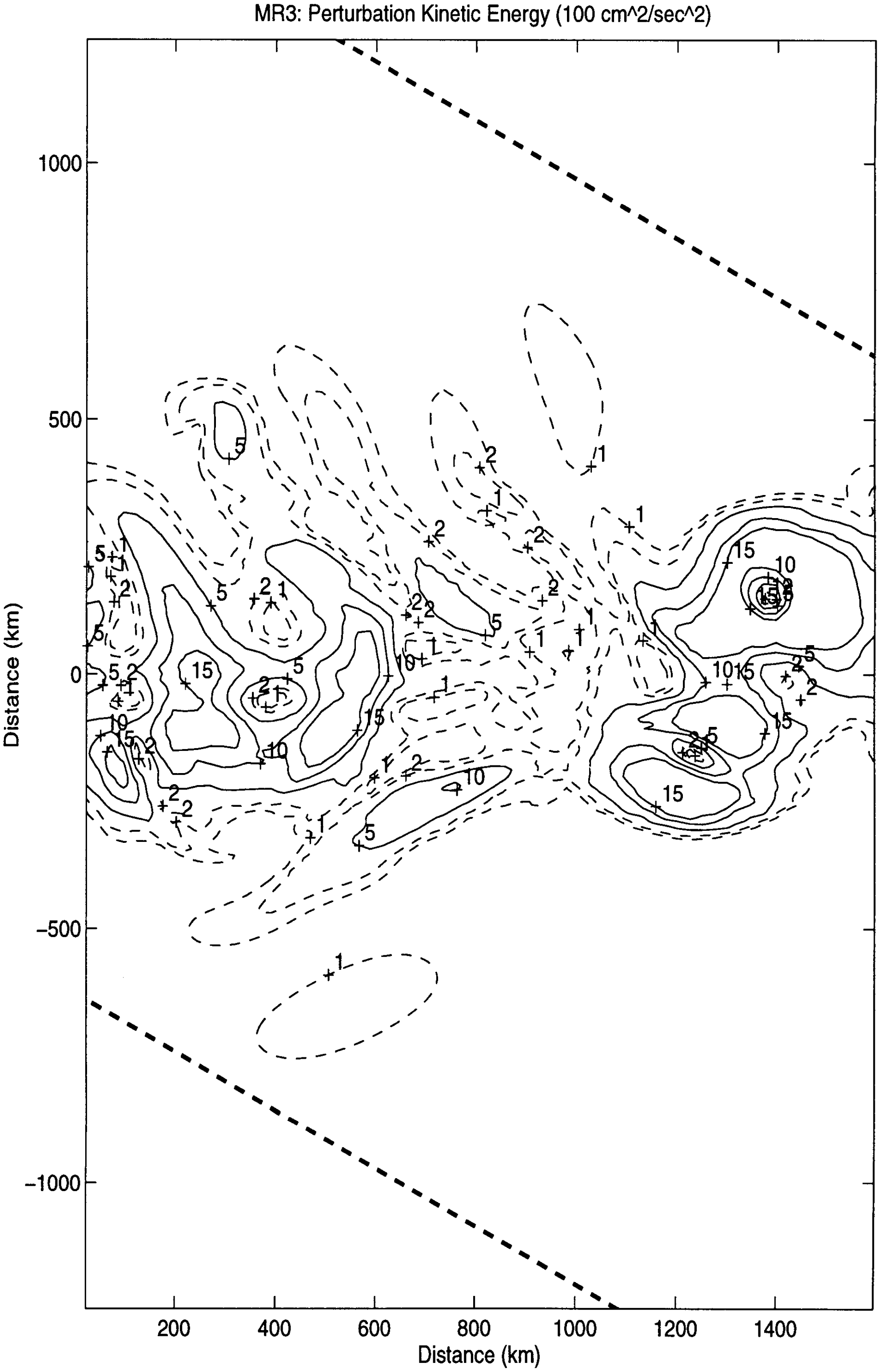

Figure 7.4: As in 7.2 but for MR3

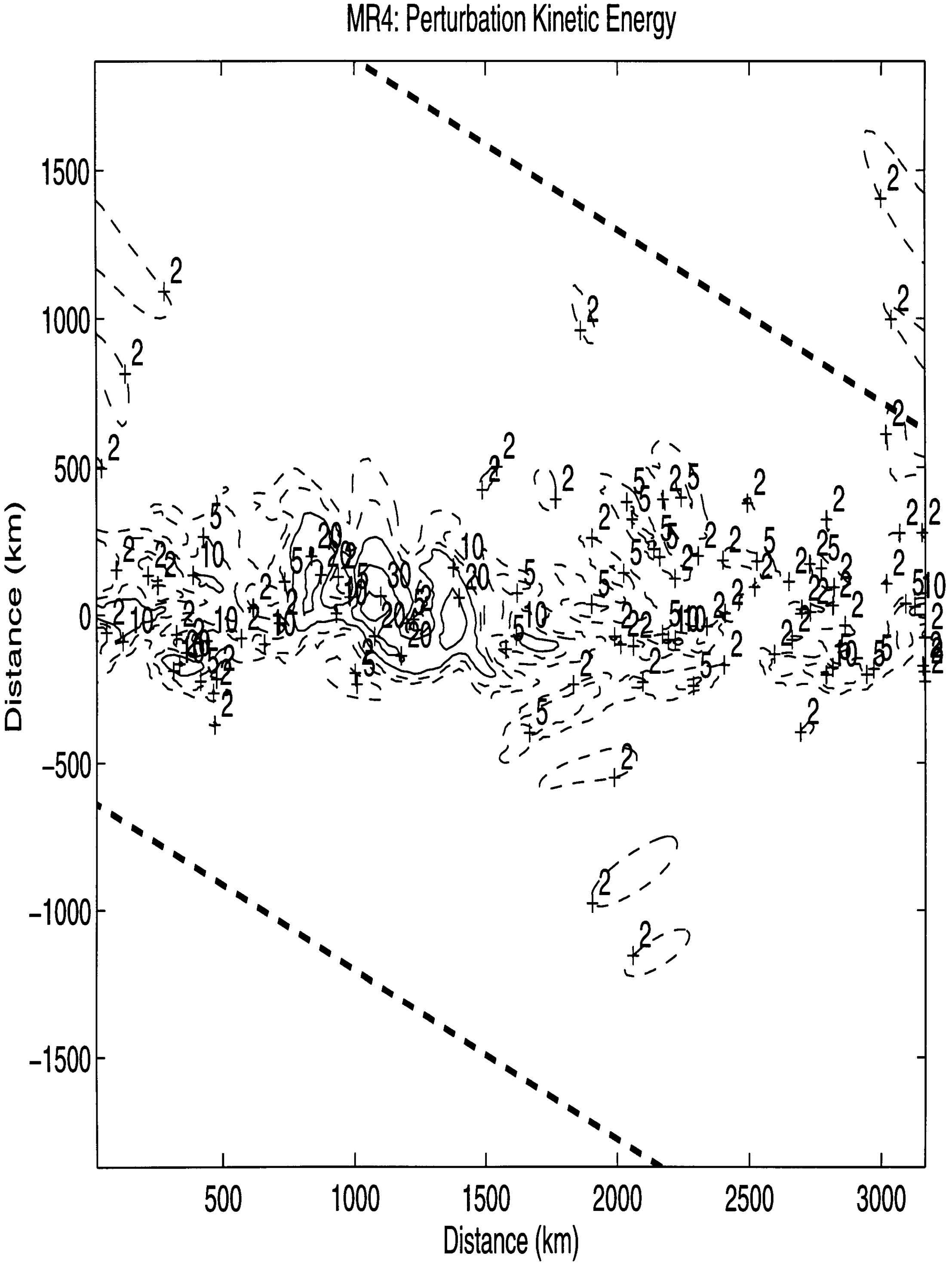

Figure 7.5: As in 7.2 but for MR4

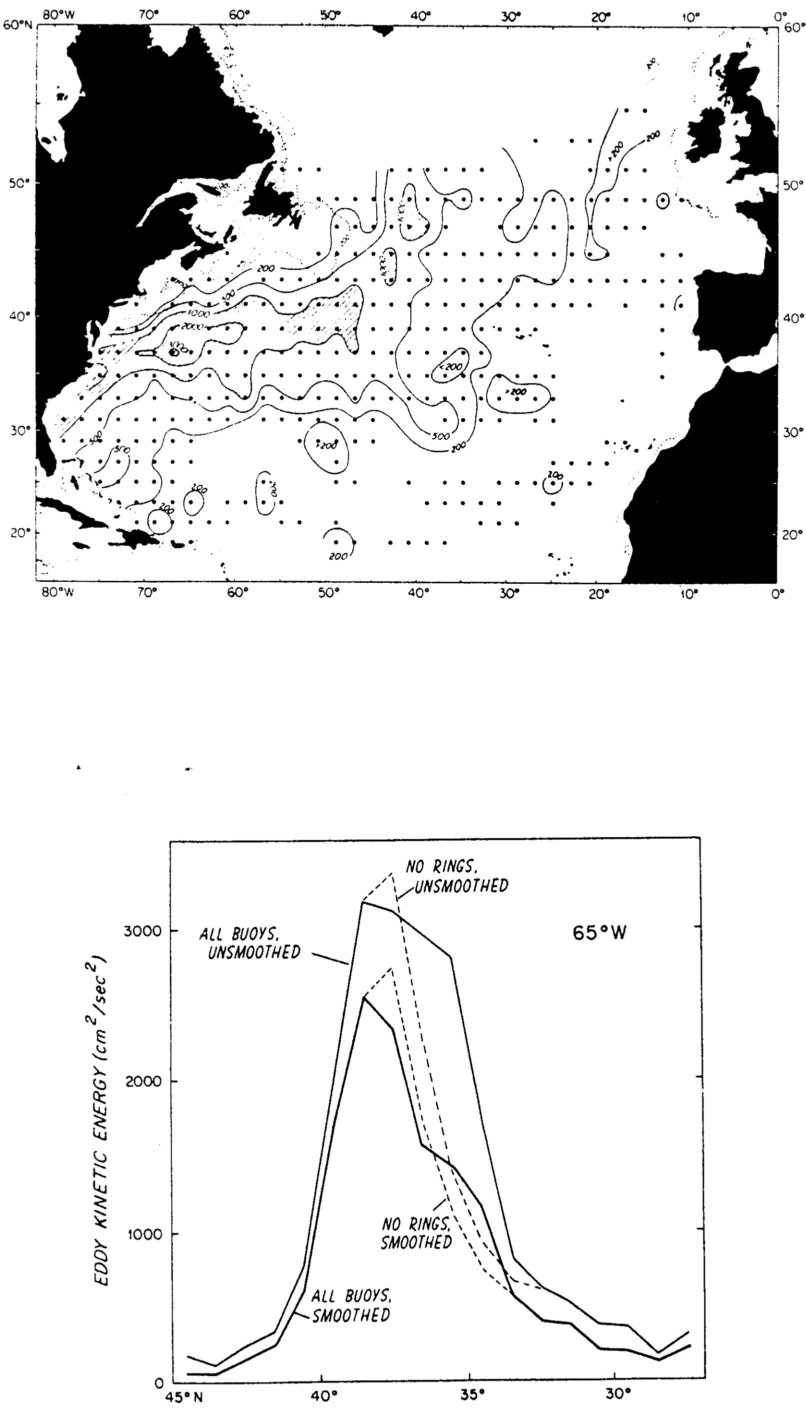

Figure 7.6: Upper panel: EKE ($cm^2 s^{-2}$) in the North Atlantic. After Richardson, (1983), Fig.10. Lower panel: EKE at 65^oW. Different curves show the effect of smoothing the data and excluding ring observations. After Richardson, (1983), Fig.13.

maps. The resulting values of the eddy kinetic energy in the Gulf Stream region are 2 times as high as those obtained from the ship drift measurements (Wyrtki *et al.*, 1976). The results from the article are reproduced in Fig. 7.6.

The observed EKE (Fig. 7.6) is generally higher than the PKE in the model. The peak values as high as 3000 cm^2/s^2 are observed in the Gulf Stream region, which are twice as high as the corresponding peak values produced by the model.

The band of high observed EKE with values of more than 1000 cm^2/s^2 is centered in the Gulf Stream axis and has a width of approximately 500 km after the current leaves the coast and then broadens to almost 1000 km width (Fig. 7.6; upper panel). If we accept the factor of 2 as the overall difference between the observed values of EKE and the barotropic PKE produced by the model, we can conclude that the meridional scale of the high energy region is reproduced correctly by the model.

There are a number of reasons for the difference between the observed values of EKE and the model results apart from the simplicity of the model. First of all, the data describe near-surface values of EKE, whereas the eddy field in our barotropic model is depth-independent. The observed EKE in the vicinity of the Gulf Stream significantly decreases with depth; for example, the EKE decreases by more than 15 times from the depth of 400 m to the depth of 2000 m at 68^oW in the vicinity of the Gulf Stream axis (Schmitz and Luyten, 1991; see also the Table 7.1 below). The difference is lower in the regions away from the stream. It is not therefore surprising to find the values of depth-averaged kinetic energy to be smaller than those observed at the surface.

Another reason is associated with the difficulty of choosing the correct initial conditions for our simple model as it was discussed in the introduction to this chapter. The level of the PKE produced by a numerical run depends on the amount of the initial kinetic energy. We can compare, for example, MR1 and MR3. In the latter case, Mode 2 is added in addition to a single Mode 1 of MR1. As a result, MR3 corresponds to higher values of PKE than does MR1. We, therefore, need to reiterate that we are looking for features common to all four cases (MR1-MR4) that have very different initial conditions.

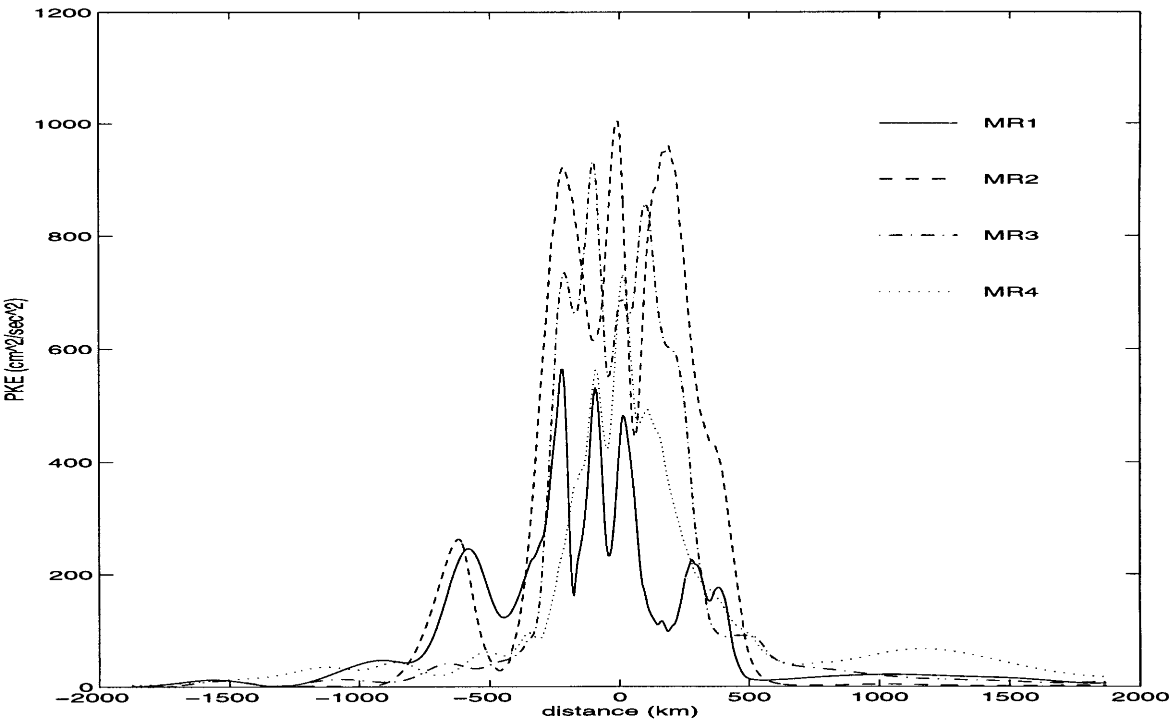

Figure 7.7: PKE averaged in the downstream direction for all four cases. Types of lines corresponding to the each of four cases are given in the plot. The negative values of y correspond to the region to the south from the jet axis.

The downstream dependence of the mean current is neglected in the model. As a result, we cannot expect the model to reproduce the observed downstream increase of the EKE related to the increased meander activity. We now look at the distance at which PKE penetrates into the regions away from the Gulf Stream axis.

Our numerical solution is a sum of a number of waves which results in several isolated maxima of PKE. As a result, the decay scale of the PKE in the meridional direction is difficult to estimate from the 2D contour plots. Instead, we choose to analyze the profile of the downstream-averaged energy (Fig.7.7) and estimate the decay scale in the cross-stream direction.

All four cases (MR1-MR4) are shown in the figure. As one can observe in the plot, MR2 and MR3 correspond to larger values of the averaged kinetic energy than do MR1 and MR4. Note also that the maximum x-averaged values are smaller than the absolute maximum values in the 2D plot due to the strong x-dependence of the PKE.

The approximate distances in the direction perpendicular to the jet axis over which the x-averaged PKE e-folds are then computed. One should keep in mind that the jet axis is tilted in the model and the cross-jet direction does not coincide with the longitude circles.

The approximate decay scales are as follows ("S" means to the south, "N" means to the north): MR1 - 350km (N) and 250km (S); MR2 - 300km (S) and 250km (N); MR3 - 250km (S) and 250km (N); MR4 - 250km(S) and 200km (N).

We can summarize the results saying that the model predicts the e-folding decay scale of 250-300 km on average. The decay scale to the south from the jet axis ($y < 0$) is longer than to the north ($y > 0$) for MR1 and MR2; the distribution of x-averaged PKE is more symmetric for MR3 and MR4.

The distribution of the observed EKE shows the good agreement with the model results in terms of the spatial decay scales in the cross-jet direction. For example, at 65°W the energy reaches e-folding at larger than 320 km from the axis to the south and less than 280 km to the north (Fig. 7.6). The less rapid decay in the EKE to the south from the stream axis is reproduced by the model results MR1 and MR2. The ability of our simple model, that attempts to study the energy radiation in the cross-stream direction, to reproduce the observed meridional decay scale of EKE is encouraging.

7.2.2 Reynolds stress.

The next dynamical quantity to be analyzed is the off-diagonal Reynolds stress component uv. In the model, we consider the process of radiation in the rotated coordinate frame. Although the orientation of the coordinate frame does not affect the values of PKE, the values of uv do depend on the orientation of x- and y axis. We therefore choose to define the uv in the conventional, non-rotated coordinate frame. The velocity components in this frame are defined as:

$$u = -\psi_y cos\alpha - \psi_x sin\alpha, \quad v = -\psi_y sin\alpha + \psi_x cos\alpha$$

where ψ is the streamfunction in the rotated coordinate frame used in our model.

The results for four cases MR1-MR4 are presented in Figs.7.8 - 7.11. The first thing to notice is the fact that uv is not of a definite sign in each of the northern and southern half-planes. That is, both negative and positive values are found either to the north and to the south from the jet axis for all four cases. The uv is mostly negative at the distance more than 300 km to the north from the jet axis for MR3 and MR4.

The results are qualitatively different from those in the problem in which radiation from a zonal meandering boundary is studied (Malanotte-Rizzoli *et al.*, 1987b; Hogg, 1988; Bower and Hogg, 1992, etc.). The zonal model predicts negative values of uv to the north from the jet and positive values to the south. The reasons for the difference with our model are the following.

If a radiated Rossby wave propagates from a zonal current to the south, its y-component of the group velocity is negative, which implies $kl < 0$. The uv is proportional to $-kl$ and is therefore positive. A similar argument gives negative uv to the north from the stream axis.

If a wave carries energy to the right from the downstream direction of a current which axis is tilted horizontally, the y-component of the group velocity in the *rotated* coordinate frame is negative. However, the group velocity can have either negative or positive component in the meridional direction. Therefore, kl in the *nonrotated* coordinate frame is either negative or positive, making the resulting uv either positive or negative.

In addition, the radiated field in our model does not consist of pure plain Rossby waves. Rather, the disturbances decay away from the jet region and their amplitudes strongly depend on time throughout the whole development. Furthermore, nonlinear effects of wave-wave interactions between different Fourier components of the solution alter the solution from the linear wave-like form.

Another important property of the obtained uv maps is the wide bands of the high values ($> 100\ cm^2/s^2$). In particular, for MR1 and MR2, the regions with high values extend to the 700 km to the south from the jet axis. The analogous penetration scale to

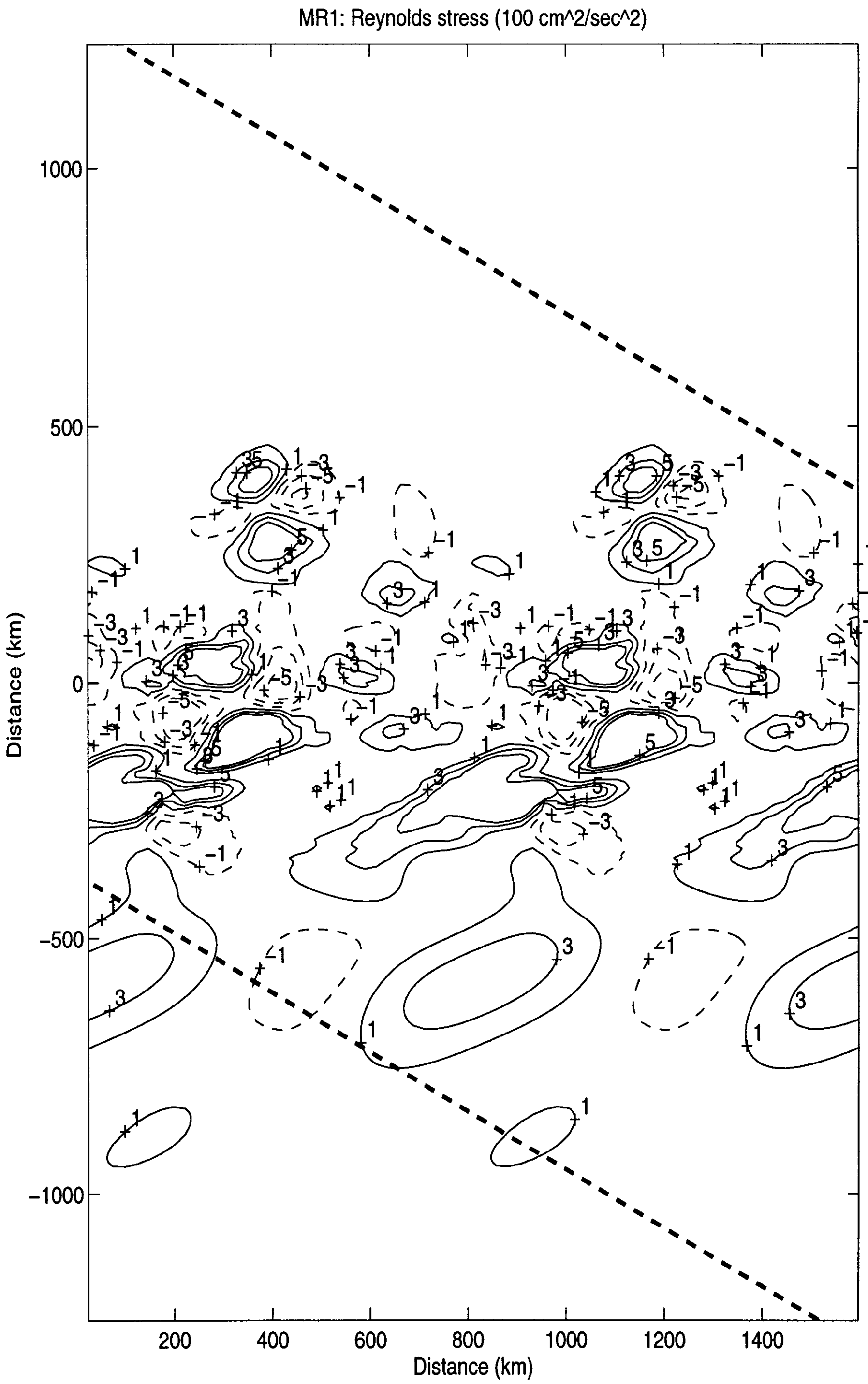

Figure 7.8: uv for MR1. The solid contour lines show positive values; the dashed contour lines show negative values. The heavy dashed lines show latitude circles. Units are 100 cm^2/s^2

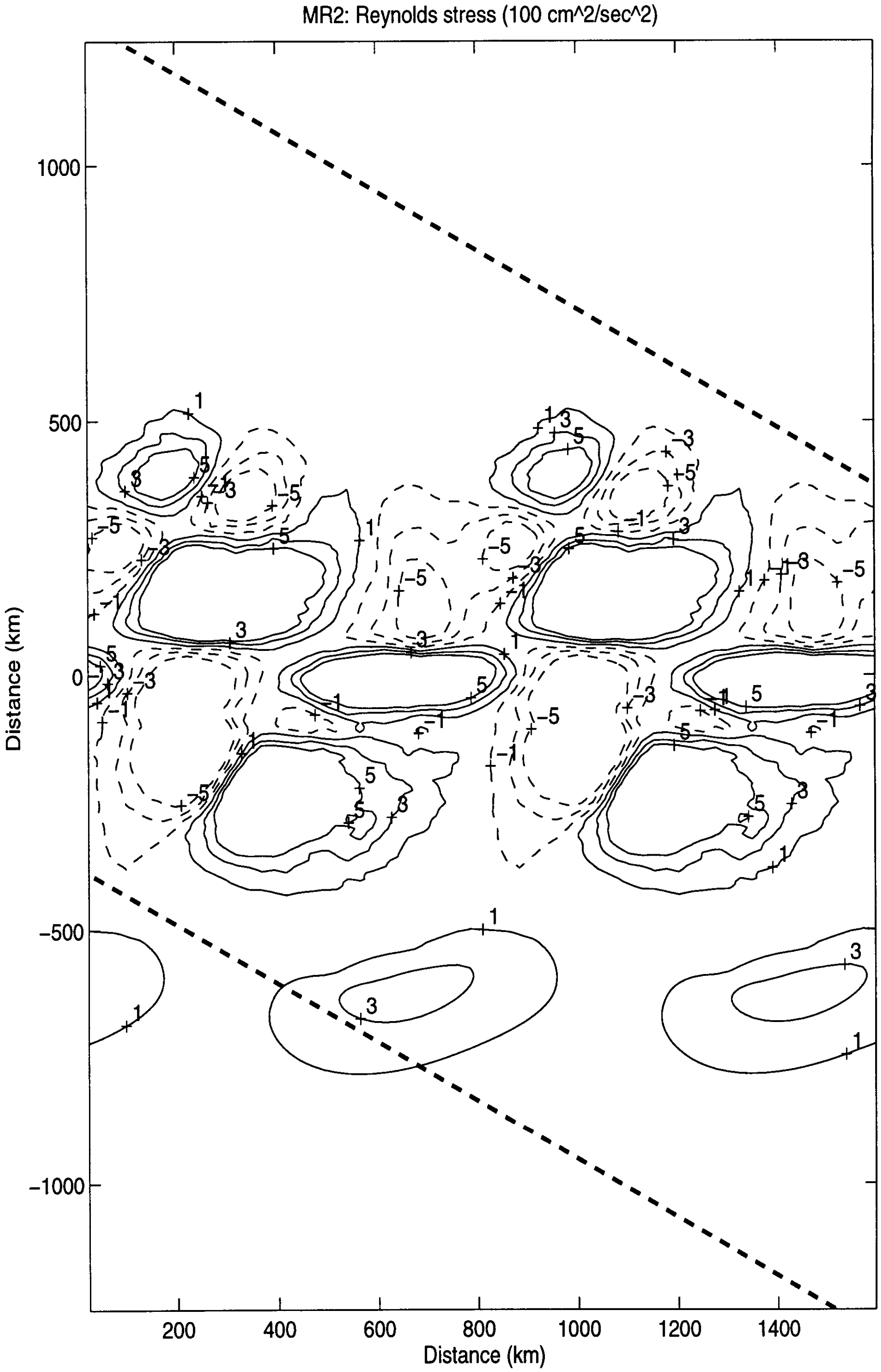

Figure 7.9: As in 7.8 but for MR2

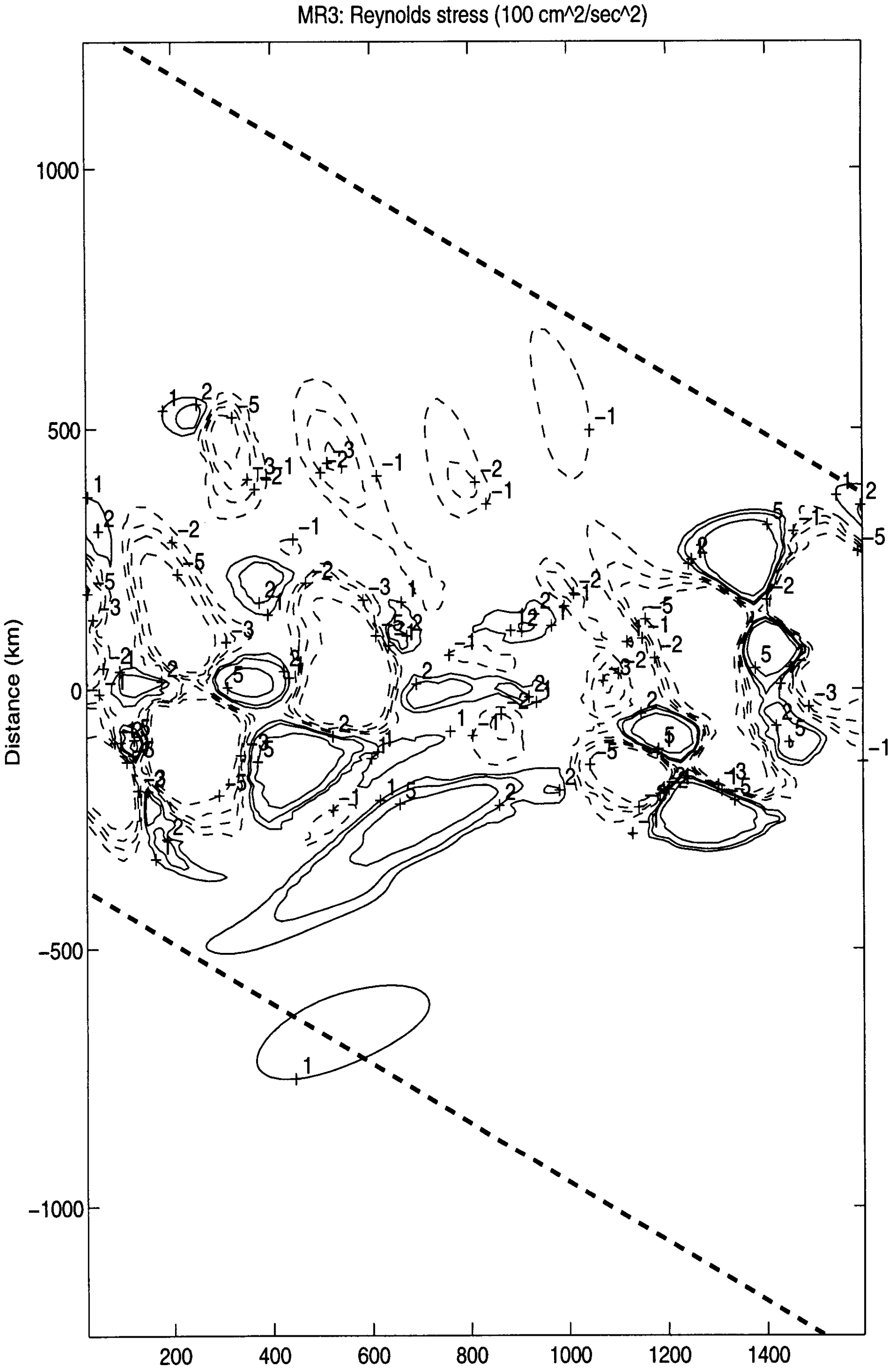

Figure 7.10: As in 7.8 but for MR3

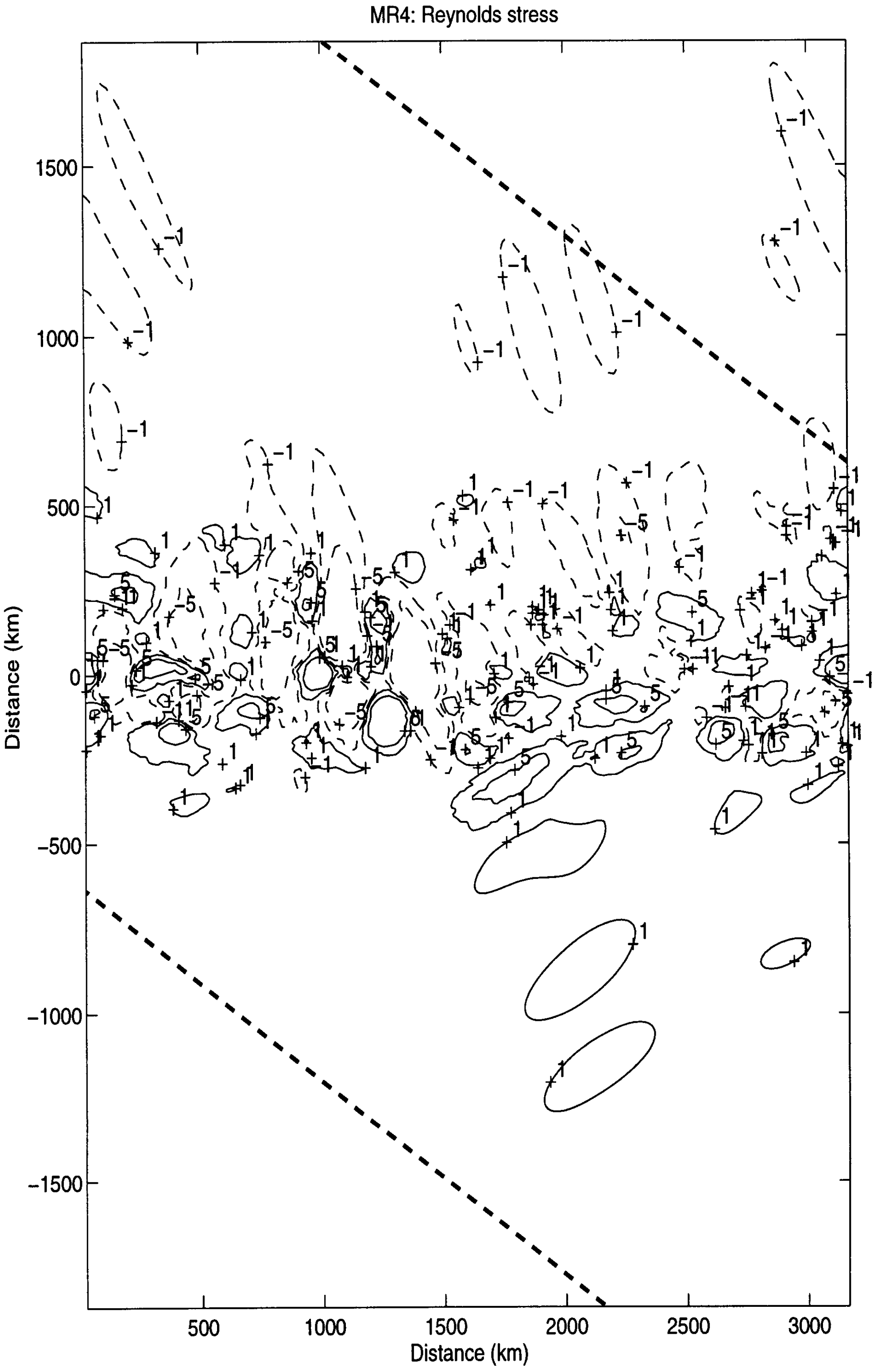

Figure 7.11: As in 7.8 but for MR4

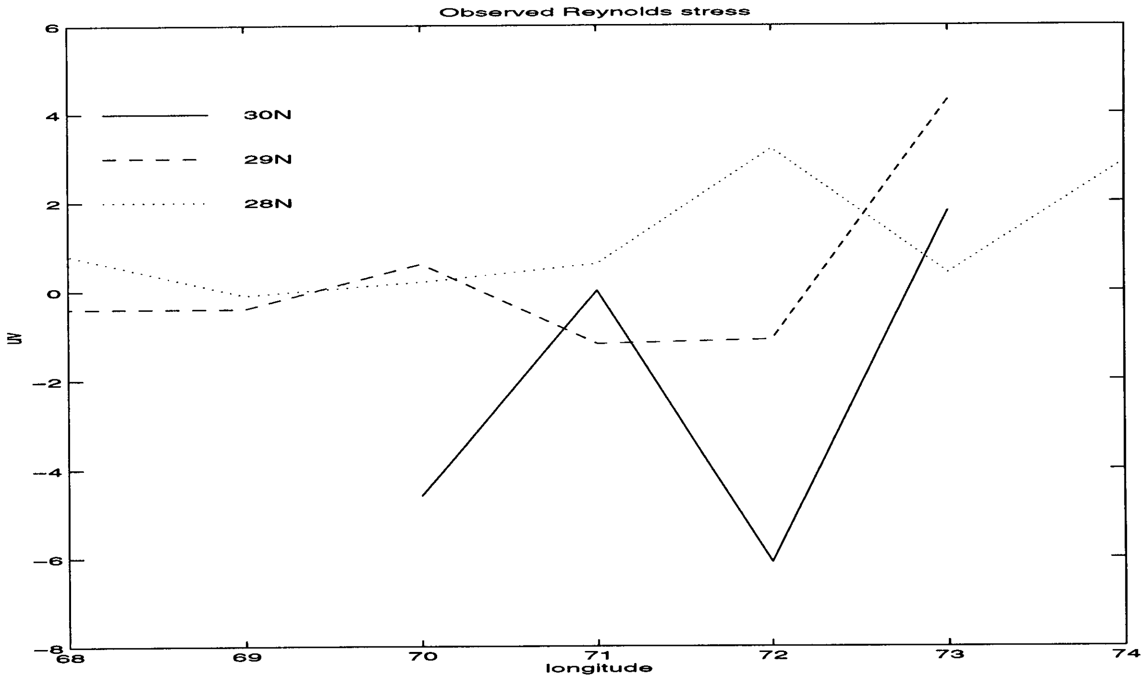

Figure 7.12: Observed values of $\overline{uv}$ in cm^2/s^2 after Freeland *et al.*, (1975), Table 1.

the north from the stream axis is shorter: less than 400 *km*.

For the comparison with the data we first turn to Freeland *et al.*, (1975). Neutrally buoyant SOFAR floats are used to measure the currents at 1500 *m* depth in Sargasso Sea; the statistical behavior of the floats is reported in the article. The reported results include second moments of velocity (u^2, v^2 and uv) and phase propagation patterns.

For the present purposes, we look at the values of uv computed by averaging over all floats passing through 1° squares (Table 1 in Freeland *et al.*, (1975)). The presented numbers (Fig. 7.12) give us an idea about the distribution of uv with longitude in the region far from the Gulf Stream axis (more than 700 *km* from it). In addition, the amplitude of the first baroclinic mode is likely to be smaller at the 1500 *m* depth than it is at the surface; the barotropic component may then be better pronounced in data at this depth.

The first thing to notice is the fact that the observed values are lower in magnitude than those predicted by the model; the reason is that the observed values correspond to a

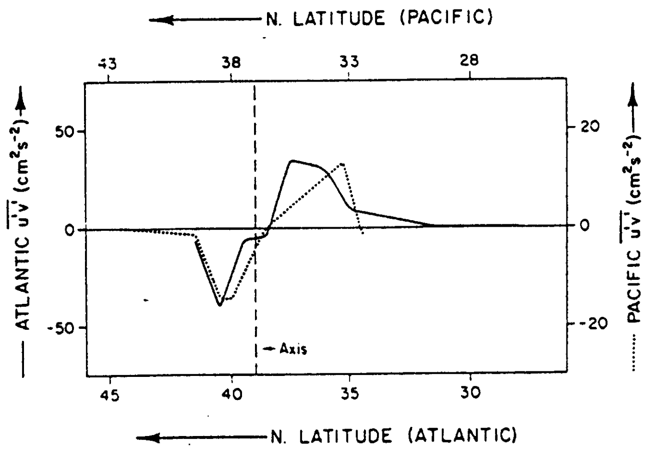

Figure 7.13: Values of $\overline{u'v'}$ for Western North Atlantic (solid line, ordinate scale on left) at 55^oW at 4000 m depth. After Schmitz (1982), Figure 1.

considerable depth of 1500 m. The predicted by our model values of uv, which represent the eddy field averaged over the upper 2000 m can therefore exceed the observed values at depth.

The sign of uv is a more convenient property for the comparison. In the general agreement with the model results, we observe mostly negative values at 30^oN and values changing their sign and being smaller in magnitude for 29^oN and 28^oN in Fig.7.12.

The uv changing sign to the south from the Gulf is also observed at greater depth, at 4000 m (Bower and Hogg, 1992). A number of current meter datasets from the large area in the North Atlantic is used for the analysis in the article. The alternating negative and positive values are reported everywhere in the North Atlantic.

An attempt to account for the effects of topography in the region is then made and the uv is recomputed in a coordinate system aligned with the ambient potential vorticity gradient at each location. As a result of such transformation, values to the north from the current where topography is the most important, become mostly negative in the agreement with the predictions of the linear zonal model in Hogg (1988). However, values to the south from the Gulf Stream axis remain negative at many locations.

The horizontal dependence of the observed uv can be estimated from Schmitz, (1982) (reproduced in Fig. 7.13). We find the regions of high values within approximately 700 *km* to the south from the Gulf Stream axis and less than 400 *km* to the north from it. As one can see, the model captures this aspect of the latitude dependence correctly. The observed uv also has a minimum in the magnitude at the stream axis. However, despite the fact that some zero contours cross the jet axis in Fig.7.8 - 7.11, the minimum in the magnitude is not well-pronounced in our results.

7.2.3 Time scales.

We now focus on the analysis of the time scales of the eddy motions produced by our model. In the linear theory, it is fairly straightforward to determine what time scales any particular linear solution corresponds to. In fact, linear theory provides two different time scales for a linear wave of the form $Re\left[e^{\omega_i t}e^{k(x-c_r t)}\phi(y)\right]$: e-folding time scale $1/\omega_i$ which if divided by two defines the time interval over which the energy of a wave increases by e, and the period of the phase oscillations $2\pi/kc_r$.

Both time scales vs. corresponding wavelengths for two linear modes are shown in Fig. 7.14. As one can see in the figure, both the time scales are different for either of the modes. In particular, periods tend to be much longer than the e-folding time scales for the long waves of both the modes.

We now briefly compare some facts that can be deduced from the figure to the data taken from the article by Pickart (1995). In the article, an inverse ray tracing model is applied to observations of 40-day Rossby waves near the Cape Hatteras. The results strongly suggest that such waves are radiated by the Gulf Stream in the region $71^o - 72^o W$. The radiation is well-correlated with the bursting 40-day meanders that have a typical wavelength of 370 *km*.

The most important fact to notice from Fig. 7.14 is that the most unstable wave in the problem (corresponding to the minimum of the e-folding time scale) has the wavelength of 390 km which is remarkably close to the observed most unstable wavelength (370 km). The wave has a period of 35 days and therefore can be identified with the 40-day waves

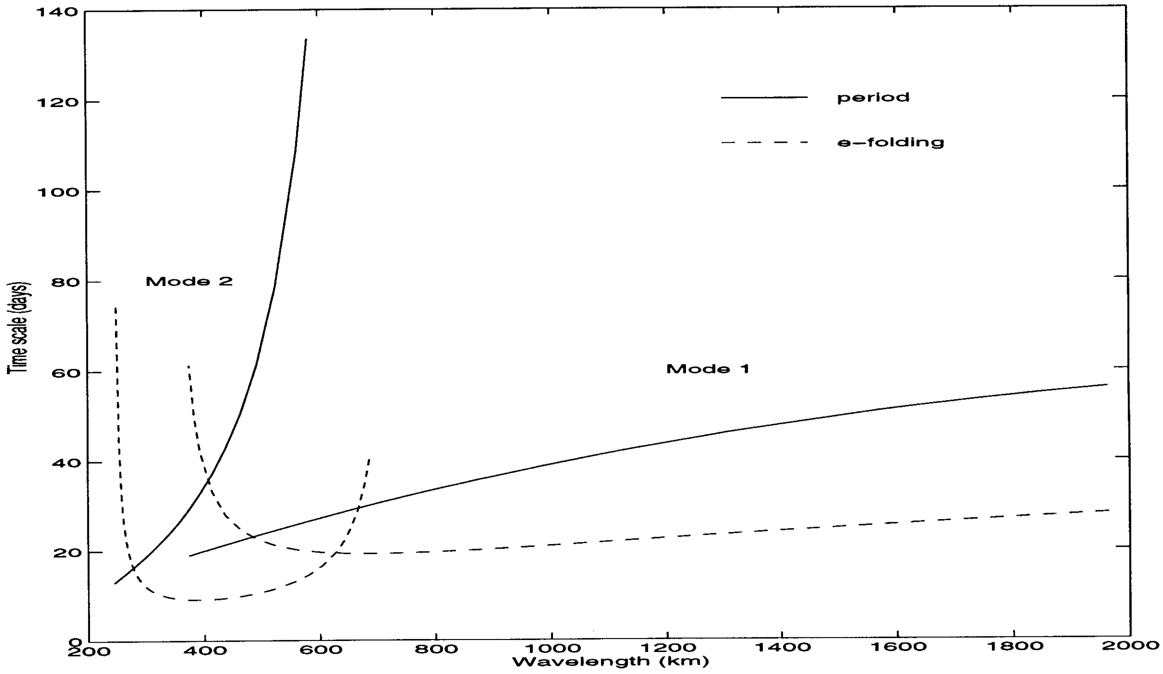

Figure 7.14: Period of phase oscillations (solid lines) and *e*-folding time scale (dashed lines) vs. wavelengths for Mode 1 and Mode 2 of the linear problem. $\beta = 1$ and $\alpha = 30°$.

to which the Gulf Stream is particularly unstable (Pickart, 1995).

One needs to realize that the nonlinear results are more relevant to the observations. It is in the finite-amplitude regime when the radiation for all wavelengths begins. As we observed in Chapter 5, both the linear time scales change significantly in the course of the nonlinear evolution. In particular, the growth rate of the kinetic energy slows during the nonlinear equilibration (sections 5.2-5.4); the phase propagation speed also changes by the beginning of the radiation in the agreement with the phase speed condition (see section 5.4.1).

However, the structure of the nonlinear solution is more complicated than that of a linear wave. To deduce the prevailing time scales, we choose to analyze the spectral time scales. That is, we look at the distribution of the Power Spectral Density (PSD) computed for the time series of spatially integrated PKE. The MATLAB routine *spectrum* is used for computing the PSD; the procedure involves dividing the time series into overlapping sections, each of which is detrended and windowed by a Hanning window. The results for cases MR1-MR4 are presented in the variance-preserving form in Fig.7.15.

Several features of the spectra are evident in the figure. All spectra have a simple form with a single maximum. The spectra peak at the following periods: MR1 at 50 days; MR2 at 70 days; MR3 at 40 days; MR4 at 80 days. The spectra are red in the short-period (high frequency) part for all cases and are slightly more white in the long-period (low frequency) part especially for MR2 and MR4. We now compare the general shape typical for all spectra computed and make the comparison with the analogous spectra obtained from the data in the North Atlantic.

For the data source, we use an article by Schmitz and Luyten (1991) in which the authors use several current meter records from different locations in the world's ocean to compute the shape of the spectrum for low-frequency fluctuations. The spectrum is divided into three broad frequency bands: high frequency (period of 2 to 20 days), eddy scale (20 to 150 days) and secular scale (150 to twice the record length). The portion of the kinetic energy that is contained within each of the three bands is reported.

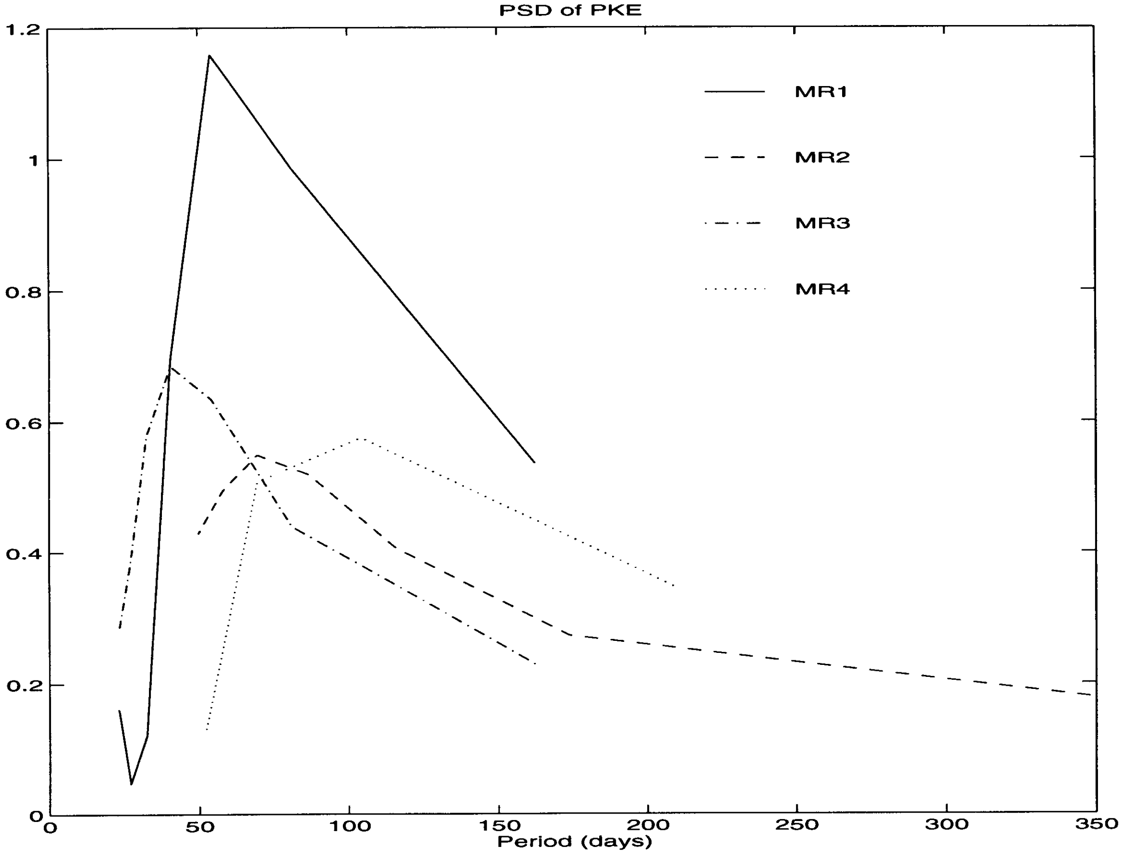

Figure 7.15: Power Spectral Density computed for the time series of PKE for four cases vs. corresponding spectral periods.

mooring	depth (m)	Secular (%)	Mesoscale(%)	HF (%)	Total EKE
771	400	48	42	19	1059
	700	47	41	12	321
	2000	33	54	13	69
780	500	38	51	11	527
	1000	39	53	8	161
	1500	34	54	11	141
784	500	23	65	12	470
	1500	27	66	7	68
788	148	18	62	20	322
	448	20	69	11	198
	998	24	69	7	42

Table 7.1: After Schmitz and Luyten (1991).

We now notice that the Nyquist frequencies of the time series of PKE in the model is too low for the detailed comparison of our results with those reported in the article for the high frequency band (Fig.7.15). Nevertheless, the comparison of the general form of the spectra is still possible if we assume smooth continuation of any of the four spectra in Fig.7.15 into the high frequency (HF) band.

For the comparison, we choose four moorings in the North Atlantic: mooring 771 at $37.6N$ $68W$ (Fig. 15 in the article), mooring 780 at $60W$ in the proximity to the Gulf Stream axis (Fig. 16), mooring 784 at $36.5N$ $63W$ (Fig. 17) and mooring 788 at $34N$ $70W$ (Fig. 18). The percentages of the total energy corresponding to each of the frequency bands are listed in the Table 7.1 for several depths.

The EKE associated with secular and mesoscale bands are close in value at moorings 771 and 780, which both are located on the Gulf Stream axis. In contrast, the HF band corresponds to much lower EKE at both moorings. In fact, the EKE associated with secular band is larger than that of the HF band for all four moorings considered. This general "redness" of the spectra is represented well by model results MR1 and MR4.

The spectra at moorings 784 and 788, which are located to the south from the Gulf Stream axis are sharply peaked at the eddy band. We now notice that all four spectra MR1-MR4 produced by our model resemble the spectra at moorings 784 and 788 in this regard: All of them to have peaks at the time scales from 40 to 80 days, as is discussed above. The ability of our simple model with the energy radiation to reproduce the general shape of the EKE spectrum in the regions away from the Gulf Stream is encouraging.

7.3 Summary

An attempt to compare the results of our simple model to the observations in the North Atlantic is made in the chapter. In doing the comparison, we keep in mind the limitations of the model and its inability to reproduce the observed dynamical fields in detail. However, several general dynamic features of the observed phenomena in the North Atlantic are captured by the model convincingly well.

Three physical quantities are chosen for the comparison. First, the perturbation kinetic energy is compared to the eddy kinetic energy observed in the North Atlantic. The level of PKE in the model appears to be close to the observed one despite the limitations of our simple model. The spatial decay scale in the cross-stream direction is reproduced remarkably well by the model. The model prediction of 300 km for the e-folding scale is supported by observations.

The distribution of uv is then analyzed. The model does not require this quantity to be of a definite sign in each of the regions to the south and to the north from the stream. Rather, the alternating positive and negative values are produced in a general agreement with observations. As for the PKE, the horizontal spatial decay scales are realistic in the model.

The analysis of the time scales completes the chapter. The most unstable linear disturbance predicted by the model has a realistic frequency and wavelength. The spectral power density for the time series of the kinetic energy for nonlinear solutions is then considered. The analyzed spectra are sharply peaked at the periods from 40 to 80 days and have shapes that resemble the observed spectra in the regions to the south from the Gulf Stream axis.

Chapter 8

Conclusions.

The present study concerns the ability of a nonzonal ocean current to support unstable disturbances that are not spatially trapped to the current, but rather are of radiating nature. These radiating instabilities can effectively transfer the kinetic energy of the basic current initially localized in space, into the regions remote from such an energy source. An energetic eddy field can be induced in the far-field as a result.

Two main issues are addressed in the study. The first is the difference in radiating and stability properties between a zonal and nonzonal flow. The second is the effects that nonlinear interactions have on the radiating properties of a solution in the finite-amplitude regime.

A simple QG model with a nonzonal current as a basic state is used in the study. Most computations are performed for a barotropic ocean. The work consists of two major parts: linear theory and nonlinear computations. The main findings are listed below and divided in the two parts accordingly.

Linear theory.

The dynamical properties in the linear model with a nonzonal basic current are different from those in a conventional model with a zonal flow. The differences in the stability properties can be illustrated by the example of the derived sufficient condition for the absence of any stable solutions for a nonzonal flow (see section 2.2 for details). The criterion becomes a conventional sufficient condition for *stability* if the stream axis is made zonal.

The vulnerability of a nonzonal current to radiation can be anticipated from the new form of the phase speed condition. This widely used criterion for radiation requires the possibility of the coupling between an unstable disturbance and a free Rossby wave. If a mean current is nonzonal, the phase speed condition allows the downstream propagating disturbances to be radiating. In contrast, such coupling between downstream propagating disturbances and westward propagating Rossby waves is not possible for an eastward zonal flow.

The fast exponential growth of linear unstable solutions generally leads to their strong spatial trapping to the basic current. Therefore, the task of determining if a growing disturbance is truly evanescent or its radiating nature is simply disguised by the effects of the fast growth, is difficult in the linear problem. The only way to distinguish between those two types of solutions is to consider the limit of the vanishing growth rate. If in this limit a solution becomes purely wave-like in the far-field, we classify it as radiating.

The detailed stability analysis confirms our expectations that a nonzonal current is a more radiating basic state than a zonal flow. Slowly growing long waves are radiating if the current axis is tilted horizontally, whereas all solutions for a zonal flow are spatially trapped. The radiation is observed as long as the angle of the tilt is nonzero. The energy equation for radiating solutions becomes a balance between the energy conversion term, that transfers the energy from the basic state to the growing perturbations and the flux terms, that carry energy into the far-field.

The addition of a second moving layer does not change the structure of the radiating solutions. In fact, the depth-averaged part of the solutions is still radiating, whereas the baroclinic part is trapped to the jet region. The barotropic energy conversion term dominates over the baroclinic term, making the radiation essentially a barotropic process.

Nonlinear studies

The radiation of short waves that are strongly linearly unstable and trapped during the initial stage of development, takes place during the nonlinear equilibration in the model with a nonzonal current. The fast initial growth of those waves, which is the main cause for their spatial trapping, slows significantly during the equilibration and a solution starts to expand in the cross-jet direction.

As in the linear problem, the difference in the radiating properties between a zonal flow and a nonzonal current is large. The radiation by the zonal flow is weak and takes place as a result of the transient growth of secondary instabilities in the model. In contrast, the radiation is robust and very energetic if the horizontal tilt is different from zero.

We initialize the model with either a single linear mode or a pair of unstable waves. A wide spectrum of secondary modes is generated in the course of nonlinear development, in addition to the primary modes, as a result of wave-wave interactions. All these components become radiating when they reach finite amplitude. The radiation typically starts in the form of the x-independent component that represents the change in the x-averaged momentum. The other harmonics in x follow; they extend into the regions remote from the axis of the basic current resulting in the complex spatial structure of the radiating response in the far-field.

Although the details of the development depend on the initial conditions used in any particular numerical experiment, the transfer of energy is effective in all cases. A large portion of the perturbation kinetic energy is contained in the far-field by the end of all numerical experiments described in the present work.

The consideration of several parameters allowed us to conclude that the strength of radiation is mainly controlled by the value of the horizontal tilt. Therefore, it is the nonzonal orientation of the basic current axis that is a key factor in the new discovered mechanism for radiation.

Despite its simplicity, the model successfully reproduces some observed phenomena in the North Atlantic. In particular, the general features of the horizontal structure of the observed eddy kinetic energy and Reynolds stress are captured correctly by the model.

These results stress the possibility to describe the eddy variability in the North Atlantic interior as being in large part remotely generated by the Gulf Stream.

Following a series of similar studies, the presented work emphasizes the importance of the energy radiation from boundary currents as one of the main mechanisms for the generation of eddies in the oceanic interior. As it is demonstrated by the results, taking into account such dynamical features of the structure of radiating basic states as their nonzonal orientation can enhance the mechanism. Further elaboration of the models with radiating basic states should include more realistic downstream and vertical dependence of the basic current.

Two main results of the present research provide some guidance for the use of ocean general circulation models. First, the correct representation of the nonzonal orientation of the Gulf Stream leaving the coast is crucial for the reproduction of the large-scale distribution of eddy kinetic energy in the North Atlantic. Second, the importance of the non-local mechanism for the eddy generation calls for the revision of some existing techniques for the eddy parameterization in coarse resolution models.

Appendix A

A.1 Dispersion relation for the two-layer top-hat profile

The solution consists of the sum of four waves $A_n e^{il_n y}$ in the internal region ($n = 3, 4, 5, 6$) and two waves of the same form in each of the external regions: $y < -1$ ($n = 1, 2$) and $y > 1$ ($n = 7, 8$). The application of the jump conditions 4.6, 4.7 results in the linear problem:

$$\mathbf{DA} = \mathbf{0},$$

where **A** is a 8 by 1 amplitude vector, and **D** is a following 8 by 8 matrix:

$$\begin{pmatrix} -e^{-il_1} & -e^{-il_2} & e^{-il_3} & e^{-il_4} & e^{-il_5} & e^{-il_6} & 0 & 0 \\ 0 & 0 & e^{il_3} & e^{il_4} & e^{il_5} & e^{il_6} & -e^{il_7} & -e^{il_8} \\ -l_1 e^{-il_1} & -l_2 e^{-l_2} & l_3 e^{-il_3} & l_4 e^{-il_4} & l_5 e^{-il_5} & l_6 e^{-il_6} & 0 & 0 \\ 0 & 0 & l_3 e^{il_3} & l_4 e^{il_4} & l_5 e^{il_5} & l_6 e^{il_6} & -l_7 e^{il_7} & -l_8 e^{il_8} \\ -c^2 l_1^2 e^{-il_1} & -c^2 l_2^2 e^{-il_2} & B_3 e^{-il_3} & B_4 e^{-il_4} & B_5 e^{-il_5} & B_6 e^{-il_6} & 0 & 0 \\ 0 & 0 & B_3 e^{il_3} & B_4 e^{il_4} & B_5 e^{il_5} & B_6 e^{il_6} & -c^2 l_7^2 e^{il_7} & -c^2 l_8^2 e^{il_8} \\ -E_1 e^{-il_1} & -E_2 e^{-il_2} & C_3 e^{-il_3} & C_4 e^{-il_4} & C_5 e^{-il_5} & C_6 e^{-il_6} & 0 & 0 \\ 0 & 0 & C_3 e^{il_3} & C_4 e^{il_4} & C_5 e^{il_5} & C_6 e^{il_6} & -E_7 e^{il_7} & -E_8 e^{il_8} \end{pmatrix}$$

where

$$B_n = c^2 l_n^2 - c(k^2 + l_n^2) - \beta_2 + \beta_1 \frac{l_n}{k}$$

$$C_n = l_n^3 c(1-c) + l_n^2 \frac{\beta_1}{k}(2c-1) + l_n(c(k^2+F) + \beta_2 - F) + cF)$$

$$E_n = -l_n^3 c^2 + l_n^2 \frac{\beta_1}{k} 2c.$$

The dispersion relation $c = c(k; F, \beta_1, \beta_2)$ is found numerically from solving the nonlinear equation $det\mathbf{D} = 0$ using the modified Newton Method.

A.2 Continuous jet: numerical method

A.2.1 Barotropic problem

The method of solution involves writing the problem in the finite interval: $-1 < y < 1$. Since the form of the solution in the external regions is known for us, $\phi(y) = Ae^{ily}$, from the continuity of the solution at $y = \pm 1$ we can derive the following boundary conditions:

$$\phi_y - il_{1,4}\phi = 0 \qquad at \qquad y = \mp 1$$

$l_{1,4}$ is defined by (3.1) with the appropriate choice of the sign of an imaginary part satisfying the condition of the spatial decay at infinity (7). In other words, $Imag(l_1) < 0$ and $Imag(l_4) > 0$.

Then, we can use the Shooting Technique. We start from an initial guess of c, and integrate the equation (2.6) from -1 to 1. Function $F(c) = (\phi_y - il_4\phi)|_{y=1}$ is our discrepancy function and we find value of c that makes F zero using initial guess improvement,

$$c = c - F(c)\left(\frac{\partial F(c)}{\partial c}\right)^{-1},$$

until the desired accuracy is met. The derivative $\partial F/\partial c$ is computed numerically:

$$\frac{\partial F(c)}{\partial c} = \frac{F(c+\delta c) - F(c)}{\delta c}$$

A.2.2 Two-layer problem

Solution now consists of the sum of two waves in the each of the external regions: $A_1 e^{il_1 y} + A_2 e^{il_2 y}$ in $y < -1$ and $A_7 e^{il_7 y} + A_8 e^{il_8 y}$ in $y > 1$ (the notation is kept the same as in appendix A). From the continuity of the streamfunction and its first derivative in both layers we can derive boundary conditions for the problem in a finite interval:

$$F_1 = (l_{1,7} - l_{2,8})\phi_y + \phi_2(K_{1,7}l_{2,8} - K_{2,8}l_{1,7}) + i\phi_{2y}(K_{1,7} - K_{2,8}) = 0$$

$$F_2 = (l_{1,7} - l_{2,8})\phi_{1y} + i\phi_2(K_{1,7} - K_{2,8})l_{1,7}l_{2,8} + \phi_{2y}(K_{2,8}l_{2,8} - K_{1,7}l_{1,7}) = 0$$

at $y = -1, +1$; where $K_n = (c(k^2 + l_n^2 + F) + \beta_2 - FU - \beta_1 l_n/k)/cF$. $K = \pm 1$ in the external regions($U = 0$).

For the solution of the stated problem we use Shooting Technique described above. We pick two unknown values: c and $\gamma = \phi_{2y}$ at $y = -1$. We normalize the solution choosing $\phi_2(-1) = 1$. Next, we compute $\phi_1(-1), \phi_{1y}(-1)$ from the boundary conditions at $y = -1$ and integrate (4.3). We improve our guess, using

$$\begin{pmatrix} c \\ \gamma \end{pmatrix} = \begin{pmatrix} c \\ \gamma \end{pmatrix} - \mathbf{J}^{-1} \begin{pmatrix} F_1 \\ F_2 \end{pmatrix}_{y=1},$$

where

$$\mathbf{J} = \begin{pmatrix} \frac{\partial F_1|_{y=1}}{\partial c} & \frac{\partial F_2|_{y=1}}{\partial c} \\ \\ \frac{\partial F_1|_{y=1}}{\partial \gamma} & \frac{\partial F_2|_{y=1}}{\partial \gamma} \end{pmatrix}.$$

All derivatives in matrix $\mathbf{J}$ are computed numerically. Iterations are repeated until the desired accuracy is met.

For the portion of the dispersion curve for the Mode 2 the integration was performed from $y = 1$ to $y = -1$.

A.3 Open boundary conditions

For the open boundary conditions we use the modified Orlanski boundary conditions (5.3). For the finite-difference form, we first write (5.3) with unknown propagation speed c (Blumberg and Kantha, 1985):

$$\frac{\psi_N^t - \psi_N^{t-2}}{2\Delta t} + \frac{c}{\Delta y}\left[\frac{1}{2}\left(\psi_N^t + \psi_N^{t-2}\right) - \psi_{N\mp 1}^{t-1}\right] = -\frac{\psi_N^{t-2}}{T_f} \tag{A.1}$$

The index N represents a grid point on the open boundary. The upper sign in the double-sign expressions corresponds to the boundary on the right and the lower sign corresponds to the boundary on the left. x-dependence is omitted form all expressions in this section.

The next step is to determine the propagation speed c. To do that, we write the above expression now for a grid point neighboring to the boundary $N \mp 1$, rather than at the boundary itself, and without the dumping term. We get the expression for c (Orlanski, 1976):

$$c = -\frac{\psi_{N\mp1}^{t} - \psi_{N\mp1}^{t-2}}{\frac{1}{2}\left(\psi_{N\mp1}^{t} + \psi_{N\mp1}^{t-2}\right) - \psi_{N\mp2}^{t-1}} \frac{\Delta y}{2\Delta t} \tag{A.2}$$

As is pointed out in Orlanski (1976), we need also to make sure that the disturbance propagates *to* the boundary. Therefore, c should be set to zero if the expression A.2 gives negative number for the right boundary and positive value for the left boundary.

The above conditions have proved to work very well for most cases in our model. The experiments show in particular, that open boundary conditions result in much less reflection than if sponge layers were used.

A.4 Parameters used in the numerical experiments.

Single wave	α	β	k	$A_{initial}$	t_{total}	Δt	N_y	Δy	N_x	Δx
Mode 1	0	1	1	.013	96	.005	600	.05	65	.1963
Mode 1	5	1	1	.013	72	.005	600	.05	65	.1963
Mode 1	30	1	1	.013	72	.005	600	.05	65	.1963
Mode 1	30	1	.25	.058	96	.0016	1000	.05	65	.3927
Mode 1	30	.25	1	.058	112	.005	600	.05	65	.1963
Mode 2	30	1	1.8	.055	52	.0025	400	.1	65	.2182
Pair of waves										
Mode 1 Mode 2	30	1	1 2	.067 .028	52	.0016	800	.05	65	.1963
Mode 1 Mode 2	30	1	1 1.5	.067 .045	52	.0016	800	.05	65	.1963
Mode 1 Mode 1	30	1	.25 1	.055 .014	64	.0016	1000	.05	129	.1963

References

Blumberg, A.F., and Kantha, L.H. 1985. Open boundary condition for circulation models. *J. Hydraulic Eng.*, **111**(2).

Bower, A.S., and Hogg, N.G. 1992. Evidence for barotropic wave radiation from the Gulf Stream. *J. Phys. Oceanogr.*, **22**, 42–61.

Drazin, P.G., Beaumont, D.N., and Coaker, S.A. 1982. On Rossby waves modified by basic shear, and barotropic instability. *J. Fluid Mech.*, **124**, 439–456.

Durran, D.R., Yang, M-J, Slinn, D.N., and Brown, R.G. 1993. Toward more accurate wave-permeable boundary conditions. *Mon. Wea. Rev.*, **121**, 604–620.

Flierl, G.R., and Kamenkovich, V.M. 1975. Gulf Stream meandering and Gulf Stream Ring eddy production mechanisms. *Pages 115–118 of:* Robinson, A.R. (ed), *Dynamics and the analysis of MODE-1.* MIT.

Freeland, H.J., Rhines, P.B., and Rossby, T. 1975. Statistical observations of neutrally buoyant floats in the North Atlantic. *J. Mar. Res.*, **33**, 383–404.

Gill, A.E., Green, J.S.A., and Simmons, A.J. 1974. Energy partition in the large-scale ocean circulation and the production of mid-ocean eddies. *Deep-Sea Res.*, **21**, 499–528.

Halkin, D., and Rossby, T. 1985. The structure and transport of the Gulf Stream at 73W. *J. Phys. Oceanogr.*, **15**, 1439–1452.

Hall, M.M., and Bryden, H.L. 1985. Profiling the Gulf Stream with a current meter mooring. *Geoph. Res. Let.*, **12**, 203–206.

Held, I.M., and Larichev, V.D. 1995. A scaling theory for horizontally homogeneous baroclinically unstable flow on a beta plane. *J. Atmos. Sci.*, **53**, 946–952.

Hogg, N.G. 1988. Stochastic wave radiation by the Gulf Stream. *J. Phys. Oceanogr.*, **18**, 1687–1701.

Hogg, N.G. 1992. On the transport of the Gulf Stream between Cape Hatteras and the Grand Banks. *Deep-Sea Res.*, **39**, 1231–1246.

Hogg, N.G. 1994. Observations of Gulf Stream meander induced disturbances. *J. Phys. Oceanogr.*, **24**(12), 2534–2545.

Ierly, G.R., and Young, W.R. 1991. Viscous instabilities in the western boundary layer. *J. Phys. Oceanogr.*, **21**, 1323–1332.

Johns, W.E., Shay, T.J., Bane, J.M., and Watts, D.R. 1995. Gulf Stream structure, transport, and recirculation near 68° W. *J. geoph. res.*, **100**, 817–838.

Kamenkovich, I., and Pedlosky, J. 1996. On the correct matching and boundary conditions for a radiating broken-line current. *J. Phys. Oceanogr.*, **26**, 1664–1665.

Kang, Y.Q., Price, J.M., and Magaard, L. 1982. On stable and unstable Rossby waves in non-zonal oceanic shear flow. *J. Phys. Oceanogr.*, **12**, 528–537.

Larichev, V.D., and Held, I.M. 1995. Eddy amplitudes and fluxes in a homogeneous model of fully developed baroclinic instability. *J. Phys. Oceanogr.*, **25**, 2285–2297.

Lee, D.K., and Niler, P.N. 1987. The local baroclinic instability of geostrophic spirals in the Eastern North Pacific. *J. Phys. Oceanogr.*, **17**, 1366–1377.

Malanotte-Rizzoli, P., Haidvogel, D.B., and Young, R.E. 1987a. Numerical simulation of transient boundary-forced radiation. Part I: The linear regime. *J. Phys. Oceanogr.*, **17**, 1440–1457.

Malanotte-Rizzoli, P., Haidvogel, D.B., and Young, R.E. 1987b. Numerical simulation of transient boundary-forced radiation. Part II: The modon regime. *J. Phys. Oceanogr.*, **18**, 1546–1569.

Malanotte-Rizzoli, P., Hogg, N.G., and Young, R.E. 1995. Stochastic wave radiation by the Gulf Stream: Numerical experiments. *J. Phys. Oceanogr.*

McIntyre, M.E., and Wessman, M.A. 1978. On radiating instabilities and resonant overreflection. *J. Atmos. Sci.*, **35**, 1190–1196.

Orlanski, I. 1976. A simple boundary condition for unbounded hyperbolic flows. *J. Comput. Phys.*, **21**, 251–269.

Pedlosky, J. 1964. The stability of currents in the atmosphere and the ocean. Part I. *J. Atmos. Sci.*, **21**, 201–219.

Pedlosky, J. 1975. A note on the amplitude of baroclinic waves in the mid-ocean. *Deep-Sea Res.*, **22**, 575–576.

Pedlosky, J. 1977. On the radiation of meso-scale energy in the mid-ocean. *Deep-Sea Res.*, **24**, 591–600.

Pedlosky, J. 1987. *Geophysical fluid dynamics.* Second edn. Springer-Verlag.

Pickart, R.S. 1995. Gulf Stream-generated topographic Rossby waves. *J. Phys. Oceanogr.*, **25**, 574–586.

Press, W.H., Teukolsky, S.A., Vetterling, W.T., and Flannery, B.P. 1992. *Numerical Recipes.* Second edn. Cambridge University Press.

Richardson, P.L. 1983. Eddy kinetic energy in the North Atlantic from surface drifters. *J. Geophys. Res.*, **88**, 4355–4367.

Rossby, T. 1987. On the energetics of the Gulf Stream at 73W. *J. Mar. Res.*, **45**, 59–82.

Schmitz, W.J. 1982. A comparison of the Mid-Latitude Eddy Fields in the Western North Atlantic and North Pacific Oceans. *J. Phys. Oceanogr.*, **12**, 208–210.

Schmitz, W.J., and Luyten, J.R. 1991. Spectral time scales for mid-latitude eddies. *J. Mar. Res.*, **49**, 75–107.

Spall, M.A. 1992. Rossby wave radiation in the Cape Verde frontal zone. *J. Phys. Oceanogr.*, **22**, 796–807.

Spall, M.A., Richardson, P.L., and Price, J. 1993. Advection and eddy mixing in the Mediterranean salt tongue. *J. Mar. Res.*, **51**, 797–818.

Talley, L.D. 1983. Radiating barotropic instability. *J. Phys. Oceanogr.*, **13**, 972–987.

Wunsch, C.I. 1983. *Eddies in marine science.* Springer-Verlag. Chap. West Atlantic interior., pages 46–65.

Wyrtki, K., Magaard, L., and Hager, J. 1976. Eddy energy in the oceans. *J. Geophys. Res.*, **81**, 2641–2646.

Yun, Jae-Yul. 1986. *Baroclinic instabilities of nonzonal ocean currents with application to the Kuroshio Extention current.* Ph.D. thesis, University of Hawaii.

Yun, Jae-Yul, Price, J.M., and Magaard, L. 1995. Radiating instability of nonzonal oceanic shear flows with application to the Kuroshio Extention Current. *J. Phys. Oceanogr.*, **25**, 1788–1804.